Nonlinear Dynamics of a Loosely-Supported Cylinder in Cross-Flow

by

Njuki W. Mureithi

Department of Mechanical Engineering

McGill University

Montreal, Canada

May 1993

A Thesis submitted to the Faculty of Graduate Studies and Research
in partial fulfilment of the requirements for the degree of
Doctor of Philosophy

ISBN 0-315-91705-9

kũrĩ maitũ Wangarĩ

ABSTRACT

Loosely supported cylinders subjected to cross-flow may underge fluidelastic instability in the support inactive mode resulting in cylinder/support impacting. The cylinder/support interaction forces and, in turn, the resulting cylinder wear rates are strongly dependent on the detailed dynamical response. This Thesis examines the response of a loosely supported cylinder located in the third row of an otherwise rigid rotated triangular array. The feasibility and potential of a modern nonlinear dynamics approach to the understanding of the underlying dynamics is investigated.

A nonlinear quasi-steady model was formulated to model the dynamical behaviour. The steady fluid force field, required as input to the model, was measured experimentally for a cylinder within a rotated triangular array. A linear stability analysis showed the cylinder stability behaviour to be strongly dependent on cylinder position. This result serves as a possible explanation for the rare occurrence of, theoretically predicted, multiple instability regions in experimental measurements.

The nonlinear analysis uncovered two important transition routes to chaos. The first, a *switching mechanism* prevalent at the onset of impacting. The second and most important is the *intermittency* route to chaos. The theoretical model showed good agreement with experiments in predicting the bifurcation sequences and transitions to chaos — comparisons were quantified via fractal dimensions and *saddle orbit* distributions.

The identification of *type I intermittency* leads to a quantitative estimate of the probability distribution of the length of laminar phases. It is shown that the average duration of laminar phases and the associated frequency may provide better estimates of integration time and frequency for wear-rate computation.

SOMMAIRE

Les tubes attachés aux supports intermédiaires lâches et soumis à un écoulement transversal peuvent subir des instabilités fluidélastiques dans le mode inactif du support qui entraînent des chocs entre le tube et le support. Les forces d'interaction tube/support, puis les taux d'usure des tubes qui en résultent, dépendent en grande partie de la réponse dynamique détaillée. Cette Thèse se propose d'étudier la réponse d'un tel tube situé dans la troisième rangée d'un faisceau de tubes rigides à géométrie triangulaire pivotée. Elle examine la possibilité d'utiliser une approche de la dynamique non-linéaire moderne qui permettrait de mieux comprendre la dynamique sous-jacente.

Pour modéliser le comportement dynamique, un modèle non-linéaire quasi-constant a été élaboré. Le champ constant de force du fluide, requis par le modèle, a été obtenu expérimentalement pour un tube situé dans un faisceau à géométrie triangulaire pivotée. Une analyse de stabilité linéaire a démontré que la stabilité du tube repose surtout sur sa position. Ce résultat explique peut-être pourquoi peu de zones d'instabilité multiple prédites de manière théorique se retrouvent dans les mesures expérimentales.

L'analyse non-linéaire identifie deux routes importantes de transition vers le chaos. La première correspond à un *mécanisme de commutation* prédominant aux vitesses d'écoulement proches du premier du choc. La seconde, qui est aussi la plus importante, est *la route d'intermittence* vers le chaos.

Les résultats obtenus au moyen du modèle théorique correspondent bien avec ceux obtenus expérimentalement en prédisant les séquences de bifurcation et les transitions vers le chaos. Des mesures quantitatives, qui incluent les dimensions fractales et les distributions *d'orbites de col*, elles-mêmes associées aux attracteurs chaotiques dans le système expérimental, ont également été assez bien prédites.

L'identification de *l'intermittence de type I* conduit à une estimation quantitative de la distribution de la probabilité de la longueur de phases laminaires dans le régime à réponse intermittente. On a montré que la longueur des phases laminaires et la fréquence associée pourraient donner de meilleures estimations de taux d'usure du tube.

ACKNOWLEDGEMENTS

The author is greatly indebted to Professors S.J. Price and M.P. Paidoussis for their invaluable advice and guidance throughout the course of this work.

The helpful suggestions and constructive discussions with fellow colleagues in the fluid-structure interaction group were invaluable to this research. For this the author is grateful.

Many thanks to Mr. Bill Mark for his advice and help with data acquisition aspects of the project. Special thanks to Mr. S. Markhauser for his help with the construction of the experimental apparatus.

To Mũthoni, nĩweega mũno nĩ marĩa moothe ũũnjĩkĩire.

To Dr. Lang'at Cheluget, koongoi miising.

Special thanks are extended to the author's family for their unwavering support and encouragement — Mũaathani amũraathime mũno.

The financial support of the Natural Sciences and Engineering Research Council of Canada and Le Fonds pour la Formation de Chercheurs et l'Aide à la Recherche du Québec (FCAR) is acknowledged with gratitude.

Statement of Contribution to Original Knowledge

Experimenters investigating the wear of loosely supported unstable cylinders have concluded that cylinder wear rates are intimately related to the detailed dynamical behaviour. The dynamics of a loosely supported cylinder is the subject of the study presented here. Below are the contributions of this Thesis to original knowledge:

- Position dependent steady fluid forces were for the first time measured in a rotated triangular array for all tube positions in the third row of the array. A linear stability analysis showed that variations in cylinder position may drastically alter expected cylinder stability.

- The detailed dynamical behaviour of a loosely-supported cylinder was determined. To the author's knowledge this is the first quantitative elucidation, of the detailed dynamics, involving direct comparison of theory and experiments. The identification of *types I and III intermittency transitions* to chaos as well as the *switching mechanism* is believed to be a first in fluid-structure interaction.

- The average duration of *laminar phases*, and corresponding frequency, are shown to be applicable to wear-rate computation.

Table of Contents

List of Figures

List of Tables

NOMENCLATURE

a	ratio of gap velocity to free-stream velocity, $U/U_\infty = T/(T - D/2)$, T being the cylinder spacing in the y direction
c	cylinder material damping coefficient
c_s	squeeze-film damping
$C(\epsilon)$	pairwise correlation of points in phase space
C_D, C_L	drag and lift coefficients based on U_∞
C_{ma}	added mass coefficient
C_V	fluid damping coefficient
C_K	fluid stiffness coefficient
d_c	capacity dimension
d_{cr}	(average) correlation dimension
D, D_i	(outer) cylinder diameter, internal cylinder diameter
D	dimension
$\mathbf{D}$	fluidelastic damping matrix
e	coefficient of restitution
e_r	radial tube/support clearance
$\tilde{e}_r$	non–dimensional tube/support clearance, e_r/D
E_k	kinetic energy
EI	flexural rigidity
f	cylinder fluidelastic frequency
f_0	cylinder natural frequency
F_{xf}, F_{yf}	fluid force in the in-flow and cross-flow directions
F_{xs}, F_{ys}	support force in the in-flow and cross-flow directions
$\mathbf{F}_{xs}, \mathbf{F}_{ys}$	generalized support-force vectors in the in-flow and cross-flow directions

F_r	radial force at support
F_{ri}, F_{rd}	stiffness and damping related components of F_r
F_θ	tangential force at support
$\mathbf{F_0}$	steady fluid-force vector
$Im(\ )$	Imaginary part of ( )
K	Connor's constant
K_s	effective contact stiffness
$\mathbf{K}$	fluidelastic stiffness matrix
l	cylinder length
L	in-flow spacing between cylinder rows
m	cylinder mass per unit length
m_a	added mass per unit length
$\mathbf{M}$	mass matrix, including added mass
$\mathcal{M}$	moment
$\tilde{m}$	non-dimensional cylinder mass per unit length, $m/\rho D^2$
P	center-to-center inter-cylinder pitch
P_l	probability distribution of laminar-phases durations
p_i	ith mode generalized coordinate in the in-flow direction
q_i	ith mode generalized coordinate in the cross-flow direction
r	tube radial position, $(x^2+y^2)^{1/2}$
$Re(\ )$	Real part of ( )
Re	Reynolds number
St	squeeze-film Stokes number
t	time
t_l	laminar-phase duration
t_s	support thickness
U_∞	free-stream velocity
U	reference gap flow velocity
U_c	critical gap flow velocity

U_r	flow velocity relative to moving cylinder
u_r, u_t	radial and tangential tube velocities before impact
v_r, v_t	radial and tangential tube velocities after impact
v_θ	transverse sliding velocity
V	dimensionless reference gap flow velocity, $U/\omega D$
V_c	dimensionless critical flow velocity
V_{cf}	intermittency threshold
$\mathcal{V}$	shear force
$\mathbf{w}$	cylinder displacement vector in generalized coordinates
$\overline{\dot{W}}$	average wear work-rate
X	in-flow peak displacement
x, y	in-flow and cross-flow cylinder displacements
$\tilde{x}$, $\tilde{y}$	non-dimensional cylinder displacements
$\tilde{x}_0$, $\tilde{y}_0$	non-dimensional cylinder response amplitudes
α	flow approach angle
$\overline{\beta}$	empirical squeeze-film damping factor
δ	in-air cylinder mechanical logarithmic decrement
$\overline{\delta}$	Dirac delta function
Δt	time delay
ΔE_k	kinetic energy change
ζ	combined fluid and mechanical damping factor
ζ_0	tube mechanical damping factor
ζ_{sf}	squeeze-film damping
ζ_{vs}	viscous shear damping
$\tilde{\zeta}_i$	modal damping
λ	eigenvalue
μ	bifurcation parameter
μ_c	critical bifurcation parameter value
μ_{fr}	Coulomb coefficient of dry friction at tube/support contact surface

μ_p	intermittency parameter, $(V - V_{cf})/V_{cf}$
μ_r	flow retardation parameter
ν	Poisson's ratio
ν_f	fluid viscosity
ρ	fluid density
ρ_s	support-material density
τ	non-dimensional time, ωt
ϕ_i	ith beam eigenfunction
Ψ	Heaveside function
ω	cylinder radian oscillation frequency
ω_{sn}	saddle orbit frequency

Chapter 1

INTRODUCTION

As research into the problem of fluid-structure interaction in cylinder arrays subjected to cross-flow enters its fourth decade of concerted effort, significant developments have taken place both in understanding the underlying governing mechanisms, as well as towards theoretical modelling for prediction of structural response to fluid excitation. The understanding of flow-induced vibration in cylinder arrays is vital for the design of heat exchangers, to eliminate undesired tube[1] instabilities which may lead to gradual tube wear or catastrophic failure.

Identification of two of the three excitation mechanisms to which such systems are subjected, turbulent buffeting and flow periodicities, derived naturally from studies aimed at understanding the fundamental fluid dynamics of turbulent flows and the earlier observations of periodic vortex shedding for flow over solitary bluff bodies.

The third and most potent mechanism, that underlying fluidelastic instability, was more elusive. For cylindrical structures subjected to cross-flow, fluidelastic instability is only possible for multiple cylinders. Hence, unlike the other two mechanisms, no analogy could be made with the case of a single cylinder subjected to cross-flow. Fluidelastic instability is characterized by a critical flow velocity, past which cylinder instability is initiated. The instability is the result of a positive feedback mechanism through which net energy is extracted from the flowing fluid, to balance the energy loss through both the cylinder internal structural damping and the external flow-induced damping.

[1]The words "tube" and "cylinder" will be used interchangeably; in some cases this is necessary for consistency in reference to other investigators' work.

1.1 DEVELOPMENTS IN FLUIDELASTIC INSTABILITY THEORIES

Following the identification of fluidelastic instability as a distinct phenomenon, several theoretical models have been developed, enabling approximate prediction of the critical instability velocity as well as an understanding of the governing mechanisms. In this section, the developments leading to the present understanding of fluidelastic instability are reviewed. This review is by no means exhaustive. It is intended to give the reader a good overall picture of the collective effort of numerous researchers. There is also an intentional bias in detail, towards work that leads directly to the subject treated in this Thesis, which clarifies the motivation for the present study.

The first attempt to analytically model and explain fluidelastic instability was by Roberts (1962, 1966), who proposed a jet-switching mechanism behind a staggered row of cylinders which, when synchronized with cylinder motion, could result in net energy input to the cylinder per cycle of oscillation. In his model, fluidelastic instability was predicted for in-flow cylinder vibration. A crucial component of the model is the hysteresis in the variation of the cylinder base pressure with cylinder displacement, which makes positive energy feedback possible for large enough cylinder displacement.

Unquestionably the most widely accepted and used formula for predicting the critical flow velocity for fluidelastic instability was developed by Connors (1970). Studying a flexible row of cylinders, Connors proposed a semi-empirical quasi-static model, in which a time-dependent displacement mechanism resulted in net energy being extracted from the fluid by the vibrating cylinders. Connors measured cylinder lift (C_L) and drag (C_D) coefficients as functions of inter-cylinder positions; where cylinder displacements were along trajectories following an idealized mode of vibration during instability. The same hysteretic discontinuity in C_D as obtained by Roberts (1962, 1966) was again observed in the experimental measurements. However, Connors subtracted this jet-switch effect, having recognized that it was not the predominant effect, thus being left with a "pure" displacement-related variation; Connors remarked that a highly specialized set of circumstances was required for the occurrence of jet-switching coupled with a finite minimum time necessary for the jet-switch to be possible. The now famous stability criterion of Connors was derived by equating fluid-energy input per cycle to the energy dissipation through damping. The critical flow velocity for fluidelastic instability U_c is given by

$$\frac{U_c}{f_0 D} = K\sqrt{\frac{m\delta}{\rho D^2}} \tag{1.1}$$

where U is the flow velocity through the minimum gap between adjacent cylinders in the same row (subscript c indicating a critical velocity), and m, δ and f_0 are cylinder mass per unit length, logarithmic decrement of damping and natural frequency, respectively; for a staggered row of cylinders with inter-cylinder spacing $P/D = 1.41$, $K = 9.9$ was obtained by Connors. As noted later in reviews by Paidoussis (1983), Weaver & Fitzpatrick (1988) and others, equation (1.1) was extensively, and incorrectly, used for heat exchanger *cylinder array* design, despite its having been derived for a *row* of flexible cylinders.

Blevins (1974, 1977, 1979) re-derived Connors' displacement mechanism model, albeit following a different approach, and extended the theory to cylinder arrays. The stability criterion obtained by Blevins was an expression for the critical flow velocity of the same form as equation (1.1). For the single row of cylinders studied by Connors, Blevins' stability criterion reduced to equation (1.1) if Connors' experimental force coefficients were utilized. Two other developments by Blevins were (i) an attempt to analytically determine the fluid force coefficients which lead to the value of the constant K and (ii) an extension of the theoretical model to account for the flow-dependent fluid damping.

The basic form of equation (1.1) was retained by many researchers who concentrated their efforts on experimental measurements of U_c and on correlating with $m\delta/\rho D^2$ to determine K for various array geometries and inter-cylinder spacing. Suggested values for K vary from 0.8 (Paidoussis, 1980) to 8.6 (Blevins, 1977). The value

$K = 3.3$ (Pettigrew *et al.*, 1978; Connors, 1978) has been widely accepted by heat exchanger designers, although recently it was revised downwards (Pettigrew & Taylor, 1991). In their review, Weaver & Fitzpatrick (1988) discuss the various efforts undertaken to determine K from correlation with experimental results, and they also provide design guidelines to avoid fluidelastic instability.

It was clear from the outset, however, that better modelling and determination of fluid force coefficients was required. The complexity of the flow structure within the array made analytical determination of the fluid forces practically impossible. Nevertheless, for arrays with small wake regions, an attempt to determine the fluid forces using potential flow theory was made by Chen (1975, 1978), Balsa (1977) and Paidoussis *et al.* (1984). Forces proportional to fluid inertia (added mass effects) were found to agree well with experimental measurements. On the other hand, velocity- and displacement-dependent forces, which are strongly affected by fluid viscosity, could not be correctly determined. Inviscid potential flow theory also rendered the system conservative; hence, no dynamic instabilities could be precipitated by the fluid forces therein. While potential flow models made it possible to determine added mass effects relatively accurately, it became clear that fluid viscous effects could not be ignored. Paidoussis *et al.* (1985) therefore incorporated heuristically a phase lag between cylinder motion and the resulting fluid forces to account for the viscous nature of the flow. An analysis of a rotated triangular array with $P/D = 1.3$ or 1.5 showed that dynamic instabilities occurred for non-zero values of the phase lag, while static instabilities were predicted with a zero phase lag value. The stability boundary was found to be extremely sensitive to the magnitude of the phase lag, and comparison with experimental data showed that critical flow velocities were overestimated by a factor of approximately 5.

A semi-analytical approach was taken by Lever & Weaver (1982, 1986a,b) and Yetisir & Weaver (1988) in which the flexible array stability was approximated by that of a single flexible cylinder. In their analysis, the presence of neighbouring cylinders resulted in a wavy stream-cylinder channel flow around the flexible cylinder under consideration. A second flow region consisted of wake flow attached to the cylinder.

Assuming that cylinder motion results in a redistribution of the stream-tube area, expressions were obtained for the time variation of this area, the gap flow velocity and the pressure, for sinusoïdal cylinder motion. Similarly to Paidoussis *et al.* (1985), it was recognized that for the stream-tube flow it was necessary to introduce a phase lag due to fluid inertia effects. Using the unsteady continuity and momentum equations, the pressure distribution and hence resulting fluid forces could then be determined. The criterion for instability was that the total system damping be zero, hence predicting single mode negative damping instability. Good agreement with experimental results was obtained for rotated triangular arrays with $P/D = 1.375$.

The analytical approaches reviewed above have contributed to the understanding of the mechanisms underlying fluidelastic instability in cylinder arrays. It has also become clear, however, that for the accurate determination of stability boundaries, an experimental input, of some of the important parameters that cannot as yet be analytically determined, is necessary. The resulting semi-empirical models require varying amounts of experimental input.

Semi-empirical theoretical models have successfully been applied for the determination of instability flow velocities. In general, improved accuracy is obtained with increased experimental data input. These models fall broadly into two categories: general unsteady models and quasi-steady models.

Tanaka & Takahara (1981) were the first to develop a theoretical model which took into account "all" first order components of the unsteady fluid dynamics forces. The in-line array geometry studied by Tanaka & Takahara is shown in Fig.1.1. Considering the central cylinder O, the fluid forces acting on the cylinder are due to displacements of cylinders L,R,U and D, as well as cylinder O itself. Three types of fluid forces may be identified: inertia forces proportional to cylinder acceleration, fluid damping forces proportional to cylinder velocity, and stiffness forces due to dynamic pressure and cylinder displacement. Considering cross-flow motion, the total fluid dynamic force per unit length may be expressed as

$$F_y = \frac{1}{2}\rho D^2 C_M \, \ddot{y} + \frac{1}{2}\rho DUC_V \, \dot{y} + \frac{1}{2}\rho U^2 C_K \, y + O(y^2), \tag{1.2}$$

where C_M, C_V and C_K are respectively the added mass, damping and stiffness coefficients; $O(y^2)$ denotes second order terms. The fluid dynamic force F_y is, in general, a non-linear function of y; hence, equation (1.2), with the second order terms neglected, is a linear approximation about the equilibrium position $y = 0$. Assuming a sinusoidal displacement $y = Ye^{i\omega t}$, equation (1.2) can be written in the form

$$F_y = \frac{1}{2}\rho U^2 \left[\frac{-4\pi^2\omega^2 D^2 C_M}{U^2} + i(\frac{2\pi\omega DC_V}{U}) + C_K\right] Y = \frac{1}{2}\rho U^2 C_f(U) Y. \tag{1.3}$$

Corresponding to displacement of cylinder O and each of the neighbouring cylinders is a component of the coefficient $C_f(U)$, identified as C_{yjy} (or C_{yjx}) proportional to the induced component of F_y when cylinder j is displaced in the y (or x) direction. The total force F_y, therefore, becomes

$$F_y = \frac{1}{2}\rho U^2 \sum_{j=1}^{5} (C_{yjx} X_j + C_{yjy} Y_j). \tag{1.4}$$

The coefficient C_{yjx}, for example, may be interpreted as the partial derivative $\partial C_y / \partial X_j$, evaluated at $X_j = 0$. In equation (1.4), the assumption is made that the fluid forces sum linearly. Equation (1.4) may also be viewed as a Taylor series expansion of F_y in the displacements X_j and Y_j, in which only the first order terms are considered, rendering it a linear expansion. Using this complete set of first order, unsteady fluid forces, Tanaka & Takahara obtained instability boundaries that were in excellent agreement with experimental results. An important finding of their work was the discontinuous variation of instability flow velocity with fluid density. This was attributed to a change in the orbital motion, which for high density fluids was essentially in cross-flow, while coupled in-flow/cross-flow motion occurred for low density fluids.

Chen (1983a,b) generalized the unsteady model above, rendering it applicable to arbitrary cylinder configurations. Using the data of Tanaka & Takahara, Chen studied the stability of cylinder configurations ranging from a single flexible cylinder (in an array) with one degree-of-freedom, to multiple flexible cylinders executing predetermined orbital motion patterns. With his study, came probably the next most important fundamental contribution after Connors' work, which was the identification of *two distinct mechanisms* independently capable of precipitating fluidelastic instability. The first is the so called damping controlled mechanism and the second, the stiffness controlled mechanism.

The damping controlled mechanism is predominant for high fluid density flows (low $m/\rho D^2$), and requires but a single degree-of-freedom. Instability is precipitated when the component of the fluid force in phase with cylinder velocity overcomes the mechanical damping force; i.e., essentially via the vanishing of the total damping in a given degree of freedom. In low fluid density flows (high $m/\rho D^2$), the fluid dynamic stiffness controlled mechanism comes into play, in which fluid force changes due to relative cylinder displacements predominate. Multiple-flexible cylinders are required, resulting in fluid-dynamically coupled degrees of freedom. Due to the non-conservative nature of the fluid-force field, net positive energy can be extracted from the flow, which, at a critical flow velocity, overcomes the mechanical damping.

Using unsteady models, it has become possible to accurately predict the onset of fluidelastic instability, and explain the fundamental aspects of the underlying mechanisms. As predictive tools, however, these models require a prohibitive amount of experimental data, when one considers that the fluid force coefficients in equation (1.4) depend on array geometry and inter-cylinder spacing; measurements must also be taken for a range of Reynolds numbers and reduced frequencies (fD/U).

The need for simpler but still accurate models has therefore arisen, in order to enable a stability analysis unencumbered by the intensive data requirements of the fully unsteady models. One such theoretical model has been developed by Price & Paidoussis (1982, 1983, 1984, 1985, 1986a,b), belonging to a class of what are termed quasi-steady models. Fundamental to the quasi-steady models is the assumption that the instantaneous fluid forces acting on an oscillating cylinder are the same as on a static cylinder located at the reference instantaneous static position; it is only necessary to account for the relative velocity between the cylinder and the fluid when determining the fluid-dynamics, the forces being considered to be independent of cylinder oscillation frequency; (a frequency effect is, however, considered, as discussed later.)

In the original version of their model, Price & Paidoussis (1982, 1983) analysed the stability of a double row of cylinders (Fig.1.2(a)). For a given cylinder the fluid force in cross flow, for instance, could be expressed as

$$F_y = \frac{1}{2}\rho D l U_\infty^2 \left[C_L(1 - \frac{2\dot{x}}{U}) - \frac{\dot{y}}{U} C_D \right] + \frac{1}{2}\rho D^2 C_{ma}\ddot{y} + O(y^2), \tag{1.5}$$

where $\dot{y}D/U = \alpha$ is the induced incidence of the flow approaching the cylinder, and U the gap flow velocity given by $U = U_\infty T/(T - D/2)$, (Fig.1.2). Equation (1.5) is identical, in form, to the unsteady formulation given in equation (1.2), if motion in the in-flow direction is not considered. The difference is manifested in the determination of the fluid force coefficients.

Price and Paidoussis, considering C_L and C_D to be functions of position and induced incidence, assumed a linear approximation near the cylinder equilibrium position. The lift force coefficient, for instance, could then be expressed as

$$C_L^k(x, y, \alpha) = C_{L0}^k + \sum_{i=1}^{n} (x_i \frac{\partial C_L^k}{\partial x_i} + y_i \frac{\partial C_L^k}{\partial y_i} + \alpha \frac{\partial C_L^k}{\partial \alpha}) \tag{1.6}$$

for cylinder k in a generalized staggered array, where n corresponds to the number of neighbouring cylinders. The complexity of the flow structure within the array renders the definition and measurement of α, hence of $\partial C_L^k/\partial\alpha$, difficult and inherently susceptible to uncertainty.

Recognizing the difficulty in determining $\partial C_L^k/\partial\alpha$, Price and Paidoussis circumvented this problem in later revisions of their model (e.g. Price & Paidoussis (1984, 1986a,b)), by expressing C_L and C_D in terms of relative "apparent" inter-cylinder displacements, hence eliminating the need for an explicit inclusion of the flow approach angle α. An important component of the analysis is consideration of the time lag between the displacement of cylinder i and its effect being propagated by the flow to be manifested at cylinder k; secondly, cross-flow cylinder motion results in an angular displacement of the cylinder wake relative to the free stream flow. With the time delay and wake relative orientation considered in determining apparent inter-cylinder displacements ξ_i and η_i, the lift coefficient C_L^k on cylinder k, induced by its own motion and all immediately neighbouring cylinders 1 to n becomes

$$C_L^k = C_{L0}^k + \sum_{i=1}^{n}(\xi_i \frac{\partial C_L^k}{\partial \xi_i} + \eta_i \frac{\partial C_L^k}{\partial \eta_i}), \tag{1.7}$$

where ξ_i and η_i are the apparent cylinder displacements.

As observed by Simpson & Flower (1977), fluid approaching the stagnation point upstream of a cylinder decelerates, resulting in a retardation in comparison to steady flow. Price and Paidoussis found this retardation effect to be extremely important in cylinder arrays and indeed imperative for the precipitation of a negative damping instability, and hence incorporated it in their model. Despite the quasi-steady theoretical foundations of this model, the analysis therefore, crosses over into the unsteady regime, by modelling approximately the most important effects of unsteadiness in the fluid dynamics.

In its general form, Price & Paidoussis' (1984,1985) model results in large matrices when coupled motion involving many cylinders is considered. The model was therefore extended and simplified by assuming an inter-cylinder modal pattern (similar to Connors' (1970)), in which fixed phase differences between the motion of adjacent cylinders were applied; this essentially constrained the array modal response to certain orbital patterns. It was then possible to decouple the motion of a small representative kernel of cylinders from the general array, thereby much simplifying the solution of the governing equations. This constrained-mode analysis was found to yield very good agreement with both the generalized analysis and experimental results.

Based on the identification of the two instability mechanisms by Chen (1983a,b) as well as experimental evidence, Price & Paidoussis (1986b) and Paidoussis & Price (1988) undertook a single flexible cylinder analysis. The basic assumption in this analysis was that the stability behaviour of the fully flexible array could be reasonably represented by that of a single flexible cylinder in an otherwise rigid array. This holds true only when instability is of the negative damping type — predominant for low values of the mass damping parameter ($m\delta/\rho D^2 < 300$). A single cylinder analysis is clearly appealing, due to its simplicity as well as the minimal amount of experimental data required. For the array geometries studied, fluidelastic instability was found to primarily occur in the cross-flow direction. The time delay due to flow retardation was found to be an important determining factor for the instability to occur — introducing a phase difference between cylinder displacements and the fluid dynamic forces. The instability condition requires that the total system damping vanish. The resulting expression for the critical flow velocity is an implicit nonlinear algebraic equation relating the reduced critical flow velocity U_c/fD to the cylinder mass damping parameter $\tilde{m}\delta$ (where $\tilde{m} = m/\rho D^2$). Considering cross-flow motion for instance, the stability boundary equation is

$$-p^2\left[1+\frac{\pi C_{ma}}{4\tilde{m}}\right]+ip\left[\frac{\delta}{\pi}-\frac{C_{D0}}{2a\tilde{m}}\frac{U}{2\pi fD}\right]+$$
$$\left\{1-\frac{1}{2\tilde{m}}\left(\frac{U}{2\pi fD}\right)^2\frac{\partial C_L}{\partial y}\left[\cos\left(\frac{-p\mu_r}{aU/2\pi fD}\right)+i\sin\left(\frac{-p\mu_r}{aU/2\pi fD}\right)\right]\right\}=0, \quad (1.8)$$

where p is the dimensionless frequency. For large enough values of U/fD, the trigonometric functions can be linearized, yielding the following expression for the critical flow velocity:

$$\frac{U_c}{fD}=\left(\frac{4}{-C_D-\mu_r D(\partial C_L/\partial y)}\right)\frac{m\delta}{\rho D^2}, \quad (1.9)$$

where μ_r is a positive flow retardation parameter of $O(1)$ and the derivative $\partial C_L/\partial y$ is evaluated at the equilibrium position $y = 0$. According to equation (1.9) single-mode instability is only possible for large and negative $\partial C_L/\partial y$.

For low values of the mass damping parameter $m\delta/\rho D^2$, the non-linear stability boundary equation (1.8) has to be solved by an iterative procedure. Multiple instability boundaries are obtained, which is attributed to the sign changes in the trigonometric functions as the phase lag changes. The condition of large and negative $\partial C_L/\partial y$ is no longer necessary; depending on the phase lag, a large and positive value of this derivative will also precipitate instability.

1.2 POST INSTABILITY CYLINDER DYNAMICS

The linear theoretical models discussed above can only be used to predict the onset of fluidelastic instability. Investigators have been interested in post instability cylinder dynamics due to the damage potential of the ensuing cylinder vibrations (see, for instance, Paidoussis (1980)).

Fluidelastic instability may cause large amplitude cylinder vibration which for high enough flow velocities results in impact with loose supports and even inter-cylinder clashing. Two kinds of non-linearities need to be included in the theoretical models for post-instability analysis. The first is the non-linear variation of fluid-dynamic forces with cylinder displacement and velocity (the second being discussed in the next paragraph). Non-linear components of the fluid-dynamic forces introduce damping into the system [2] which, together with dissipation, balances the energy input due to instability at a given cylinder oscillation amplitude; the result is limit cycle motion.

Heat exchanger tubes are supported at several locations along their span by tube support plates (TSP). To allow for thermal expansion and ease of assembly, TSP holes are drilled with slightly larger diameters than the tube diameter, resulting in tube/support gaps of up to $0.25D$, D being the tube diameter. At some flow velocity $U > U_c$, the limit cycle amplitude reaches the clearance gap value, resulting in

[2] Not all fluid-force non-linearities are necessarily stabilizing; non-linear stiffness effects are responsible for the instability observed by Roberts (1962,1966), for instance. The existence of non-linear fluid forces related with flow periodicities is also noted; the associated frequencies are, however, often far enough from the fluidelastic frequency allowing these forces to be neglected.

tube/support impacting, often referred to as a TSP-active condition. This structural non-linearity in the system, involving a discontinuous jump in the stiffness, is the second non-linear aspect that needs to be considered when modelling post-instability tube behaviour.

1.2.1 Review of Support-Influenced Dynamics in Cross-Flow

To study purely fluid excited non-linear cylinder response, Price & Valerio (1990) extended the quasi-steady model of Price & Paidoussis (1986b) to include velocity- and displacement-dependent non-linearities. The relative velocity vector U_r (Fig.1.2(b)), was expressed as a Taylor series expansion including up to second order terms in the cylinder cross-flow velocity, $\dot{y}$. Experimental measurements had shown the fluid dynamic force coefficients (C_L and C_D) to be strongly non-linear functions of cylinder displacement. Fifth order polynomial curve fits were performed on the experimentally determined force coefficient variations with cylinder cross-flow displacement, y. Approximate analytical solutions for limit cycle amplitudes in various array geometries were obtained using the Krylov and Bogoliubov (K & B) averaging method. A requirement of the K & B method is that non-linear terms remain small in magnitude; this was satisfied by limiting calculations to higher values [3] of the mass damping parameter $m\delta/\rho D^2$. In the analysis, only cross-flow motion was considered; thus, the only instability mechanism would be of the one-degree-of-freedom negative damping type. Their analysis showed that the rate of increase of limit cycle amplitude with flow velocity for lower values of $m\delta/\rho D^2$ was much greater than for high values.

System non-linearity introduced by impacting at loose supports has received wider attention than fluid force related non-linearity. Investigators are primarily interested in determining tube wear rates due to impacting with the support, following instability. Numerous experimental data have been collected, correlating tube wear rates and tube excitation (e.g., Ko (1979)). Numerical prediction of tube wear rates

[3] For the rotated triangular array, this corresponds to values of reduced flow velocity $U/fD > 1.1$.

has also been attempted by Frick *et al.* (1984), Antunes *et al.* (1988) and Fricker(1988) among others. A host of dynamical experiments, where a tube is mechanically excited (e.g., Blevins (1975), Goyder (1982), Axisa *et al.* (1988)) have also been conducted.

The complexity of the problem is undisputed. It is particularly evident in the margin of uncertainty in wear-rate measurements and calculations. Cylinder/support interaction, characterized by impact and sliding contact forces and resulting wear are determined by the detailed cylinder dynamics. To improve the ability to predict wear rates, it is clear that an understanding of the underlying cylinder dynamics by accurate modelling and analysis is required.

Significant effort has already gone into modelling post-instability tube dynamics with impacting. Axisa *et al.* (1988) studied the response of a multi-span tube with loose supports under fluidelastic instability excitation. The model studied was a pin-ended tube, supported at midspan; tube motion was limited to one direction only, hence modelling an anti-vibration bar (AVB) rather than a circular support. The loose support was modelled as a trilinear spring. The resulting support impact force was therefore given by

$$\begin{aligned} F_s &= -K_s(|x| - e_r), & |x| > e_r, \\ F_s &= 0, & |x| < e_r, \end{aligned} \tag{1.10}$$

where x is the transverse tube displacement, e_r the tube/support clearance and K_s the effective support contact stiffness. Following their earlier work (Axisa *et al.*, 1984), the support stiffness K_s was estimated to be that due to local tube ovalization given by

$$K_s = 1.9\frac{Et_w^2}{D}\left(\frac{t_w}{D}\right)^{1/2}, \tag{1.11}$$

where E is the Young's modulus and t_w the tube thickness. Suggestions for possible refinements of this model, such as inclusion of non-elastic impact effects and consideration of fluid effects at the impact location were also given.

In Axisa's *et al.* work, fluidelastic instability was modelled following Connors' quasi-static approach. Assuming the existence of a destabilizing fluid damping force proportional to the flow velocity U, the total modal damping ζ_n^* was expressed as

$$\zeta_n^* = \zeta_n \left[1 - \left(\frac{U}{U_c}\right)^2\right], \tag{1.12}$$

U_c being the critical instability reference-gap velocity, and ζ_n the modal structural damping in stagnant fluid. This being a linear fluid model, limit cycle amplitudes would grow unhindered for $U > U_c$, to be limited only by the loose support when the amplitude attains the clearance value e_r. Assuming non-linearities to be strictly localized at the support, modal superposition was considered to be sufficient for the structural modelling. The resulting modal equations were integrated using an explicit Devogelaere algorithm. Results of their numerical simulations showed the tube response to undergo a distinct sequence of bifurcations which in some cases resulted in drastic increases in tube wear rates (the primary object of their investigation). Strictly periodic motion was obtained in the velocity range $U/U_c < 2.0$. Above this limit, an unidentified bifurcation resulted in a chaotic-like response which was corroborated by evidence in phase-space plots and PSD calculations. Return to periodic motion, albeit with higher oscillation frequencies, occured starting at $U/U_c \approx 3$. Axisa *et al.* observed and remarked on the importance of ζ_n^* which determines the linear instability growth rate, where small changes in ζ_n^* would significantly alter the observed response, hence the wear rates. Finally they concluded that fluidelastic vibration limited by a loose support does not have a unique vibratory "signature".

Fricker (1988) studied the dynamics of a loosely supported cantilever beam, the loose support modelling an anti-vibration-bar (AVB). Similarly to Axisa *et al.*, a fluidelastic instability model was developed by assuming a destabilizing force in phase with tube vibrational velocity having the form

$$F = \frac{1}{2} U^2 D l \overline{K} \frac{\dot{y}}{\omega D}, \tag{1.13}$$

$\overline{K}$ being an unknown fluidelastic constant, characteristic of the array geometry, D and

l the tube diameter and length, respectively, ω the vibrational frequency, and $\dot{y}$ the tube velocity transverse to the flow. From equation (1.13), and a similar expression for the mechanical damping force, Fricker obtained the following expression for the effective total system damping:

$$\zeta = \zeta_0 \left[1 - \frac{\omega_n}{\omega} \left(\frac{U}{U_c} \right)^2 \right], \tag{1.14}$$

where ζ_0 is the mechanical damping factor and ω_n the nth modal natural frequency. Equation (1.14) is similar to the expression obtained by Axisa *et al.* (equation (1.12)), with the difference of the inclusion of the effect of vibrational frequency on the fluid damping.

A finite element approach was taken by Fricker to determine the system structural matrices. Long time simulations showed that complete convergence of the solution (to a simple periodic motion) did not occur. It was found that small changes in the accuracy of the solution completely changed the details of the impact forces after a short period. Fricker concluded that the tube response was primarily periodic, but with a superimposed chaotic component. Impacting with a loose support was found to have a stabilizing effect; this was due to the effective change of tube boundary conditions from clamped free to clamped-pinned. Support damping made it possible for the flow velocity to be increased well beyond the critical value for the clamped-pinned configuration. However, this instability could be initiated by impulsively loading the tube at mid-span. This non-linear effect suggests a subcritical instability which can be triggered by a large displacement.

In more recent work, Fricker (1991) reports the existence of truly periodic motion, as well multiple solutions in the response of a U-bend tube with an AVB support. With the tube symmetrically located within the AVB, double-sided impacting motion predominated for $U > U_c$. Due to the linear modelling of the impact stiffness and the fluidelastic forces, Fricker found that changing the gap size had no effect on the vibrational frequency, while vibration amplitudes and impact forces scaled linearly. Bifurcations of the tube response as U was varied resulted in discontinuous changes in vibration frequencies and impact forces. The bifurcations did not occur abruptly, but rather over small but finite velocity ranges, over which several solutions co-existed. In an attempt to gain some insight into the complex response observed, a one degree-of-freedom oscillator, modelling only the most important characteristics of the impacting system was developed. This model was found to provide reasonable bounds for the frequency ratio and impact forces obtained with the complete model.

Cai & Chen (1991) modelled the impacting response of a loosely supported tube subjected to non-uniform flow. In their analysis, the complete unsteady model of Chen (1983a,b) was used. In their structural model the tube parameters were considered to change during tube/support contact; the two sets of structural boundary conditions being pinned-pinned-free and pinned-pinned-spring-loaded corresponding to TSP-inactive and TSP-active modes respectively; in the latter case, an equivalent spring constant representing the effective support stiffness was introduced. Following the instability of the TSP-inactive mode, vibration amplitudes increased until impacting occurred. Energy loss on impact reduced the vibration amplitude, and the growth cycle was repeated. Cai *et al.* did not attempt to analyze the tube dynamics observed, except for acknowledging the complexity underlying the tube response.

In another recent study, Paidoussis & Li (1991, 1992) have studied the response of a loosely supported tube within an in-line array. The purpose of their study was to investigate the possibility and proof of existence of chaotic vibrations in such a system. In their model, tube motion was considered only in cross-flow. Impact dynamics were modelled via either a cubic or tri-linear spring. Their work was a pioneering effort in using modern non-linear dynamics concepts and methods to study and quantify the tube dynamics. Bifurcation diagrams were used to summarize in a 2-D representation the variation of the tube response with flow velocity, making transitions in the response easily identifiable. Lyapunov exponents were for the first time calculated for a set of delay-differential equations; this made it possible to unequivocally confirm the existence of chaos; this could only be done for the analytical cubic support model. With the tri-linear spring impact model, chaotic-like motion was obtained right from the onset of impacting. To further investigate the route to chaotic motion, a simplified one-dimensional impact oscillator, capturing just the essence of the complete system, was also studied. For this model the Poincaré technique could be used to determine the condition for the occurrence of period-doubling and saddle-node bifurcations. This model enabled clarification of the existence of quasi-periodic motion previously suspected to be chaotic. Multiple impact quasi-periodic motions were found to lead to the observed chaotic response, following the onset of impacting for the tri-linear support model.

1.2.2 Nonlinear Dynamics Concepts

As first envisioned by Paidoussis & Li (1991), any hope of understanding the complex system of a loosely supported multi-span tube in cross-flow lies in a wider application of non-linear dynamics concepts. Recently developed methods have given new hope in deciphering and understanding the behaviour of non-linear systems. Stability and bifurcation theories coupled with mathematical topology underly the study of non-linear dynamics. The stability of the equilibrium solutions (attractors), as well as the robustness of the governing equations of motion can be investigated. In this section, we introduce some basic definitions and methodology used to analyze dynamical systems. Inevitably the complete details cannot be presented here; hence the reader is referred to the excellent texts by Guckenheimer & Holmes (1983), Moon (1987) and Wiggins (1990).

For the system studied here, we attempt to understand the dynamical behaviour as a parameter μ (primarily the flow velocity) is varied. The solution undergoes a sequence of bifurcations; this referring to qualitative changes in the phase portrait representing the steady state solution, or simply changes from one type of attractor to another. An attractor may be defined as the transitive set in phase-space, ultimately filled by a single steady state trajectory, representing the time evolution of the dynamical system.

To fix ideas, we consider the response of a tube subjected to cross-flow and vibrating only in its first mode; hence, a one degree-of-freedom system. The equation of motion for this system is

$$\ddot{y} + 2\omega\zeta\dot{y} + \omega^2 y = F(y, \dot{y}, \ddot{y}, \mu), \tag{1.15}$$

F representing the fluid force and the parameter μ here being the flow velocity. Defining a vector $\mathbf{Y} = \{\dot{y}, y\}^T$, equation (1.15) may be recast in the form

$$\dot{\mathbf{Y}} = \mathbf{F}(\mathbf{Y}, \mu), \tag{1.16}$$

where $\mathbf{F}$ is now a vector function given by

$$\mathbf{F} = \{F - 2\omega\zeta\dot{y} - \omega^2 y, \dot{y}\}^T. \tag{1.17}$$

Equation (1.16) governs the time evolution of the state vector $\mathbf{Y} = \{\dot{y}, y\}^T$ in phase-space. The function $\mathbf{F}$ is a vector, tangent to the trajectory of the phase point, hence, referred to as a vector field. A study of the vector field $\mathbf{F}$ yields information on the system equilibria and their stability, as well as other information as follows.

The system equilibria or fixed points are determined by solving the equation

$$\mathbf{F}(\mathbf{Y}, \mu) = 0. \tag{1.18}$$

For the example above, the state of rest, $\mathbf{Y} = \mathbf{Y}_0 = \mathbf{0}$, is the unique stable fixed point. Hence, the equilibrium, motionless state of a cylinder for $\mu < \mu_c$ (or equivalently $U < U_c$) corresponds to a point attractor in phase space.

Of interest is the stability of the fixed point $\mathbf{Y}_0$; $\mathbf{Y}_0$ is stable if every nearby solution of equation (1.16) stays nearby. Taylor-expanding equation (1.16) about $\mathbf{Y}_0$, yields

$$\dot{\mathbf{Y}}(t) = \mathbf{DF}(\mathbf{Y}_0, \mu)\mathbf{Y}(t) + O(\mathbf{Y}^2(t)). \tag{1.19}$$

The eigenvalues $\lambda(\mu)$ of the Jacobian derivative $\mathbf{DF}(\mathbf{Y}_0, \mu)$ determine the stability of

$\mathbf{Y}_0$. Fluidelastic instability, associated with a Hopf bifurcation, occurs at $\mu = \mu_c$, when $Re(\lambda(\mu_c)) = 0$.

The limit cycle is the second simplest attractor. Similarly to the fixed point, a stability analysis of the limit cycle can be undertaken, yielding information on the rate of convergence of nearby trajectories to the limit cycle — a measure of stability. This can be achieved by calculating Floquet multipliers (Guckenheimer & Holmes, 1983). Loss of stability of the limit cycle is characterized by a crossing of the unit circle by any one of the multipliers. The unstable limit cycle may be replaced by quasi-periodic motion for instance, the result of a Hopf bifurcation of the limit cycle. A phase-plane plot of the quasi-periodic motion would be characterized by two incommensurate frequencies, with the trajectory describing a 2-D attractor, graphically similar to a toroidal surface. Alternatively, the original limit cycle may undergo a saddle-node bifurcation, resulting in an asymmetric limit cycle. This is often a precursor to the period doubling (flip) bifurcation cascade, which ultimately leads to chaos (Feigenbaum, 1978). A saddle-node bifurcation may also lead to an intermittency transition to chaos. The quasi-periodic motion above may also undergo another Hopf bifurcation, introducing a third incommensurate frequency. Quasi-periodic motion with three incommensurate frequencies has been shown to be unstable under small perturbations (Ruelle & Takens, 1971) and can degenerate into chaotic motion. Some of these routes to chaos will be discussed further in later chapters.

The final attracting set or "recurrent" behaviour has been dubbed *the strange attractor*. While the classical attractors described in the foregoing are associated with classical geometrical objects (n-dimensional surfaces, where n is an integer), strange attractors can only be described in terms of fractal sets, allowing the attracting set to have a non-integral dimension. An excellent treatment of fractal geometry is given by Mandelbrot (1983). A treatment of fractal dimensions as applied to dynamical systems, as well as a numerical procedure for their determination is given by Moon (1987). Phase-plane plots of motion on a strange attractor show repeated stretching and folding of trajectory bundles. Consequently, initially nearby states show locally exponential divergence with time; the baker's transformation (Farmer *et al.*, 1983) vividly describes this scenario. The horse-shoe map (Smale, 1963, 1967), responsible for similar stretching and folding has been found to be common to all strange attractors.

Thus far, the bifurcations discussed belong to the class of local bifurcations. Local bifurcations can be characterized as qualitative changes in phase portraits occurring near a single point; this holds for bifurcations of the limit cycle when the phase flow is reduced to a Poincaré mapping in which a limit cycle corresponds to a fixed point. Qualitative changes may also occur in the behaviour of a dynamical system involving global aspects of the phase-space flow. An example of this is the transversal intersection of homoclinic orbits for planar vector fields. The simplest global bifurcation occurs for a homoclinic orbit containing a single saddle point. A change in the system parameter results in the disappearance of a periodic orbit associated with the saddle loop, resulting in a qualitative change or (homoclinic) bifurcation of the phase-space flow. Less degenerate global bifurcations are obtained, for example, with loops formed from multiple saddle separatrices (Guckenheimer & Holmes, 1983).

Associated with local bifurcations is a simplification of the dynamics in the neighbourhood of the fixed point. In reality only a few "modes" will be associated with the bifurcation. The system can therefore be reduced to the lowest order part of the vector field **F** on which the bifurcation depends. The appropriate reduction procedures are the subject of the Centre Manifold and Normal Form theories (Guckenheimer & Holmes, 1983), through which systematic computation to determine the local dynamics can be done.

In general, such calculations are only possible for simple analytical forms of the vector field **F**. However, using such simple forms of **F** it is possible to enumerate and classify all possible local bifurcations (see, for instance, Thompson (1986)). The local bifurcations are associated with unique and distinctive topological changes in the phase-plane plot which can be identified purely geometrically. Identification of these local structures therefore becomes a powerful tool for analyzing complex systems not amenable to analytical manipulation. This fact will prove invaluable to the present study.

1.3 OBJECTIVES OF PRESENT WORK

The study to be presented aims to build on the knowledge of non-linear tube dynamics on two fronts. On the first, the problem of fluidelastic instability is revisited; of particular interest is the fluid-force field. On the second front, a non-linear dynamical analysis, involving theory and experiment of the support influenced tube dynamics is undertaken.

1.3.1 The Non-Linear Fluid Force Field and Limit Cycle Motion

To date, studies on support-influenced tube motion have used linearized theories to model the fluid-dynamic aspect of the problem — hence no limit-cycle motion is possible without the presence of the support. Also, while the assumption of linear fluid dynamics may be valid for small tube displacements, static force measurements by Price & Paidoussis (1986b) have shown the fluid forces to be strongly non-linear functions of tube displacement. Fig.1.3 shows an example of the variation of C_L with tube non-dimensional cross-flow displacement, $\tilde{y}$; it is clear that the linear assumption is valid only in the region near $\tilde{y} = 0$. Linearized theories are no longer valid in the post-instability regime, in which they predict an infinite amplitude growth. While this is countered by the presence of the support, the rate of energy addition to the tube for $U > U_c$ is inflated, due to the absence of non-linear fluid-damping forces.

A rotated triangular array geometry, shown schematically in Fig.1.4, will be the focus of this study. This geometry, with tube spacing $P/D = 1.375$, has been found to be highly unstable (Price & Paidoussis, 1986b). Fluidelastic instability was found to be of the one-degree-of-freedom negative damping type, with motion predominantly in the cross-flow direction. A single flexible cylinder model will therefore give a reasonably accurate representation of the flexible array behaviour.

The fluid force field is investigated first. It is presently not known how C_L and C_D vary with in-flow and cross-flow tube displacements. Accurate static force measurements are conducted over a grid covering the complete area within which the tube can move, thus enabling a mapping of the complete static force field in this array for the first time. A study of this force map is also undertaken. Using the same force field, a linear stability analysis is performed to determine tube stability away from the geometrical equilibrium position.

To date, the only existing non-linear model capable of predicting limit-cycle amplitudes (near $U = U_c$) is that by Price & Valerio (1990), albeit with tube motion limited to the cross-flow direction only. With the complete two dimensional static force field known, non-linear quasi-steady theory is used to investigate coupled (x, y), i.e. orbital, motion and the effect of fluid coupling on the limit cycle motion. The effect of system parameters such as tube natural frequencies, and mass-damping is also quantified.

1.3.2 Support-Influenced Tube Dynamics

In the second part of this Thesis, a study of the tube dynamics under the influence of impacting will be undertaken. This system poses special challenges in the attempt to understand the resulting complex tube response coupled with bifurcation sequences, as system parameters are varied, for the following reasons. The discontinuity in the stiffness at the loose support renders the system non-analytic. The governing equations of motion are stiff delay differential equations; stiffness in the equations, which is the result of large variations in the effective system stiffness, brings about numerical stability problems. Delay terms in the equations, from the quasi-steady model, result in delay differential equations which have no analytical solution; conversion to ordinary differential equation form is, nevertheless, possible for small delays via Taylor series expansions.

In the analysis, the key bifurcations in the solution as system parameters are varied are identified and enumerated. Particular attention is paid to local bifurcations and their topological structures. Details of the characteristics of such bifurcations are already well known; hence, system behaviour following such bifurcations can be predicted.

Reduction of the effective system dimension via the Poincaré section is performed near certain bifurcations where the geometry of the underlying attractor is expected to be uncovered via such an approach. In particular, the possibility of uncovering behaviour approaching one- or two-dimensional maps (solutions to difference equations) is very rewarding; one-dimensional maps can be fully analyzed, while the theory for certain two-dimensional maps is well founded and understood. The period-doubling route to chaos, for instance, is exhibited by the 1-D map

$$\mathrm{p}_{n+1} = \mu(1 - \mathrm{p}_n)\mathrm{p}_n. \tag{1.20}$$

Feigenbaum (1978) showed that the critical parameter at which successive period doublings occur satisfies the relation

$$\frac{\mu_{n+1} - \mu_n}{\mu_n - \mu_{n-1}} = 4.6692. \tag{1.21}$$

This gives a specific criterion for testing the onset of chaotic behaviour when a period doubling cascade occurs in any dynamical system.

The flow velocity is but one of the important parameters affecting the dynamics. Others include the clearance to the support, e_r, the tube mass damping parameter $m\delta/\rho D^2$, and the frequency ω_n. The effect of varying these parameters is also investigated.

The robustness of the dynamical behaviour obtained depends on the structural stability of the vector field, $\mathbf{F}$, which represents the theoretical modelling of the physical system. Both the fluid and structural models are approximate to some degree. It is important to test to what extent the dynamical behaviour obtained is affected by changes in the theoretical modelling. In view of the complexity entailed in an accurate model, it is of interest to evaluate the extent to which simplifications may be carried out while maintaining the correct dynamical picture.

An exploration of the dynamical behaviour of a simple two degree-of-freedom model is the starting point of the non-linear analysis. The simplicity of this low-dimensional system makes geometrical interpretation of phase space behaviour possible; tube motion occurs essentially in a plane (2-D space). This simplified model is also accurately representative of the system behaviour up to and including the first Hopf bifurcation. Hence, it is expected that bifurcations at higher flow velocities will give an idea of the dynamical behaviour of the complete infinite-dimensional system.

Following this preliminary work, an in-depth study of the dynamical behaviour of a non-uniform cantilever tube is undertaken. This presents us with an infinite-dimensional system with motion occurring in 3-D space. Coupling occurs not only between the orthogonal in-flow and cross-flow directions, but also between the various modes in a given direction. The resulting dynamical behaviour can therefore be expected to be much more complex, as compared to the two degree-of-freedom system studied in the foregoing. The accuracy of the predicted behaviour is tested by experiments — in fact, conducted prior to the 3-D analysis.

The experimental tests are conducted in a water tunnel. Motion of the cantilevered tube utilized is limited by a circular support at its upper end when vibration amplitudes exceed the tube/support clearance. The flow velocity is varied in the range $0-2.5\ U_c$, where U_c is the critical flow velocity for the Hopf bifurcation. A typical range for operational support clearances $0.07D < e_r < 0.23D$ is used in the tests. Interstitial gap fluid effects are also investigated by conducting tests with impacting occurring in air and water. The dynamical behaviour is characterized via response spectra, phase-space portraits, fractal dimensions as well as *saddle orbit* distributions. Bifurcation diagrams are constructed to create a global picture of the dynamical behaviour in parameter space.

Theoretically, further studies on parameter effects and more importantly on possible model simplifications are carried out; particular attention is paid to the possibility of obtaining low-dimensional maps via the Poincaré section reduction. Lyapunov exponent and fractal dimension computations are used to characterize any attractors obtained.

The non-uniform cantilever tube in the experimental tests is designed such that the two lowest transverse natural frequencies are separated by a wide margin from the higher frequencies, keeping a large percentage of the system energy and hence the dynamics in the two lowest modes. Tubes within steam generators and heat exchangers have uniformly distributed mass and stiffness and, hence, will not have a large disparity in the frequencies of the lower and the higher modes. In the final part of this work, this more realistic condition is modelled by studying a two-span loosely supported tube with a loose support at mid-span. Of interest will be the implications of the results obtained from the analysis of the low dimensional systems above to this more complex system.

1.4 THESIS OUTLINE

In Chapter 2, the complete theoretical model is presented. The quasi-steady model for the fluid dynamic aspects is based on the work of Price & Paidoussis (1984, 1986b). In the second part of this chapter the problem of modelling the loose support is considered.

With the theoretical formulation in place, the next task is the determination of the fluid force field. Experimental apparatus and test procedure are the subjects of Section 3.1 of Chapter 3. In Section 3.2, the measured force field is analysed and its implications on tube stability discussed at length.

The dynamical behaviour of the reduced one-mode, two-degree-of-freedom model under the influence of this force field is considered in Chapter 4. In the same chapter, the loose support is introduced in the dynamical problem; its implications form the subject of the latter part of this chapter.

In Chapter 5, results of an experimental study of the post-fluidelastic instability behaviour of a non-uniform tube are presented. Experimental results are also compared with a theoretical analysis of the same system.

The study concludes, in Chapter 6, with a brief presentation of the response of a two-span uniform tube with a loose support at mid-span with particular focus on the implications of the preceding low dimensional analyses to this high dimensional system. This chapter closes with some remarks on the implication of the chaotic transition to wear-rate computation; possible improvements in the wear computation procedure are suggested.

In Chapter 7, a retrospective summary of this study, as well as possible directions for future work are presented.

Chapter 2

THEORY

The governing equations of motion will now be presented. The system under consideration is a circular flexible tube subjected to non-uniform cross-flow $U(s)$ as depicted in Fig.2.1. The flexible tube is located in row 3 of a rotated triangular array, as shown schematically in Fig.1.4. At a location $s = s_p$ along the tube span, a loose support with clearance e_r exists. Although the tube shown in Fig.2.1 has clamped-pinned boundary conditions, the response of a clamped-free tube will also be studied.

For this two-span model, for small clearance, vibration amplitudes will remain small relative to the tube length l; the linearized Euler-beam equations therefore will be sufficient. The mechanical coupling between the spatially orthogonal directions will also be negligible; hence, the governing equations of motion are

$$EI\frac{\partial^4 x}{\partial s^4} + c\,\frac{\partial x}{\partial t} + m\frac{\partial^2 x}{\partial t^2} = F_{xf}(x, \dot{x}, ...) + \overline{\delta}(s - s_p)F_{xs}(x, y) \tag{2.1}$$

for the x–direction, and

$$EI\frac{\partial^4 y}{\partial s^4} + c\,\frac{\partial y}{\partial t} + m\frac{\partial^2 y}{\partial t^2} = F_{yf}(y, \dot{y}, ...) + \overline{\delta}(s - s_p)F_{ys}(x, y) \tag{2.2}$$

for the y-direction, where $x(s,t)$ and $y(s,t)$ are, respectively, the streamwise (in-flow) and cross-stream (cross-flow) tube displacement, m is the tube mass per unit length, EI the flexural rigidity and c the material damping coefficient. Subscripts f and s on the right-hand side indicate fluid and support forces, respectively, and $\overline{\delta}(s - s_p)$ is the Dirac delta function.

2.1 THE QUASI-STEADY FLUID-DYNAMIC MODEL

The quasi-steady approach of Price & Paidoussis (1986b) analyzing a single flexible cylinder is followed in determining the fluid-dynamic forces. Several modifications are made to their basic model. The complete position-dependent non-linear fluid force field is utilized in the present work. Second-order terms in tube velocities $(\dot{x}(s,t), \dot{y}(s,t))$ are also included. Axial variation of the fluid forces, resulting from tube deflection and a non-uniform flow velocity, is also accounted for in the model.

A linear superposition of fluid force components dependent on cylinder acceleration, velocity and displacement leads to the following formulations (Price & Paidoussis 1986b):

$$F_{xf} = -m_a \frac{\partial^2 x}{\partial t^2} + \frac{1}{2a^2} \rho U_r^2 D \left[C_L(x_d, y_d) \sin\alpha + C_D(x_d, y_d) \cos\alpha \right] , \qquad (2.3)$$

$$F_{yf} = -m_a \frac{\partial^2 y}{\partial t^2} + \frac{1}{2a^2} \rho U_r^2 D \left[C_L(x_d, y_d) \cos\alpha - C_D(x_d, y_d) \sin\alpha \right] , \qquad (2.4)$$

where ρ is the fluid density, m_a the added mass, $U_r(s)$ is the flow velocity relative to the tube, and α the flow approach angle as depicted in Fig.1.2(b). The factor a accounts for the fact that C_L and C_D are based, as measured, on the upstream flow velocity U_∞. The gap flow velocity U is related to U_∞ by $U/U_\infty = T/(T - D) = a$. The delayed displacements, accounting for the effect of a phase lag between cylinder displacement and the fluid forces are given by

$$x_d = x(s, t - \Delta t), \quad y_d = y(s, t - \Delta t). \qquad (2.5)$$

The time delay Δt is approximated by $\Delta t = \mu_r D/U$, where $\mu_r \approx O(1)$ (Price & Paidoussis, 1984).

2.2 THE SUPPORT RELATED FORCES

At the loose support, several forces come into play. Considering a cross-section at the support location $s = s_p$, the tube geometrical centre is limited to move within a circle of radius e_r, as shown in Fig.2.2; a typical impact with local incident tube velocity u and restitution velocity v is depicted. For such an impact, radial and tangential forces are manifested. The most significant is the normal impact force F_{ri}, which is proportional to the support stiffness and is a function of the local contact geometry. Coupled with F_{ri} is a damping force, F_{rd}, representing energy loss due to effects such as plastic deformation and stress-wave generation in the tube. The presence of a significantly viscous fluid in the interstitial gap also introduces squeeze-film damping. Explicit formulations for F_{ri} and F_{rd} do not exist. Hence, in the next two subsections we turn to approximate analyses, coupled with empirical results to determine some approximate formulations for these forces.

2.2.1 Empirical Formulation for the Stiffness Force F_{ri}

The impact stiffness force is a function of the deformation, referred to as the "approach", σ, (of the centres of mass of the impacting bodies), Fig.2.3. It is also strongly dependent on the geometry of the contacting surfaces. In general, the impact force can only be analytically determined for simple geometries, where impacting bodies are compact. For the so called stereo-mechanical impact of compact bodies, Hertzian theory (Engel 1976) gives a force-approach law of the form

$$F_n = K_n \sigma^{3/2}, \tag{2.6}$$

σ being the approach, or relative displacement of the impacting bodies, and K_n an effective stiffness. For two spheres of equal radius r_s and of the same material, we have

$$K_n = \frac{2E}{3(1-\nu^2)}\sqrt{r_s/2}, \tag{2.7}$$

E being the material modulus of elasticity and ν Poisson's ratio.

Permanent deformations occur in materials with high surface hardness, even at very low impact velocities. Impact involving metals, in which plastic deformations invariably occur, cannot be modelled by Hertzian theory. The Meyer law (Goldsmith, 1960), which has been found to be reasonably accurate, is an empirical relation of the form

$$F_n = K_n \sigma^{\xi}, \tag{2.8}$$

where the exponent ξ will vary in the range $0 < \xi < 1$, indicating impacting that varies between ideal plasticity and elasticity. In reality, a combination of plastic and elastic deformations occur. The exact value of ξ has been found to have minimal effect on the total response of a tube under impacting (Goldsmith 1960); it is only necessary that the contact force time-history exhibit the correct total impulse for the correct prediction of the resulting response.[1]

While tube-to-support impacting is well beyond the realm of compact body interaction one can envisage a force-approach law (at $s = s_p$) similar to equation (2.8), albeit with a different constant and exponent. Using a relation of the form of equation (2.8), the force F_{ri} can be expressed as

$$F_{ri}(t) = K_s \sigma^{\xi}(t), \tag{2.9}$$

where $\sigma(t)$ is the approach at $s = s_p$ and is given by $\sigma(t) = r(s_p, t) - e_r$, with $r(s_p, t) = \sqrt{x^2(s_p, t) + y^2(s_p, t)}$ being the tube radial displacement at the support location, see Fig.2.3. K_s is an effective contact stiffness, which can be determined experimentally.

[1]Note, however, that local stresses will be strongly dependent on the accuracy of the force time-history.

2.2.2 The Impact Damping Force F_{rd}

F_{rd} may be expressed as a viscous force as follows:

$$F_{rd} = c_s(\sigma)\dot{r} + c_{sf}(\sigma, e_r)\dot{r}. \tag{2.10}$$

The damping coefficient c_s is a non-linear function of σ and is related to direct impacting energy loss, while c_{sf} relates to squeeze-film damping effects; c_s and c_{sf} can only be determined approximately. As discussed later, considerabiy more effort has gone into the estimation or measurement of c_{sf}. Firstly, we turn to a theoretical analysis for the determination of c_s.

2.2.2.1 Estimation of the equivalent viscous damping coefficient c_s

Traditionally, the mechanics of impacting bodies has been treated by introducing a coefficient of restitution to represent the resulting energy loss. From experimental tests, the coefficient of restitution is known to be a non-linear function of the impact velocity u_r and of the form

$$e = 1 - \alpha_1 u_r + \alpha_2 u_r^2 + ... \tag{2.11}$$

(Goldsmith 1960), in which $u_r > 0$. The coefficient of restitution method does not give an explicit expression for the impact damping force as sought for in equation (2.10), nor indeed any details regarding the impact process. It is, however, possible to obtain an expression for the impact damping force $c_s(\sigma)\dot{\sigma}$ from knowledge of the dependence of e on u_r (equation (2.11)) and the choice of a functional form of $c_s(\sigma)$ which meets certain experimentally determined criteria. The resulting analysis was first proposed by Hunt & Crossely (1975) who studied the stereomechanical impact of two spheres. For the present analysis, cylinder/support impacting is not a stereomechanical process, hence beam modal deflection needs to be considered.

For the equivalent viscous damping force to be representative of the energy dissipation mechanism during an impact, the functional form of $c_s(\sigma)$ must satisfy the following conditions:

(i) the total energy dissipated by the equivalent viscous force should equal the energy loss indicated by the coefficient of restitution;

(ii) $c_s(\sigma)$ should increase smoothly from zero at $\sigma = 0$ and vanish smoothly at the end of the impact; hence the force variation should be as depicted by the solid line in Fig.2.4 which is in concordance with experimental observation (the dotted curve in Fig.2.4 depicts the discontinuous jump, at $\sigma = 0$ in the damping force (incorrectly) predicted when $c_s = const.$);

(iii) the resulting impact history should be reasonably representative of a real impact process.

In the analysis that follows will shall refer back to these conditions and show how they apply.

The impact process may be represented by Fig.2.3 if the moving body is taken to be the cylinder (the cross-section shown here being at the axial location $s = s_p$); furthermore, to simplify the analysis we consider only planar transverse tube motion in the first mode, hence, $r(s,t) = y(s,t) = \phi(s)q(t)$; $\phi(s)$ is the first-mode beam eigenfunction. The tube approaches the support with an incident velocity $u_r = \dot{y}(s_p, t_i)$ and leaves the support with a restitution velocity $v_r = \dot{y}(s_p, t_o)$, where u_r and v_r are related via the coefficient of restitution e, which is a function of u_r as indicated by equation (2.11).

The difference in kinetic energies before and after impact is

$$\Delta E_k = \frac{1}{2} m I_1 \left[\dot{q}^2(t_i) - \dot{q}^2(t_o)\right]. \tag{2.12}$$

where $I_1 = \int_0^l \phi^2(s) ds$.

Equation (2.11) may be written in terms of the generalized coordinate $q(t)$ by substituting $u_r = \phi(s_p)\dot{q}(t_i)$. The result is the following relation between $\dot{q}(t_i)$ and

$\dot{q}(t_o)$:

$$\left|\frac{\dot{q}(t_o)}{\dot{q}(t_i)}\right| = e = 1 - \alpha_1\phi(s_p)\dot{q}(t_i) + \alpha_2\phi^2(s_p)\dot{q}^2(t_i) + ..., \qquad \alpha_1 > 0. \tag{2.13}$$

Using equation (2.13) to the linear term, the following is obtained for the energy loss (2.12):

$$\begin{aligned}\Delta E_k &= \frac{1}{2}mI_1\dot{q}^2(t_i)\left[1 - \{(1 - 2\alpha_1\phi(s_p)\dot{q}(t_i) + (\alpha_1\phi(s_p)\dot{q}(t_i))^2 + (...2\alpha_2\phi^2(s_p)\dot{q}^2(t_i)...)\}\right] \\ &\simeq mI_1\alpha_1\phi(s_p)\dot{q}^3(t_i). \end{aligned} \tag{2.14}$$

Condition (i) on p.32 requires that the equivalent viscous force result in energy dissipation equal to ΔE_k. This leads to the equality

$$\oint c_s(\sigma)\dot{\sigma}d\sigma = \Delta E_k. \tag{2.15}$$

The loop integral is performed around the solid curve shown in Fig.2.4. Approximating this by twice the integral from $\sigma = 0$ to $\sigma = \sigma_m$, and using the final result in equation (2.14), equation (2.15) becomes

$$2\int_0^{\sigma_m} c_s(\sigma)\dot{\sigma}d\sigma = mI_1\alpha_1\phi(s_p)\dot{q}^3(t_i). \tag{2.16}$$

Guided by condition (ii), the following functional form of $c_s(\sigma)$ is taken:

$$c_s(\sigma) = \bar{c}_s\sigma^{\xi}, \tag{2.17}$$

where $\bar{c}_s$ is an unknown constant. The solution of equation (2.16) for $c_s(\sigma)$, which is our primary goal, then simply reduces to the determination of the constant $\bar{c}_s$.

As yet, equation (2.16) can still not be solved since the approach velocity during the impact ($\dot{\sigma}$) and the maximum approach σ_m remain unknown. $\dot{\sigma}$ and σ_m will be determined using condition (iii) as a guide. The total energy lost at impact is generally a small fraction of the total energy of the cylinder. It is therefore expected that for the real impact process, $\dot{\sigma}$ and σ_m will not deviate significantly from the velocity time-history and maximum approach for the case of a perfectly elastic impact. Estimates of $\dot{\sigma}$ and σ_m will therefore be obtained by considering a perfectly elastic impact.

From the onset of the impact process, the total system energy is

$$E_t = \frac{1}{2} m I_1 \dot{q}^2(t) + \frac{1}{2} I_2 q^2(t) + \int_0^{\sigma} K_s \sigma^{\xi} d\sigma, \tag{2.18}$$

where $I_1 = \int_0^l \phi^2(s)ds$ and $I_2 = \int_0^l EI\left[\phi''(s)\right]^2 ds$. The last term in equation (2.18) is the potential energy stored in the support as a result of the support stiffness force given by equation (2.9).

The tube energy at the instant the impact commences (at $t = t_i$) is, from equation (2.18)

$$E_t = \frac{1}{2} m I_1 \dot{q}^2(t_i) + \frac{1}{2} I_2 q^2(t_i). \tag{2.19}$$

Equations (2.18) and (2.19) may be equated, to obtain an expression for tube velocity variation during a perfectly elastic impact. The resulting expression for $\dot{q}(t)$ is

$$\dot{q}(t) = \left[\dot{q}^2(t_i) - \frac{I_2}{mI_1}\left(q^2(t) - q^2(t_i)\right) - \frac{2K_s}{mI_1(\xi+1)}\sigma^{\xi+1}\right]^{1/2}. \tag{2.20}$$

The following relations between the physical and generalized coordinates are used in obtaining an expression for $\dot{\sigma}$:

$$\begin{aligned} \sigma &= y(s_p, t) - e_r \\ &= \phi(s_p)\left[q(t) - q(t_i)\right]; \end{aligned} \tag{2.21}$$

hence,

$$\dot{\sigma} = \phi(s_p)\dot{q}(t). \tag{2.22}$$

Equation (2.21) can also be used to express $q(t)$ in terms of σ, specifically noting that

$e_r = \phi(s_p)q(t_i)$, thus yielding

$$q^2(t) - q^2(t_i) = \frac{\sigma}{\phi(s_p)}\left(2q(t_i) + \frac{\sigma}{\phi(s_p)}\right). \tag{2.23}$$

Finally substituting (2.20) into (2.22) and using (2.23), the following expression is obtained for the approach velocity variation:

$$\dot{\sigma} = \phi(s_p)\left\{\dot{q}^2(t_i) - \frac{I_2}{mI_1}\left[\frac{\sigma}{\phi(s_p)}\left(2q(t_i) + \frac{\sigma}{\phi_{sp}}\right)\right] - \frac{2K_s\sigma^{\xi+1}}{mI_1(\xi+1)}\right\}^{1/2}. \tag{2.24}$$

The maximum approach σ_m occurs when $\dot{\sigma} = 0$. Hence, from equation (2.24), σ_m satisfies the equation

$$\dot{q}^2(t_i) - \frac{I_2}{mI_1}\left[\frac{\sigma_m}{\phi(s_p)}\left(2q(t_i) + \frac{\sigma_m}{\phi_{sp}}\right)\right] - \frac{2K_s\sigma_m^{\xi+1}}{mI_1(\xi+1)} = 0. \tag{2.25}$$

With the expressions for $\dot{\sigma}$ and σ_m determined, equation (2.16) can be solved for the damping constant which gives

$$\overline{c}_s = \frac{mI_1\alpha_1\dot{q}^3(t_i)}{\int_0^{\sigma_m} 2\sigma^\xi\left[\dot{q}^2(t_i) - (a_1\sigma + a_2\sigma^2 + a_3\sigma^{\xi+1})\right]^{1/2}d\sigma}, \tag{2.26}$$

where

$$a_1 = \frac{2e_rI_2}{mI_1\phi^2(s_p)}, \quad a_2 = \frac{I_2}{mI_1\phi^2(s_p)}, \quad \text{and } a_3 = \frac{2K_s}{mI_1(\xi+1)}. \tag{2.27}$$

2.2.2.2 The squeeze-film damping coefficient c_{sf}

For a radial tube/support approach the presence of fluid within the tube/support gap introduces squeeze-film damping (ζ_{sf}) into the system. A tangential relative motion between tube and support also results in viscous shear damping (ζ_{vs}). ζ_{sf} is particularly important when the radial eccentricity surpasses $e_r/2$. The determination of ζ_{sf} has been undertaken by Jendrzejczyk (1986) theoretically and Rogers & Ahn (1986) and Kim *et al.* (1988) experimentally. The same investigators have shown that ζ_{vs} is generally small compared to ζ_{sf}. Kim *et al.* obtained the following empirical expression for ζ_{sf} by correlating with their experimental data:

$$\zeta_{sf} = \beta\left(\frac{2t_s}{l}\right)\left(\frac{t_s}{D}\right)^{0.7}\left(\frac{D}{2e_r}\right)^{0.4}\left(\frac{1}{1-r/e_r}\right)\mathrm{St}^{-0.6}, \tag{2.28}$$

where t_s is the TSP (tube support plate) thickness, r the tube eccentricity within the support, f the oscillation frequency, and β is an empirical factor equal to 100. St is the squeeze-film Stokes number defined as $\mathrm{St} = 2\pi f e_r^2/\nu_f$, where ν_f is the fluid viscosity. Following Jendrzejczyk (1986), c_{sf} was related to ζ_{sf} by $c_{sf} = [2ml\omega_1/\phi_1^2(s_p)]\,\zeta_{sf}$.

2.2.3 Final Form of Support Related Forces

In summary, referring to equations (2.9) and (2.10), the sum total of support related forces becomes

$$F_r = K_s(r-e_r)^{\xi} + \left[\bar{c}_s(r-e_r)^{\xi} + \bar{\beta}\left(\frac{1}{1-r/e_r}\right)\right]\dot{r} \tag{2.29}$$

for the radial direction, where

$$\bar{\beta} = 4\beta\left(\frac{m\omega_1 t_s}{\phi_1^2(s_p)}\right)\left(\frac{t_s}{D}\right)^{0.7}\left(\frac{D}{2e_r}\right)^{0.4}\mathrm{St}^{-0.6}, \tag{2.30}$$

and $\bar{c}_s$ is given by equation (2.26) and, as in equation (2.28), $\beta = 100$. Tangentially to the contact location (see Fig.2.2), friction effects come into play, resulting in a force

$$F_\theta = \mu_{fr}F_r; \qquad v_t > 0, \tag{2.31}$$

where μ_{fr} is the Coulomb dry-friction coefficient. As indicated, equation (2.31) is only correct when the resulting F_θ does not result in direction reversal of the tangential velocity v_t (i.e. during sliding motion). Otherwise, an iterative procedure is required to determine the unknown contact force (during sticking) to ensure that a final state of $v_t = 0$ is attained. This will be considered further in Chapter 4.

Transforming the support forces to Cartesian coordinates (Fig.2.2) we obtain

$$\begin{aligned} F_{xs} &= F_\theta \sin\theta - F_r \cos\theta \\ &= \left\{K_s(r-e_r)^\xi + \dot r\left[\bar c_s r^\xi + \bar\beta\left(\frac{1}{1-r/e_r}\right)\right]\right\}(\mu_{fr}\sin\theta - \cos\theta), \end{aligned} \tag{2.32}$$

$$\begin{aligned} F_{ys} &= -F_\theta \cos\theta - F_r \sin\theta \\ &= -\left\{K_s(r-e_r)^\xi + \dot r\left[\bar c_s r^\xi + \bar\beta\left(\frac{1}{1-r/e_r}\right)\right]\right\}(\mu_{fr}\cos\theta + \sin\theta). \end{aligned} \tag{2.33}$$

2.3 THE FINAL SYSTEM EQUATIONS

The governing equations of motion (2.1 - 2.4, 2.32 - 2.33) are rendered non-dimensional by introducing the following non-dimensional quantities:

$$\begin{aligned} \tilde x &= \frac{x}{D}, \quad \tilde y = \frac{y}{D}, \quad \tilde s = \frac{s}{l}, \quad \tilde m = \frac{m}{\rho D^2}, \quad \tilde s_p = \frac{s_p}{l}, \\ \omega_1^2 &= \lambda_1^4\left(\frac{EI}{ml^4}\right), \quad \tau = \omega_1 t, \quad V = \frac{U}{\omega_1 D}, \quad \tilde K_s = \frac{K_s D^{\xi-1}}{m\omega_1^2}, \\ \tilde c_s &= \bar c_s \frac{D^\xi}{m\omega_1}, \quad \tilde\beta = \frac{\bar\beta}{m}, \quad \zeta = \frac{c}{2m\omega_1}, \quad C_{ma} = \frac{m_a}{\rho\pi D^2/4}, \\ \tilde r &= \frac{r}{D}, \quad \tilde e_r = \frac{e_r}{D}. \end{aligned} \tag{2.34}$$

After some algebraic manipulation, the equations in their non-dimensional form are: for the in-flow direction,

$$\begin{aligned} &\left(1+\frac{\pi C_{ma}}{4\tilde m}\right)\frac{\partial^2\tilde x}{\partial\tau^2} + 2\zeta\frac{\partial\tilde x}{\partial\tau} + \frac{1}{\lambda_1^4}\frac{\partial^4\tilde x}{\partial\tilde s^4} = \\ &\frac{1}{2\tilde m a^2}\left[(V-\frac{\partial\tilde x}{\partial\tau})^2 + \frac{\partial\tilde y}{\partial\tau})^2\right]^{\frac12}\left(\frac{\partial\tilde y}{\partial\tau}C_L + (V-\frac{\partial\tilde x}{\partial\tau})C_D\right) \\ &+\delta(\tilde s-\tilde s_p)\left\{\tilde K_s(\tilde r-\tilde e_r)^\xi + \tilde r'\left[\tilde c_s\tilde r^\xi + \tilde\beta\left(\frac{1}{1-\tilde r/\tilde e_r}\right)\right]\right\}(\mu_{fr}\sin\theta - \cos\theta); \end{aligned} \tag{2.35}$$

and for the cross–flow direction,

$$
\begin{aligned}
&(1+\frac{\pi C_{ma}}{4\tilde{m}})\frac{\partial^2\tilde{y}}{\partial\tau^2}+2\zeta\frac{\partial\tilde{y}}{\partial\tau}+\frac{1}{\lambda_1^4}\frac{\partial^4\tilde{y}}{\partial\tilde{s}^4}= \\
&\frac{1}{2\tilde{m}a^2}\left[(V-\frac{\partial\tilde{x}}{\partial\tau})^2+(\frac{\partial\tilde{y}}{\partial\tau})^2\right]^{\frac{1}{2}}\left((V-\frac{\partial\tilde{x}}{\partial\tau})C_L-\frac{\partial\tilde{y}}{\partial\tau}C_D\right) \\
&-\delta(\tilde{s}-\tilde{s}_p)\left\{\tilde{K}_s(\tilde{r}-\tilde{e}_r)^{\xi}+\tilde{r}'\left[\tilde{c}_s r^{\xi}+\tilde{\beta}\left(\frac{1}{1-\tilde{r}/\tilde{e}_r}\right)\right]\right\}(\mu_{f_r}\cos\vartheta+\sin\theta). \qquad (2.36)
\end{aligned}
$$

The time delay requires that the force coefficients be evaluated as follows:

$$
\begin{aligned}
C_L &= C_L(\tilde{x}(\tau-\Delta\tau),\tilde{y}(\tau-\Delta\tau)), \\
C_D &= C_D(\tilde{x}(\tau-\Delta\tau),\tilde{y}(\tau-\Delta\tau)), \qquad (2.37)
\end{aligned}
$$

the non-dimensional time delay $\Delta\tau$ being given by

$$\Delta\tau=\frac{\mu_r\omega_1 D}{U},$$

where $\mu_r \approx O(1)$.

A standard Galerkin expansion for the orthogonal beam displacements is utilized as follows:

$$
\begin{aligned}
\tilde{x}(\tilde{s},\tau) &= \sum_{i=1}^{N}\phi_i(\tilde{s})\tilde{p}_i(\tau)\ , \\
\tilde{y}(\tilde{s},\tau) &= \sum_{i=1}^{N}\phi_i(\tilde{s})\tilde{q}_i(\tau)\ , \qquad (2.38)
\end{aligned}
$$

where $\phi_i(\tilde{s})$ are the beam eigenfunctions which, for constant m, satisfy the orthogonality conditions

$$\int_0^1\phi_i(\tilde{s})\phi_j(\tilde{s})d\tilde{s}=\begin{cases}1 & \text{for} \quad i=j\\ 0 & \text{for} \quad i\neq j\end{cases} \quad \text{and} \quad \int_0^1\phi_i(\tilde{s})\frac{d^4\phi_j(\tilde{s})}{d\tilde{s}^4}\,dx=\begin{cases}\lambda_i^4 \ \text{for}\ i=j\\ 0\ \text{for}\ i\neq j.\end{cases}$$

Substituting (2.38) into the governing equations (2.35, 2.36) and then multiplying through by $\phi_j(\tilde{s})$ and integrating with respect to $\tilde{s}$ we obtain,

$$\gamma\tilde{p}_i'' + 2\tilde{\zeta}_i\tilde{p}_i' + (\frac{\lambda_i}{\lambda_1})^4\tilde{p}_i = \frac{1}{2\tilde{m}a^2}\int_0^1 \left[(V - \frac{\partial\tilde{x}}{\partial\tau})^2 + (\frac{\partial\tilde{y}}{\partial\tau})^2\right]^{1/2}\left(C_L\frac{\partial\tilde{y}}{\partial\tau} + (V - \frac{\partial\tilde{x}}{\partial\tau})C_D\right)\phi_i d\tilde{s} + \phi_i(\tilde{s}_p)\left\{\tilde{K}_s(\tilde{r} - \tilde{e}_r)^\xi + \tilde{r}'\left[\tilde{c}_s\tilde{r}^\xi + \tilde{\beta}\left(\frac{1}{1 - \tilde{r}/\tilde{e}_r}\right)\right]\right\}(\mu_{fr}\sin\theta - \cos\theta), \quad (2.39)$$

$$\gamma\tilde{q}_i'' + 2\tilde{\zeta}_i\tilde{q}_i' + (\frac{\lambda_i}{\lambda_1})^4\tilde{q}_i = \frac{1}{2\tilde{m}a^2}\int_0^1 \left[(V - \frac{\partial\tilde{x}}{\partial\tau})^2 + (\frac{\partial\tilde{y}}{\partial\tau})^2\right]^{1/2}\left((V - \frac{\partial\tilde{x}}{\partial\tau})C_L - C_D\frac{\partial\tilde{y}}{\partial\tau}\right)\phi_i d\tilde{s} - \phi_i(\tilde{s}_p)\left\{\tilde{K}_s(\tilde{r} - \tilde{e}_r)^\xi + \tilde{r}'\left[\tilde{c}_s r^\xi + \tilde{\beta}\left(\frac{1}{1 - \tilde{r}/\tilde{e}_r}\right)\right]\right\}(\mu_{fr}\cos\theta + \sin\theta). \quad (2.40)$$

$$i = 1, 2, ...N.$$

where, $\gamma = (1 + \pi C_{ma}/(4\tilde{m}))$ and $\tilde{\zeta}_i = \zeta(\lambda_i/\lambda_1)^2$ is the modal damping.

Equations (2.39) and (2.40) fully describe the tube response under fluid excitation, limited by impacting at the loose support. It is reiterated that the friction term is employed with caution to ensure that no reversal of the tube tangential velocity occurs following an impact. The fluid force coefficients C_L and C_D are empirical inputs to the theoretical model. The experimental determination of these coefficients is the subject of Chapter 3.

2.4 REDUCTION TO A TWO-DEGREE-OF-FREEDOM SYSTEM

A natural starting point for the study of the system represented by equations (2.39) and (2.40) is a linearized stability analysis. For this purpose, it is sufficient to reduce the system to its lowest order, which still exhibits the initial cylinder instability behaviour; in this case a linearized 2-d.o.f system, in which only the first mode in the two orthogonal directions is considered. Two simplifications may be considered. Firstly, the support-related forces are zero at the cylinder equilibrium position where cylinder stability is investigated. The second is linearization of the position- and velocity-dependent fluid force terms.

To linearize the velocity terms, the following approximation is used

$$\left[(V - \frac{\partial \tilde{x}}{\partial \tau})^2 + (\frac{\partial \tilde{y}}{\partial \tau})^2\right]^{1/2} \simeq V\left(1 - \frac{1}{V}\frac{\partial \tilde{x}}{\partial \tau}\right). \tag{2.41}$$

Without loss of generality in the stability analysis, we may also consider planar (x, y) tube motion, hence the physical and generalized coordinates are identical; e.g. $\tilde{x} = \tilde{p}_1$, which is physically equivalent to analyzing a rigid, flexibly mounted tube. Furthermore, the position-dependent force coefficients are linearized via the Taylor expansions

$$\begin{aligned} C_L &\simeq C_{L0} + e^{-\lambda\Delta\tau}\left(\tilde{p}_1 \frac{\partial C_L}{\partial \tilde{p}_1} + \tilde{q}_1 \frac{\partial C_L}{\partial \tilde{q}_1}\right), \\ C_D &\simeq C_{D0} + e^{-\lambda\Delta\tau}\left(\tilde{p}_1 \frac{\partial C_D}{\partial \tilde{p}_1} + \tilde{q}_1 \frac{\partial C_D}{\partial \tilde{q}_1}\right). \end{aligned} \tag{2.42}$$

The factor $\exp(-\lambda\Delta\tau)$, where λ is a complex number, represents the time-delay effect in the fluid forces; harmonic tube motion, for flow velocities in the neighbourhood of the critical instability velocity, is implicitly assumed in this formulation (Price & Paidoussis, 1986b).

Equations (2.41) and (2.42) are substituted into (2.39) and (2.40), maintaining only linear terms. Introducing the vector $\mathbf{w} = \{\tilde{p}_1, \tilde{q}_1\}^T$, the resulting linearized equation system may be conveniently expressed in the following vector form:

$$[\mathbf{M}]\ddot{\mathbf{w}} + [\mathbf{D}]\dot{\mathbf{w}} + [\mathbf{K}]\mathbf{w} + \mathbf{F}_0 = \mathbf{0}, \tag{2.43}$$

where

$$[\mathbf{M}] = \begin{bmatrix} \gamma & 0 \\ 0 & \gamma \end{bmatrix},$$

$$[\mathbf{D}] = \begin{bmatrix} 2\tilde{\zeta}_1 + \frac{VC_{D0}}{\tilde{m}a^2}, & -\frac{VC_{L0}}{2\tilde{m}a^2} \\ \frac{VC_{L0}}{\tilde{m}a^2}, & 2\tilde{\zeta}_1 + \frac{VC_{D0}}{2\tilde{m}a^2} \end{bmatrix},$$

$$[\mathbf{K}] = \begin{bmatrix} 1 - \frac{V^2e^{-\lambda\Delta\tau}}{2\tilde{m}a^2}\frac{\partial C_D}{\partial \tilde{p}_1}, & -\frac{V^2e^{-\lambda\Delta\tau}}{2\tilde{m}a^2}\frac{\partial C_D}{\partial \tilde{q}_1} \\ 1 - \frac{V^2e^{-\lambda\Delta\tau}}{2\tilde{m}a^2}\frac{\partial C_L}{\partial \tilde{p}_1}, & -\frac{V^2e^{-\lambda\Delta\tau}}{2\tilde{m}a^2}\frac{\partial C_L}{\partial \tilde{q}_1} \end{bmatrix},$$

and

$$[\mathbf{F}_0] = \begin{bmatrix} -\frac{V^2C_{D0}}{2\tilde{m}a^2} \\ -\frac{V^2C_{L0}}{2\tilde{m}a^2} \end{bmatrix}.$$

For the purpose of a stability analysis, the steady force $\mathbf{F_0}$ determines the tube static equilibrium position, $\mathbf{w_e}$, at which the matrices [D] and [K] are evaluated; equivalently, the Taylor series expansions in equation (2.42) are for a coordinate system centred at this equilibrium position. For a given flow velocity, $\mathbf{w_e}$ may be obtained by solving the non-linear force balance equation

$$\mathbf{w_e} = -[\mathbf{K}(\mathbf{w_e}, \mathrm{V})]^{-1}\mathbf{F_0}(\mathbf{w_e}, \mathrm{V}). \tag{2.44}$$

A stability analysis of equation (2.43) is carried out using standard eigenvalue techniques. With the complete position-dependent fluid force-field known, the effect of the tube equilibrium position on the instability flow velocity can also be determined. For the moment, however, we turn to the experimental determination of the fluid force field.

Chapter 3

THE STATIC FLUID-FORCE FIELD

Lift and drag forces were measured for a test-cylinder mounted on a biaxial force balance in a blow-down wind-tunnel. The test-cylinder was part of an array of otherwise rigidly fixed cylinders. The array consisted of seven cylinder rows, with alternate rows containing 14 and 15 cylinders, respectively. The rigid cylinders spanned the test-section and were mounted on aluminium plates, which were in turn fixed to the top and bottom test-section surfaces. The test-cylinder protruded outside the test-section, being mounted to the force balance at the bottom. To eliminate any cylinder vibration, a damping mechanism was attached to the upper end of the test cylinder as shown in Fig.3.1.

The wind tunnel test section measures 609×914 mm, and has free-stream turbulence of 0.5%. A maximum wind speed of 40 m/s can be attained in the empty test section. Blockage introduced by the array reduces this maximum velocity to approximately 15 m/s.

3.1 FORCE BALANCE CALIBRATION

The force balance employs two linear displacement transducers to sense the displacement of two pairs of short rectangular beams positioned orthogonally to each other. The transducer signal is amplified and multiplied by a calibration factor to give the static force reading.

Calibration of the force balance was performed by applying a known static force and measuring the corresponding voltage output. Weights, ranging from 0.1 N to 10

N, provided the required force.

Fig.3.2 shows the calibration curves for the drag and lift directions, respectively. The force balance exhibits excellent linearity in the force range considered for both the orthogonal directions. During the experiments the highest load on the force balance corresponded to an output of approximately 1000 mV which is well within the linear range.

3.2 THE EFFECT OF REYNOLDS NUMBER ON C_D

Tests were first conducted to investigate the variation of C_D with Reynolds number, Re. For these tests the upstream flow velocity U_∞ was varied in the range $1.3 < U_\infty < 7.5$ m/s. This corresponds to a Re range, $2.15 \times 10^3 \leq \mathrm{Re} \leq 1.24 \times 10^4$.

The variation of C_D with Re, for the cylinder located at the array equilibrium position, is shown in Fig.3.3. Results for increasing and decreasing flow velocity are plotted, showing good repeatability and little hysteresis (if any). C_D shows a decreasing trend, initially at a high rate. For $\mathrm{Re} \geq 10^4$, C_D almost levels off to an average value of 6.5. In comparison, a nearly constant C_D value is obtained for a solitary cylinder in the same Re range (not shown). Hence, in the array, there is a slower migration with Re of the separation point, responsible for the gradual decrease in C_D; this may be related to the confinement of the flow within the inter-cylinder channels in the array.

The lift coefficient variation is also shown in Fig.3.3. Array symmetry dictates that C_L be zero for the cylinder position tested. As shown later, C_L is extremely sensitive to cross-flow cylinder position ($\tilde{y}$) near $\tilde{y} = 0$. This sensitivity is reflected in the slightly non-zero value of C_L in Fig.3.3. Indeed, a cylinder displacement of 5/1000 in. (0.127 mm) resulted in a significant change in C_L.

3.3 VARIATION OF C_L AND C_D IN THE RANGE $-0.23 \leq (\tilde{x}, \tilde{y}) \leq 0.23$

In the primary force measurement tests, C_L and C_D were measured over a range of in-flow and cross-flow cylinder displacements. An area of $0.46D \times 0.46D$ was covered by a grid of size $D/52$ ($\equiv 1/52$ in., or 0.49 mm). The force balance was mounted on a bi-directional traverse mechanism which made possible accurate cylinder displacements. The displacement range, which corresponds to an area of 0.0529 in^2 was covered with 625 grid points. With the cylinder positioned at each grid point, a 1 minute settling period was allowed. A 10 sec. time average of the force outputs was then taken, using a HP 3562A FFT spectrum analyzer.

Fig.3.4 shows the variation of C_L and C_D with cross-flow displacement $\tilde{y}$ with the movable cylinder at its the equilibrium in-flow position ($\tilde{x} = 0$). Most striking is the extreme sensitivity of C_L near $\tilde{y} = 0$, the cross-flow equilibrium position. As shown by Price & Paidoussis (1986b), the large and negative value of $\partial C_L/\partial \tilde{y}$ makes this cylinder location very susceptible to instability. C_L also varies nearly linearly at this location; although only three data points show this linearity, repeated tests showed this to be always the case. C_L reaches extremum values of ± 4.1 at $\tilde{y} = \mp 0.055$. This variation in C_L may be associated with the cylinder emerging from the wake of its upstream neighbour and being subjected to the high speed channel flow between the cylinder columns, Fig.3.5. A gradual drop in $|C_L|$ to an average value of 3.0 occurs as the cylinder approaches either of its row-2 neighbours (cylinders 2 and 3 in Fig.3.5).

The drag coefficient (Fig.3.4(b)) shows local maxima, also at $\tilde{y} = \pm 0.055$, with a peak average value of $C_D = 7.0$, again an effect of exposure to the streaming channel flow. At $\tilde{y} = 0$, the test cylinder falls directly behind a row-1 cylinder resulting in a local minimum in C_D. For $|\tilde{y}| > 0.055$ C_D decreases monotonically as more of the test cylinder falls in the "shadow" of the neighbouring row-2 cylinder.

When the in-flow tube position $\tilde{x}$ is changed, the C_L and C_D versus $\tilde{y}$ trends observed in Fig.3.4 vary differently, depending on whether for the new in-flow position

$\tilde{x} > 0$ (corresponding to a downstream displacement) or $\tilde{x} < 0$ (an upstream displacement). Note, however, that this does not imply the existence of symmetry at $\tilde{x} = 0$, but rather that the neighbourhood of $\tilde{x} = 0$ is a transition region. The proximity of the test cylinder to its upstream or downstream neighbours, and the associated inter-cylinder gaps determine the changes that occur in the force coefficients.

Considering first an upstream displacement of the test cylinder to $\tilde{x} = -0.173$, the resulting force coefficient variations are shown in Fig.3.6. At this position, both the magnitudes and trends in the force coefficients variation with cross-flow displacement differ appreciably from the trends at the equilibrium cylinder location $\tilde{x} = 0$. C_L shows increased magnitudes in the range $0.05 < |\tilde{y}| < 0.20$, attaining a maximum absolute value of 7.0. The C_L variation is also approximately piecewise linear over the complete $\tilde{y}$ range. Proximity to either of the row-2 cylinders has a drastic effect on C_L, resulting in a reversal of the lift force direction at $\tilde{y} = \pm 0.23$. Coincidentally with this reversal in lift force direction, a large drop in C_D occurs, Fig.3.6(b). For $\tilde{x} = -0.173$ the test cylinder is located deeper within the wake of the row 1 cylinder which accounts for the overall reduction in C_D. The drastic drop in C_D and simultaneous vanishing of C_L occur when the cylinder essentially blocks the streaming channel flow on one side (e.g. between cylinders 1 and 2 in Fig.3.5) while widening the available channel area on the opposite side.

The force coefficient variation changes significantly for downstream positions of the cylinder $\tilde{x} > 0$. Fig.3.7 shows the results for $\tilde{x} = +0.173$. In this case the variation is largely determined by proximity to row-4 and -5 cylinders as well as the inter-cylinder gap. A large and negative value of $\partial C_L/\partial \tilde{y}$ is obtained not only in the neighbourhood of $|\tilde{y}| = 0$, but essentially over the complete range of $-0.23 < \tilde{y} < +0.23$; the only exception being the two inflection points at $\tilde{y} = \pm 0.06$. At the extreme positions, $\tilde{y} = \pm 0.23$, an extremum C_L value with magnitude $|C_L| = 8.5$ is obtained. A reversal in the C_D trend is observed at $|\tilde{y}| = 0.12$, resulting in increased drag. This is due to the cylinder increasingly blocking the downstream inter-cylinder gap, which results in C_D values as high as 7.0 for $\tilde{y} = \pm 0.23$.

In the complete test area, $-0.23 \leq \tilde{x}, \tilde{y} \leq +0.23$, the force coefficients exhibit a smooth transition between the three scenarios described above. In Fig.3.8 are presented results in the form of 3-D plots for the complete test area. Note that the axes and flow directions are different for the two maps; the perspectives were chosen for optimum visualization. The neighbourhood of $\tilde{x} = 0$ is seen to be a transition region between the two trends in the force coefficient variations discussed above. At the extreme upstream and downstream positions (and for $|\tilde{y}| > 0.22$) very large changes in C_L and C_D occur. Near $\tilde{x} = -0.23, \tilde{y} = \pm 0.23$, a reversal in the lift force direction results. This has significant consequences for cylinder stability, since a reversal in the force direction indicates that the cylinder would be susceptible to a static instability *but not* a dynamic instability at this position (in the cross-flow direction). In the in-flow direction, large C_D values coupled with positive $\partial C_D/\partial \tilde{x}$ imply increased cylinder stability far downstream. It is expected that for other cylinder positions also, the significant variations in C_L and C_D will be reflected in the cylinder stability characteristics.

Contour plots corresponding to the 3-D plots are shown in Fig.3.9. The large and negative $\partial C_L/\partial \tilde{y}$ in the corridor centred about $\tilde{y} = 0$ (Fig.3.9(a)) vanishes downstream, near $\tilde{x} = 0.10$, resulting in a region where the cylinder experiences no lift force. With the exception of the extreme cylinder positions, the overall variation in C_D magnitudes is relatively small (Fig.3.9(b)) in comparison to the variations observed for C_L. A convolution of the lift and drag coefficients gives a net fluid force vector as shown in Fig.3.10. The length of the arrows is proportional to a normalized force magnitude. Over most of the test region, the steady force is directed towards the symmetry line $\tilde{y} = 0$. The locations of possible cross-flow static instability are evident at $\tilde{x} = -0.17, \tilde{y} = \pm 0.20$ where the net force changes direction and $C_L \simeq 0$. The steady force increases for downstream cylinder positions primarily due to higher C_D values.

Chapter 4

THE DYNAMICS OF A TWO-DEGREE-OF-FREEDOM SYSTEM

The fluid force variation discussed in Chapter 3 suggests the possibility of highly unstable cylinder behaviour in the neighbourhood of the corridor $\tilde{y} = 0$. Moreover, for some cylinder positions far upstream, a necessary condition for static instability was seen to exist. This is significant since this array is well known for being highly unstable dynamically but not statically (when stability in the neighbourhood of $\tilde{x} = \tilde{y} = 0$ is considered).

A detailed analysis of cylinder stability behaviour will be presented in the first part of this chapter. Using a linear stability analysis, the effect on cylinder stability of varying the cylinder position over the range of the experimental tests will be determined. The study is initially restricted to the analysis of the system in which only first modes in the two orthogonal directions are considered.

The linear stability study is a precursor to a complete nonlinear analysis under fluid excitation of the system to be presented in Section 4.2. By systematically including initially the fluid-related non-linearities, and later support related non-linearities, in the 2-d.o.f model of Section 2.4, it will be possible to elucidate the effects specific to either one of the non-linear effects without the added complication of higher modes. As discussed in Section 4.2, the effect of the support is introduced via a simple restitution model both for simplicity and also for consistency with the structural simplification to a single mode (in each of the orthogonal directions) in the present system. The complete support model developed in Chapter 2 is utilized in the analysis of the higher dimensional systems later, in Chapters 5 and 6.

4.1 LINEAR STABILITY ANALYSIS AND EFFECT OF THE TUBE EQUILIBRIUM POSITION

Restricting the analysis to obtaining a stability boundary, a solution to the linearized equations (2.43) will suffice. Considering a solution of the form $\mathbf{w}(\tau) = \mathbf{w}_0 \exp(\lambda\tau)$ and substituting into the linear equations, and "neglecting" the steady force $\mathbf{F}_0$,[1] we obtain,

$$\{\lambda^2[\mathbf{M}] + \lambda[\mathbf{D}(V)] + [\mathbf{K}(\lambda, V)]\}\mathbf{w}_0 \exp(\lambda\tau) = 0. \tag{4.1}$$

For a solution to exist we must have

$$\mathrm{Det}\left[\lambda^2[\mathbf{M}] + \lambda[\mathbf{D}(\mathrm{V})] + [\mathbf{K}(\lambda, \mathrm{V})]\right] = 0. \tag{4.2}$$

On the stability boundary, purely imaginary or zero eigenvalues exist. An iterative procedure is used to solve equation (4.2), the iteration starting with an initial, assumed value of λ.

4.1.1 Low $\tilde{m}\delta$ versus High $\tilde{m}\delta$ Stability Behaviour

For low values of the mass-damping parameter $\tilde{m}\delta$, stability behaviour is characterized by regions of instability interspersed with stable regions as the flow velocity is varied. Fig.4.1 shows plots of $Re(\lambda)$ and $Im(\lambda)$ as functions of non-dimensional flow velocity, V, for the cylinder parameters $\tilde{m} = 100, \delta = 0.001$, and the tube equilibrium position at $\tilde{x} = 0, \tilde{y} = 0$. The eigenvalue λ_1 corresponds to cross-flow motion while λ_2 relates to the in-flow direction.

Starting iterations at the low flow velocity $V = 0.020$, the first instability occurs at $V = 0.065$ as evidenced in Fig.4.1(a) by $Re(\lambda_1) > 0$. The instability is the result of

[1]The results thus obtained pertain to a single cylinder model of a fully flexible array for which $\mathbf{F}_0$ causes no change in the relative cylinder positions; this is discussed further in Section 4.1.2.

a Hopf bifurcation, resulting in a purely imaginary eigenvalue. The instability occurs in only the cross-flow direction; hence, λ_2, associated with the in-flow direction, has a negative real part, confirming that the instability is of the single degree-of-freedom negative damping type. As V is increased, restabilization occurs ($Re(\lambda) < 0$) at $V = 0.077$. The alternation between stability and instability is repeated at $V = 0.112$ and $V = 0.153$. Final instability, above which no restabilization occurs, is at $V = 0.343$. This sequence is typical for low mass damping parameter values, at least when the tube is located at the array equilibrium position. Fig.4.1(b) shows that the predicted fluidelastic frequency remains within 0.5% of the no flow frequency for the cross-flow direction, while essentially no change in in-flow frequency is observed.

For high mass damping parameter values, $\tilde{m} = 10,000$ and $\delta = 0.1$, and tube position $\tilde{x} = 0, \tilde{y} = 0$, only one stability boundary exists. A monotonic increase in $Re(\lambda_1)$ is observed in this case, as shown in Fig.4.2(a), while $Re(\lambda_2)$ remains negative. A corresponding 11.5% increase in frequency is observed in cross-flow at the instability velocity, relative to the no flow frequency.

4.1.2 Effect of Cylinder Position on Instability

The damping and stiffness matrices, **D** and **K**, are nonlinear functions of the cylinder position being composed of C_L, C_D and their derivatives with respect to position (see equation (2.43)). With these quantities known from the experimental measurements, it is possible to evaluate the effect of displacing the cylinder from the array equilibrium position on the resulting stability behaviour. This reflects the scenario in reality where, more often than not, a tube within an array will not be perfectly aligned.

The eigenvalue analysis was performed for cylinder equilibrium positions within the force measurement range, ($-0.23 < \tilde{x} < 0.23$, $-0.23 < \tilde{y} < 0.23$). The tube static equilibrium position varies with flow velocity due to the steady force $\mathbf{F_0}$. Linear stability analysis does not consider this effect of tube equilibrium position variation with flow, but only the final tube position. Nonlinear dynamical effects may alter the final state as the tube migrates towards the static equilibrium position; hence, for instance, stability may not be regained if lost while the cylinder passes through an unstable location, despite a predicted final stable equilibrium position. The results obtained more closely represent the case of a cylinder deep inside a fully flexible array, in which $\mathbf{F_0}$ causes equal static displacement of all cylinders, hence relative cylinder positions remain unchanged; a cylinder equilibrium position then, refers to the zero flow cylinder position.

Fig.4.3 shows contour and 3-D plots of cylinder instability velocity for the low mass damping parameter $\tilde{m} = 100, \delta = 0.01$. The instability boundary considered here is the final one, past which no restabilization occurs. Increasingly darker shades of grey in Fig.4.3(a) correspond to increased instability; the most lightly shaded areas correspond to complete cylinder stability.[2]

As predicted by a study of the fluid forces in Chapter 3, cylinder position variation markedly affects the resulting stability behaviour. The stability behaviour not only changes, but in some cases, instabilities no longer occur, e.g. at $\tilde{x} = +0.06, \tilde{y} = \pm 0.08$. The corridor $|\tilde{y}| \leq 0.04$ is highly unstable, as are most upstream positions in the range $\tilde{x} < -0.10, |\tilde{y}| < 0.20$. For most of the unstable region, the instability is dynamic. In the two small regions centred about $\tilde{x} = -0.18, \tilde{y} = \pm 0.20$, however, static instability occurs. This is in concordance with the observation of a vanishing of C_L with $\partial C_L/\partial \tilde{y} > 0$ in this region, as discussed in Chapter 3.

The dependence of V_c on cylinder position correlates with the variation of the derivative $\partial C_L/\partial \tilde{y}$; compare Figs.4.3(a) and 4.4(a). The distinct stable islands centered at $\tilde{x} = +0.06, \tilde{y} = \pm 0.08$ coincide with high and *positive* values of $\partial C_L/\partial \tilde{y}$.

For the central position $\tilde{x} = \tilde{y} = 0$ an unstable velocity range exists, below the final instability velocity, as shown in Fig.4.5(a,b). When the cylinder position is changed in the cross-flow direction by 0.02 cylinder diameters, (to position 'A' in Fig.4.3(a)), the low velocity instability range disappears as seen in Fig.4.5(c,d). The disappearance of this instability region for a displacement of only 2% of the cylinder diameter is very

[2] A cylinder position was considered stable if no instability occurred at 10 times the instability velocity at $\tilde{x} = \tilde{y} = 0$.

significant, as it may explain why these instability regions have remained elusive to experimenters, despite their theoretical prediction in the present work and previously by others, e.g. Price & Paidoussis (1986b) and Lever & Weaver (1986b). Only in highly specialized and precisely controlled experiments have multiple instability regions been observed (Andjelić *et al.* 1990). For the present array at least, it is clear that the precision in tube positioning (to within $0.02D$), makes it nearly impossible to observe these instabilities in ordinary experiments or operational heat exchangers. This, of course, is good news to the designer, since the most important instability (and possibly the only one likely to occur) is the highest-velocity instability.

Fig.4.6 shows eigenvalue plots for positions increasingly farther away from the symmetry line $\tilde{y} = 0$; (a,b) and (c,d) correspond to position 'B' ($\tilde{x} = 0.16,\ \tilde{y} = 0.02$) and 'C' ($\tilde{x} = 0.06,\ \tilde{y} = 0.19$) respectively in Fig.4.3. Final instability occurs at $V_c = 0.43$ for location 'B' and at $V_c = 0.40$ for position 'C'. No multiple instability regions are observed for these positions; the graphs of $Re(\lambda_1)$ in fact show the likelihood of the occurrence of multiple instability regions to be diminished.

At high mass-damping parameter values $\tilde{m} = 10,000$ and $\delta = 0.1$, the stability boundary contour plot, Fig.4.7, shows overall similarity to the low $\tilde{m}\delta$ case. For the present set of parameters, however, stability is more widespread. This is mainly associated with the change in time-delay, as compared to the low mass-damping parameter case.

4.2 SUPPORT-INACTIVE CYLINDER RESPONSE

For the purpose of determining the non-dimensional critical flow velocity (V_c) for fluidelastic instability, as well as the uninhibited rate of growth of the limit cycle amplitude, the tube support was initially ignored. Hence, the support reaction, represented by the terms F_{xs} and F_{ys} in equations (2.1, 2.2) is zero. In the analysis to follow, the cylinder equilibrium position is at $\tilde{x} = \tilde{y} = 0$.

Previous studies have shown that, at large values of the mass damping parameter ($\tilde{m}\delta$), V_c varies approximately linearly with $\tilde{m}\delta$. For $\tilde{m}\delta = 1000$, the non-linear analysis gives a critical flow velocity of $V_c = 10.8$, in agreement with the linearized analysis. Fig.4.8(a) shows the post-instability limit cycle amplitude for cross-flow motion as a function of non-dimensional flow velocity, V. The instability was found to be of the supercritical Hopf type; hence, for $V < V_c$, tube oscillations decayed to zero for all initial conditions. The lowest limit cycle amplitude is $\tilde{y} = 0.02$. This value of $\tilde{y}$ corresponds to the limit of the band (centred around $\tilde{y} = 0$) in which C_L varies linearly with $\tilde{y}$, as described earlier. Due to this linear behaviour of C_L near $\tilde{y} = 0$ (for the most part of the $\tilde{x}$ range), the minimum limit cycle amplitude is 0.02, for any velocity at which the system is unstable. For $V > V_c$ the limit cycle amplitude increases almost linearly with V. As predicted by the linear analysis the instability was of the negative damping type, and occurred only in the cross-flow direction. In-flow vibration resulting from fluid coupling exhibits a similar trend, as depicted in Fig.4.8(b), albeit with more pronounced non-linearity in the amplitude growth compared to the cross-flow case. Note that in-flow amplitudes are two orders of magnitude lower than the cross-flow amplitudes. The drag coefficient, C_D, is relatively independent of $\tilde{y}$ near the equilibrium position ($\tilde{x} = \tilde{y} = 0$); hence, despite large cross-flow vibration, there is little in-flow motion.

Low $\tilde{m}\delta$ linear stability behaviour are charaterized by regions of instability, interspersed with stable regions over a certain range of V — until a final velocity is reached, past which, stability is no longer regained.

Fig.4.9(a,b) shows in-flow and cross-flow limit cycle amplitude variations with V for $\tilde{m} = 100, \delta = 0.01$. An unstable region is observed prior to the final instability. Notice that in the unstable velocity range, the lowest cross-flow amplitude is 0.02.

In-flow motion (Fig.4.9(a)) is three orders of magnitude smaller than its cross-flow counterpart. Once again, the in-flow direction is stable and motion is only induced through the weak fluid coupling between the orthogonal directions.

When δ is decreased by a factor of 10 to 0.001, cross-flow vibration amplitudes increase to approximately double their values at $\delta = 0.01$, Fig.4.9(c). For this lower damping level, a second instability region exists in the lower velocity range $0.065 < V < 0.077$. A third instability region is observed when δ is reduced to 0.0001, Fig.4.9(d).[3] The velocity ranges corresponding to these instability regions are identical to those predicted by the linearized analysis. The increase in amplitude with the second reduction in δ is much lower than that associated with the first, being only approximately 15% at $V = 0.13$ and less than 5% at $V = 0.45$. This variation in limit cycle amplitude with δ is summarized in Fig.4.10, where the amplitude at a constant non–dimensional flow velocity $V = 0.13$ is plotted versus δ.

4.3 THE EFFECT OF A LOOSE SUPPORT ON THE 2-D.O.F. SYSTEM RESPONSE

In this section the presence of the motion-limiting loose support is taken into account. The most important effect of the support is to introduce strong coupling between the two orthogonal directions, once vibration amplitudes surpass the cylinder/support clearance value, e_r. The primary goal, at the present stage, is to investigate the effect on the global tube dynamics of the presence of the support. To avoid delving into details of the cylinder/support interaction *during* an impact, in the spirit of the present simplified 2-d.o.f. model, the complex support model of equations (2.32, 2.33) in Section 2.2 is replaced by a simple restitution/impact model.

The cylinder response may be thought of as comprised of two regimes. In the 'flight' regime, the cylinder is under the influence of the fluid force field only. In the second, the 'impact' regime, support interaction forces arise. The tube velocities before and after impact are related via the restitution model as follows. Consider the planar motion of the cylinder centre of mass as represented in Fig.4.11(a). At the contact location c, the tube approach velocity is u, while the velocity after impact is

[3]It should be remarked that it is not pretended that such low values of δ are achievable in practice; the intention here was to see what the effect of increasing or decreasing δ is on the number of unstable regions.

v. Considering the momentum change in the radial direction, we have

$$m\, u_r + N_r = m\, v_r, \tag{4.3}$$

where N_r is the impulse of the radial impact force and where u_r and v_r are the radial components of u and v; they are magnitudes as defined in Fig.4.11(a) rather than vectors. The corresponding equation for the momentum change in the transverse direction t is,

$$m\, u_t + N_t = m\, v_t. \tag{4.4}$$

To account for the energy loss at impact (radial direction only), a coefficient of restitution, e, is used; hence,

$$\tfrac{1}{2}\, m\, v_r^2 = e^2 \left(\tfrac{1}{2}\, m\, u_r^2\right). \tag{4.5}$$

The normal and transverse impulses are related by the coefficient of friction,

$$\mu_{fr} = N_t / N_r. \tag{4.6}$$

By using equations (4.3) and (4.5) we obtain

$$N_r = m|u_r|(1+e). \tag{4.7}$$

From equations (4.4), (4.6) and (4.7), the transverse velocities before and after impact are related by

$$v_t = u_t - \mu_{fr}\, u_r(1+e), \qquad (v_t > 0), \tag{4.8}$$

where the velocity directions are as defined in Fig.4.11(a). Clearly equation (4.8) is only valid if $v_t > 0$; otherwise we have the adherence condition, for which $v_t = 0$. The velocity vector diagram in Fig.4.11(b) relates the polar coordinate velocities derived above to their Cartesian counterparts. The transformation equations before impact, for instance, are

$$\begin{aligned}\tilde{x}' &= (u_r \cos\theta - u_t \sin\theta)/\omega_0 D,\\ \tilde{y}' &= (u_r \sin\theta + u_t \cos\theta)/\omega_0 D,\end{aligned} \tag{4.9}$$

where, for instance, the dimensionless velocity $\tilde{x}' = \dot{x}/\omega_0 D$. The angle $\theta = \tan^{-1}(\tilde{y}/\tilde{x})$ and $\tilde{x}, \tilde{y}$ are dimensionless coordinates of the impact location c. When $u_r = 0$, pure sliding motion occurs. The radial tube/support contact force is then mu_t^2/e_r. This results in a transverse frictional force given by $\mu_{fr} mu_t^2/e_r$.

4.3.1 Solution of the Equations of Motion

The final form of the equations of motion is

$$\begin{aligned}\tilde{x}'' + \tilde{c}\tilde{x}' + \tilde{x} &= \left(\frac{1}{2\tilde{m}a^2}\right)\left\{(V - \tilde{x}')^2 + \tilde{y}'^2\right\}^{1/2}\\ &\quad \times \left[\tilde{y}'\, C_L(\tau) + (V - \tilde{x}')C_D(\tau)\right],\\ \tilde{y}'' + \tilde{c}\tilde{y}' + \tilde{y} &= \left(\frac{1}{2\tilde{m}a^2}\right)\left\{(V - \tilde{x}')^2 + \tilde{y}'^2\right\}^{1/2}\\ &\quad \times \left[(V - \tilde{x}')\, C_L(\tau) - \tilde{y}'\, C_D(\tau)\right],\end{aligned} \tag{4.10}$$

where $C_L(\tau)$ and $C_D(\tau)$ are determined as discussed in Section 2.1 to account for the time delay.[4] Equations (4.10) are valid as long as the tube radial displacement $\tilde{r} = (\tilde{x}^2 + \tilde{y}^2)^{1/2}$ is less than $\tilde{e}_r$, the radial clearance. When $\tilde{r} = \tilde{e}_r$, impacting occurs.

Equations (4.10) are numerically integrated using a fourth order Runge–Kutta algorithm. The cylinder and support parameters are

$$\tilde{m} = 10,\ \ \delta = 0.05,\ \ \omega_0 = 62.3,\ \ \tilde{e}_r = 0.08,\ \ \mu_{fr} = 0.10 \ \text{ and } \ \mathrm{e} = 0.70.$$

[4]**Frequency components far above the fluidelastic frequency arise for support-active cylinder vibration. Fluid-inertia and -viscosity effects, however, limit the frequency at which fluctuations in the fluid force can occur —the limiting frequency is proportional to $1/\Delta t$; the time-delayed response is therefore numerically filtered to reflect this effect.**

The starting set of initial conditions is $\tilde{y} = 0.04$, $\tilde{x} = \tilde{x}' = \tilde{y}' = 0$. When the impact condition ($\tilde{r} = \tilde{e}_r$) is satisfied, equations (4.5) and (4.8) are used to determine the new velocities after impact, which are converted to Cartesian coordinate velocities through a transformation similar to equation (4.9).

4.3.2 Overview of Tube Response Variation with V

Similarly to the purely flow-induced vibration case, cylinder response for the support-influenced tube motion may be summarized by plotting peak cylinder displacement as a function of the flow velocity, V. Unlike the previous case where a single smooth curve was obtained after the initial instability, sudden discontinuities or bifurcations occur. Furthermore, at a given flow velocity, a multiplicity of amplitudes may occur indicating (quasi)periodic motion with multiple frequencies, or chaotic motion. In modern nonlinear dynamics parlance such a plot is an example of a bifurcation diagram, in this case the velocity V being the bifurcation parameter.[5]

Fig.4.12 displays the bifurcation diagram for the $x-$ (in-flow) and $y-$ (cross-flow) responses, respectively. The first instability, the result of a Hopf bifurcation of the original stable equilibrium, occurs at $V_c = 0.32$. As V is increased, cross-flow amplitudes quickly grow, resulting in impact at $V = 0.35$. Following the onset of impacting the response undergoes a complex sequence of bifurcations. The increased y/x coupling results in in-flow amplitudes of the same order of magnitude as the cross-flow amplitudes, as seen in Fig.4.12 for $V > 0.35$. Over most of the velocity range, bifurcations result in transitions between periodic solutions. However, two significant chaotic regimes are also manifested. We now turn to a closer investigation of the types of bifurcations involved and the resulting responses.

Over a small range of V above V_c the vibration amplitudes remain below the support clearance value e_r. As observed in Section 4.2, coupling to the stable in-flow direction is minimal for pure fluid excitation. However, a distinct orbital x/y

[5]The bifurcation diagram may be obtained using any quantity representative of the system behaviour; hence, tube velocities instead of amplitudes can also be plotted as is demonstrated below.

motion can be identified, with the in-flow vibration occurring at double the cross-flow frequency. Fig.4.13(a) shows this orbital motion for $V = 0.34$. A time trace of the induced in-flow vibration and the corresponding frequency spectrum as well as other cross-flow results, are also shown in Figs.4.3(b-g).

The limit cycle amplitude quickly grows to reach e_r. At $V = 0.36$, double-sided impacting occurs. The resulting orbital motion is complex and appears chaotic, Fig.4.14(a). This non-periodic motion is manifested as a set of peak amplitude values in the bifurcation diagrams (Fig.4.12) at $V = 0.36$. A closer look at the in-flow time trace, Fig.4.14(b), gives some insight into the underlying instability mechanism. The in-flow response at $\omega \simeq 2\omega_0$ is seen to be no longer stable. Hence, after several cycles (in which the amplitude is non-constant) a subharmonic bifurcation occurs, resulting in in-flow orbital motion at $\omega \simeq \omega_0$ for a period of time (see Fig.4.14(b) near $\tau = 450$). At some point, the response at $\omega \simeq 2\omega_0$ is reinstated, and the cycle is repeated. It is important to note, however, that the duration of the above mentioned cycle is not constant; the bursts of subharmonic orbiting motion occur intermittently at seemingly random time intervals. The chaotic character of the in-flow response is well evidenced in the in-flow response phase plot and spectrum, Fig.4.14(d,f). Cross-flow motion, on the other hand, remains predominantly periodic as shown in Fig.4.14(c,e,g).

The velocity range over which this chaotic motion occurs is fairly limited, such that at $V = 0.40$, a return to periodic motion occurs. It is interesting to note that impacting is single-sided, occurring once per oscillation as seen in Fig.4.15(a-c) for $V = 0.40$. Both the in-flow and cross-flow responses are now at the same frequency $\omega \simeq \omega_0$ resulting in an ovalling type motion of comparable in-flow and cross-flow amplitudes. As V is further increased, a subharmonic bifurcation occurs, resulting in period-2 motion. Fig.4.15(d-f) shows the period-2 motion for $V = 0.45$. Inspection of a sequence of x/y orbital plots similar to Fig.4.15(d) shows that, as V is increased above $V = 0.45$, a decreasing trend in the asymmetry of the orbital motion occurs.

The velocity $V = 0.48$ is a limiting velocity at which the period-2 response loses stability. The result is a double-sided impacting period-1 response at the frequency

$\omega \simeq \omega_0$. A second period-1 solution, albeit with a much higher in-flow frequency, $\omega \simeq 3\omega_0$, and coexisting with the low frequency solution appears near $V = 0.55$. Fig.4.16 shows the co-existing solutions ((a-c) and (d-f), respectively) at $V = 0.57$. The dashed line in the bifurcation diagram (Fig.4.12) depicts the existence of an unstable solution separating the two stable solutions. The high frequency solution is seen to be nearly purely in cross-flow, noting the expanded x-axis scale in Fig.4.16(d,e), in contrast to the low frequency orbiting solution of Fig.4.16(a). The low frequency solution disappears near $V = 0.66$. At $V = 0.68$, the high frequency solution is no longer stable and is replaced by asymmetric solutions, which corresponds to the two branches in the bifurcation diagrams in the range $0.68 < V < 0.92$ (Fig.4.12). In the same velocity range, in-flow response is characterized by nearly linear amplitude growth, while the converse is true for the orthogonal direction cross-flow response.

A symmetrical solution reemerges in the velocity range $0.92 < V < 1.06$. In this velocity range in-flow response amplitudes approach cross-flow amplitude values. Fig.4.17 shows cylinder orbital x/y motion and the corresponding phase plots within this velocity range for $V = 1.00$. Impacting occurs at essentially two locations, the resulting coupling introducing significant in-flow amplitudes. At $V = 1.06$ this solution becomes unstable and the response degenerates into chaotic motion. Fig.4.18 shows an example of the resulting response in the chaotic regime for the velocity $V = 1.09$. The orbital and phase plane plots show that the chaotic response comprises mostly of double impacting orbits with continuously varying impact locations; hence, no single orbit is repeated as is characteristic of chaotic solutions. The in-flow frequency spectrum, Fig.4.18(f), indicates that in-flow motion is strongly chaotic, exhibiting a broad-banded spectrum particularly at low frequencies, as is typical of chaotic solutions. The cross-flow spectrum on the other hand (Fig.4.18(g)) shows that a significant periodic component still exists, albeit with a widening of the peak at the major response frequency to indicate a chaotic component in the response. A periodic window in the bifurcation appears near $V = 1.10$. The orbital motion in this periodic window is shown in Fig.4.19 for $V = 1.10$. Chaotic motion predominates for $V > 1.10$, until permanent contact with the support occurs due to the steady drag.

4.3.3 Characterization of the Cylinder Response

It is evident, as one might have suspected from the outset, that, even for this simple form of our dynamical system, a wealth of dynamical behaviour exists.

The bifurcations just described are of the codimension one type, since they occur as a single system parameter, in this case V, is varied. Other bifurcation sequences are obtained when other parameters, e.g. the friction coefficient μ_{f_r} or support clearance e_r, are varied, as will be discussed in due course.

In this section we shall investigate further the bifurcations in Fig.4.12. Specifically, the goal will be to identify the bifurcation types and analyze their characteristics. As discussed in Chapter 1, a host of standard bifurcations in nonlinear dynamical systems have already been uncovered and extensively studied. We shall draw on this wealth of existing knowledge and apply some of the techniques and methods developed to unravel the dynamics underlying the behaviour exhibited by our system.

Furthermore, for the velocity regimes in which chaotic motion is predicted, we would like to identify the route to chaos, and characterize the underlying strange attractor via Poincaré sections, fractal dimension and the largest Lyapunov exponent — which is a measure of the degree to which the attractor is chaotic.

4.3.3.1 Transition to Chaos following Onset of Impacting

It was shown in Section 4.1 that the present system has a single fixed point, which is a stable focus for $V < V_c$. A Hopf bifurcation of the fixed point occurred in the cross-flow direction at $V = V_c$. In the ensuing limit cycle motion, limited coupling to the stable in-flow direction occurs as discussed in Section 4.2.

A natural starting point to analyze the effect of impacting on the initial limit cycle is therefore a local analysis of the limit cycle stability. A standard approach to study locally based bifurcations is the Poincaré reduction of the system and subsequent stability analysis of the resulting fixed point(s). A direct analogy exists between the stability behaviour in the reduced Poincaré map and stability behaviour in the original high dimensional system. Hence, for instance, loss of stability of a fixed point in the discrete Poincaré map corresponds to destabilization of a limit cycle in the differential system. The Poincaré map, which is lower dimensional, has the advantage of being a relatively simpler system to analyze.

As a first approximation, the four-dimensional (4-D) system is projected onto a 1-D manifold. The result is a return map relating subsequent values of a selected quantity representative of the response on a defined hypersurface. The resulting map may be expressed in the form

$$X_{n+1} = F(X_n). \tag{4.11}$$

The Poincaré surface $\sum$ selected is given by $\{\sum | \dot{x} = 0, y > 0\}$. Hence, in equation (4.11), X_n and X_{n+1} are successive extrema of x when $y > 0$. Equation (4.11) is a discrete difference equation relating successive in-flow amplitudes.

At $V = 0.326$, the system response lies on a simple limit cycle attractor. Figs.4.20(a-e) show the orbital x/y motion, time trace and phase plane plots as the system approaches the stable orbit; for this velocity, no impacting occurs. Fig.4.20(f) shows an iteration sequence in which successive iterates finally lead to the stable fixed point P; hence, a limit cycle in the higher dimensional system is manifested as a fixed point on the 1-D map. The iteration points (in Fig.4.20(f)) are replotted in Fig.4.20(g), revealing they fall on a simple curve; hence the function F in equation (4.11) exists and is of relatively simple form. It should be noted, that the reduction to a 1-D map of a high dimensional system, does not always necessarily lead to a tractable map, hence the existence of such a map for the present system is an important result. A direct analogy exists between the stability of the fixed point P (defined by $X_{n+1} = X_n$) of this discrete dynamical system and that of the limit cycle. The stability of the fixed point P is determined by the eigenvalues λ_p of the Jacobian matrix of F; for a 1-D map this reduces to the derivative dF/dX_n evaluated at P; the fixed point P is stable if $|\lambda_p| < 1$, in which case successive iterates converge to the fixed point. This is the case in Fig.4.20(f,g). However, $|dF/dX_n|$ at P is just below unity. This makes it likely that as V is varied, the condition $|dF/dX_n| = 1$ might be met, which would lead to an instability of the fixed point P. A value of $\lambda_p = -1$, which is the most likely from Fig.4.20(g), leads to a flip or subharmonic bifurcation. In fact, such a bifurcation does occur as evidenced by the in-flow response of Fig.4.14(b) and as we shall see below.

In mathematical formalism, $F(X_n)$ in equation (4.11) may be approximated by a polynomial to yield

$$X_{n+1} = F(X_n, \epsilon) = -(1+\epsilon)X_n + aX_n^2 + bX_n^3 + O(X_n^4), \tag{4.12}$$

where ϵ is related to the bifurcation parameter. For $\epsilon > 0$, the fixed point P is unstable. Equation (4.12) is the so called *normal form* [6] for a flip or subharmonic bifurcation.

For $V = 0.330$, slightly, above the critical impact velocity, Fig.4.21 shows the orbital x/y motion, time traces and phase plane plots, as well as the corresponding Poincaré return map. While the basic figure-of-eight orbit is maintained (Fig.4.21(a)), the in-flow time trace shows bursts of amplitude growth followed by a gradual decay and settling on the periodic orbit corresponding to P in Fig.4.21(g). Note, however, that inspite of the presence of impacting, the energy transfer is fairly limited, such that the cross-flow response appears completely periodic and of nearly constant amplitude (Fig.4.21(c)) — this is also well depicted in the phase plane plots of Fig.4.21(d,e). The return map predicts well the return to the neighbourhood of P following an amplitude burst. However, this 1-D map fails to unearth the instability mechanism leading to the escape of iterates from the neighbourhood of P. In Fig.4.21(f), where a number of iterations are shown, it is seen that an unstable branch appears along which iterates escape from the neighbourhood of P. Thus the onset of impact introduces a new unstable manifold in the return map, but the original orbital motion is still relatively stable.

The fixed point P of the return map becomes unstable at $V = 0.3425$, signified by a slope of $\lambda_p = -1$ at P. This indicates that the original limit cycle, to which the

[6] The *normal form* is the simplest form to which, a system of equations exhibiting a given bifurcation, can be reduced.

response was attracted after the amplitude bursts, is no longer stable. This instability is associated with a subharmonic (flip) bifurcation in the dynamical system. It is manifested as the appearance of orbital motion at half the original in-flow orbital frequency (recall that in-flow response is coupled to cross-flow response at $\omega \simeq 2\omega_0$). Fig.4.22 shows results for $V = 0.343$, which is slightly above this new instability threshold. The subharmonic motion is evidenced by comparing the time traces of Fig.4.22(b,c), which show periods of equal frequency in the two orthogonal directions, but also periods where the two frequencies are related a factor of 2. The corresponding phase plots are presented in Fig.4.22(d,e), showing the dominant effect of the instability to be in the in-flow direction. Fig.4.22(f,g) shows the Poincaré return map. $F(X_n)$ is no longer a smooth continuous function; instead, it has a discontinuity on the first bisectrix near the original fixed point P. Hence, not only do we have a flip bifurcation but also an instability leading to two new fixed points $\overline{P}_1$ and $\overline{P}_2$. The slope $|dF/dX_n| > 1$ at $\overline{P}_1$ hence, on this lower branch the fixed point is unstable. The subharmonic bifurcation is evidenced by the existence of another pair of points, labelled p1 and p2 in Fig.4.22(g), that are mutual images which reflects the existence of a periodic orbit on the iterated map; [7] in the neighbourhood of these points the response is approximately period-2. The approximation to period-2 motion is supported by the concentration of iterates in the neighbourhood of p1 and p2 in Fig.4.22(g). As seen in the return map, the subharmonic orbit (p1 $\rightarrow$ p2) is unstable, occurring only intermittently for a few cycles before breaking up. A period-2 orbit born of a subcritical bifurcation is unstable, hence the resulting response veers away from the orbit after several cycles — leading to the in-flow amplitude burst seen in Fig.4.22(b).

The qualitative behaviour, specifically the aspects associated with the flip bifurcation and the resulting unstable p1 $\rightarrow$ p2 orbit, described above fits in well with the Pomeau-Manneville Intermittency transition route to chaos. Intermittency coupled with a subharmonic bifurcation was labelled as "type III intermittency" by Manneville

[7] Note that a period-1 orbit on the iterated map corresponds to a period-2 orbit in the actual system.

and Pomeau. The neighbourhood of p1,p2 has been dubbed the "laminar regime" of the response (Pomeau & Manneville, 1980), as contrasted to the outlying "turbulent regime" visited by the iterates during a turbulent burst. The intermittency route to chaos is well documented. It has been uncovered in diversely varying systems. The simplest are 1-D return maps. More complex systems include the Lorenz model for atmospheric convection, temperature-gradient-driven Rayleigh-Bénard convection (Bergé *et al.*, 1980) in fluid dynamics and the Belousov-Zhabotinsky chemical reaction system (Pomeau *et al.*, 1981). Intermittent transition to turbulence has been known by fluid dynamicists for many years. Sreenivasan & Ramshankar (1986) have shown that there are significant similarities between such transitions in pipe flow to the intermittency observed in the low dimensional dynamical systems enumerated above. The wide variance in the dynamical systems exhibiting the intermittency transition — with quantitative measures and characteristics in common — attests to the ubiquity of this route to chaos.

To sum up, there is evidence that type III intermittency plays the dominant role leading to chaotic behaviour at the onset of impacting. There also exists, however, a second mechanism which introduces an unstable manifold (Fig.4.22) thus contributing to the chaotic behaviour. Although not quantitatively confirmed, the second mechanism is suspected to be the so called *switching mechanism*; this mechanism is discussed in greater detail in Chapter 5.

4.3.3.2 Bifurcation of Periodic Solutions

The frequency of intermittent bursts of chaotic motion increases with increasing flow velocity, such that at $V = 0.365$ no laminar phase is discernible in the in-flow direction time trace. Following this, an apparent reversal of the original flip bifurcations occurs culminating in a single-sided impacting periodic solution with a frequency $\omega \simeq \omega_0$.

It is clear that a symmetry-breaking pitchfork bifurcation has also occurred, resulting in asymmetry in the period-1 motion. Fig.4.23(a) shows an example of the stable asymmetric period-1 motion at $V = 0.40$ for the initial cross-flow displacement $\tilde{y}(0) = 0.04$. A change in sign of $\tilde{y}(0)$ to $\tilde{y}(0) = -0.04$ results in the mirror image (about $y = 0$) orbit of Fig.4.23(b). While the velocity at which the pitchfork bifurcation occurs cannot be ascertained, it is most likely coincident with the onset of impacting, determined by the condition $y > 0$ or $y < 0$ when impact commences. The orbits in the chaotic regime just described, although continuously varying, allude to an asymmetry in the long term response.

Instability of the new period-1 motion is once again via a flip bifurcation, at $V = 0.43$. In this case, however, the bifurcation is supercritical leading to stable period-2 motion. Three impacts per cycle occur in the new response (Fig.4.15(d)). Period doubling bifurcation of an asymmetric period-1 solution, in systems with symmetry, is often the initiation of a cascade of period doublings (the Feigenbaum cascade) culminating in chaos. Such a cascade does not materialize for the present system. Instead, the period-2 motion is destabilized, reverting to period-1 motion. This is a bifurcation qualitatively similar to period 'bubbling'; however, the change in in-flow amplitude in this case shows a discontinuous jump as seen in Fig.4.12(a). Closer examination of the orbital motion as V approaches the (period bubbling) bifurcation velocity, $V = 0.48$, reveals that the two half orbits comprising the period-2 motion approach each other. A quantitative measure of the convergence is given by a trace of the bifurcation in the impact velocities in this range. Fig.4.24 shows bifurcation diagrams of the radial and tangential impact velocities. The bifurcation parameter is the flow velocity V, as previously; u_r and u_t are respectively the radial and tangential cylinder/support approach velocities. The disappearance of period-2 motion at $V = 0.48$ occurs when the radial and the tangential velocities of the two half orbits coincide indicating merging to a single orbit. This limiting orbit is, however, unstable, resulting in a jump to a new period-1 double-sided impacting orbit with new angular impact positions.

Fold bifurcations, commensurate with the appearance of a parameter range of coexisting periodic solutions, are common in nonlinear systems. An oscillator with cubic stiffness, the Duffing system, is an example of such a system. In the parameter range of coexisting stable orbits, the stable orbits are separated by an unstable limit cycle. An important feature of the fold phenomenon is the hysterisis effect, accompanied by a jump phenomenon. The foregoing characterizes the bifurcation behaviour in the vicinity of $V = 0.55$. The hysteretic jump occurs between the asymmetric motion at $\omega \simeq \omega_0$, and a new symmetric periodic response as depicted in Fig.4.16. The symmetric response in-flow amplitude is almost ten times smaller than the asymmetric response as seen by comparing Figs.4.16(a) and (d) (noting the magnification of the x-axis in Fig.4.16(d)). The fold phenomenon is delineated in Fig.4.12(a) and also in Fig.4.24. Fig.4.24 shows that for the symmetrical response, the cylinder approaches the support purely radially, hence, $u_t = 0$. As was the case in the preceding, the stability of this symmetrical solution is short lived (in parameter space) and undergoes a symmetry breaking pitchfork bifurcation at $V = 0.68$ as is well demonstrated in Figs.4.12 and 4.24. In Fig.4.24 it is seen that, after the bifurcation, the radially approaching impact ($u_t = 0$) for one of the impacts, while for the second $u_t \neq 0$ and corresponds to the lower branch in the u_r bifurcation diagram for $0.68 < V < 0.92$.

The original symmetrical orbit exists, albeit as an unstable limit cycle demarcating the domains of attraction of the asymmetrical stable solutions. At $V = 0.92$ the symmetrical orbit regains stability. While this is associated with a smooth merging of the u_r branches of the asymmetrical orbits, the tangential impact velocity u_t shows a discontinuous jump at the instability velocity in Fig.4.24.

4.3.3.3 Final Transition to Chaos

The chaotic character of motions at high enough V ($V > 1.06$) is well supported by the bifurcation diagrams of Figs.4.12,4.24. The concentration of points near $u_r = 0$ in Fig.4.24(a) suggests the occurrence of significant sliding motion in the second chaotic regime. The low density or reduced occurrence of impacts with $u_t = 0$ implies also that pure impact type motions are also reduced. At this point, the unanswered question is: how does the bifurcation to chaos come about — i.e., what is the route to chaos.

Period doubling and quasi-periodic routes are ruled out since none of the characteristic bifurcations associated with either of these routes are observed. This is also true for global bifurcations associated with homoclinic orbits, since these do not exist in the present system.

Fig.4.25 shows time traces for three velocities $V = 1.07, 1.09$ and 1.15 fully chaotic respectively. $V = 1.07$ is just above the transition velocity to chaos. Both the in-flow and cross-flow traces at $V = 1.07$ (Fig.4.25(a,b)) exhibit long durations of almost periodic response interrupted by brief, large amplitude bursts, which results in loss of temporal correlation. This suggests intermittency as a candidate for the route to chaos, in this case also. The frequency of turbulent bursts increases with flow velocity and ultimately, e.g. at $V = 1.15$, regions of the laminar phase are no longer discernible — further evidence of an intermittency transition. For $V < 1.07$ the turbulent bursts occur less and less frequently; the limiting velocity is the transition velocity $V_{cf} = 1.06$.

In order to ascertain our claim of an intermittency route to chaos, as well as determine the intermittency type, we now proceed to a qualitative analysis to show the existence of some universal characteristics and measures which would confirm it. As previously, the approach taken is an analysis of a reduced Poincaré return map of the system. Near the critical velocity to chaos, a 1-D map is extracted from the system. The 1-D map relates the in-flow amplitudes as follows:

$$X_{n+1} = G(X_n, V). \tag{4.13}$$

We seek a form of the function G in the vicinity of the original fixed point, i.e. in the laminar phase of the intermittent response. This can then be compared with the expected form for a map exhibiting a specific intermittency transition.

Fig.4.26(a) shows a map corresponding to equation (4.13) at $V = 1.07$ which is just above the critical velocity for the onset of final chaos $V_{cf} = 1.06$. The laminar region is distinguished near the point marked P. In this region, iterates fall on a simple curve; hence, it is possible to obtain a simple form for $G(X_n, V)$ for the laminar regime. The collapse of $G(X_n, V)$ onto a single curve strongly suggests that the system has a 1-D centre manifold on which the bifurcation occurs. This curve is also tangent to the first bisectrix near P at $V = 1.07$ which is just above the intermittency threshold velocity, $V_{cf} = 1.06$. The characteristics of the map of Fig.4.26(a), coupled with intermittent responses of Fig.4.25 point to the so called "type I intermittency" route to chaos. This transition is characterized by a saddle-node or tangent bifurcation of a simple fixed point (on the Poincaré plane).

For the map of Fig.4.26(a), the transition may be described as follows. For $V < V_{cf}$, $G(X_n, V)$ has two fixed points of opposite stability near the tangency point labelled P. The stable fixed point corresponds to the period-1 limit cycle motion existing for $V < V_{cf}$. As V is increased, the two fixed points merge (at P) and disappear at $V = V_{cf}$. The disappearance of the two fixed points at $V = V_{cf}$ is the result of a saddle-node bifurcation which occurs when the eigenvalue $\lambda_r = +1$; for the 1-D map, λ_r is simply the slope at the fixed point P — this is evidently the case in Fig.4.26(a), quantitatively confirming the bifurcation. For V slightly above V_{cf}, a narrow channel opens up such as in Fig.4.26(a). Successive iterates travel along the channel, as demonstrated in Fig.4.16(b), which requires a large number of iterations; in fact the closer $G(X_n, V)$ is to the first bisectrix, the larger the number of iterations, hence cycles in the laminar phase. The iterates eventually escape from the narrow channel. Outside the channel, the correlation exhibited in the laminar region vanishes as the system explores unstable regions of phase space; this is signified by the scatter of points in Fig.4.26(a) away from the neighbourhood of P. In the system response, this corresponds to the turbulent burst of chaotic motion. Following a turbulent burst then, the return of the system to the laminar phase corresponds to a reinjection into the channel, a process referred to as relaminarization. A case of reinjection into the channel following an escape may be seen in Fig.4.26(b). The duration of a given laminar phase is determined by the reinjection point into the channel; hence, shorter laminar phases correspond to reinjection deeper within the channel.

Type I intermittency has been observed both in simple low dimensional systems as well as in complex high dimensional systems. The baker's transformation, which we discuss later in Chapters 5 and 6, is an example of a simple map exhibiting type I intermittency. Examples of complex dynamical systems include the Lorenz model for Rayleigh-Bénard convection and the Belousov-Zhabotinsky chemical reaction.

An important feature of intermittency transitions is that, near critical parameter values, where a significant laminar regime exists, the system behaviour remains close to the original periodic solution. This makes possible for quantitative estimation of important parameters such as the probability distribution of the duration of laminar phases — that is, the average time spent by the attractor near the original stable orbit. We return to this important analysis in Chapter 6.

4.3.4 Attractor Characterization and Quantitative Measures

In the preceding section, evidence supporting the existence of a chaotic attractor for the present system has been found, most significantly in the high flow velocity range. This was supported not only by the observation of a chaotic character of the motions in the time traces and phase plane plots but also in the characteristic broad-banded frequency spectra with high low-frequency content, typical of chaotic solutions. Most significant, however, is the distinctive intermittent transition route to chaos, well supported both qualitatively and quantitatively.

We close the present discussion with a characterization of the high velocity chaotic attractor and determination of some standard attractor measures.

While the transition to chaos may imply total loss of order in the conventional sense, investigators have uncovered remarkable organization or geometry in a response that has become chaotic. The Poincaré section is a geometrical construction utilized to view the attractor phase plane plot on a reduced dimension and is a tool for revealing such organization. The Poincaré section selected for the present 4-D space is defined by the plane $\tilde{y} = 0$. For the flow velocity $V = 1.09$, the result of a projection of the Poincaré section (which is itself embedded in 3-D space) onto the 2-D plane $\tilde{y} = 0$

results in the geometrical object presented in Fig.4.27.[8] Distinct structure is observed as is typical of chaotic attractors; the structure showed no variation in the relative density of iterates after a certain minimum number of iterates required to reveal its basic form.

For the fractal attractor revealed by the Poincaré section there exists a fractal dimension, a characteristic of attractors associated with dissipative systems. There exist several variants for the definition of the fractal dimension, as detailed by Grassberger & Procaccia (1983). For brevity the two variants deemed most significant in the present context are considered.

Firstly we examine the *capacity dimension*, d_c, which is most closely related to the traditional idea of dimension, i.e. the topological dimension in Euclidean space. Let A denote the set of points making up the attractor and assume A to be bound by a subset of R^m — for our case $m = 3$. Let $N(\epsilon)$ denote the minimum number of m-dimensional cubes of side ϵ needed to cover A. For small ϵ, $N(\epsilon)$ increases as

$$N(\epsilon) \propto \epsilon^{-d_c}, \tag{4.14}$$

and in the limit

$$d_c = \lim_{\epsilon \to 0} \frac{\log[N(\epsilon)]}{\log[\epsilon]}. \tag{4.15}$$

One easily sees that $N(\epsilon) = 1$, L/ϵ, S/ϵ^2 for a point, line and surface, respectively, leading to $d_c = 0, 1, 2$ for these three standard geometrical objects.

Another definition for the fractal dimension is called the *correlation dimension*, d_{cr}. The underlying idea in this definition is that the pairwise correlation $C(\epsilon)$ in a hypersphere of size ϵ about points in A scales exponentially with ϵ. Mathematically,

$$C(\epsilon) = \lim_{N \to \infty} \frac{1}{N^2} \sum_{i,j=1}^{N} \Psi(\epsilon - |\mathbf{x}_i - \mathbf{x}_j|), \quad i \neq j, \tag{4.16}$$

[8]Note that in Fig.4.27 the $\bar{x}$ position, rather than amplitude, is plotted.

where $\Psi(p)$ is the Heaviside function

$$\Psi(p) = 0, \qquad p < 0,$$
$$\Psi(p) = 1, \qquad p > 0; \tag{4.17}$$

d_{cr} is then given by

$$d_{cr} = \lim_{\epsilon \to 0} \frac{\log[C(\epsilon)]}{\log[\epsilon]}. \tag{4.18}$$

Grassberger & Procaccia (1983) have shown that the fractal dimensions defined above are related by

$$d_{cr} \leq d_c, \tag{4.19}$$

and also that for most attractors $d_{cr} \approx d_c$.

For the attractor corresponding to Fig.4.27, d_{cr} was computed. In Fig.4.28(a) the variation of $C(\epsilon)$ with ϵ is shown on a log-log plot. The *correlation dimension* is determined from the linear portion of the graph giving a value of $d_{cr} = 2.07$. For comparison, the result of a similar computation, this time for the periodic response at $V = 0.40$ (cf. Fig.4.15), is presented in Fig.4.28(b); $d_{cr} = 1.036$ for this case, which is reasonably close to the expected value of $d_{cr} = 1.0$ for a period-1 response.

Intuitively the dimension of a space denotes the amount of information needed to specify a location. Equation (4.15) suggests that for fractal sets the dimension need not be an integer. For high dimensional systems attractors are often found with a significantly lower fractal dimension. The practical significance of this result is that the dynamics on the attractor, hence the system, can be captured on a significantly reduced dimension space relative to the original embedding phase space dimension. A value of $d_{cr} = 2.07$ for the attractor of Fig.4.27 suggests that the attractor is limited to under 3 dimensions of the 4-dimensional phase space.

A hallmark of chaotic attractors is the effect of exponential divergence of initially nearby states as a result of stretching and folding. The rate of divergence of nearby states is a measure of the extent to which an attractor is chaotic. This divergence rate is determined by the Lyapunov exponents of the system. We shall be particularly interested in the largest, or most positive, exponent — this being sufficient for the identification of chaos. To define the Lyapunov exponent consider a system

$$\dot{\mathbf{x}} = \mathbf{F}(\mathbf{x}), \tag{4.20}$$

for which there exists a solution $\phi(\tau)$. For two solutions $\phi_1(\tau), \phi_2(\tau)$ commencing at nearby initial conditions, one can define a variational vector function

$$\mathbf{u}(\tau) = \phi_1(\tau) - \phi_2(\tau). \tag{4.21}$$

When the condition $|\mathbf{u}| << 1$ is satisfied, the time evolution of the variational vector is determined by the linear equation

$$\dot{\mathbf{u}} = \mathrm{D}\mathbf{F}(\phi)\mathbf{u}, \tag{4.22}$$

where $\mathrm{D}\mathbf{F}(\phi)$ is the Jacobian matrix function of the vector field $\mathbf{F}(\mathbf{x})$.

The solution to the first-order matrix differential equation (4.22) takes the form

$$|\mathbf{u}(\tau)| = \mathbf{u}(0)e^{\overline{\sigma}\tau}. \tag{4.23}$$

Hence the Lyapunov exponent $\overline{\sigma}$ determines the exponential rate of divergence of nearby solutions. The exponential growth of $\mathbf{u}(\tau)$ cannot continue indefinitely, since the attractor is bounded; hence $\overline{\sigma}$ has to be determined from many different initial conditions. The formal definition of the Lyapunov exponent is

$$\overline{\sigma} = \lim_{N\tau\to\infty} \sum_{i=1}^{N} \frac{1}{N\tau} \ln\left[\frac{|\mathbf{u}_i(\tau)|}{|\mathbf{u}_i(0)|}\right], \tag{4.24}$$

where $\mathbf{u}_i(0)$ is the initial variational vector for the i^{th} initial condition along the test orbit $\phi(\tau)$.

When the vector field $\mathbf{F}$ is analytic, $\mathrm{D}\mathbf{F}(\phi)$ can be obtained, in which case $\overline{\sigma}$

is easily determined by simultaneously integrating (numerically) equations (4.20) and (4.22). For systems in which **F** is non-analytic such as the one under study, or experimental systems where the form of **F** is unknown, a numerical procedure is necessary to track the evolution of $\mathbf{u}(\tau)$ on a reconstructed phase space. For this purpose, an algorithm developed by Wolf *et al.* (1985) was adapted for the present system.

The algorithm works by analyzing a database of phase space vectors that trace a trajectory $\phi(\tau)$. Ensuring a large enough number of orbits around the attractor, an initial variational vector $\mathbf{u}(\tau)$ is determined by two phase points within a distance d_0. Subsequent phase points are tracked over a distance along the attractor corresponding to a predetermined evolution time τ_e, resulting in a final separation d_e. For one such iteration, an estimate of the largest Lyapunov exponent is given by

$$\overline{\sigma}_e = \frac{1}{\tau_e} \ln \left[\frac{d_e}{d_0} \right] . \tag{4.25}$$

Since the initial phase points separated by d_0 may be located anywhere on the attractor, individual values of $\overline{\sigma}_e$ will differ significantly, reflecting local attractor behaviour such as stretching or folding; $\overline{\sigma}$ is therefore the average of a large number of $\overline{\sigma}_e$.

For a periodic solution the Lyapunov exponent $\overline{\sigma} = 0$. This serves as a test for the algorithm. Fig.4.29(a) shows the convergence to an average value of $\overline{\sigma}$ for the period two solution at $V = 0.45$ (Fig.4.15). Convergence to the expected value of $\overline{\sigma} = 0$ is found to be very good and occurs within about 30 iterations.

An estimate for $\overline{\sigma}$ in the chaotic regime at $V = 1.09$ is shown in Fig.4.29(b). Although convergence is not as smooth as in the periodic case, an average value of $\overline{\sigma} \simeq 1.4$ is obtained for this attractor. The positive Lyapunov exponent supports the earlier conclusions of the chaotic nature of the response and the existence of a strange attractor in this high velocity regime.

4.3.5 Codimension 2 Bifurcations

The tube–support gap spacing $\tilde{e}_r$ is possibly the second most important system parameter after the flow velocity from a dynamics point of view. Varying $\tilde{e}_r$ results in significant changes in system response. The totality of the range of system responses as the parameters V and $\tilde{e}_r$ are varied is summarized in a bifurcation set diagram, Fig.4.30. The clearance $\tilde{e}_r$ was varied in the range $0.02D$ to $0.08D$.

The various types of tube responses may broadly be divided into five regions, as shown Fig.4.30. Region I corresponds to limit–cycle motion, immediately following the Hopf bifurcation at $V_c = 0.32$. In this region, limit–cycle amplitudes remain below the tube–support clearance and no impacting takes place; the cylinder exhibits a figure–of–eight orbital motion, as depicted by inset (a). Once the limit–cycle amplitude surpasses the tube–support clearance, complex orbital motion ensues, as shown in insets (b) and (c) in Region II. For a given velocity, V, the type of response obtained (in Region II) depends on the dimensionless clearance $\tilde{e}_r$. For low clearances, $\tilde{e}_r \lesssim 0.04$, the tube response is complex quasi–periodic, as depicted in inset (c). At higher $\tilde{e}_r$, this quasi–periodic motion intermittently breaks down into chaotic motion; an example is shown in inset (b). For $\tilde{e}_r = 0.08$, the response is chaotic, which is particularly evident in the in–flow component of the motions, as discussed earlier in Section 4.3.3.

The responses in Region III may be considered to mark the onset of impact–dominated motion, for $\tilde{e}_r \gtrsim 0.05$. Taking for example the case of $\tilde{e}_r = 0.07$, the chaotic response of Region III develops into an asymmetric period–2 orbital motion; see inset (d) for Region IIIa. For higher V, this period–2 motion collapses into a period–1 orbital motion; see inset (e), Region IIIb. As V is increased further, the next bifurcation generates a symmetric high–frequency motion, almost purely in the cross–flow direction — see Region IIIc, inset (g). At still higher V, a pitchfork–like bifurcation results in loss of symmetry in the motion, as shown in inset (h), Region IIId; then, this bifurcation is reversed and in Region IV we once more have symmetric high–frequency response.

These results, applicable for $0.05 \lesssim \tilde{e}_r \lesssim 0.08$, are quite similar to those depicted in the bifurcation diagram of Fig.4.2 for $\tilde{e}_r = 0.08$. It is of interest that the dynamics in this range of $\tilde{e}_r$ is much richer than for smaller $\tilde{e}_r$; the number of types of response increases with $\tilde{e}_r$. In fact, the set of responses at given values of $\tilde{e}_r$ is always a superset of the equivalent set for a smaller value of $\tilde{e}_r$. Thus, for $\tilde{e}_r \lesssim 0.04$, the sequence of bifurcations of Region III does not occur. Instead, the quasi–periodic motion of Region II collapses directly into the high–frequency response of Region IV — see inset (f).

For all clearance values, it is the high–frequency response of Region IV that undergoes an abrupt breakdown, resulting in chaos (Region V). The orbital motion in the chaotic regime is similar for all values of V and $\tilde{e}_r$ — suggesting a similarity or identity in the underlying chaotic attractor.

4.3.6 Frequency Variation

The non-dimensional frequencies of oscillation in the in–flow and cross–flow directions as V is increased are shown in Fig.4.31. For chaotic and quasi–periodic motions, $\overline{\omega}_x$ and $\overline{\omega}_y$ are simply the dominant frequencies, which appear to always be discernible. Various regimes may be distinguished, corresponding to those in Fig.4.12. These are identified by the letters P or C corresponding to periodic and chaotic regimes respectively. Region P1 is the first periodic region with no impacting, at the lowest end of which the motion is in the figure–of–eight pattern so that $\overline{\omega}_x \simeq 2\overline{\omega}_y$. C1 and P2 are the first chaotic and next periodic regions, respectively, over which $\overline{\omega}_x \simeq \overline{\omega}_y \simeq 1$; i.e., $\overline{\omega}_x$ and $\overline{\omega}_y$ are sensibly close to the zero–flow values. For $V \simeq 0.6$, corresponding to the drastic reduction in in–flow motion shown in Fig.4.12 and in Fig.4.16(d-f) the frequency of oscillation increases significantly by a factor of 3 approximately for $\overline{\omega}_x$ and 1.5 for $\overline{\omega}_y$, where once more $\overline{\omega}_x \simeq 2\,\overline{\omega}_y$. The frequency continues to increase with V, but more gradually, in region P3 — to a maximum, at the end of this region, of $\overline{\omega}_x \simeq 3.7$ and $\overline{\omega}_y = 1.9$. In C2, the main chaotic region, the frequencies are reduced abruptly back to $\overline{\omega}_x \simeq 2\,\overline{\omega}_y \simeq 3$, but again gradually increase, reaching eventually $\overline{\omega}_x \simeq 2\,\overline{\omega}_y \simeq 4$ in the periodic window near the maximum V shown in Fig.4.31.

Chapter 5

AN EXPERIMENTAL STUDY OF CYLINDER DYNAMICS IN WATER-FLOW AND COMPARISON WITH THEORY

The theoretical analysis of Chapter 4 has shown that a wealth of complex dynamical behaviour is exhibited by the system under study. Most interesting is the finding that transition to chaos occurred via a 'standard' route which is well understood and leads to a response with properties that can easily be measured experimentally.

For continuation of the analysis, an experimental system will now be studied. The goal of the experimental study is to determine the dynamical behaviour under more complex real conditions. In particular, it is of interest to ascertain and identify distinct bifurcations in the response, as well as examine the characteristics of the resulting behaviour. The effect of several parameters on the resulting tube response is also investigated. These parameters include cylinder/support clearance, interstitial gap fluid at the support, as well as the Coulomb friction coefficient at the support.

In the second part of this chapter, the full theoretical model developed in Chapter 2 is applied to the experimental system. The ability of the model to predict the cylinder dynamical behaviour is tested. Further analysis is also possible, including a qualitative analysis of the dynamical system and extraction of practically useful information.

The findings of Chapter 4 will provide possible avenues for the elucidation of the dynamical behaviour of this more complex system.

5.1 DYNAMICS OF THE EXPERIMENTAL SYSTEM

5.1.1 Experimental Setup and Test Procedure

Tests were conducted in a Kempf and Remmers recirculation water tunnel. Pertinent parameters for the water tunnel are: a test section of dimensions $0.26 \times 0.26 \times 1.1$ m, velocity range $0-15$ m/s, and free-stream turbulence intensity 0.5%. The upstream flow velocity was measured using a Kentlea mini-probe turbine flow meter, accurate to within 0.0005 m/s in the range $0.0-3.0$ m/s.

The system under study comprises a single flexibly-mounted cylinder located in row 3 of an array of otherwise rigidly fixed cylinders. The array consists of 7 rows of cylinders. Cylinder dimensions are: diameter 12.7 mm (0.5 in.) and 238 mm (9.37 in.) long. The test cylinder was mounted as a cantilever and consisted of a rigid section ($m = 0.301$ Kg/m), of length 356 mm (14.0 in.) which spanned the water tunnel cross section, and a lower smaller-diameter (4.8 mm (0.19 in.)) and hence flexible section fixed at its bottom end; see Fig.5.1. The flexible part of the test cylinder extended out of the water tunnel working section, in a specially designed cylindrical compartment below. The only fluid connection between the lower compartment and the test section was the clearance hole for the test tube, and hence the flexible part of the tube was immersed in essentially stagnant fluid. A close-up of the central part of the array is shown in the cross-sectional view of Fig.5.1(b). A locking setup, at the bottom of the cantilever, is provided for alignment and clamping of the test cylinder. At the upper end of the rigid (larger diameter) section of the test cylinder is mounted a solid cylindrical impact piece 25.4 mm (1.0 in.) long, protruding into an upper box-like compartment. The support piece consists of a 9.5 mm (0.375 in.) square slab with a circular hole of appropriate diameter for the desired clearance. At the impact surface, the support thickness is reduced to 3.6 mm (0.14 in.). The test cylinder logarithmic decrement of damping $\delta = 0.01$; $f_0 = 6.1$ Hz in air, and approximately 5.5 Hz in water.

Five support clearance diameters were tested, in the range $0.07D - 0.23D$; the largest being close to the maximum possible support-inactive tube displacement. Most tests were conducted with the brass tube impacting on brass support pieces. However, to investigate material effects on the tube dynamics, special tests were conducted with stainless steel and Delrin, rather than brass, supports. The interstitial fluid medium at the support location (air or water) was varied by changing the water level within the containing plexiglas compartment above the test section; the tunnel pressurization/depressurization system made it possible to maintain a steady water level.

Tube motion in two orthogonal directions was sensed by an Optron non-contacting optical motion follower, which focused and locked onto a target at the upper end of the test cylinder; the sensor output consisted of both the tube displacement and velocity, in the in- and cross-flow directions. Other components of the data-acquisition system included a Nicolet digital oscilloscope for real-time monitoring, an HP3562D FFT digital signal analyzer, a Racal analog tape recorder and an HP9000 series computer.

During a typical test, the flow velocity was incremented in the range 0 to 0.18 or 0.25 m/s (depending on support clearance). On attaining a steady state, response spectra were calculated, giving vibration amplitudes and the corresponding frequencies. Simultaneously, velocity and displacement signals were recorded for further analysis. Recording durations were kept short (typically between 3 and 10 minutes), to ensure that relatively constant support conditions were maintained throughout the test.

5.1.2 Hopf Bifurcation and Support-Inactive Cylinder Response

Preliminary tests were conducted to determine the critical flow velocity for fluidelastic instability and the limit-cycle amplitude-growth rate. The maximum clearance available to the cylinder was $0.25D$, this being the inter-cylinder clearance. During the experiments the test cylinder is constantly subject to turbulent buffeting, hence, the "initial conditions" (position and velocity) are indeterminate. The response results presented therefore may be considered to correspond to the most likely attractor in cases where multiple attractors (solutions) may be possible; the attractor most likely to be manifested in the experiment is the one with the largest basin of attraction. However, the repeatability of the results suggests that the variability of initial conditions did not affect the final results.

Typical graphs of rms vibration amplitude response of the test cylinder versus velocity are shown in Fig.5.2; $\tilde{y}_0$ and $\tilde{x}_0$ represent the non-dimensional cross-flow and in-flow amplitude, respectively. Fluidelastic instability occurs at $U_c \simeq 0.10$ m/s. Several tests have been conducted, and an average value of $U_c = 0.105$ m/s was obtained which yields $V_c = 0.216$; this is the value for V_c that will henceforth be used. The instability is sharply defined. In-flow amplitudes remain approximately five times smaller than their cross-flow counterparts, reflecting the existence of weak fluid coupling between C_D and the cross-flow displacement $\tilde{y}$.

Fig.5.3 shows the cross-flow and in-flow response power spectra and the corresponding phase plots at $V = 1.05\ V_c$. The slight deviation from a periodic orbit, most noticeable in the in-flow direction, reflects the effect of unsteadiness in the flow velocity; this was found to be approximately 4% of the mean velocity, despite the Ward-Leonard control for the motor driving the water tunnel impeller (perhaps because the flow velocity was so small). The limit-cycle amplitude grows to reach the maximum available clearance at $V = 1.14\ V_c$.

5.1.3 Post-Instability Response with Impacting

Tests were conducted for five non-dimensional tube/support gap sizes: $\tilde{e}_r =$ 0.067, 0.132, 0.174, 0.200 and 0.229. Preliminary tests showed that, due to the smallness of $\tilde{e}_r$, the steady drag quickly (in terms of flow velocity range) resulted in pinning the cylinder against the baffle-hole wall in the drag direction. Tests were therefore conducted with an initial upstream deflection of the test cylinder relative to the clearance hole, $\tilde{x}_e = 0.148$, so as to increase the range of useful experiments. There was also an (unwanted) offset of $\tilde{y}_e = 0.03$; note that this value of $\tilde{y}_e$ corresponds to an offset of 0.4 mm which is close to the tolerance of the cylinder alignment mechanism. The radial offset then is $\tilde{r}_e = 0.151$. Hence, for tests with $\tilde{e}_r < 0.151$, the test cylinder was initially preloaded by a support contact force.

The tube response with varying $\tilde{e}_r$ may broadly be divided into two categories. For the larger gap sizes ($\tilde{e}_r > 0.170$), periodic motion, or motion with a distinct periodic component, was predominant over the complete test flow-velocity range, with the exception of a small chaotic band. For smaller gap sizes ($\tilde{e}_r < 0.170$), on the other hand, the response culminated in chaos for high values of the flow velocity and thereafter remained chaotic. The behaviour of the system will be described next in detail, for the different values of impact clearance.

5.1.3.1 Results for $\tilde{e}_r = 0.174$

We first present results for gap size $\tilde{e}_r = 0.174$ and for various flow velocities; the tube impact-piece and support material was brass, with impacting occurring in air.

Following the Hopf bifurcation (hence, onset of fluidelastic instability) the limit-cycle amplitude grows sufficiently for impacting to occur at $V = 1.17\ V_c$. At this velocity, interaction with the support has a significant damping effect such that, for several cycles after impacting, the amplitude is reduced to below $\tilde{e}_r$. Fig.5.4(a) shows the orbital (x, y) motion at $V = 1.17\ V_c$. The induced in-flow motion is nearly quasi-periodic, the second frequency representing the time interval between impacts; the time interval in-between impacts , however, appears to be random, thus introducing a chaotic component in the response. This quasi-periodic like character is well depicted by the in-flow and cross-flow time traces of Fig.5.4(b,c). The corresponding frequency spectra, Fig.5.4(d,e) show the period-1 motion to be predominant.

Double-sided impacting commences at $V = 1.2\ V_c$. Typical results are shown in Fig.5.5 for $V = 1.24\ V_c$. It is seen that motion is predominantly in the cross-flow direction (Fig.5.5(a)), albeit slightly skewed. The cross-flow time trace, (Fig.5.5(c)), has an almost constant amplitude. This motion is close to a simple limit cycle of period-1, as evidenced by the power spectra in Fig.5.5(d,e).

Another bifurcation occurs at $V \simeq 1.43\ V_c$; the double-sided impacting response intermittently loses stability, breaking down into a complex ovalling motion, as shown in Fig.5.6 for $V = 1.47\ V_c$. While the cross-flow amplitude remains almost constant (Fig.5.6(a,c)), in-flow motion (Fig.5.6(a,b)) exhibits bursts of amplitude growth during the orbiting phase. It is the in-flow component of motion that introduces a chaotic element to the response, since the bursts of amplitude-growth are intermittent. At the onset of intermittency, nearly-periodic motion (corresponding to a laminar phase) is still predominant over any given period of time of the intermittent response. The in-flow and cross-flow power spectra in Fig.5.6(d,e) indicate that a significant periodic component still exists in the response. This type of response is commonly encountered in operational heat exchangers and is referred to as breathing type response. It is characterized by bursts of periods of audible impacting, which are interspersed between relatively long quiet durations. In the experiments, audible impacting occurred in the double-sided impacting phase, while the orbiting motion was relatively quiet.

As V is increased further, the time between intermittent bursts of amplitude growth is diminished; a comparison of Fig.5.7(b), showing in-flow response at the higher velocity $V = 1.54\ V_c$, and Fig.5.6(b) shows this diminution. The increased chaotic content in the response is also reflected in the spectra of Fig.5.7(d,e). At $V = 1.69\ V_c$ periodicity in the in-flow response has vanished altogether, as seen in Fig.5.8, marking the onset of generalized chaotic motion, as evidenced by both the orbital plot and the time trace of Fig.5.8(a,b); further evidence is provided by the in-flow power spectrum of Fig.5.8(d), which shows significant low frequency content as well as overall broad-bandedness typical of chaotic response spectra (cf. Figs.5.6(d) and 5.7(d)). In the above described scenario, there is evidence purporting transition to chaos via intermittency. This will be investigated in due course.

The intermittently orbiting response occurs over the range of flow velocities, $1.69 \leq V/V_c \leq 1.80$. At the higher end of this range the component of the response at $2f_n$ in the in-flow direction becomes predominant. This marks a transition to a response with in-flow frequency double the cross-flow frequency. As shown in Fig.5.9 for $V = 1.91\ V_c$, the doubling of the in-flow frequency results in a figure-of-eight orbital motion; at this velocity, significant sliding at the support occurs, introducing a chaotic component to the response. This latter type of motion is sustained for higher values of V/V_c, until 'sticking', due to blow-back occurs at $V \simeq 1.95\ V_c$.

The cylinder response described above, and associated bifurcations, is unchanged for the two larger $\tilde{e}_r$, namely $\tilde{e}_r = 0.200$ and 0.229. The identical bifurcation sequence is repeated. For the larger gap sizes, however, the chaotic regime occurred over a wider velocity range. This finding suggests that the bifurcation sequence is quite robust and might possibly represent 'typical' behaviour for this system in the parameter range tested. The results for the gap size $\tilde{e}_r = 0.200$ are compared with theoretical findings in Section 5.2.2.

5.1.3.2 Results for Small Gap sizes

Significant changes in the overall cylinder response occur when the cylinder/support clearance is significantly reduced. Initial cylinder/support contact at zero flow, which results in preloading of the cylinder, is primarily responsible for the overall change in the response. For $\tilde{e}_r = 0.132$ for instance, initial preload results in a delay in the appearance of cylinder vibration until $V = 1.05V_c$. The quasi-periodic like and double-sided impacting responses do not occur for this gap size. Instead, the Hopf bifurcation leads directly to combined double-sided impacting with intermittent orbiting response. This response is shown in Fig.5.10 for $V = 1.29V_c$. Similarly to the case with $\tilde{e}_r = 0.174$, this response is replaced at higher velocities by a figure-of-eight orbiting response as seen in Fig.5.11 for $V = 1.62V_c$. This motion, despite being mainly periodic, exhibits bursts of amplitude growth which introduces a chaotic component in the response.

Next, some results for a relatively small gap-size are presented, namely $\tilde{e}_r = 0.067$, two times smaller than in the foregoing case. The initial preload introduces even stronger nonlinearities, both due to the larger lifting force necessary to overcome the initial preload and the directly related friction force. The cylinder is initially in contact with the support, and single-sided impacting therefore, occurs after the onset of fluidelastic instability. The result is dynamical behaviour which is distinctly different. For $V = 1.10V_c$, the first signs of fluidelastic instability are manifested.

As shown in Fig.5.12, the destabilizing fluidelastic force occasionally lifts the cylinder from the support. The response appears to already be chaotic. Single-sided impacting chaotic motion occurs for $V = 1.20V_c$, as seen in Fig.5.13. The preload contact force is large enough such that no double-sided impacting motion occurs. Instead, at a higher velocity $V = 1.43V_c$, the single-sided impacting motion has a significant orbiting component, Fig.5.14. At $V = 1.58V_c$, the large incident angle of impact results in significant coupling between the cross-flow and in-flow motions. The result is x and y components of comparable amplitude, as seen in Fig.5.15. In Fig.5.16 is shown the tube response at $V = 1.71V_c$, where occasionally the cylinder/support contact force causes sticking.

5.1.3.3 Co-dimension 2 Response Bifurcation Diagram

The results obtained for all gap sizes may conveniently be summarized in the 2-D bifurcation diagram of Fig.5.17. It is clearly seen that the number of bifurcations in the response increases with increasing $\tilde{e}_r$, although it is possible that some or all may still exist for small $\tilde{e}_r$, but over inconsequentially small ranges of V. On the other hand, chaotic response is confined to a small, intermediate range of V for large $\tilde{e}_r$, whereas for smaller $\tilde{e}_r$ it occurs earlier and lasts much longer; for small enough $\tilde{e}_r$, the response is chaotic over the complete velocity range.

5.1.4 Effect of Different Support Materials on Impacting Response

For the gap size of $\tilde{e}_r = 0.200$, the effect on the impact dynamics of two material combinations, other than brass-on-brass, was investigated. For this purpose, the immobile impact piece, forming the "baffle hole", was changed to either stainless steel or Delrin (Actal). The pertinent physical parameters are summarized in Table 5.1.

By comparing the response of the brass/stainless-steel (b/s) combination to the brass/brass (b/b) one, the effect of increased support stiffness may be assessed, while the Coulomb friction coefficient μ_{fr} remains essentially unchanged. Delrin, because of

Table 5.1: Physical properties of support materials; ρ is the density of water and ρ_s is the density of the support-plate material

Material	E (N/m^2)	μ_{fr}	ρ_s/ρ
Brass	8.96×10^{10}	0.4	8.55
Stainless Steel	2.0×10^{11}	0.4	7.80
Delrin	3.33×10^{9}	0.01	1.54

its lubricating properties, provides (in the brass/Delrin (b/d) combination) information on the effect of a low coefficient of friction on the dynamics, while support stiffness is still maintained high.

Fig.5.18 shows a comparison of rms response amplitudes for the b/b, b/s and b/d cases. The cross-flow response amplitudes are seen to be quite independent of material combination over most of the flow velocity range. Hence, the cross-flow amplitude is largely determined by the maximum possible clearance in the cross-flow direction for a given in-flow deflection (due to steady drag).

The high friction coefficient for the b/b and b/s combinations results in sticking at $V \simeq 2.0\ V_c$. For the b/d case, however, sliding motion continues to higher flow velocities, due to the lower μ_{fr} involved.

The dominant response frequencies for the b/b and b/d combinations are compared in Fig.5.19. As might have been expected, no significant differences were observed between the b/b and b/s cases. Noting the expanded scale of the ordinate in Fig.5.19, it is clear that for $V < 1.62\ V_c$, the frequencies remain approximately the same; however, a significant increasing trend in the response frequency occurs for b/b starting near $V = 1.62\ V_c$. For b/d impacting, this trend is delayed to $V \simeq 1.71\ V_c$. Period-2 in-flow motion occurs for b/b starting at $V \simeq 1.80\ V_c$; the in-flow response frequency $f_x = 2f_y$ in the velocity range $V \geq 1.80\ V_c$, and hence is off-scale in Fig.5.19. Coincidentally with a doubling of the in-flow response frequency, a reversal of the increasing trend in the cross-flow motion occurs, marking the transition to a motion that is less impact-dominated and with a larger sliding component. This transition does not occur for the case of b/d impacting, where a period-2 component is discernible but does not become dominant until just prior to sticking; instead, orbiting motion persists for b/d. Figs.5.20(a-c) show this response for $V = 1.60V_c$ and b/d impacting; this response is to be contrasted with that shown in Fig.5.8 for b/b impacting showing much lower in-flow amplitudes. At $V = 1.90V_c$ large in-flow amplitudes are sustained for b/d impacting as shown in Fig.5.20(d,e).

5.1.5 Effect of Interstitial Support Gap Fluid

Next, we investigate how the tube response is affected by the interstitial fluid at the support location. The effect of water at the contact location is expected to be twofold: firstly, a lubricating effect on the contact surfaces, hence reduced frictional resistance to sliding. Secondly, additional squeeze-film fluid damping at the support; this should be particularly important for small $\tilde{e}_r$.

Comparison tests were once again conducted for the gap size $\tilde{e}_r = 0.200$. Fig.5.21 shows the response amplitudes and frequencies for wet and dry impacting tests. The increased fluid damping for the wet tests (a portion of the test cylinder is now immersed in still water) raises the critical velocity to $V_c = 0.120$ m/s, as seen in the amplitude plots of Fig.5.21(a). A decrease in the vibration frequencies also occurs for the wet tests as shown in Fig.5.21(b). Comparing the wet and dry tests, the cylinder cross-flow response amplitude is seen to be approximately equal over the velocity range $1.20 < V/V_c \leq 2.00$; hence, it is determined by the maximum possible cross-flow clearance, depending on the cylinder static equilibrium position due to blow-back. This suggests that energy loss through squeeze-film damping at the support is negligible for this gap size. The expected lubricating effect is apparent for $V > 2.00\ V_c$, where, while sticking occurs for dry impacting, orbital motion is now sustained up to $V \simeq 2.15\ V_c$. On the other hand, a difference in the in-flow amplitudes is noticeable for the velocity range $V > 1.70\ V_c$. Similarly to the Delrin tests, the increased in-flow response for $V \geq 1.70\ V_c$ is the result of a decrease in the effective friction coefficient at the support.

The final bifurcation in the tube response is different for impacting in water. For the dry tests, the complex orbiting motion collapsed into a figure-of-eight motion.

Decreased friction in the wet tests results in a new orbital motion, with a significant continuous sliding component. This motion has been found to be chaotic, albeit with a prominent periodic component.

The difference in the response frequencies for wet and dry tests shown in Fig.5.21(b) is by-and-large an added mass effect, hence, not primarily introduced by the presence of water at the support. Stronger fluid coupling between the orthogonal directions is also introduced for the wet tests. The bifurcation to the final chaotic orbital motion is reflected by a tendency toward levelling off of the response frequencies for the wet tests for $V > 1.70\ V_c$.

5.2 THEORETICAL ANALYSIS OF THE CYLINDER RESPONSE

In this section, the theoretical model, developed in Chapter 2, is applied to the experimental system. The first goal is to test the ability of the model to predict the dynamical behaviour exhibited by the experimental system. Using the theoretical model, further numerical experiments are carried out so as to determine some quantitative measures of the system behaviour where it appears to lie on a strange attractor.

5.2.1 The Governing Equations of Motion

The governing equations of motion, derived earlier in Chapter 2, are as follows:

$$\gamma\tilde{p}_i'' + 2\tilde{\zeta}_i\tilde{p}_i' + (\frac{\lambda_i}{\lambda_1})^4\tilde{p}_i = \frac{1}{2\tilde{m}a^2}\int_0^1 \left[(V - \frac{\partial\tilde{x}}{\partial\tau})^2 + (\frac{\partial\tilde{y}}{\partial\tau})^2\right]^{1/2}\left(C_L\frac{\partial\tilde{y}}{\partial\tau} + (V - \frac{\partial\tilde{x}}{\partial\tau})C_D\right)\phi_i d\tilde{s} +$$
$$\phi_i(\tilde{s}_p)\left\{\tilde{K}_s(\tilde{r} - \tilde{e}_r)^\xi + \tilde{r}'\left[\tilde{c}_s\tilde{r}^\xi + \tilde{\beta}\left(\frac{1}{1 - \tilde{r}/\tilde{e}_r}\right)\right]\right\}(\mu_{fr}\sin\theta - \cos\theta), \quad (5.1)$$

$$\gamma\tilde{q}_i'' + 2\tilde{\zeta}_i\tilde{q}_i' + (\frac{\lambda_i}{\lambda_1})^4\tilde{q}_i = \frac{1}{2\tilde{m}a^2}\int_0^1 \left[(V - \frac{\partial\tilde{x}}{\partial\tau})^2 + (\frac{\partial\tilde{y}}{\partial\tau})^2\right]^{1/2}\left((V - \frac{\partial\tilde{x}}{\partial\tau})C_L - C_D\frac{\partial\tilde{y}}{\partial\tau}\right)\phi_i d\tilde{s} -$$
$$\phi_i(\tilde{s}_p)\left\{\tilde{K}_s(\tilde{r} - \tilde{e}_r)^\xi + \tilde{r}'\left[\tilde{c}_s\tilde{r}^\xi + \tilde{\beta}\left(\frac{1}{1 - \tilde{r}/\tilde{e}_r}\right)\right]\right\}(\mu_{fr}\cos\theta + \sin\theta). \quad (5.2)$$

where, $i = 1, 2, ...N$, $\gamma = (1 + \pi C_{ma}/(4\tilde{m}))$ and $\tilde{\zeta}_i = \zeta(\lambda_i/\lambda_1)^2$ is the modal damping.

Several simplifying assumptions are made in the equations above. To facilitate the evaluation of the integrals involving C_L and C_D, approximate analytical forms for these force coefficients are desirable. A study of Fig.3.8 and previous discussion indicated that for $|\tilde{y}| \leq 0.20$, $C_L(\tilde{x}, \tilde{y})$ exhibits reasonably similar trends over a range of $\tilde{x}$. Furthermore, results of *ad hoc* calculations on the two degree-of-freedom model using the curve $C_L(\tilde{x} = 0, \tilde{y})$ compared very well with those using the complete map $C_L(\tilde{x}, \tilde{y})$. An approximate analytical form of $C_L(\tilde{x} = 0, \tilde{y})$ was determined by performing a least-squares, fifth-order polynomial fit on the experimental data.

Average C_D variation is less than 20% of the mean value in the range $|\tilde{x}|, |\tilde{y}| \leq 0.20$. The results of Chapter 4 also showed that no instability associated with the C_D variation is manifested; this is also supported by the experimental results, which confirm the stability of in-flow motions. Hence, a constant value of $C_D = C_D(\tilde{x} = 0, \tilde{y} = 0)$ is used in equations (5.1,5.2). The expressions for C_L and C_D are then

$$\begin{aligned} C_D &= C_D(\tilde{x} = 0, \tilde{y} = 0), \\ C_L &= \sum_1^5 \alpha_i \tilde{y}^i, \end{aligned} \tag{5.3}$$

where $\alpha_1 = -31.30, \alpha_3 = 2.935, \alpha_5 = -863.7$, and $\alpha_i = 0 \quad$ for $i = 2, 4$. The magnitude of the relative velocity vector in equations (5.1,5.2) is approximated by V.

The fact that the test cylinder is subjected to non-uniform flow needs also to be considered. To account for this, as well as the non-uniformity of the composite cylinder itself, we introduce the functions ψ_i [1] to express these spanwise variations, hence

$$\begin{aligned} \overline{m}(\tilde{s}) &= \tilde{m}\psi_1(\tilde{s}); \quad \overline{EI}(\tilde{s}) = EI\psi_3(\tilde{s}); \\ \overline{V}(\tilde{s}) &= V\psi_2(\tilde{s}); \quad \overline{C}_{ma}(\tilde{s}) = C_{ma}\psi_2(\tilde{s}); \end{aligned} \tag{5.4}$$

[1] Note that the functions ψ_i are not strict mathematical functions; they are just intended to indicate the existence of discontinuities, hence cannot be operated on: Thus, for instance, $(\overline{V}(\tilde{s}))^2 = V^2\psi_2(\tilde{s})$.

where

$$
\begin{aligned}
\psi_1(\bar{s}) &= 1 \quad \text{for} \quad \bar{s} \le 1, \\
&= 5.31 \quad \text{for} \quad \bar{s} > 1, \\
\psi_2(\bar{s}) &= 0 \quad \text{for} \quad \bar{s} < 1, \bar{s} > 2.54, \\
&= 1 \quad \text{for} \quad 1 < \bar{s} < 2.54, \\
\psi_3(\bar{s}) &= 1 \quad \text{for} \quad \bar{s} \le 1, \\
&= 0 \quad \text{for} \quad \bar{s} > 1.
\end{aligned}
$$

Using the simplifications above, equations (5.1,5.2) may be expressed as

$$
[\mathbf{M}]\mathbf{p}'' + [\overline{\mathbf{D}}]\mathbf{p}' + [\mathbf{K}]\mathbf{p} = \overline{\mathbf{F}}^1 + [\overline{\mathbf{F}}^2]\mathbf{q}' + \mathbf{F}_{xs}
$$

$$
[\mathbf{M}]\mathbf{q}'' + [\mathbf{D}]\mathbf{q}' + [\mathbf{K}]\mathbf{q} = \mathbf{F}^1 + [\mathbf{F}^2]\mathbf{p}' + \mathbf{F}_{ys} \tag{5.5}
$$

where

$$
\begin{aligned}
M_{ij} &= \int_0^{\bar{s}_p} \{[\psi_1(\bar{s}) + C_{ma}\psi_2(\bar{s})]\}\phi_i(\bar{s})\phi_j(\bar{s})d\bar{s}, \\
D_{ij} &= \zeta_{ij} + \int_0^{\bar{s}_p} \frac{VC_D}{2\bar{m}a^2}\psi_2(\bar{s})\phi_i(\bar{s})\phi_j(\bar{s})d\bar{s}, \\
\overline{D}_{ij} &= \zeta_{ij} + \int_0^{\bar{s}_p} \frac{VC_D}{\bar{m}a^2}\psi_2(\bar{s})\phi_i(\bar{s})\phi_j(\bar{s})d\bar{s}, \\
K_{ij} &= \int_0^{\bar{s}_p} \frac{\lambda_i^4}{\lambda_1^4}\psi_3(\bar{s})\phi_i(\bar{s})\phi_j(\bar{s})d\bar{s}, \\
F_j^1 &= \int_0^{\bar{s}_p} \frac{V^2}{2\bar{m}a^2}C_L\psi_2(\bar{s})\phi_j(\bar{s})d\bar{s}, \\
\overline{F}_j^1 &= \int_0^{\bar{s}_p} \frac{V^2}{2\bar{m}a^2}C_D\psi_2(\bar{s})\phi_j(\bar{s})d\bar{s}, \\
F_{ij}^2 &= -\int_0^{\bar{s}_p} \frac{V}{\bar{m}a^2}C_L\psi_2(\bar{s})\phi_i(\bar{s})\phi_j(\bar{s})d\bar{s}, \\
\overline{F}_j^2 &= \int_0^{\bar{s}_p} \frac{V}{2\bar{m}a^2}C_L\psi_2(\bar{s})\phi_i(\bar{s})\phi_j(\bar{s})d\bar{s}.
\end{aligned} \tag{5.6}
$$

$\zeta_{ij} = \bar{\zeta}_i$ for $i = j$, and 0 for $i \neq j$.

Table 5.2: Theoretically determined test-cylinder modal parameters

Mode	$\lambda_i l$	a_i	ω_{th}	ω_{exp}
1	0.357	0.941	41.3	38.3
2	1.542	0.693	768.7	691.2
3	4.805	1.015	7458.1	6189.9

$\mathbf{F}_{xs}$ and $\mathbf{F}_{ys}$ are the support forces. The ith components of these forces are given by the last terms in equations (5.1) and (5.2), respectively.

To determine the beam modes ϕ_i, the test cylinder was considered as comprising two parts, a flexible section to which a 'rigid' section is attached. Hence the upper rigid section could be replaced by an equivalent moment $\mathcal{M}$ and shear force $\mathcal{V}$ at the free end of the flexible cylinder. The appropriate boundary conditions to be applied to the general solution of the Euler-Bernoulli beam equation are

$$\begin{aligned}
\phi(0) &= \phi'(0) = 0, \\
\phi''(1) &= \frac{I_r\omega^2}{EI}\phi'(1), \\
\phi'''(1) &= \frac{-M_r\omega^2}{EI}\phi'(1),
\end{aligned} \tag{5.7}$$

where M_r and I_r are the mass and moment of inertia of the rigid section.

The boundary conditions (5.7) were applied to the general solution to the Euler-Bernoulli beam equation and the ϕ_i were determined using Mathematica. The resulting beam mode shapes are given by

$$\phi_i = \phi_i(\tilde{s}) \qquad 0 < \tilde{s} < 1 \tag{5.8}$$

$$= \phi_i(1) + (\tilde{s} - 1)\phi_i'(1), \quad 1 < \tilde{s} < \tilde{s}_p, \tag{5.9}$$

where

$$\phi_i(\tilde{s}) = a_i(\cos\lambda_i\tilde{s} - \cosh\lambda_i\tilde{s}) + \sin\lambda_i\tilde{s} + \sinh\lambda_i\tilde{s}. \tag{5.10}$$

The constants a_i and eigenvalues λ_i are given in Table 5.2, where the predicted theoretical natural frequencies are compared to measured values for the first three modes.

The deviation of the theoretical frequencies from their experimental counterparts could be attributed partly to the quality of the welding at the joint between the flexible and rigid sections of the test cylinder. A certain amount of flexibility occurred at high frequency, making the joint less than rigid and giving measured frequencies lower than theoretically predicted.

The integrals (5.6) were evaluated using a Mathematica routine presented in Appendix I. The sample run presented in the appendix corresponds to a two-mode Galerkin expansion in the x and y directions.

A value of the exponent $\xi = 1$, where ξ relates the radial support stiffness force to the approach at the support (equation (2.9)), was found to be reasonable for small magnitudes of the approach, which is the case here. The added mass coefficient C_{ma} was determined from potential flow theory, by considering a seven cylinder kernel in quiescent fluid (Paidoussis *et al.* 1984), yielding $C_{ma} = 1.332$; the variation of C_{ma} with changes in local array geometry, as the cylinder is displaced from the equilibrium position, was found to be negligible. Other system parameters in equations (5.5) — see (5.1, 5.2) are as follows:

$$K_s = 10^6 \quad \mathrm{N/m^2}, \quad \mu_{fr} = 0.35 \quad \text{and} \quad a = 1.7236. \tag{5.11}$$

The dimensionless support damping constant $\tilde{c}_s$ $(= \bar{c}_s D^{\xi}/(m\omega_1))$, depends on the initial impact velocity (2.26). For each impact, the maximum approach σ_m was estimated from equation (2.25). Thereafter, equation (2.26) could be integrated to give $\bar{c}_s$, and hence, $\tilde{c}_s$. $\tilde{\beta}$, which is related to squeeze-film damping, is zero for in air impacting.

Equations (5.5) were solved using a fourth order Runge-Kutta routine; when sticking occurred, an implicit iterative algorithm was applied to determine the correct force balance. Unless otherwise stated, initial conditions applied in the numerical simulations were

$$q_1 = 0.001, \qquad q_i = q_i' = 0, \quad i > 1;$$

$$p_i = p_i' = 0, \quad i \geq 1.$$

For the purpose of determining the tube dynamics, a three-mode Galerkin expansion was found to be sufficient.[2] This is due to the special design of the test cylinder, with the result that a large separation in the modal stiffnesses exists between the first two modes and the higher modes (see Table 5.2).

5.2.2 Predicted Cylinder Response and Underlying Dynamics

The initial Hopf bifurcation which results in fluidelastic instability is predicted theoretically at $V = 0.185$. This is in reasonably good agreement with the experimental value of $V_c = 0.216$. From hereon, all velocities (theoretical and experimental) are expressed relative to the experimental critical flow velocity, $V_c = 0.216$.

Figs.5.22 to 5.26 show comparison between experimental and theoretically predicted responses over a range of flow velocities for the gap size $\tilde{e}_r = 0.200$. These results correspond to brass/brass impacting with air as the interstitial support-gap fluid.

The single-sided impacting motion found to occur following the Hopf bifurcation is predicted by the theoretical model as shown in Fig.5.22 for $V = 1.10V_c$. The modulation effect which is characteristic of this motion is also observed in the corresponding in-flow time traces. Cross-flow time traces, on the hand, show only minimal modulation. A comparison of the response frequencies (Fig.5.22(d,h)) indicates close agreement between theoretical and experimental results.

Bifurcation to double-sided impacting motion occurred at $V = 1.20V_c$ in the experiments and is predicted at $V = 1.24V_c$ theoretically. This response is shown in Fig.5.23 for $V = 1.29V_c$ and $V = 1.21V_c$ for theory and experiment, respectively. The cross-flow component of the response predominates in this new response regime. In-flow amplitudes are significantly smaller and non-periodic, Fig.5.23(d,h). Intermittent

[2]Note that higher modes would still be needed for an accurate determination of the impact forces for wear rate determination.

Table 5.3: Comparison of theoretically predicted bifurcation velocities with experimental measurements

Transition	V_{th}/V_c	V_{exp}/V_c	Err. %
Hopf	0.86	1.00	-14
DS Impact	1.24	1.20	3
Interm't'cy	1.52	1.41	7.8
Chaos	1.86	1.70	9.4
P2	2.10	1.95	7.2

breakdown of this double sided-impacting motion leads to the predominant response for the present gap size: double-sided impacting orbiting response. Measured and predicted velocities for the onset of intermittency are, respectively, $V = 1.41V_c$ and $V = 1.52V_c$. Experimental and theoretical examples of this motion are shown in Fig.5.24, the corresponding velocities being $V = 1.76V_c$ and $V = 1.62V_c$ for theory and experiment, respectively. The intermittent amplitude bursts, particularly in the in-flow direction, are well depicted in the time traces of Fig.5.24(b,f). A chaotic character is introduced in the response by these amplitude bursts, which occur at uncorrelated time intervals. This is reflected in the broad-banded effect at the dominant response frequency in the corresponding in-flow spectra, Fig.5.24(d,h).

Experimental tests show that the time interval between turbulent bursts vanishes near $V = 1.7V_c$. The result is a chaotic response as shown in Fig.5.25. Theoretically chaotic motion is predicted at $V = 1.90V_c$; the experimental response at this velocity is shown in Fig.5.25(e-h). In both theory and experiment it is clear that the final breakdown to chaos is a result of the vanishing time interval between turbulent bursts. In-flow time traces and response spectra display the chaotic character of the response. In the cross-flow direction, on the other hand, despite the existence of a chaotic component, period-1 motion is still predominant in Fig.5.25(c,g) and Fig.5.25(d,h).

In the final bifurcation, the system response becomes more periodic, which is a stabilization of the period-2 attractor; Fig.5.26 shows this final period-2 response. The theoretical model predicts this final transition very well and fairly accurately, giving a transition velocity near $V = 2.10V_c$ as compared to the experimental value $V \simeq 1.95V_c$.

In summary, the theoretical model is able to reasonably accurately predict the dynamical behaviour. Not only are all the bifurcations in the response predicted, but also the critical bifurcation velocities are obtained within an average discrepancy of 10%, and in most cases better, as tabulated in Table 5.3.

It is important that a theoretical model accurately predict the detailed cylinder dynamics since, ultimately, this completely determines the cylinder/support force history and hence wear rates. With this in mind, we proceed to investigate, in further detail, the dynamical behaviour within the various bifurcation regimes. The analysis provides a better understanding of the system. Furthermore, comparison criteria in cases where the response is non-periodic allow for further quantitative comparison of theory and experiment.

5.2.3 Characterization of the System Attractors: Underlying Mechanisms and Some Associated Discrete Dynamical Systems

It is clear from the preceding that, like any other nonlinear dynamical system, a distinct sequence of bifurcations is uncovered as the parameter V is varied over the range of interest. Identification of the bifurcation types and underlying mechanisms provides valuable information for a better understanding of the dynamical system. Although the system is infinite-dimensional, the experimental results, supported by the theoretical findings, indicate that the mechanisms underlying the observed bifurcations may involve only a few dimensions. In nonlinear dynamics parlance, the centre manifold associated with these bifurcations is expected to be low-dimensional. This is a gratifying result, the reason being that there is then a much better chance of uncovering the underlying mechanisms that determine the bifurcations and associated system dynamics.

5.2.3.1 Dynamical behaviour at onset of impacting

The dynamical behaviour at the onset of impacting is characterized by a quasi-periodic-like response. Intuitively the underlying mechanism is rather obvious. The vibration amplitude in the unstable cross-flow direction grows to attain the support clearance value $\tilde{e}_r$. During the impact process energy is removed from the unstable cross-flow mode and transferred to the stable modes, in particular the first in-flow mode. Two regimes in phase space may be identified. The first, a slow regime where the cylinder is in flight and the response is governed by the fluid dynamics. In this regime, cylinder in-flow motion may be described by a simple oscillator with exponentially decaying amplitude (cross-flow motion, on the other hand, exhibits exponential growth). This may be verified in the example of Fig.5.22 where this regime lasts between two and five cycles at a time. The fast regime is the impact process itself. The strong nonlinearities in this regime may lead to chaotic behaviour.

To see how this might happen, we consider an analysis of a simple 'pseudo'[3] 1-D map, whose behaviour may be considered as a first approximation to that of the present system. From the theoretical time trace of Fig.5.22(b) a Poincaré map is extracted and is shown in Fig.5.27(a); once again, here, straight line segments trace the iteration sequence . Although this map appears quite disordered at first glance, a certain pattern emerges after a careful study of the iteration sequence. First, the branch labelled b_1 is identified to correspond to the simple exponentially decaying solution. The second observation is that the trajectory may enter a region of fast motion at certain points on b_1. The points above the first bisectrix represent amplitudes immediately following such a transition. Further investigation reveals the existence of distinct trajectories or paths that are traced by successive iterations.

The trajectories, may be classified into two types, which we shall label A and B. In type A trajectories, the in-flow amplitude grows following one or more impacts, and then decays exponentially without interruption to a low value along b_1. More complex

[3]Such a qualification is necessary since the resulting map, as defined, is multivalued and non-invertible, hence, not a 1-D return map in strict mathematical definition.

behaviour is observed for type B trajectories. Decaying oscillations over a portion of branch b_1, labelled b_{11}, are interrupted at relative high amplitudes. Fig.5.27(b) is a map extracted from Fig.5.27(a), which illustrates a type A trajectory. Starting with an amplitude X_1, the system undergoes four oscillations before returning to the vicinity of X_1. Branches b_2 and b_3 represent a piecewise linear approximation of the functional behaviour above the first bisectrix determined from a study of the average location of iterates in Fig.5.27(a).[4] Piecewise linear functions, approximating the solution in the unstable direction, are also used to depict a type B orbit. The resulting map is presented in Fig.5.27(c), in which a sample orbit is illustrated. Iterates are trapped in an intermediate orbit $b_4 \rightarrow b_5$ prior to expulsion to b_3, whence type A behaviour begins.

Several conclusions may be reached from a study of Fig.5.27(b,c). Firstly, simple period-1 motion is precluded since the combined map exhibits no (stable) fixed points. This conclusion is confirmed by the experimental and numerical results. Nearly periodic orbits of order $n \geq 1$, n being the number of period-1 cycles, are however possible. The trajectory illustrated in Fig.5.27(b) suggests an orbit close to $n = 4$. This leads to the quasi-periodic-like character in the time traces as discussed above. Another important conclusion that can be drawn from these 1-D maps concerns the possibility of chaotic motion in the present velocity range. A trapping region exists from which trajectories cannot escape; therefore an attractor exists. Mixing of trajectories, an important property of chaotic attractors, clearly occurs particularly in the transition between the two maps and within the individual maps. These properties, coupled with the lack of periodic points as stated earlier, leads to the conclusion that the possibility of a strange attractor exists in the present velocity range, despite the large periodic component observed in the response.

The mechanism underlying this type of transition to chaos has been labelled a *switching mechanism* (Pikovsky & Rabinovich, 1981); the name indicating switching

[4]Note that analytical forms of these functions cannot be determined. This would require knowledge of and the existence of analytical solutions to the governing equations of motion.

between fast and slow motions as discussed above. This mechanism has been shown to underly chaotic behaviour in other very different physical systems. The first is an electronics circuit whose active element is a tunnel diode; the diode current/voltage characteristic exhibits a discontinuous jump at some critical value. The second system is the well known Belousov-Zhabotinsky chemical reaction.

The fundamental aspects of the switching mechanism are as illustrated in the following schematic:

Monotonic Energy Source (or Sink) → Oscillating System → Catastrophic Energy Drop (or Input)

The scenario depicted in the schematic is precisely the one at play at the onset of impacting for a loosely supported cylinder. It is therefore expected that this mechanism might play an important role in efforts to understand and quantify the cylinder dynamics in this regime.

5.2.3.1 Intermittency Transition and Restabilization of Period-2 Motion

As observed in section 5.2.2.1, the double-sided impacting orbiting response results from a loss of stability of the double-sided impacting response. A study of in-flow time traces revealed the existence of durations of low amplitude period-2 motion interrupted by large amplitude period-1 orbiting motion. The period-1 motion then decays gradually and the cycle is repeated. Bursts of period-1 motion occurred intermittently at apparently random time intervals.

This intermittent behaviour was even more clearly exemplified by a one-mode two-degree-of-freedom reduction of the system. Fig.5.28(a) shows [5] in-flow response, in the one-mode model, for $V = 2.0V_c$. Just prior to the onset of intermittency, a

[5] In this case, the one mode reduction shows poorer agreement with experiments for the intermittency range which should be $1.4 < V/V_c < 1.7$.

subharmonic bifurcation occurs in the in-flow direction, hence, intermittency results from instability of the period-2 cycle. In cross-flow, on the other hand, the basic cycle is period-1 as seen in Fig.5.28(b).

The Poincaré map technique is once again utilized as a tool to investigate further the intermittency behaviour. We consider, as before, a next-peak value (X_n) map of the in-flow motion. In view of the existence of period-2 motion in this direction, a more judicious choice is to plot the map X_{n+2} versus X_n; in this case, a fixed point of the map corresponds to a period-2 orbit on the original system. The resulting Poincaré map, corresponding to the laminar region in Fig.5.28(a), is shown in Fig.5.28(c). The organization of successive iterates in a definite pattern, in this case a curve, confirms the notion of short term deterministic behaviour in the laminar regime.

The fixed point, apparent at the cusp in Fig.5.28(c), corresponds to a periodic orbit of frequency $\omega \simeq 2\omega_0$. A concentration of iterates occurs as this point is approached, as well as several iterations after. This reflects the response behaviour in the region of nearly constant-amplitude periodic motion in the middle of the laminar region in Fig.5.28(a). The cusp-shaped curve of Fig.5.28(c) suggests the possibility of similar properties between this map and a slightly modified form of the well known baker's transformation of the unit square onto itself (Bergé *et al.*, 1980). The baker's transformation is a 2-D map, on a plane defined by coordinates p_1 and p_2, defined by:

$$\begin{aligned} p_1 &\rightarrow 2p_1, \quad p_2 \rightarrow p_2/2 \qquad \text{for} \quad p_1 < 0.5, \\ p_1 &\rightarrow 2p_1 - 1, \quad p_2 \rightarrow (p_2 + 1)/2 \qquad \text{for} \quad p_1 > 0.5. \end{aligned} \tag{5.12}$$

Coordinate p_1 represents the unstable manifold along which divergence of nearby trajectories occurs; p_2, on the other hand, parametrizes the area-preserving property of the map. It is necessary to modify the form of p_2 to account for the area-contraction property of our dissipative system. The resulting map takes the form

$$p_1 \rightarrow 2p_1, \quad p_2 \rightarrow \alpha_1 p_2 \quad \text{for} \quad p_1 < 0.5,$$

$$p_1 \rightarrow 2p_1 - 1 + g(p_1), \quad p_2 \rightarrow \alpha_1(p_2 - 1) + 1 \quad \text{for} \quad p_1 > 0.5, \tag{5.13}$$

where $\alpha_1 = 0.475$, and $g(p_1) = \alpha_2 \sin(2\pi p_1) + \alpha_3 \sin(4\pi p_1)$. This formulation was first proposed by Bergé *et al.* 1980. In the present analysis, a different set of the parameters $\alpha_1 - \alpha_3$ is utilized: $\alpha_1 = 0.400, \alpha_2 = 0.23$ and $\alpha_3 = 0.10$.

Fig.5.29(a) shows trajectories of iterates for two initial conditions. A fixed point of the map exists at $p_1 = 0.75$ and $p_2 = 1.0$. The trajectory labelled '1' passes close to the fixed point, hence the concentration of iterates near P; trajectory '2' only approaches the fixed point. This attraction of iterates towards the fixed point is similar to that which occurs in the map of Fig.5.28(c). The coordinates in Fig.5.28(c) contain a combination of both the stable and unstable directions. In the case of Fig.5.29(a), however, the stable and unstable directions are isolated and are parametrized by the coordinates p_2 and p_1, respectively. To obtain the cusp shape then, a projection of the modified transformation (5.13) onto a different direction, which gives a similar 'view' of the trajectory of iterates, is necessary. The resulting return map is given by

$$\overline{p} = \alpha_4 p_1 + \alpha_5 p_2 + \alpha_6, \tag{5.14}$$

where $\alpha_4 = -0.5, \alpha_5 = -1.0$ and $\alpha_6 = 1.2$. A return map of successive iterates of $\overline{p}$ is shown in Fig.5.29(b). The similarity to Fig.5.28(c) is evident.

Figs.5.30(a,c) show close-ups of the laminar phases in the theoretical and experimental in-flow responses, respectively, presented earlier in Fig.5.24. It is seen that the single-mode model predicts the general character of the intermittent reponse (cf. Fig.5.28(a)). Poincaré maps corresponding to the Figs.5.30(a,c) are presented in Figs.5.30(b,d), respectively. These maps are quite similar to the map of Fig.5.29(b), derived from the baker's transformation. The theoretical model predicts a closer approach to the periodic orbit, hence, the sharply defined cusp in Fig.5.30(b). Experimentally, the response does not approach a periodic orbit as closely as theoretically predicted, hence, a true cusp is not formed; this might corresponds to the type '2' trajectory in Fig.5.29(a); such a trajectory results in iterations in Fig.5.29(b) crossing the first bisectrix before reaching the fixed point at the cusp tip.

It is quite interesting that, once again, a simple map exhibits some quantitative similarity with the present system. The concentration of iterates near the fixed point was shown earlier to be a property of type I intermittency. As will be shown in Chapter 6, a return map, exhibiting the narrow channel (Fig.4.26) (which is the hallmark for type I intermittency), can be obtained from the baker's transformation. This, once again, points to type I intermittency as the mechanism underlying transition to chaos in the experimental system. For the two degree-of-freedom system, intermittency resulted from the bifurcation of a period-1 orbit. In the experimental system, however, intermittency results from the bifurcation of a period-2 response.

5.2.4 Attractor Characterization and Invariant Measures

In Section 5.2.2, cylinder responses, determined theoretically and experimentally, were compared. For periodic attractors, exact comparison was possible since a periodic orbit is uniquely determined by its frequency and amplitude. As shown in the preceding, a semi-quantitative comparison is also possible in the case of non-periodic motion in the vicinity of a deterministic attractor. It is desirable to have access to equivalent measures in the case of chaotic motions that can allow for quantitative comparison of theoretical predictions with experimental results.

Lyapunov exponents and attractor fractal dimension are related to the global behaviour of the attractor and provide measures for quantitative comparison. More interestingly, the geometrical structure of the attractor can also be probed for saddle orbits. Saddle orbits provide a quantitative description of the apparent self-similarity of chaotic attractors (Auerbach *et al.*, 1987), these orbits being the essential building blocks of most typical chaotic attractors. Comparable attractors should have the same saddle orbits, with identical distributions. The attractor phase point should also visit the various orbits with the same frequency. Characterization of the chaotic attractors by saddle orbits is chosen as a tool for quantitative comparison and validation of the theoretical model. This approach has the added advantage that, as shown below, saddle orbits can easily be determined from experimental data; furthermore, only one experimental variable is necessary for complete characterization.

A property of saddle orbits is the attraction of nearby phase space trajectories along certain directions (the corresponding stable manifolds). Trajectories remain nearby for a time before escaping along an unstable manifold. An orbit is then simply determined by establishing the return of a phase point to the neighbourhood of a chosen starting point in phase space. In the orbital plot of Fig.5.24, for instance, period-1 saddle orbits are clearly evident. From the corresponding power spectra, the period-1 frequency is $\omega_{s1} \simeq \omega_0$. To determine higher order orbits, a procedure first put forward by Lathrop & Kostelich (1989) is utilized. In essence, the attracting property of saddle orbits (along the stable manifold) is exploited as follows. Consider the system state in phase space to be represented by the vector of generalized coordinates and velocities $\mathbf{X}$. Starting with a phase point $\mathbf{X_i}$, on a trajectory in phase space, the images $\mathbf{X_{i+1}}, \mathbf{X_{i+2}}....$ of $\mathbf{X_i}$ are followed until the smallest index $k > i$ is found which satisfies

$$|\mathbf{X_k} - \mathbf{X_i}| < \epsilon; \qquad \epsilon > 0. \tag{5.15}$$

$\mathbf{X_i}$ is then referred to as an (m, ϵ) recurrent point where $m = k - i$. The orbital frequency associated with the corresponding (m, ϵ) orbit of order n is

$$\omega_{sn} = m\Delta t, \tag{5.16}$$

where Δt is the temporal spacing of the phase points. ω_{sn} is determined for each phase point and the results are presented in the form of a histogram of the frequency count of the various saddle orbits encountered.

Before proceeding with the determination of saddle orbits, the question of the experimental phase space needs to be addressed. Specifically, not all phase space variables, positions and velocities for the various modes, are known; the physical displacements in the in-flow and cross-flow directions at the cylinder tip being the only readily available variables. A reconstruction of the phase is therefore necessary. The delay embedding technique used was first proposed by Packard *et al.* (1980). Pseudovectors $\mathbf{X}_i$ of the embedding dimension m are formed from the two scalar time series $\{x_i\}_{i=1}^{N}, \{y_i\}_{i=1}^{N}$ as per the formulation below:

$$\mathbf{X}_i = [x(i\Delta t),\ y(i\Delta t),\ x((i+d)\Delta t),\ y((i+d)\Delta t), ...,\\ x((i+(m/2-1)d)\Delta t,\ y((i+(m/2-1)d)\Delta t] , \tag{5.17}$$

where $d \times \Delta t$ is the delay. Takens (1980) showed that for sufficiently large m ($m >$ attractor dimension), the reconstructed pseudo-phase space has the same properties as the true phase space. The delay factor d is selected such that the reconstructed phase space reveals the topological structure of the attractor. From correlation dimension calculations on the theoretical model, an attractor dimension $d_{cr} \leq 3.5$ was obtained for the various response regimes as discussed below. An embedding dimension $m = 4$ was therefore selected for the experimental data. Fig.5.31 shows several projections of a reconstructed phase plane plot for $V = 1.62V_c$; the delay was taken as $d\Delta t = 0.1$s. The various projections reveal a clear structure in the attractor.

In determining the saddle orbits, the recurrence distance ϵ was chosen to be 2% of the maximum separation of attractor points. Fig.5.32 depicts examples of period-2 and -3 saddle orbits extracted from the reconstructed phase plot for $V = 1.62V_c$. In both cases the apparent self-crossings are the result of the projection onto a plane. The trajectory returns to the vicinity of the starting point only after the complete loop. Fig.5.33 shows the experimental and theoretical histograms of the distribution of saddle orbits for $V = 1.62V_c$. In both cases more than 90% of phase points fall on saddle orbits of order 1 to 10. The predominance of period-1 saddle orbits predicted theoretically is in concordance with experimental results. Furthermore, theoretical results concur with the experimental finding that in this velocity regime the cylinder response is primarily comprised of saddle orbits of order 1 to 7. The discrepancy in the percentage of the period-1 saddle orbits might be attributed, at least partly, to experimental noise.

A similar saddle orbit histogram plot is presented in Fig.5.34 for the lower velocity

$V = 1.20V_c$, corresponding to the single-sided impacting response. In this case, the results suggest that the corresponding experimental attractor is characterized by saddle orbits of order 1 to 4 (Fig.5.34(a)). Theoretically, the occurrence of period-3 and -4 orbits is quite infrequent and only barely observable. This difference, compared with experimental results, may be attributed to the significant effect of experimental noise, particularly in the in-flow direction where response amplitudes are relatively small. Period-3 and -4 orbit counts may be viewed, in Fig.5.34(a), to be just above the count attributed to noise, hence, reflecting the low occurrence rate suggested by the theoretical result. Overall, it can be concluded fairly confidently, that the theoretical model predicts the topological structure of the experimental attractor with reasonable accuracy.

We conclude this section by looking at a characterization of the attractor dimension in phase space. Correlation dimensions were evaluated using the procedure described in Section 4.3.4 for the same two attractors above. The single-sided impacting motion is comprised of primarily period-1 and -2 saddle orbits. The correlation dimension average value of $d_{cr} = 2.6$ for the experimental attractor as shown in Fig.5.35(a). A lower value of $d_{cr} = 2.1$, Fig.5.35(b), is predicted theoretically for the same attractor. Fig.5.36(a,b) shows the results for $V = 1.62V_c$ for the experimental and theoretical attractors respectively. An average attractor dimension $d_{cr} = 3.3$ is obtained for the experimental attractor while, $d_{cr} = 3.5$ for the theoretical attractor, hence in very good agreement. It is gratifying to find that, despite the high number of dimensions involved in this system, the resulting attractors remain well within low dimensional spaces. It is for this reason that low dimensional models (one and two dimensional maps) predict the dynamical behaviour well, both qualitatively and at least semi-quantitatively.

Chapter 6

PRACTICAL CONSIDERATIONS

The analysis of the preceding chapters has shown that the dynamics of low dimensional models of a loosely supported cylinder can be elucidated to a satisfactory degree via modern nonlinear dynamics methods. Transition routes to chaos have been identified and quantified using invariant measures (Lyapunov exponents, correlation dimensions and saddle orbit distributions).

In this final chapter the implications of these findings to a more practical situation and a possible practical application are considered.

6.1 THE EFFECT OF INCREASED NUMBER OF DEGREES OF FREEDOM

The dynamical models studied in Chapters 4 and 5 were intentionally designed to have a low number of 'active' degrees of freedom. By eliminating the added complexity associated with higher modes, the response behaviour remained transparent enough, enabling a rigorous study of the underlying dynamics.

Heat exchanger tubes have uniform mass and stiffness, hence, no large disparity exists between the lower and higher modes. As a result, a larger number of modes is required to model the resulting dynamics.

We proceed to study the response of a uniform loosely supported cylinder. A clamped-pinned tube, with a loose support at mid-span, is modelled. Of particular interest is the effect of the increased participation of higher modes on the resulting dynamical behaviour. The cylinder parameters are selected such that the first mode

Table 6.1: Uniform-cylinder modal parameters

Mode	$\lambda_i l$	ω_i
1	3.93	37.7
2	7.07	122.0
3	10.21	254.5
4	13.35	435.0
5	16.49	663.7

instability velocity is close to that of the experimental system studied in Chapter 5. Cylinder parameters are, $l = 2.64$ m, $D = 0.01$ m, $D_i = 0.009$ m, where l is the cylinder length, D the outside cylinder diameter as before, and D_i is the internal diameter. The cylinder material is considered to be steel, giving cylinder mass per unit length $m = 0.1164$ Kg/m. The cylinder is subjected to uniform flow over the complete span. It is symmetrically located within the circular support in cross-flow, while in the in-flow direction, the cylinder has an eccentricity of $0.160D$ in the upstream direction. Limiting the analysis to the flow velocity range where only the first mode is unstable, a five-mode Galerkin projection was found to be sufficient to describe the cylinder dynamics. Table 6.1 summarizes the cylinder modal properties.

The equations to be solved are equations (5.5). In evaluating the integrals of equation (5.6), clamped-pinned modal functions are utilized, and the flow and tube material properties are considered uniform. To simplify the evaluation of the integrals of equation (5.6) the delayed cross-flow displacement, $\tilde{y}_d$ (equation (2.5)), required for the evaluation of C_L, was expressed as $\tilde{y}_d(\tau) = \phi(1)q_1(\tau - \Delta\tau)$. The simplified expression was necessary to maintain a manageable number of terms in the integrals of equations (5.6). This exclusion of higher modes is equivalent to applying a filter to the delayed response for the purpose of determining the fluid force; elimination of high frequency fluctuations is desirable, as noted in Chapter 4, since fluid-inertia and viscous effects limit the frequency at which fluctuations in the fluid force can occur. Initial conditions applied in the numerical simulations were

$$q_1 = 0.005, \qquad q_i = q_i' = 0, \quad i > 1,$$

$$p_i = p_i' = 0, \quad i \geq 1,$$

where p_i and q_i are the generalized coordinates in the in-flow and cross-flow directions, respectively.

For this system, the Hopf bifurcation, associated with fluidelastic instability, occurs at $V_c = 0.265$. At $V = 1.25V_c$, in-flow cylinder response exhibits complex albeit periodic motion, Fig.6.1(a-c). Cross-flow amplitudes are large enough for impacting with the support to occur. In-flow amplitudes, on the other hand, remain significantly smaller than their cross-flow counterparts. The velocity $V = 1.30V_c$, Fig.6.1(d-f), is in a transition regime associated with a bifurcation leading to a new periodic motion with primarily period-3 and -6 components. This response becomes even more clearly defined at $V = 1.35V_c$, as shown in Fig.6.2(a-c).

The response in the velocity range $1.25 < V/V_c < 1.35$ corresponds to the double-sided impacting velocity regime in the experimental system. In the latter, period-1 motion occurred in cross-flow with similarly low in-flow amplitudes to the present case. The proximity of the higher mode frequencies to that of the first mode then results in complex periodic motion replacing the simple period-1 motion observed in the previous case. The periodic motion in Fig.6.2 undergoes a bifurcation near $V = 1.38V_c$. The result is in-flow motion of primarily period-2. This motion is, however, unstable. Hence, at indeterminate time intervals, the motion is interrupted by bursts of uncorrelated large amplitude motions, having a lower frequency; this is followed by a restabilization of the higher frequency period-1 motion. Fig.6.3 depicts the type of response for $V = 1.40V_c$. The scenario described in the foregoing is precisely the intermittency phenomenon which was found to predominate in the response in the experimental system. Comparing the in-flow responses of Fig.5.24 and Fig.6.3, the following observation can be made. The in-flow response exhibits intermittent bursts in amplitude which intersperse durations of nearly periodic motion — the laminar regime. The higher modes increase the system stiffness, resulting in reduced in-flow amplitudes in Fig.6.3. Fundamentally, however, the intermittency mechanism governs the response in both cases. This result attests to the robustness of the intermittency transition in the present system.

At $V = 1.45V_c$ a reversal of this transition to chaos has commenced resulting in a reorganization of the response, as seen in Fig.6.4 where we observe marginally stable period-2 motion in the in-flow response. As V is further increased the period-2 response becomes stable as shown in Fig.6.5(a-c) for $V = 1.50V_c$. Finally at $V = 1.60V_c$ (Fig.6.5(d-f)), period-1 motion has returned in the in-flow direction albeit at double the cross-flow frequency. The result is the now familiar figure-of-eight orbital motion which marked the final response in the experimental system.

The results in the preceding were obtained for symmetrical cross-flow cylinder location within the support. Fig.6.1 to Fig.6.5 indicate that zero eccentricity in the cross-flow direction results in a significant reduction in coupling between the in-flow and cross-flow motions. To test this conclusion, calculations were carried out for a cylinder cross-flow eccentricity of $0.03D$ at the support. Sample orbital plots are presented in Fig.6.6. The single- and double-sided impacting motions, previously encountered for the experimental system, are identified in Figs.6.6(a) and (b) for $V = 1.20V_c$ and $V = 1.25V_c$, respectively. A transition via intermittency results in an orbiting motion, as exemplified by Fig.6.6(c) for $V = 1.60V_c$. The figure-of-eight orbital motion is once again the final response, as depicted in Fig.6.6(d) for $V = 1.73V_c$.

It is quite remarkable that, despite the significant differences between the system studied here and the experimental system of Chapter 5, the bifurcation history of the response remains fundamentally similar. Two important conclusions may be drawn from the foregoing. Firstly, that the analysis of low dimensional models may lead to profound insight into the otherwise intractable dynamics of higher dimensional systems. The second pertains to analysis of support influenced cylinder dynamics in general. Experimentalists measuring tube wear have long concluded that tube wear rates are intimately related to the underlying cylinder dynamics. The present analysis gives an idea of the complexity of the dynamics. On the same note, however, the situation is not entirely hopeless. The cylinder response observed here shares common characteristics with other dynamical systems currently under study. Thus, under operational conditions fluidelastic instability is most likely to occur in the first TSP inactive mode, which is the case studied here. Over a range of flow velocities it is expected that major aspects of the response will remain in low dimensional space involving only a few modes. Furthermore, despite transition to chaos, the motion is likely to remain borderline chaotic – hence, a significant periodic component will remain, while the overall attractor will be low dimensional. An important property of borderline chaotic attractors is their relationship to nearby periodic attractors in parameter space. The intermittent response is an example of borderline chaotic motion. In the laminar phase the intermittent response is very similar to the periodic response prior to the onset of intermittency. This property makes it possible for a quantitative analysis leading to an estimate of the expected length of laminar phases in the intermittent response. We close this chapter with a closer look at this point.

6.2 TYPE I INTERMITTENCY REVISITED

In type I intermittency the dynamical behaviour, in the laminar phase, occurs on a reduced one-dimensional manifold. The archetype map describing this behaviour is

$$\mathrm{p}_{n+1} = H(\mathrm{p}_n, \mu_p) = \mu_p + \mathrm{p}_n + \mathrm{p}_n^2 + \dots, \tag{6.1}$$

where the parameter μ_p is related to the flow velocity, rescaled such that the onset intermittency is at $\mu_p = 0$. Here we define this parameter as, $\mu_p = (V - V_{cf})/V_{cf}$, where V_{cf} is the critical flow velocity for the onset of intermittency. Equation (6.1) gives a quantitative description of the system behaviour in the laminar phase. To see how an estimate of quantitative measures may be derived, consider the case when μ_p is small. In this case, equation (6.1) can be cast in the approximate differential form

$$\frac{d\mathrm{p}}{dn} = \mu_p + \mathrm{p}^2, \tag{6.2}$$

where n is now viewed as a continuous variable. An integration of equation (6.2) yields

$$\mathrm{p} = \sqrt{\mu_p}\tan[\sqrt{\mu_p}(n - n_0)]; \tag{6.3}$$

n_0 is the value of n in the narrowest part of the channel. Taking $n_0 = 0$ for convenience, p in equation (6.3) becomes unbounded when $\sqrt{\mu_p}n = \pi/2$, at which point the approximation of equation (6.2) is no longer valid. We can therefore conclude that the number of iterations during the laminar phase scales as $\sqrt{\mu_p}$. Thus, near V_{cf} the duration t_l of the laminar phases should be related to μ_p as follows:

$$t_l \propto \frac{1}{\sqrt{\mu_p}}. \tag{6.4}$$

This result is supported by the results in Fig.6.7 for the two degree-of-freedom system studied in Chapter 4, where t_l is plotted versus μ_p for a range of velocities near $\mu_p = 0$ ($V = V_{cf}$). Superimposed on the data points is the curve $t_l = 0.055/\sqrt{\mu_p}$, which shows a very good fit.

From a practical viewpoint the result of equation (6.4) gives a quantitative measure that can be tested for in any physical system suspected to be exhibiting an intermittency transition. Another result that can be put to practical use is the probability distribution of laminar phases. As shown by Bergé *et al.* (1980), the probability $P_l(t_l, \mu_p)$ of the occurrence of a laminar phase of duration t_l satisfies the equation

$$t_l = \int_0^\infty P_l(t_l, \mu_p)t_l dt_l \simeq \frac{b}{\sqrt{\mu_p}}. \tag{6.5}$$

Qualitatively, $P_l(t_l, \mu_p)$ should vary as depicted in Fig.6.8. The time needed to drift through the narrow channel (see Fig.4.26) is seen to be bounded from above, and hence, can fluctuate to lower values only. The probability distribution of impact forces will be undoubtedly be related to the distribution of Fig.6.8.

Unlike in the laminar regime, where dynamical behaviour is universally determined by equation (6.1), turbulent regime behaviour is unique to the system itself. It is possible, however, that certain aspects of the dynamics, such as the stretching and folding of trajectories in phase space which leads to sensitivity to initial conditions, as well as the relaminarization process itself, may be at least qualitatively described by simpler low dimensional maps.

The baker's transformation of the unit square describes a possible scenario leading to relaminarization after a turbulent burst. This transformation was found to yield a return map topologically equivalent to that extracted from the experimental system in the intermittency response velocity range (see Fig.5.29). The baker's transformation may be shown to exhibit type I intermittency by considering a map relating successive iterates of the coordinate p_1 (equation (5.13)). For convenience, we re-write the transformation as follows:

$$\begin{aligned} p_1 &\rightarrow -2p_1, \qquad p_1 > -0.5, \\ p_1 &\rightarrow -2p_1 + 1 - g(p_1), \qquad p_1 < -0.5, \end{aligned} \tag{6.6}$$

where, as before, $g(p_1) = \alpha_2 \sin(2\pi x) + \alpha_3 \sin(4\pi x)$. Fig.6.9(a) shows a plot of $p_{1_{n+1}}$ versus p_{1_n}. The appearance of a small channel near $p_{1_n} = -0.72$ is evident. The translation of the map normal to the first bisectrix and hence the width of the narrow channel is determined by the coefficient α_2. The coefficient α_2 is therefore proportional to μ_p. The sample iteration sequence depicted in Fig.6.9(a) demonstrates the relaminarization process for this map. It is seen that this occurs as iterates jump across the discontinuity at $p_n = -0.5$, thus returning to the laminar regime along the second branch of the map. Although equation (6.6) exhibits the intermittency phenomenon, this single coordinate map is not uniquely invertible and hence cannot represent a differential dynamical system as it stands. A second coordinate is therefore required, making the map two dimensional, which distinguishes the two branches in Fig.6.9(a).

The Poincaré return map obtained for the two degree-of-freedom model of Chapter 4 (Fig.4.26(a)) is replotted in Fig.6.9(b), in which a typical iteration is also depicted. The similarity with Fig.6.9(a) is evident, in particular the jump near $X_n =$

0.00095 which leads to relaminarization. Recalling that Fig.6.9(b) is derived from a 4-dimensional system the agreement is quite remarkable. The high dimensionality of the system results in the scatter of iterations in Fig.6.9(b). It is noteworthy, however, that the relaminarization process in the baker's transformation appears qualitatively similar to that in the 2 d.o.f. system.

6.3 IMPLICATIONS TO WEAR-RATE COMPUTATION

Statistical methods are usually used to determine tube wear rates for given impact force probability distributions. The laminar phase, in the present system, corresponds to a regime of high frequency impacting motion. During the turbulent bursts, lower frequency coupled impact/sliding motion occurs. These two types of response exhibit different wear characteristics. Information about the characteristics of the response, such as the probability distribution of the laminar phases, for example, may therefore prove useful. To see how this might be applied, we consider a typical wear rate calculation. The time-averaged wear work-rate $\overline{\dot{W}}$ is defined as

$$\overline{\dot{W}} = \frac{1}{T}\int_0^T |F_{ri} v_\theta| dt, \tag{6.7}$$

where F_{ri} is the radial contact force and v_θ the transverse sliding velocity at the support. The integration time T is chosen to ensure that the computed wear rate is stationary (Axisa *et al.*, 1988). A simplified formulation has also been proposed by Axisa *et al.*, in which the wear rate is approximated by

$$\overline{\dot{W}} = \alpha_s f_d \overline{F}_c r_{rms}, \tag{6.8}$$

where

$$\overline{F}_c = \frac{1}{T}\int_0^T |F_{ri}| dt, \tag{6.9}$$

r_{rms} is the tube rms displacement at the support, f_d the dominant frequency of the response, and α_s, a shape factor dependent on the contact geometry.

For a tube exhibiting an intermittent response, the quantitative analysis of such a response may be an aid to determining a better value for the integration time T in equations (6.7,6.9). Dividing the response into a laminar and a turbulent phase, the average length of the laminar phase provides a reasonable value for the integration time T in the wear rate calculation. For the same laminar phase, a clear dominant frequency corresponding to the original limit cycle exists, giving an estimate for f_d in equation(6.8); note that f_d may not be clearly defined when a power spectrum of the total response (laminar plus turbulent phase) is evaluated. The dominant frequency is also different for the laminar and turbulent phases (e.g., in Fig.6.3, in-flow motion during the turbulent burst occurs at a lower frequency than in the laminar phase). In view of the significant difference between the responses in the two phases, a better formulation for $\overline{\dot{W}}$ may take the form:

$$\overline{\dot{W}} = \alpha_s(f_d^l \overline{F}_c^l r_{rms}^l + f_d^t \overline{F}_c^t r_{rms}^t), \tag{6.10}$$

where the superscripts "l" and "t" distinguish between the laminar and turbulent phases, employing knowledge of the existence of different responses, hence force histories, and also the expected average duration of the respective responses. The average duration of the turbulent bursts still has to be determined via physical or numerical experiments. For systems where an identifiable relaminarization process, such as the baker's transformation above, exists, useful information regarding the statistical properties of the response may still be obtained.

Equation(6.10) is expected to be most useful near the onset of intermittency where the laminar phase is interrupted only after large time intervals.

Chapter 7

SUMMARY AND CONCLUSIONS

In this Thesis the dynamical response of a loosely supported cylinder, unstable in the first TSP-inactive mode, has been studied. Using modern nonlinear dynamics theories and techniques, this system was cast in the light of general nonlinear dynamical systems.

To determine the cylinder response in the post-fluidelastic-instability regime, the complete steady fluid-force field was measured experimentally. The cylinder drag force was found to be relatively independent of cylinder position; the exception being the extreme upstream and downstream positions where the cylinder essentially blocked off the wavy channel between the corresponding upstream and downstream neighbouring cylinders. The result was a large increase in C_D for the downstream position, while a significant decrease occurred upstream. C_L, on the other hand showed a strong dependence on the cylinder equilibrium position over the test range. This translated into a strong dependence of cylinder stability on position in a linear stability analysis. Hence, while the array is generally regarded as highly unstable, no instability occurred for certain cylinder positions. The reversal of the lift force direction resulted in the prediction of static rather than dynamic instability. The same analysis showed that small changes in cylinder position may significantly alter the resulting stability behaviour. Hence, multiple instability regions, predicted for the cylinder located at the array equilibrium position ($\tilde{x} = \tilde{y} = 0$), disappeared when the cylinder cross-flow position was altered by 2% of the cylinder diameter. This result might explain why multiple instability regions are observed only in carefully controlled high precision experiments.

To investigate the dynamics of cylinder/support interaction, the analysis of a simplified two degree-of-freedom model was chosen as a starting point. This low dimensional system exhibited a wealth of dynamical behaviour. The cylinder response was found to undergo a sequence of bifurcations as the flow velocity was varied. Not only were periodic solutions obtained, but also velocity ranges in which chaotic motion predominated. One of the most important findings in this study was first uncovered in this low-dimensional system. This is the transition to chaos via type I intermittency, in effect bringing this system into the fold of other dynamical systems exhibiting the same transition. Strong evidence suggesting type III intermittency was also uncovered at the onset of impacting — however, due to "interference" by an unknown mechanism, this transition could not be unequivocally confirmed. Another conclusion reached in the study of the two degree-of-freedom system pertains to the sensitivity of the response bifurcation to cylinder/support gap size. For large gap sizes, periodic solutions comprise a large component of the response over the flow velocity range investigated. For smaller gap sizes, chaotic motion was more prevalent. This was later confirmed for an experimental system.

The feasibility and potential of a nonlinear dynamics approach was rigorously tested by analyzing a specially designed experimental model of a loosely supported cylinder. The experimental model also served as a test-bed for the nonlinear quasi-steady model.

Experimental measurements confirmed the existence of a complex sequence of bifurcations in the post-Hopf-bifurcation cylinder response, similarly to the case of the simple theoretical model. Over a significant velocity range, a double-sided-impacting orbiting motion predominated in the response for large gap sizes. This response became destabilized, at higher velocities, leading to chaotic motion. At higher velocities still, the final bifurcation resulted in a transition to periodic motion, with in-flow response at double the cross-flow response frequency. Distinctly different bifurcation behaviour occurred for small gap sizes: chaotic motion was found over the complete velocity range; also, the initial preload, present for small gap sizes, was found to have a pivotal effect on the cylinder response, by increasing the role played by frictional effects.

The presence of water in the interstitial support gap resulted in increased lubrication, hence reduced Coulomb friction forces, leading to increased sliding motion at the support. Squeeze-film damping was not found to be significant — this is attributed to the relatively large gap at the supports used in the experiments; the small support thickness is another contributing factor. Low Coulomb friction tests using Delrin showed that reduced friction at the support significantly alters the cylinder response. In the experimental test, reduction in friction resulted in the replacement of a periodic motion by a chaotic one, with significantly reduced in-flow response frequency.

The nonlinear quasi-steady model was found to predict the cylinder response and bifurcation sequence reasonably accurately. This, in essence, also validates this model for the present system. The theoretical bifurcation velocities were within an average of 8% of the experimental values. In the chaotic response regimes experimental and theoretical results were compared by determining quantitative measures associated with the underlying chaotic attractors. Fractal dimension calculations showed the dimension of the theoretically determined attractors to be close to that of the corresponding experimental attractors for both low and high velocity regimes. These attractors were further compared by breaking them down into the individual saddle orbits comprising the attractors. Attractor characterization by saddle orbits was found to be a novel technique for quantitative comparison of the chaotic attractors, since it involves comparison at all regions of phase space. At this level, some discrepancies between theory and experiment were found, specifically in the distribution of saddle orbits. However, the theoretical model was still found to correctly predict the most predominant saddle orbits reasonably well. Experimental noise was cited as a contributing factor to the discrepancy at this level of comparison.

Two regimes of chaotic motion were identified for the experimental system. In the first regime, transition to chaos is associated with a *switching mechanism* which is predominant at the onset of impacting. This mechanism is common to systems in which gradual monotonic energy change within the system undergoes sudden discontinuous interruptions. Examples of such systems include the Belousov-Zhabotinsky chemical system as well as a modified Van der Pol oscillator containing a tunnel diode. It is expected that the switching mechanism will be commonly observed in the response of marginally unstable loosely supported cylinders.

The second transition mechanism to chaos was *type I intermittency*. The resulting double-sided impacting orbiting response was identified as the commonly observed breathing type vibration of loosely suppported tubes in heat exchangers. It is notable, as mentioned above, that this transition was also found in the simplest two degree-of-freedom system studied. This may be considered as an indication of the robustness of the intermittency transition in the present system. In type I intermittency, relaminarization is associated with a discontinuous jump which returns the system to the vicinity of the laminar regime. In the case of the loosely supported cylinder, relaminarization was attributed to the transition between sliding motion and sticking, which is characterized by such a discontinuity in the sliding velocity at the support. The modified baker's transformation modelled the intermittency behaviour reasonably well; for the two degree-of-freedom system relaminarization was at least topologically equivalent to that in the baker's transformation.

The systems in the foregoing were intentionally designed to be low dimensional. As a practical consideration, the response of a uniform cylinder with a larger number of 'active' modes was investigated. The main difference to the low-dimensional models investigated before was the occurrence of complex periodic motion which replaced the simple period-1 motion in the experimental system. Overall, however, the response bifurcation history remained fundamentally the same. In particular, intermittency occurred as predicted by the low-dimensional systems. The final figure-of-eight periodic response was also exhibited by this higher dimensional system.

These results highlight the potential for the analysis of low-dimensional models. Most remarkable is the dynamical behaviour in the laminar phase, which even for the last system, modelled in 20 dimensions, is quantitatively described by a trivial one dimensional map. An analysis of the return map yielded not only a description of the dynamical behaviour, but also resulted in prediction of quantitative measures associated with response.

The implications of an intermittency transition to wear calculations were briefly probed. It was shown that the average duration of laminar phases and the associated frequency may prove to be useful parameters for wear computations.

7.1 RECOMMENDATIONS FOR FUTURE RESEARCH

In this Thesis the potential for the application of modern nonlinear dynamics to the problem of support-influenced cylinder dynamics has been demonstrated for a small range of system parameters and a single array geometry.

The effect of varying the system parameters on the resulting bifurcation sequence needs further investigation. In particular, Coulomb friction at the support has been found to be intimately related to the resulting bifurcations; this relation needs to be elucidated.

Transition to chaos for small gap sizes is still not well understood. When coupled with initial preloads, the dynamics become quite complex. It is noted that in practical applications support gap sizes will often be small.

An extension of the present work would be the determination of cylinder wear-rates in light of the bifurcation behaviour obtained. It would be interesting to investigate the correlation between specific bifurcations and resulting wear rates. In the chaotic regime, statistical properties of the resulting attractors might be potential candidates for wear computations.

REFERENCES

Andjelić, M., Austremann, R. & Popp, K. 1990 Multiple stability boundaries of tubes in a normal triangular cylinder array. In *Flow-Induced Vibration – 1990* (eds S.S. Chen, K. Fujita and M.K. Au Yang), PVP-Vol. 189, pp.87-98. ASME:New York.

Antunes, J., Axisa, F., Beaufils, B. & Guilbaud, D. 1988 Coulomb friction modelling in numerical simulations of vibration and wear work rate of multi-span bundles. In *Proceedings ASME International Symposium on Flow-Induced Vibration and Noise*, Vol.5: Flow-Induced Vibration in Heat-Transfer Equipment (eds M.P. Paidoussis, J.M. Chenoweth, S.S. Chen, J.R. Stenner & W.J. Bryan), pp. 157-176, New York: ASME.

Auerbach, D., Cvitanović, P., Eckmann, J.P., Gunaratne, G.H., & Procaccia, I. 1987 Exploring Chaotic Motion Through Periodic Orbits *Physical Review Letters* **58**, 2387-2389.

Axisa, F., Antunes, J., & Villard, B. 1988 Overview of numerical methods for predicting flow-induced vibration. *ASME Journal of Pressure Vessel Technology* **110**, 6-14.

Balsa, T.F. 1977 Potential flow interactions in an array of cylinders in cross-flow. *Journal of Sound and Vibration* **50**, 285-303.

Bergé, P., Dubois, M., Manneville, P. & Pomeau, Y. 1980 Intermittency in Rayleigh-Bénard Convection. *Le Journal de Physique-Lettres* **41**, L-341 – L-345.

Blevins, R.D. 1974 Fluid elastic whirling of a tube row. *ASME Journal of Pressure Vessel Technology* **96**, 263-267.

Blevins, R.D. 1975 Vibration of a loosely held tube. *ASME Journal of Engineering for Industry* **97**, 1301-1304.

Blevins, R.D. 1977 Fluid elastic whirling of tube rows and tube arrays. *Journal of Fluids Engineering* **99**, 457-460.

Blevins, R.D. 1979 Fluid damping and the whirling instability of tube arrays. In *Flow-Induced Vibrations* (eds S.S. Chen & M.D. Bernstein), pp. 35-39. New York: ASME.

Cai, Y. & Chen, S.S. 1991 A theory for fluidelastic instability of tube-support-plate-inactive modes. In *Flow Induced Vibrations and Wear* (eds M.K. Au-Yang & F. Hara), PVP-Vol.206, pp. 9-18. New York:ASME.

Chen, S.S. 1975 Vibration of nuclear fuel bundles. *Nuclear Engineering and Design* **35**, 392-422.

Chen, S.S. 1978 Crossflow-induced vibrations of heat exchanger tube banks. *Nuclear Engineering and Design* **47**, 67-86.

Chen, S.S. 1983a Instability mechanisms and stability criteria of a group of circular cylinders subjected to cross-flow. Part I: theory. *ASME Journal of Vibration, Acoustics, Stress and Reliability in Design* **105**, 51-58.

Chen, S.S. 1983b Instability mechanisms and stability criteria of a group of circular cylinders subjected to cross-flow. Part II: numerical results and discussion. *Journal of Vibration, Acoustics, Stress and Reliability in Design* **105**, 253-260.

Connors, H.J. 1970 Fluidelastic vibration of tube arrays excited by cross flow. In *Flow-Induced Vibration in Heat Exchangers* (ed D.D. Reiff), pp. 42-56 New York: ASME.

Connors, H.J. 1978 Fluidelastic vibration of heat exchanger tube arrays. *Journal of Mechanical Design* **100**, 347-353.

Engel, P. A. 1976 *Impact Wear of Materials.* New York: Elsevier Scientific Publishing Company.

Farmer, J.D., Ott, E., & Yorke, J.A. 1983 The dimension of chaotic attractors. *Physica* **7D**, 153-170.

Feigenbaum, M.J. 1978 Quantitative universality for a class of non-linear transformations. *Journal of Statistical Physics* **19**, 25-52.

Frick, T.M., Sobek, T.E., & Reavis, R.J. 1984 Overview on the development and implementation of methodologies to compute vibration wear of steam generator tubes. *ASME Symposium on Flow-Induced Vibration*, Vol.3: Flow-Induced Vibration and Noise in Cylinder Arrays (eds M.P. Paidoussis, S.S. Chen & M.D. Bernstein), pp.149-161.

Fricker, A.J. 1988 Numerical analysis of the fluidelastic vibration of a steam generator tube with loose supports. In *Proceedings ASME International Symposium on Flow-Induced Vibration and Noise*, Vol.5: Flow-Induced Vibration in Heat-Transfer Equipment (eds M.P. Paidoussis, J.M. Chenoweth, S.S. Chen, J.R. Stenner & W.J. Bryan), pp. 105-120. New York: ASME.

Fricker, A.J. 1991 Vibro-impacting behaviour of fluid-elastically unstable heat exchanger tubes with support clearances. In *Proceedings I.Mech.E. International Conference on Flow Induced Vibrations*, Brighton, U.K., pp. 129-137.

Goldsmith, W. 1960 *Impact: The Theory and Physical Behaviour of Colliding Solids.*, London: Edward Arnold Publishers.

Goyder, H.G.D. 1982 Measurements of the natural frequencies and damping of loosely supported tubes in heat exchangers. In *Proceedings Vibration in Nuclear Plants*, 3rd Keswick Conference, England, May 1982, pp. 258-271.

Grassberger, P. & Procaccia, I. 1983 Characterization of strange attractors. *Physics Review Letters* **50**, 346-349.

Guckenheimer, J. & Holmes, P.J. 1983 *Nonlinear Oscillations, Dynamical Systems and Bifurcations of Vector Fields.* New York: Springer Verlag.

Hunt, K. & Crossley, F. 1975 Coefficient of restitution interpreted as damping in vibroimpacting. *Journal of Applied Mechanics* **42**, 440-445.

Jendrzejczyk, J.A. 1986 Dynamic characteristics of heat exchanger tubes vibrating in tube-support plate inactive mode. *ASME Journal of Pressure Vessel Technology* **108**, 256-266.

Kim, B.S., Pettigrew, M.J. & Tromp, J.H. 1988 Vibration damping of heat exchanger tubes in liquids: effects of support parameters. *Journal of Fluids and Structures* **2**, 593-614.

Ko, P.L. 1979 Experimental studies of tube fretting in steam generators and heat exchangers. *ASME Journal of Pressure Vessel Technology* **101**, 125-133.

Lathrop, D.P., & Kostelich, E.J. 1989 Characterization of an Experimental Strange Attractor by Periodic Orbits. *Physical Review A* **40**, 4028-4031.

Lever, J.H. & Weaver, D.S. 1982 A theoretical model for the fluid-elastic instability in heat exchanger tube bundles. *ASME Journal of Pressure Vessel Technology* **104**, 147-158.

Lever, J.H. & Weaver, D.S. 1986a On the stability behaviour of heat exchanger tube bundles. Part 1 – modified theoretical model. *Journal of Sound and Vibration* **107**, 375-392.

Lever, J.H. & Weaver, D.S. 1986b On the stability behaviour of heat exchanger tube bundles. Part 2 – numerical results and comparison with experiments. *Journal of Sound and Vibration* **107**, 393-410.

Mandelbrot, B. 1983 *The Fractal Geometry of Nature.* San Francisco: W.H. Freeman.

Moon, F. 1987 *Chaotic Vibrations, An Introduction for Applied Scientists and Engineers.* John Wiley & Sons, New York.

Packard, N. H., Crutchfield, J. P., Farmer, J.D., & Shaw, R. S. 1980 Geometry from a time series. *Physical Review Letters* **45**, 712-716.

Paidoussis, M.P. 1980 Flow-induced vibrations in nuclear reactors and heat exchangers: practical experiences and state of knowledge. In *Proceedings IAHR/IUTAM Symposium on Practical Experiences with with Flow-Induced Vibrations* (eds E. Naudascher & D. Rockwell), pp. 1-81. Berlin: Springer-Verlag.

Paidoussis, M.P. 1983 A review of flow-induced vibrations in reactors and reactor components. *Nuclear Engineering and Design* **74**, 31-60.

Paidoussis, M.P. & Li, G.X. 1991 Cross-flow-induced chaotic motions of heat-exchanger tubes impacting on loose supports. In *Flow Induced Vibrations and Wear* (eds M.K. Au-Yang & F. Hara), PVP-Vol. 206, pp. 31-41. New York: ASME.

Paidoussis, M.P. & Li, G.X. 1992 Dynamics of cross-flow-induced vibration in heat-exchanger tubes on loose supports. *Journal of Sound and Vibration* **152**, 305-326.

Paidoussis, M.P., Mavriplis, D. & Price, S.J. 1984 A potential flow theory for the dynamics of cylinder arrays in cross-flow. *Journal of Fluid Mechanics* **146**, 227-252.

Paidoussis, M.P., Mavriplis, D. & Price, S.J. 1985 A semi-potential flow theory for the dynamics of cylinder arrays in cross-flow. *ASME Journal of Fluids Engineering* **107**, 500-506.

Paidoussis, M.P., & Price, S.J. 1988 The mechanisms underlying flow-induced instabilities of cylinder arrays in cross-flow. *Journal of Fluid Mechanics* **187**, 45-59.

Pettigrew, M.J., Sylvestre, Y. & Campagne, A.O. 1978 Vibration analysis of heat exchanger and steam generator designs. *Nuclear Engineering and Design* **48**, 97-115.

Pettigrew, M.J. & Taylor, C. 1991 Fluid-elastic instability of heat-exchanger tube bundles: review and design recommendations. In *Proceedings of I.Mech.E. International Conference on Flow Induced Vibration*, pp. 349-368. London: I.Mech.E.

Pikovsky, A.S., & Rabinovitch, M.I. 1981 Stochastic oscillations in dissipative systems. *Physica D* **2**, 8-24.

Pomeau, Y. & Manneville, P. 1980 Intermittent transition to turbulence in dissipative dynamical systems. *Communications in Mathematical Physics* **74**, 189-197.

Pomeau, Y., Roux, J.C., Rossi, A., Bachelart, S. & Vidal, C. 1981 Intermittent behaviour in the Belousov-Zhabotinsky reaction. *Journal de Physique-Lettres* **42** L-271.

Price, S.J. & Paidoussis, M.P. 1982 A theoretical investigation of the parameters affecting fluidelastic instability of a double row of cylinders subject to cross-flow. *Proceedings 3rd International Conference on Vibrations in Nuclear Plant*, Keswick. U.K., pp. 107-119.

Price, S.J. & Paidoussis, M.P. 1983 Fluidelastic instability of a double row of cylinders subject to cross-flow. *ASME Journal of Vibration, Acoustics, Stress and Reliability in Design* **105**, 59-66.

Price, S.J. & Paidoussis, M.P. 1984 An improved mathematical model for the stability of cylinder rows subject to cross-flow. *Journal of Sound and Vibration* **97**, 615-640.

Price, S.J. & Paidoussis, M.P. 1985 Fluidelastic instability of a full array of flexible cylinders subject to cross-flow. In *Proceedings ASME Symposium on Fluid*

Structure Interaction and Aerodynamic Damping (eds E.H. Dowell & M.K. Au-Yang), pp. 171-192. New York: ASME.

Price, S.J. & Paidoussis, M.P. 1986a A constrained-mode analysis of the fluidelastic instability of a double row of circular cylinders subject to cross-flow: a theoretical investigation of system parameters. *Journal of Sound and Vibration* **105**, 121-142.

Price, S.J. & Paidoussis, M.P. 1986b A single-flexible-cylinder analysis for the fluidelastic instability of an array of flexible cylinders in cross-flow. *ASME Journal of Fluids Engineering* **108**, 193-199.

Price, S.J. & Valerio, N.R. 1990 A non-linear investigation of single-degree-of-freedom instability in cylinder arrays subject to cross-flow. *Journal of Sound and Vibration* **137**, 419-432.

Roberts, B.W. 1962 Low frequency, self-excited vibration in a row of circular cylinders mounted in an airstream. *Ph.D. Thesis*, University of Cambridge.

Roberts, B.W. 1966 Low frequency, aeroelastic vibrations in a cascade of circular cylinders. *I.Mech.E. Mechanical Engineering Science Monograph No. 4.*

Rogers, R.J. & Ahn, K.J. 1986 Fluid damping and hydrodynamic mass in finite length cylindrical squeeze films with rectilinear motion. In *Flow-Induced Vibration* (eds S.S. Chen, J.C. Simonis & Y.S. Shin) PVP-Vol.104, 99-105. ASME: New York.

Ruelle, D. & Takens, F. 1971 On the nature of turbulence. *Communications in Mathematical Physics* **20**, 167-192 and **23**, 342-344.

Simpson, A. & Flower, J.W. 1977 An improved mathematical model for the aerodynamic forces on tandem cylinders with aeroelastic applications. *Journal of Sound and Vibration* **51**, 183-217.

Smale, S. 1963 Diffeomorphisms with many periodic points. In *Differential and Combinatorial Topology* (ed. S.S. Cairns), pp. 63-80. Princeton: Princeton University Press.

Smale, S. 1967 Differentiable dynamical systems. *Bulletin of the American Mathematical Society* **73**, 747-817.

Sreenivasan, K.R. & Ramshankar, R. 1986 Transition to intermittency in open channel flows, and intermittency routes to chaos. *Physica* **23D**, 246-258.

Tanaka, H., & Takahara, S. 1981 Fluid elastic vibration of tube array in cross flow. *Journal of Sound and Vibration* 77, 19-37.

Takens, F. 1980 Detecting Strange Attractors in Turbulence. *Springer Lecture Notes in Mathematics* (eds D.A. Rand, L.S. Young) 898, 366-381. New York: Springer-Verlag.

Thompson, J.M.T. 1986 *Nonlinear Dynamics and Chaos: Geometrical Methods for Engineers and Scientists.* John Wiley & Sons, U.K.

Weaver, D.S. & Fitzpatrick, J.A. 1988 A review of flow induced vibrations in heat exchangers. *Journal of Fluids and Structures* 2, 73-93.

Wiggins, S. 1990 *Introduction to Applied Non-Linear Dynamical Systems and Chaos.* New York: Springer Verlag.

Wolf, A., Swift, J.B., Swinney, H.L. & Vastano, J.A. 1985 Determining Lyapunov exponents from time series. *Physica* **16D**, 285-317.

Yetisir, M. & Weaver, D.S. 1988 On an unsteady theory for fluidelastic instability of heat exchanger tube arrays. In *Symposium on FLow-Induced Vibration and Noise*, Volume 3: FLow-Induced Vibration and Noise in Cylinder Arrays (eds M.P. Paidoussis, S.S. Chen & M.D. Bernstein), pp.181-195. ASME: New York.

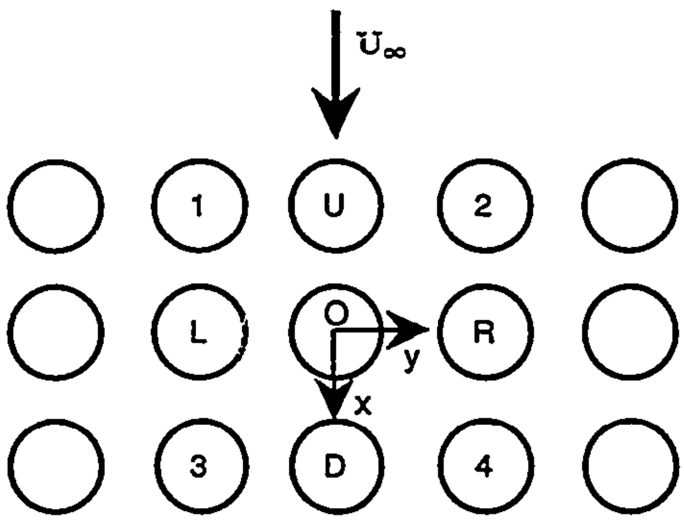

Figure 1.1: The inline array geometry studied by Tanaka & Takahara (1981).

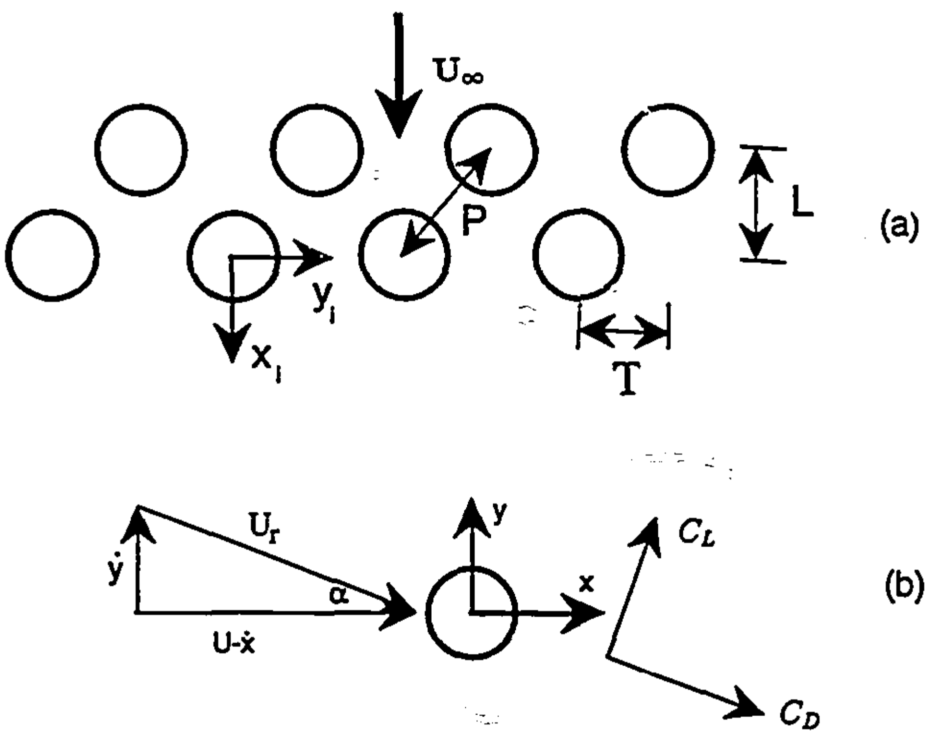

Figure 1.2: (a) The double-row array, modelled by Price & Paidoussis (1982,1983); (b) the relative-velocity vector diagram.

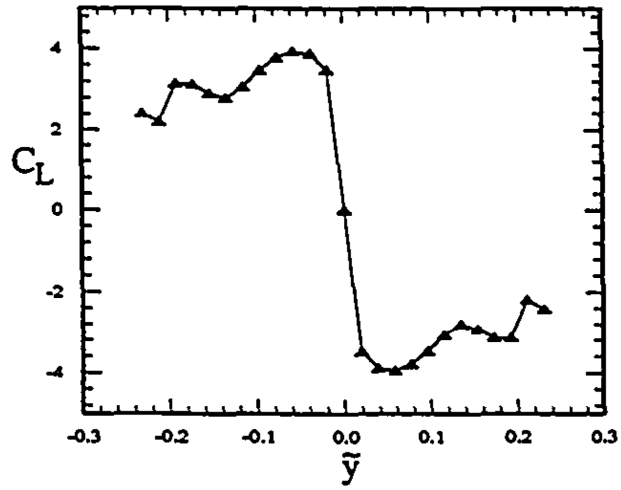

Figure 1.3: Lift coefficient variation in row 3 of a rotated-triangular array, for $\tilde{x} = 0$.

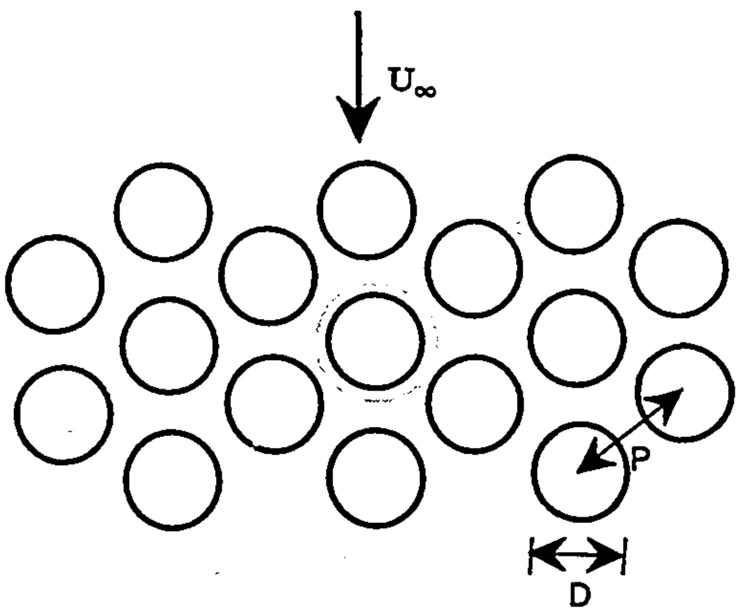

Figure 1.4: The rotated triangular array geometry.

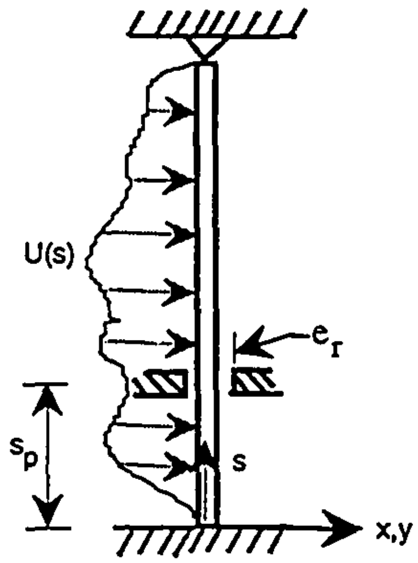

Figure 2.1: 2-span loosely supported tube subjected to non-uniform flow, $U(s)$; e_r is the tube/support clearance.

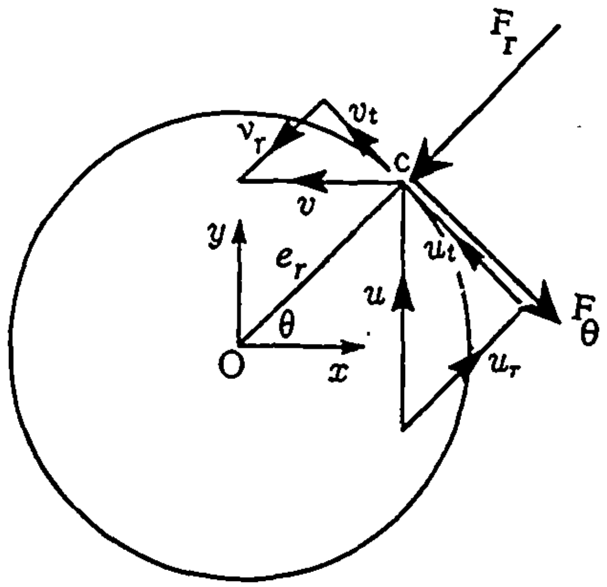

Figure 2.2: Impact circle geometry showing tube velocities and support reaction forces.

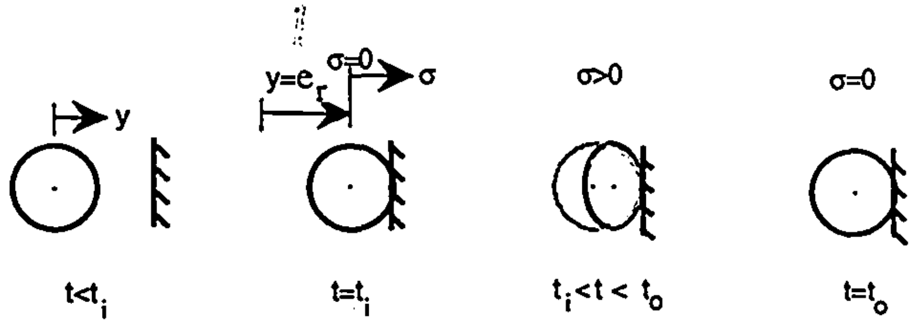

Figure 2.3: Typical impact process; the approach σ, is the displacement of the moving-body centre of mass.

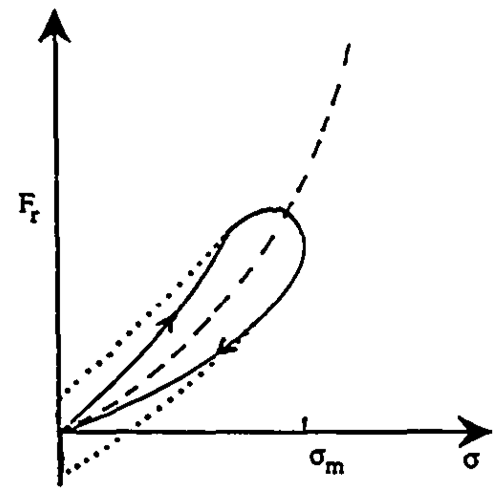

Figure 2.4: Variation of the total radial cylinder/support interaction force, F_r $(= F_{ri} + F_{rd})$, for non-constant support damping ($c_s = c_s(\sigma)$); the dotted line depicts the case $c_s = const.$

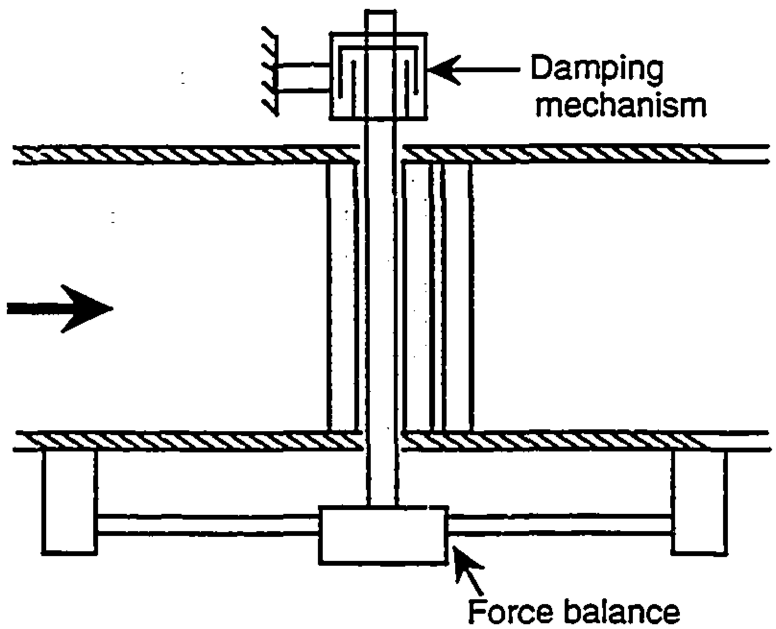

Figure 3.1: Test cylinder located within wind-tunnel test section; the force balance mounting and oil damper are shown.

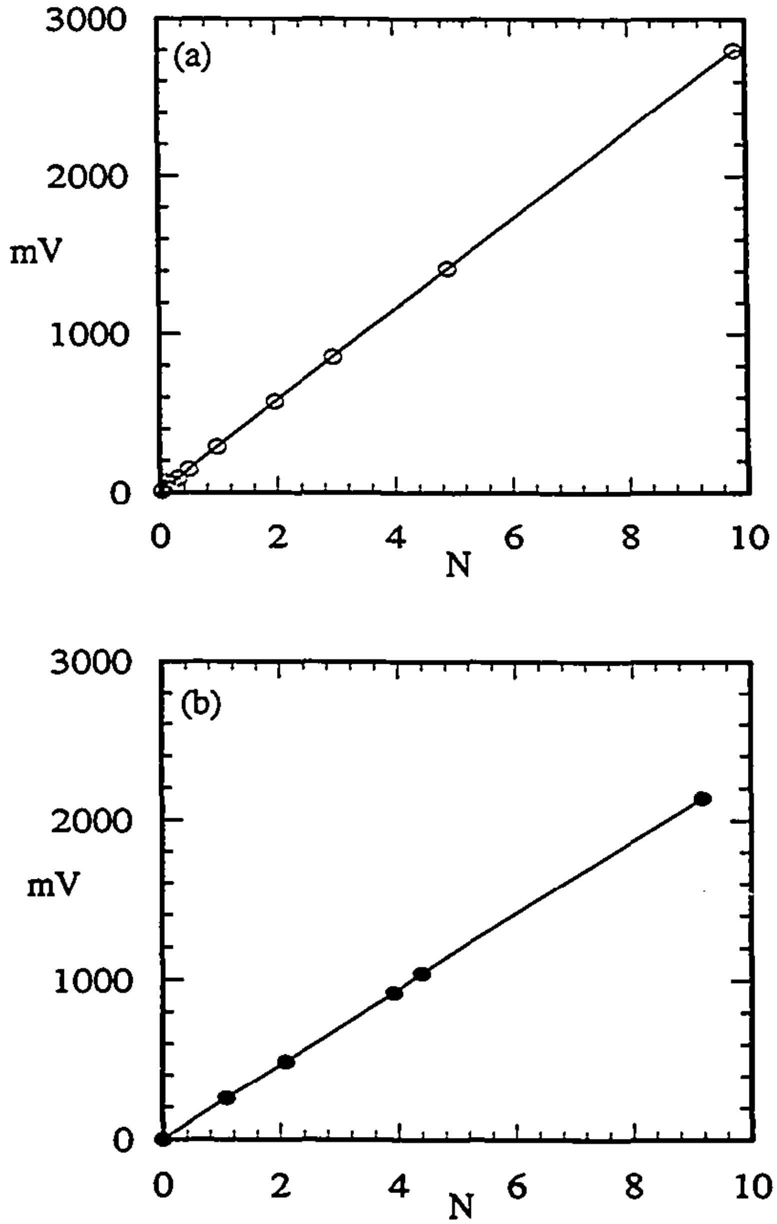

Figure 3.2: Force balance calibration curves relating output voltage to static force for (a) the in-flow and (b) cross-flow directions.

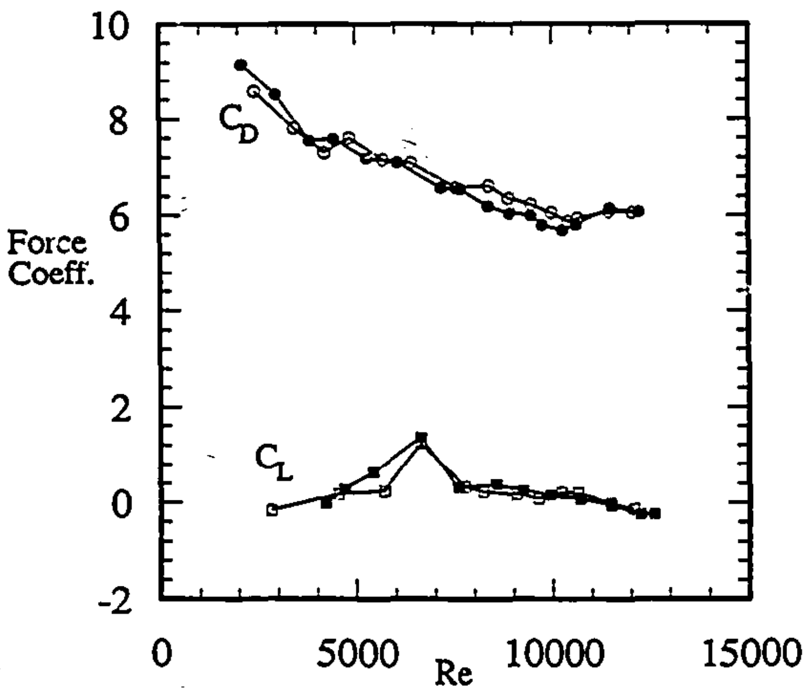

Figure 3.3: Variation of C_D with Reynolds number, Re, for the cylinder position $\tilde{x} = \tilde{y} = 0$. C_L, which should be zero for this position, is also shown; the open and filled data points, corresponding to two different tests, indicating repeatability of the measurements.

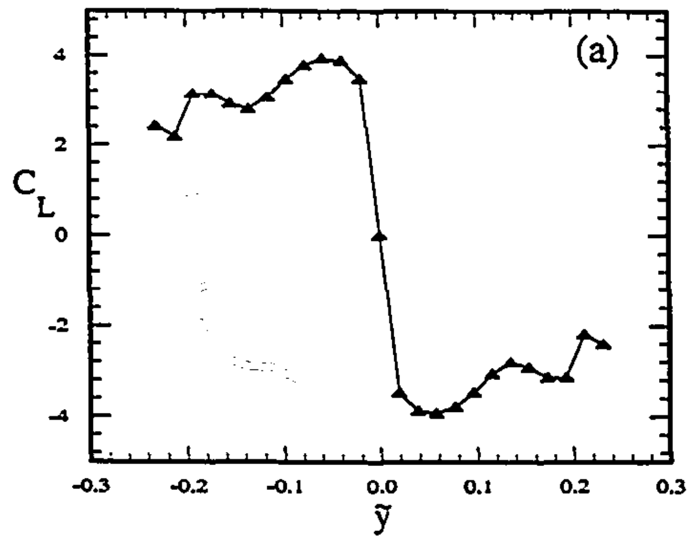

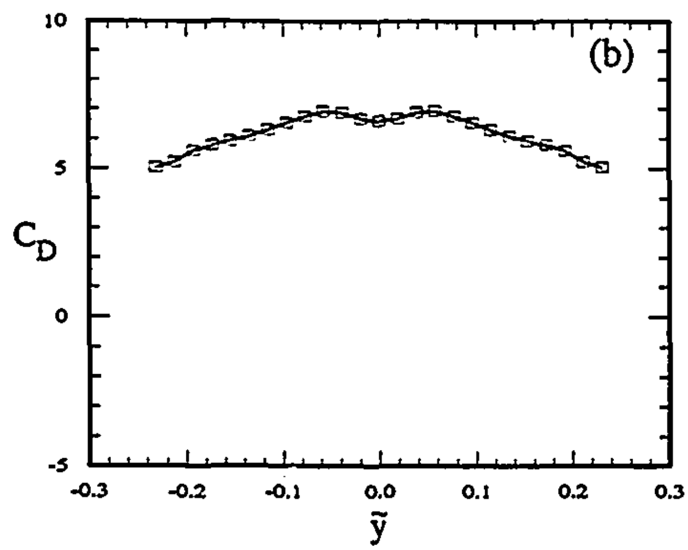

Figure 3.4: Force coefficient variation with cylinder cross-flow displacement for $\tilde{x} = 0$: (a) C_L; (b) C_D; for $Re = 1.04 \times 10^4$.

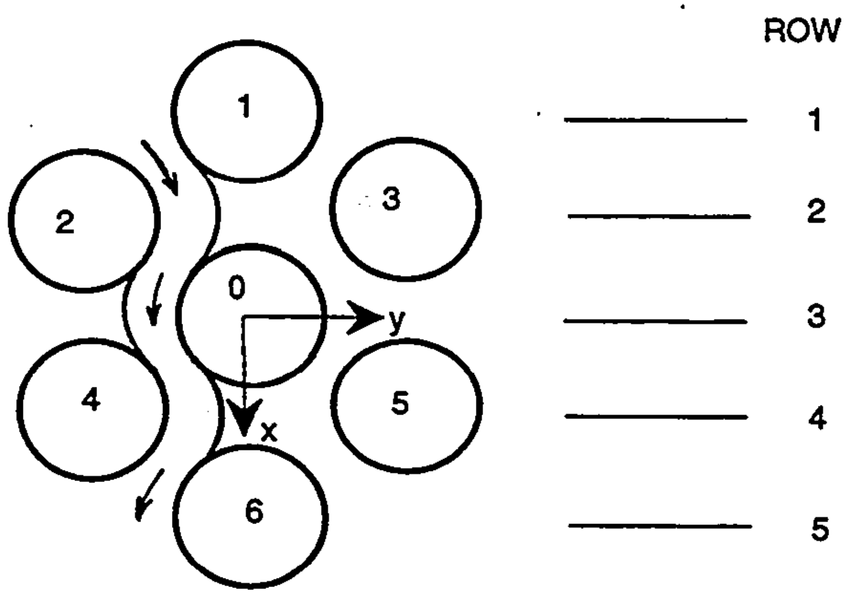

Figure 3.5: 7 cylinder kernel at the test location.

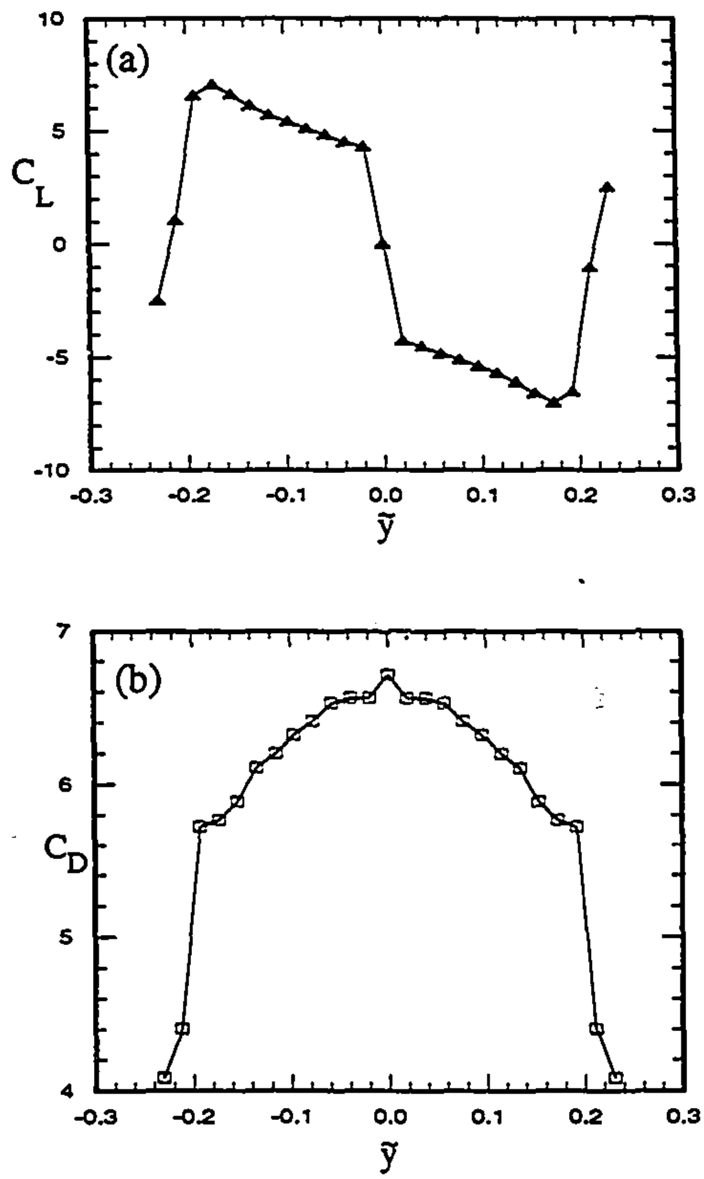

Figure 3.6: Variation of (a) C_L and (b) C_D with $\tilde{y}$, for the in-flow cylinder position $\tilde{x} = -0.173$.

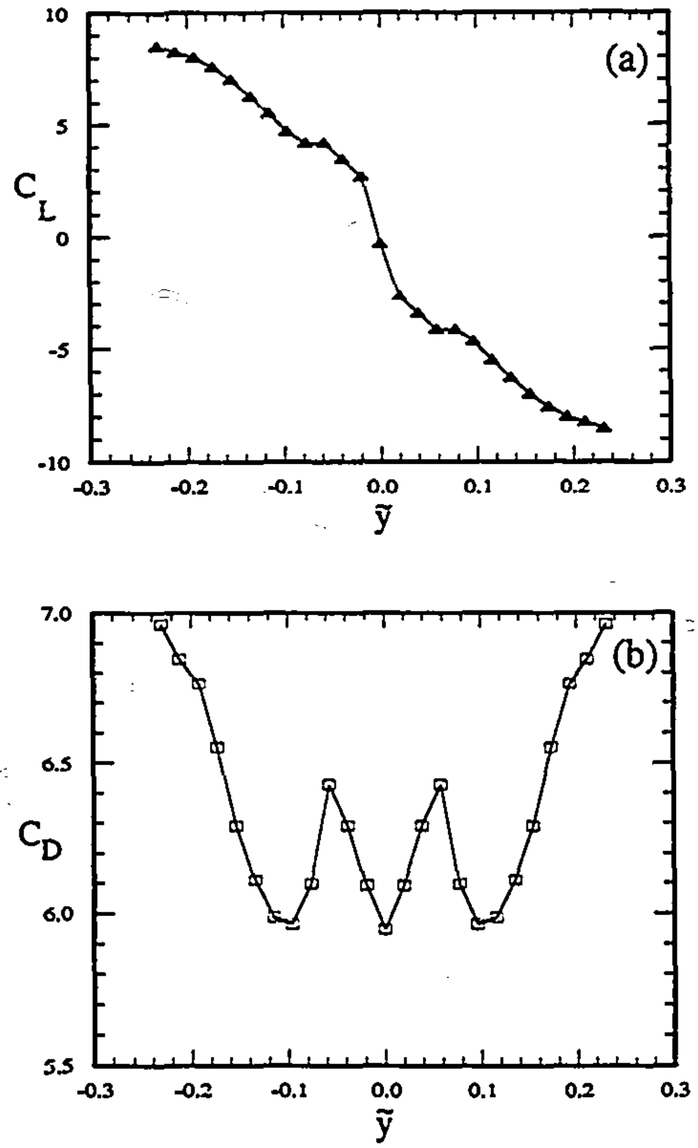

Figure 3.7: Variation of (a) C_L and (b) C_D with $\tilde{y}$, for the in-flow cylinder position $\tilde{x} = +0.173$; for $Re = 1.04 \times 10^4$.

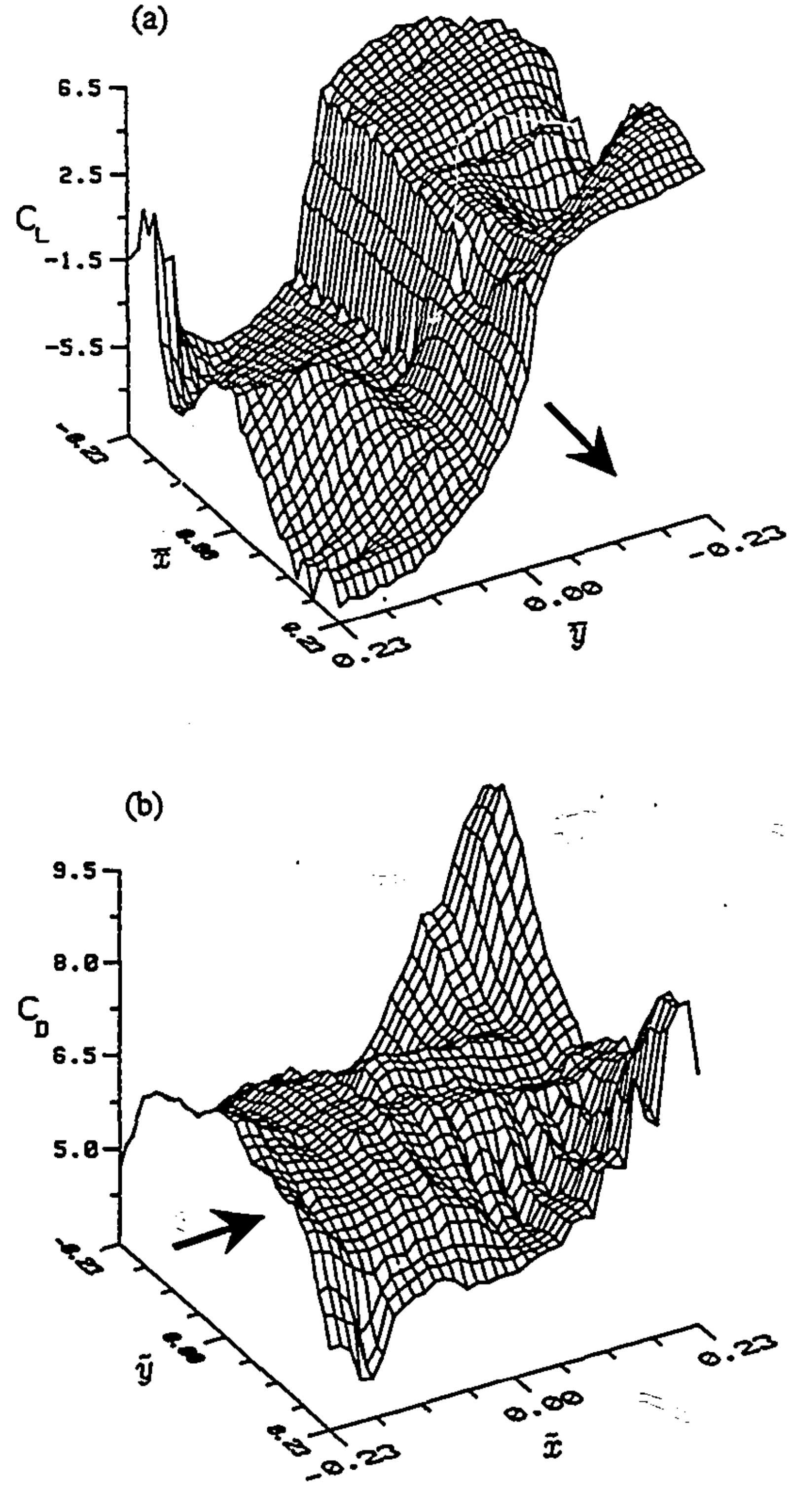

Figure 3.8: 3-D representation of the measured force coefficients: (a) lift coefficient, C_L; (b) drag coefficient, C_D; for a cylinder in the third row of the array, and $\mathrm{Re} = 1.04 \times 10^4$.

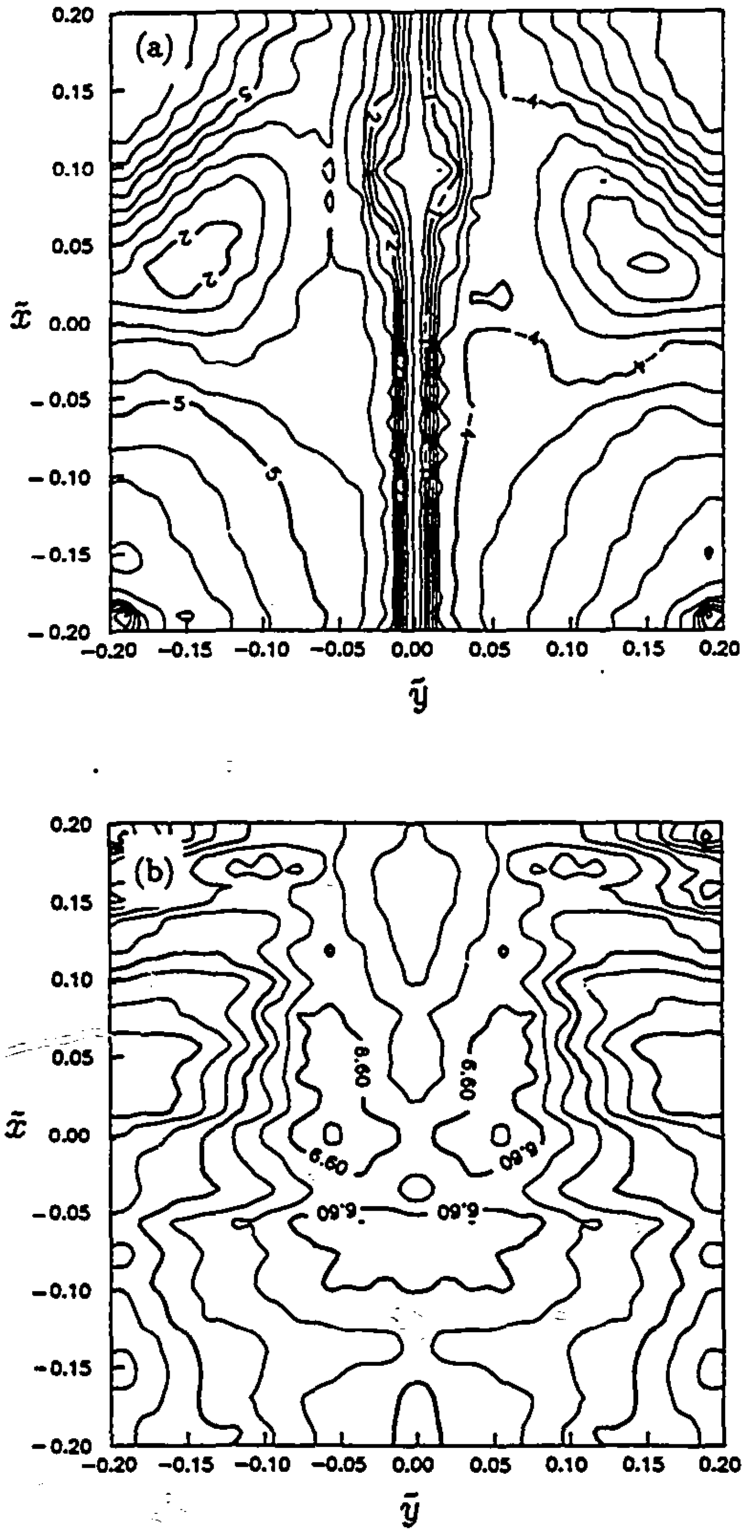

Figure 3.9: Contour plots of (a) C_L and (b) C_D; corresponding to the 3-D plots Fig.3.8.

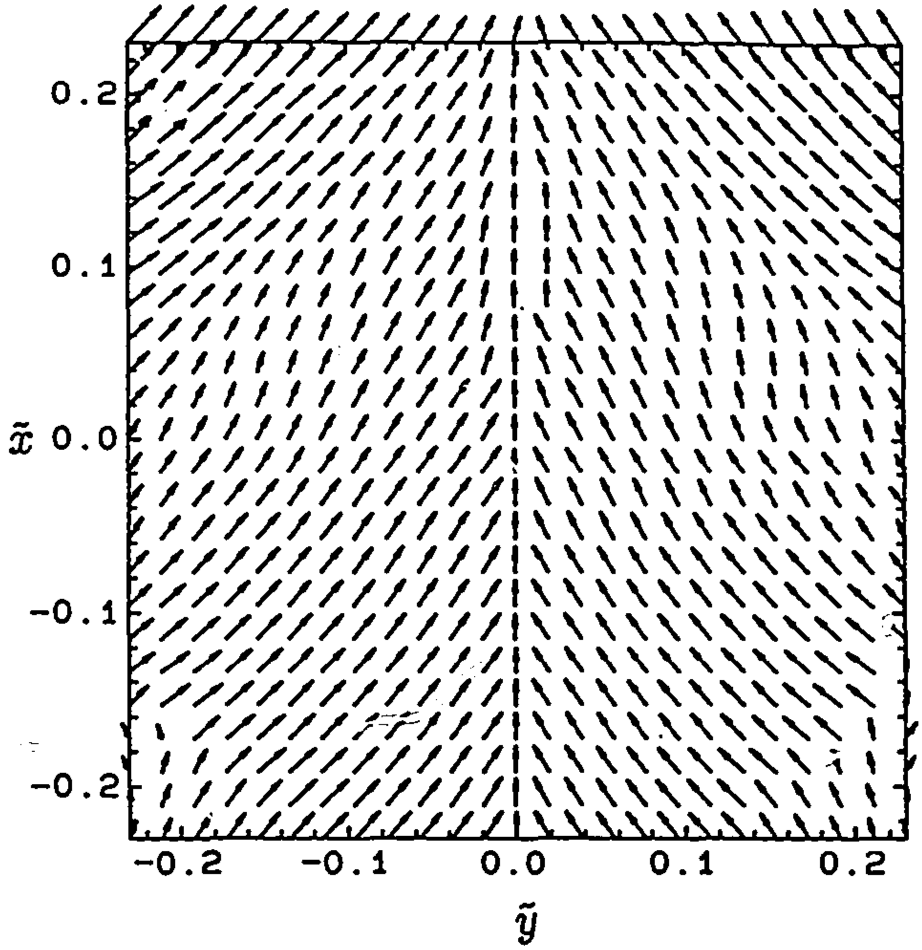

Figure 3.10: Fluid-force vector field obtained from the convolution of the lift- and drag-direction force components.

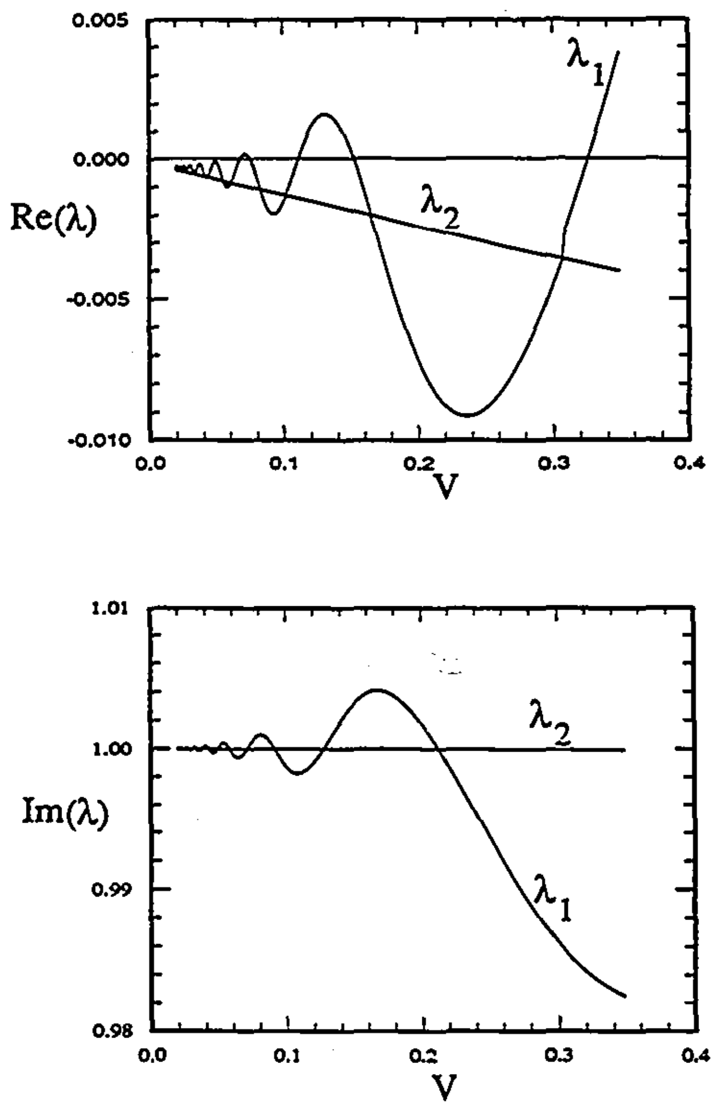

Figure 4.1: Variation of (a) real parts, $Re(\lambda)$, and (b) imaginary parts, $Im(\lambda)$, of the system eigenvalues with V for $\tilde{m} = 100$, $\delta = 0.001$, at the cylinder position $\tilde{x} = \tilde{y} = 0$.

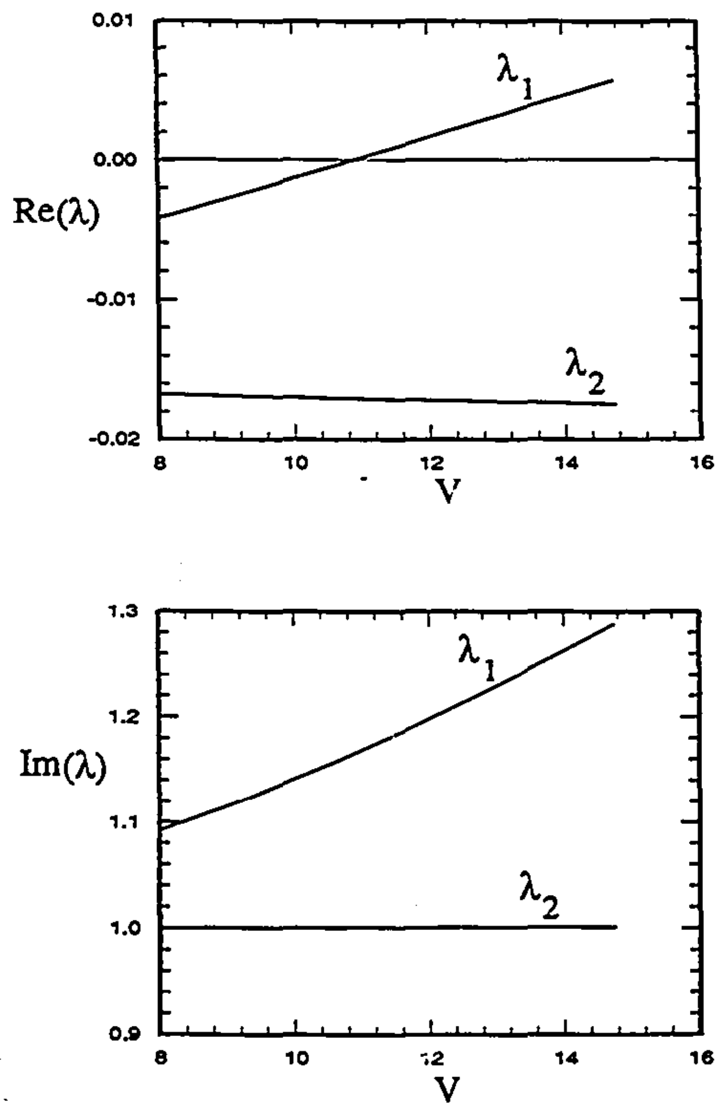

Figure 4.2: Variation of (a) real parts, $Re(\lambda)$, and (b) imaginary parts, $Im(\lambda)$, of the system eigenvalues with V for $\tilde{m} = 10,000$, $\delta = 0.1$, at the cylinder position $\tilde{x} = \tilde{y} = 0$.

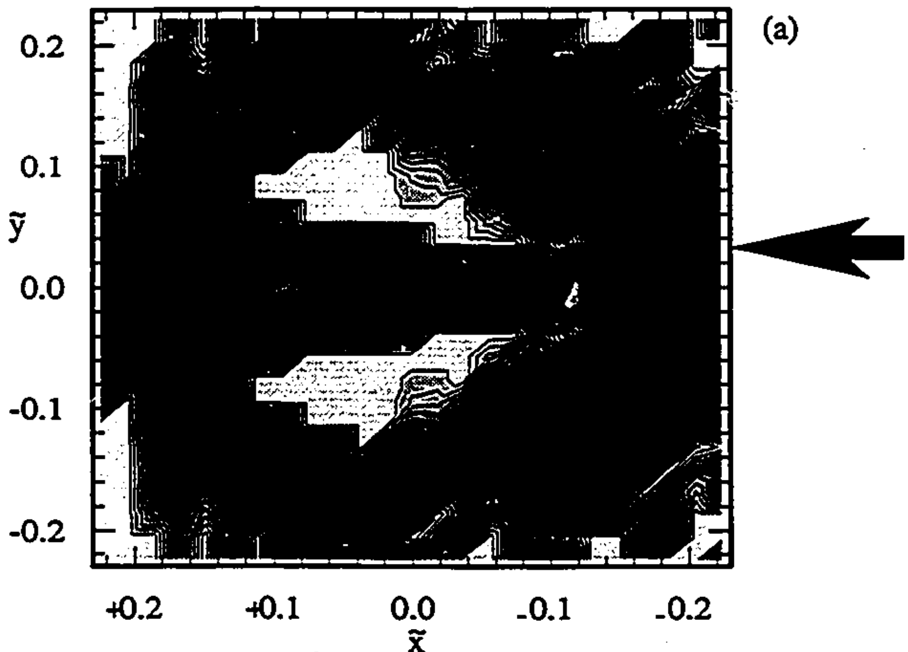

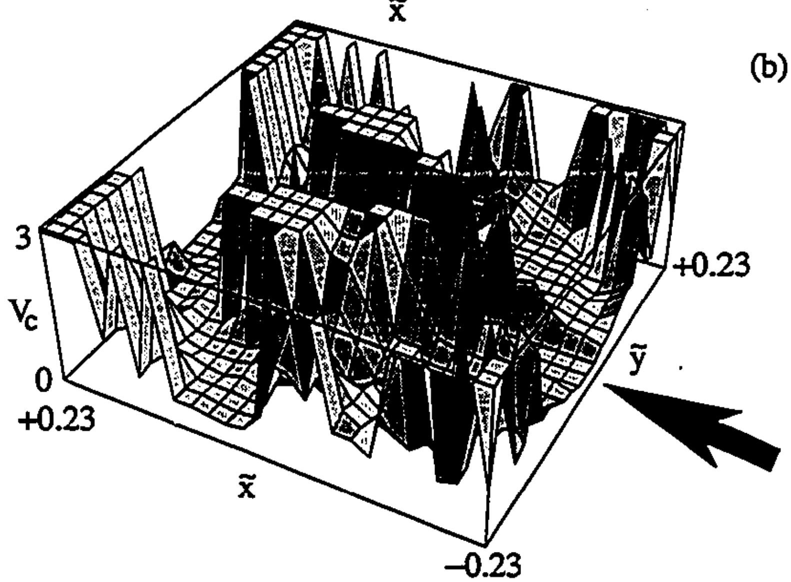

Figure 4.3: (a) Contour, and (b) 3-D plot of the critical velocity, V_c, as a function of cylinder position $(\tilde{x}, \tilde{y})$, for $\tilde{m} = 100$, $\delta = 0.01$.

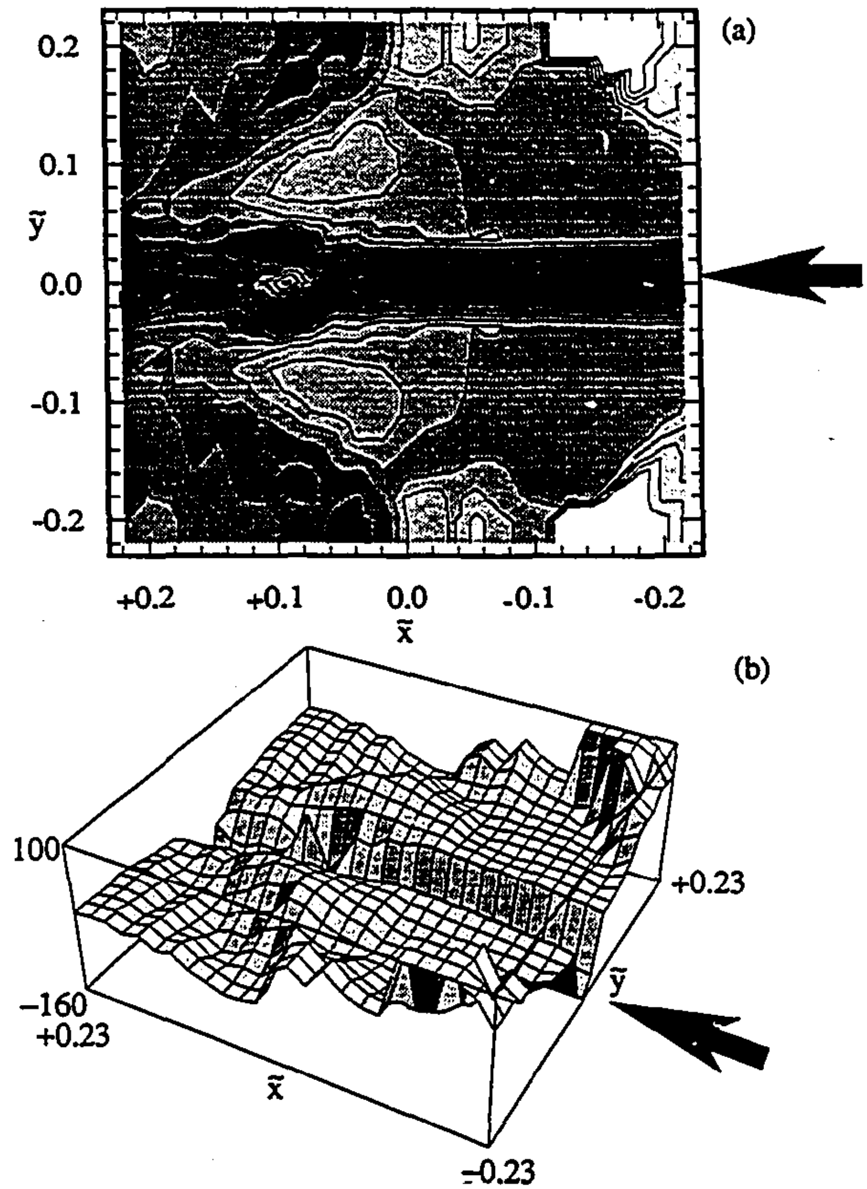

Figure 4.4: (a) Contour, and (b) 3-D plot of the partial derivative $\partial C_L/\partial \tilde{y}$.

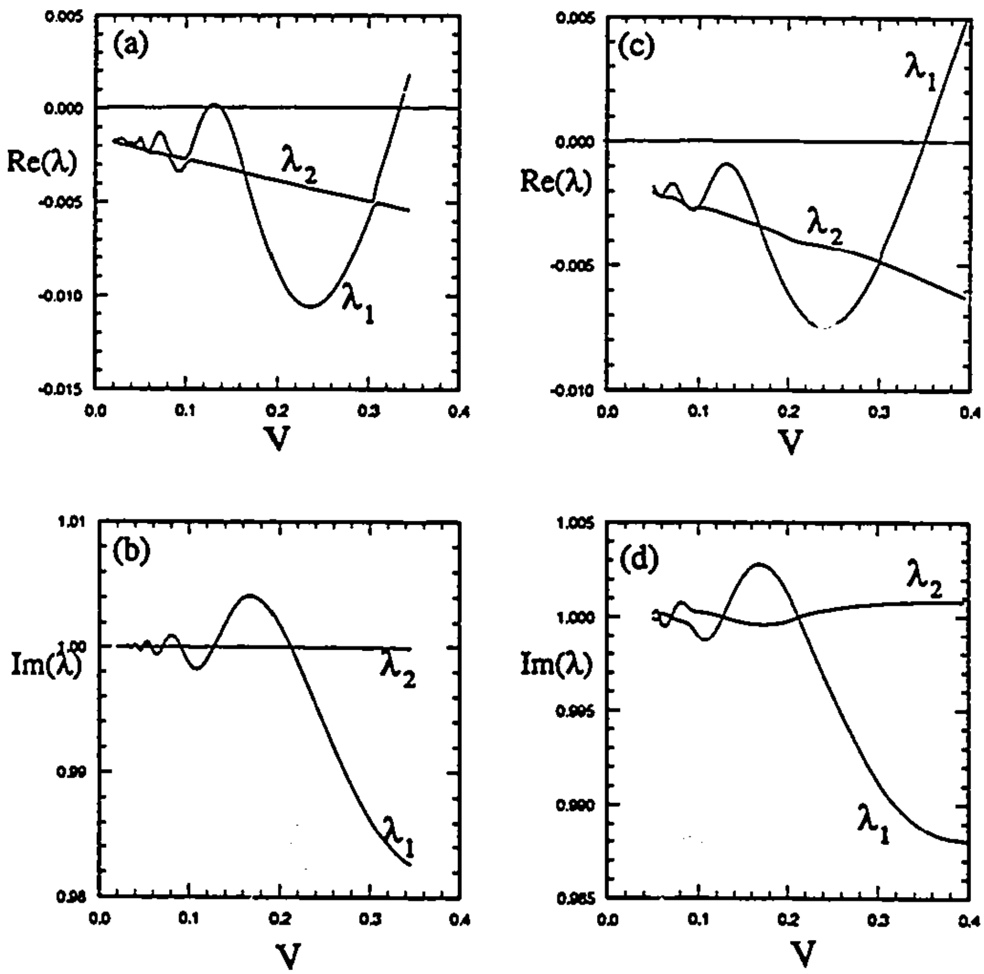

Figure 4.5: Variation of eigenvalues with flow velocity, V, for: (a,b) $\tilde{x} = \tilde{y} = 0$; and (c,d) $\tilde{x} = 0$, $\tilde{y} = 0.02$ — (labelled A in Fig.4.3(a)). Cylinder parameters are $\bar{m} = 100$, $\delta = 0.01$.

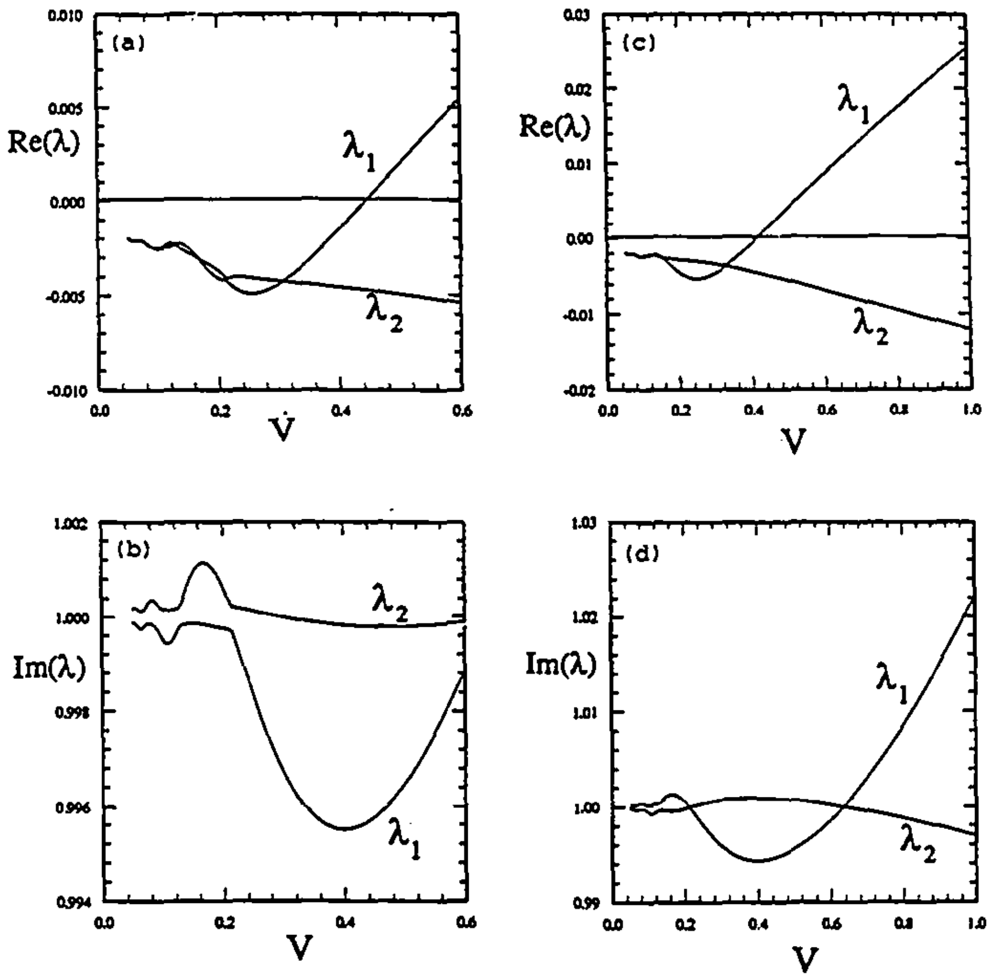

Figure 4.6: Variation of eigenvalues with flow velocity, V, for: (a,b) $\tilde{x} = 0.16, \tilde{y} = 0.02$; and (c,d) $\tilde{x} = 0.06, \tilde{y} = 0.19$ — (labelled B and C, respectively, in Fig.4.3(a)). Cylinder parameters are $\tilde{m} = 100, \delta = 0.01$.

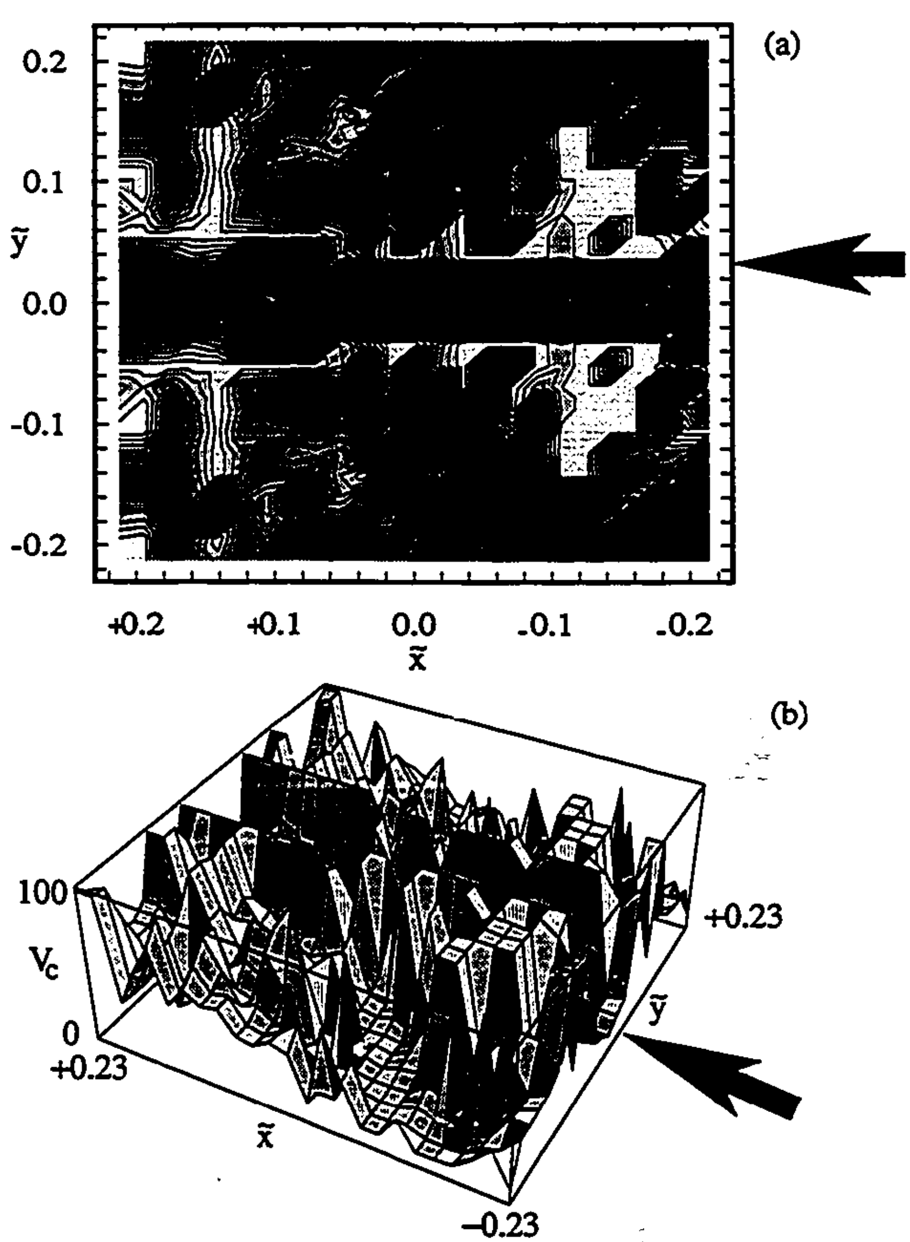

Figure 4.7: (a) Contour, and (b) 3-D plot of the critical velocity, V_c, as a function of cylinder position $(\tilde{x}, \tilde{y})$, for $\tilde{m} = 10,000$, $\delta = 0.1$.

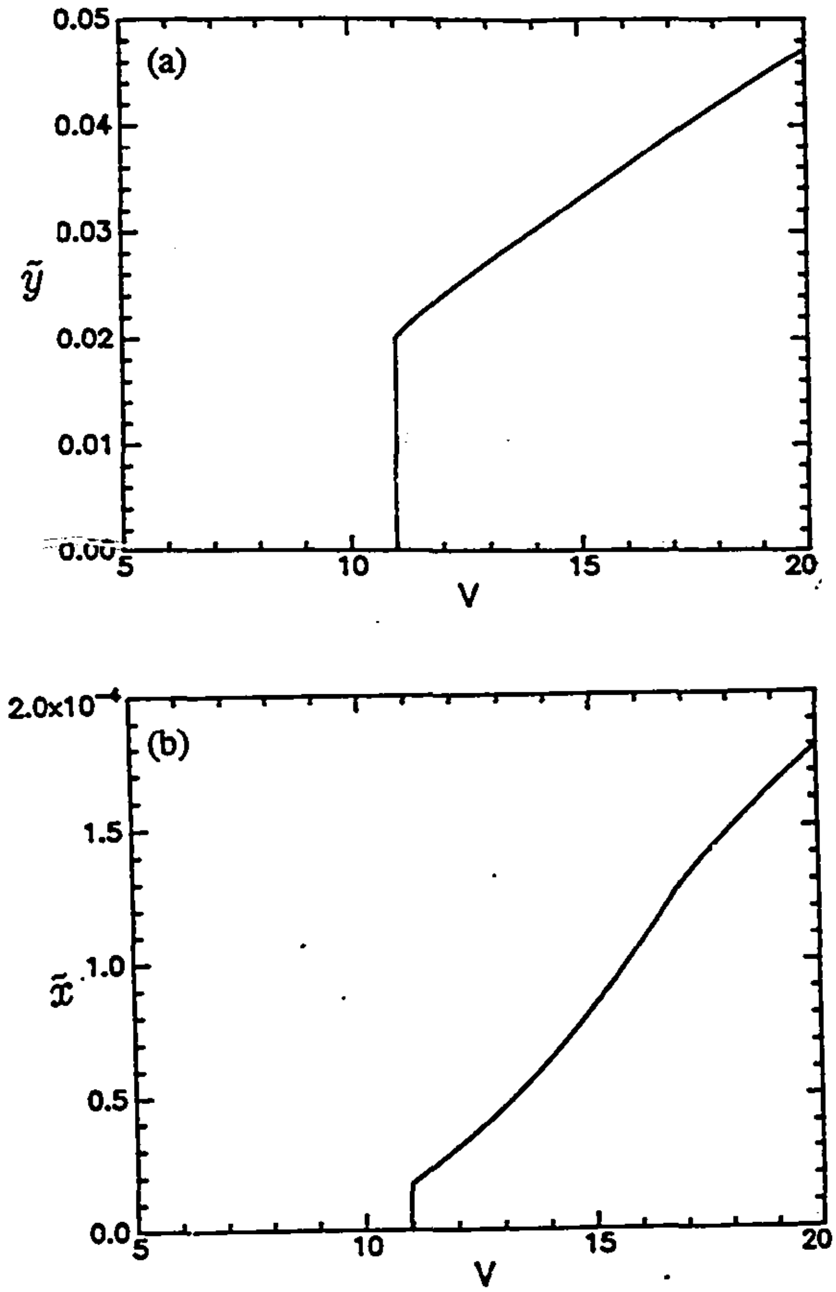

Figure 4.8: Post-instability limit cycle amplitude growth for $\bar{m} = 10,000, \delta = 0.1$; (a) for cross-flow vibration; (b) for in-flow vibration.

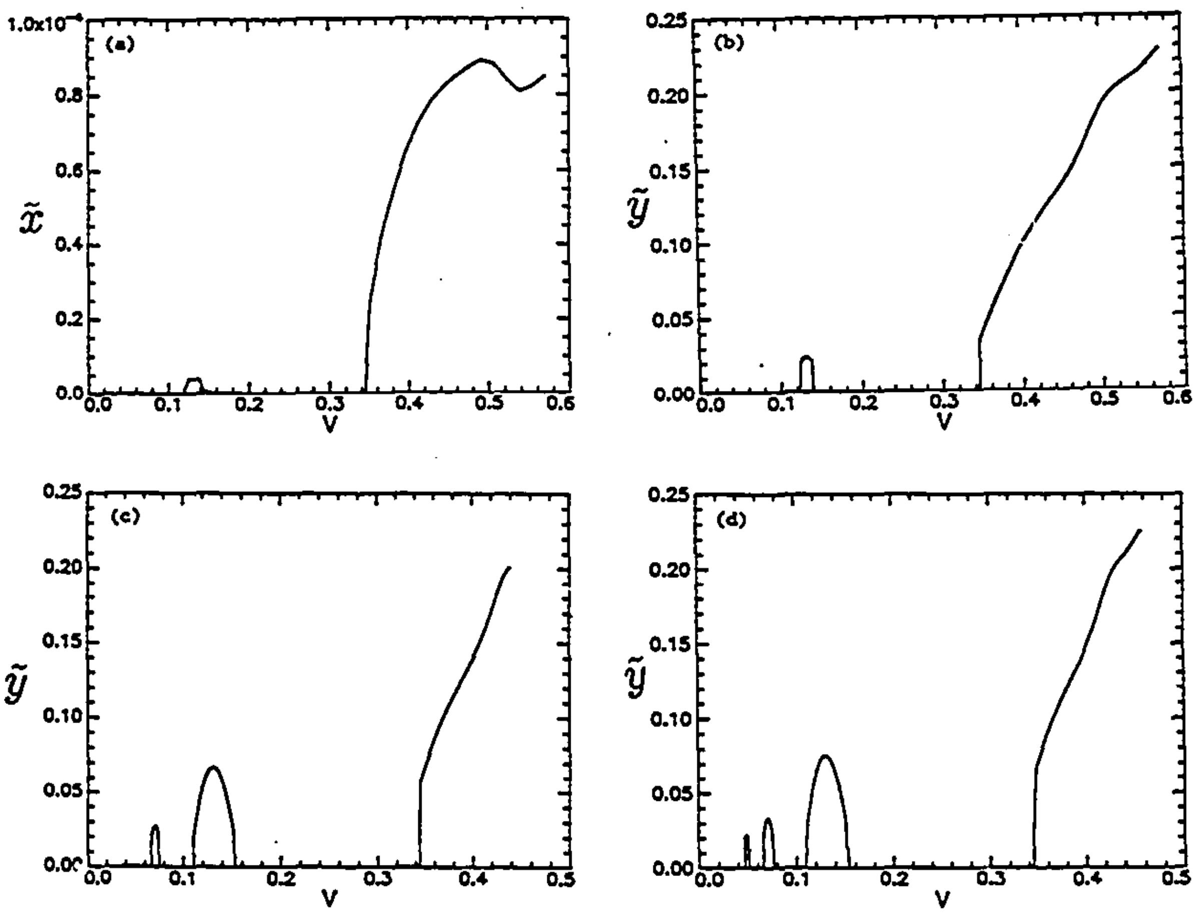

Figure 4.9: Limit-cycle amplitude growth for: (a) $\tilde{m}\delta = 1.0$, in-flow; (b) $\tilde{m}\delta = 1.0$, cross-flow; (c) $\tilde{m}\delta = 0.1$, cross-flow; (d) $\tilde{m}\delta = 0.01$, cross-flow.

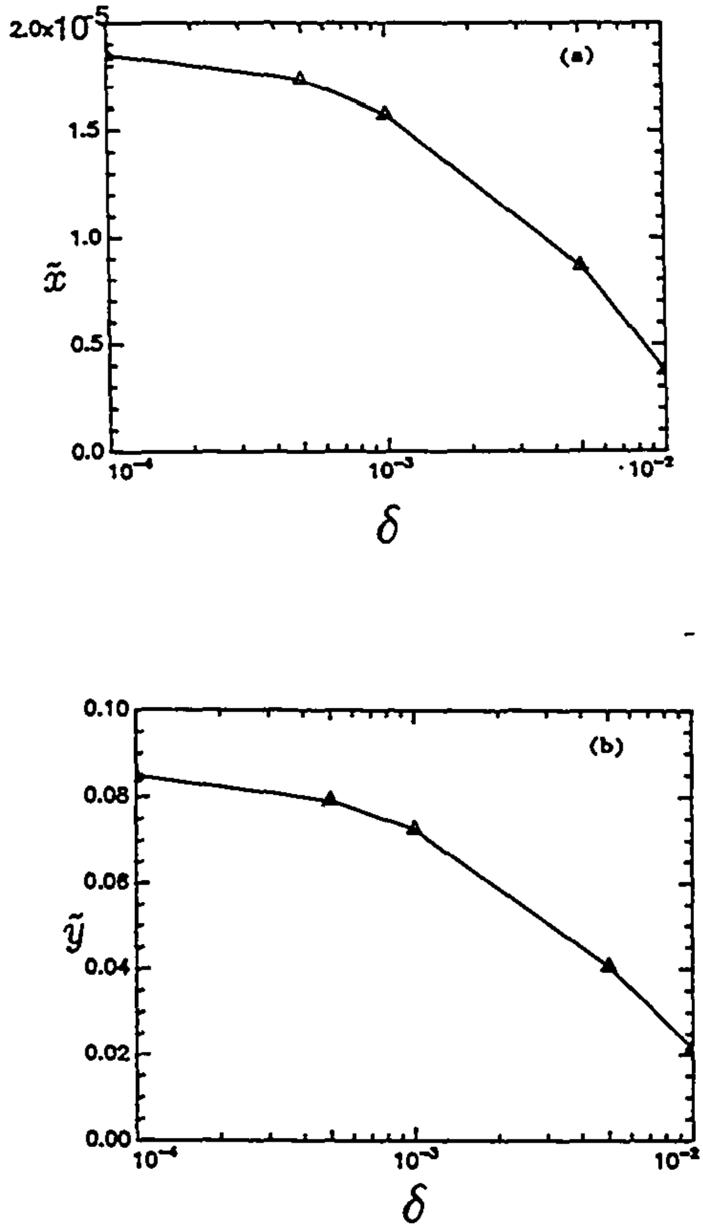

Figure 4.10: The effect of varying δ at a constant velocity $V = 0.13$ and $\tilde{m} = 100$ on limit cycle amplitude: (a) in-flow component; (b) cross-flow component.

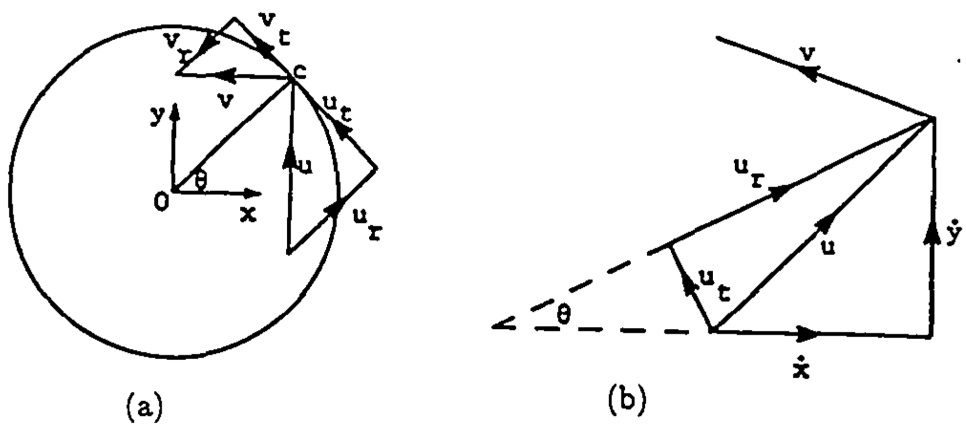

Figure 4.11: (a) Impact circle geometry; (b) velocity vector diagram for coordinate transformation.

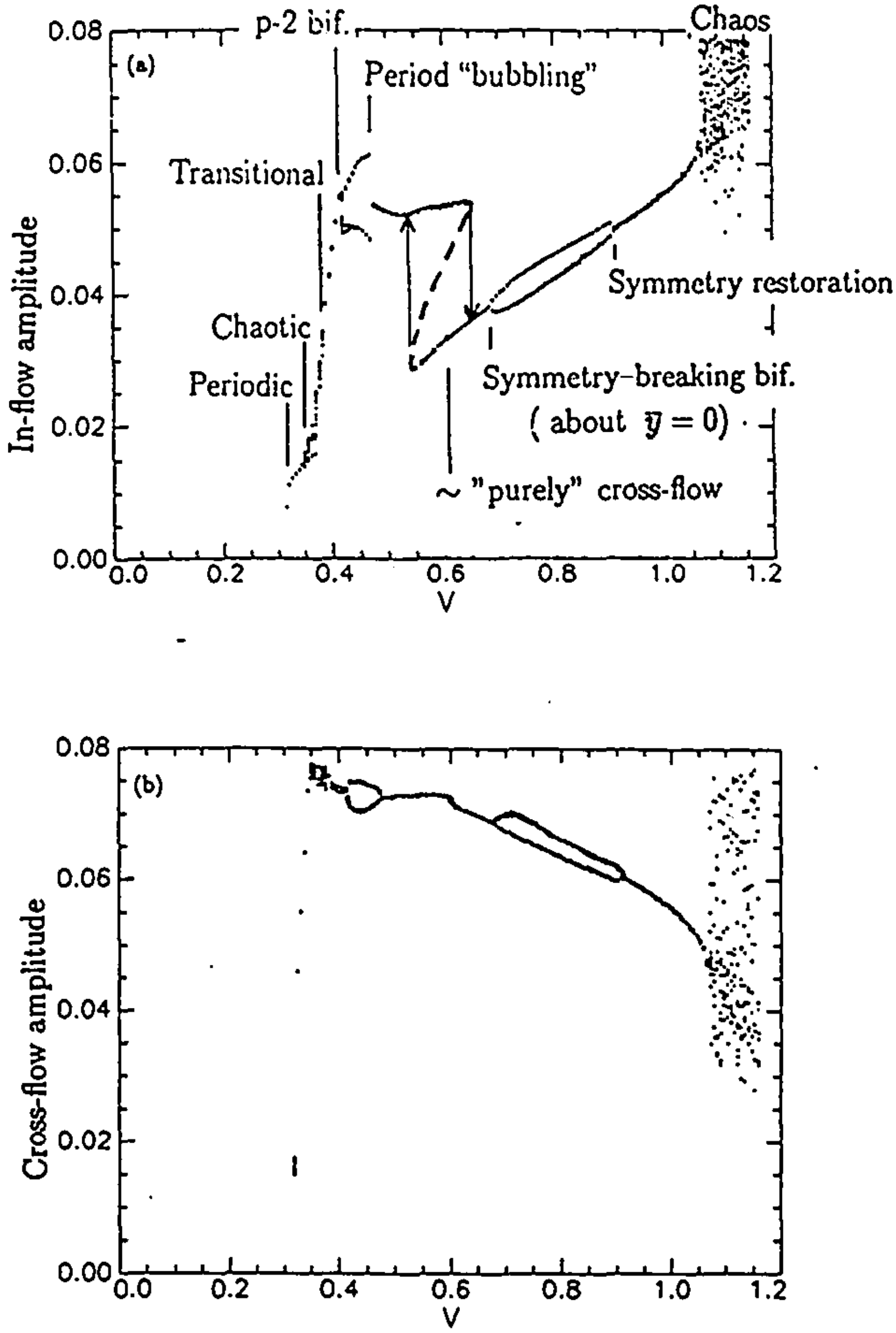

Figure 4.12: Bifurcation diagram based on V: (a) in-flow peak amplitude; (b) cross-flow peak amplitude; $\tilde{m} = 10, \delta = 0.05, \tilde{e}_r = 0.08$.

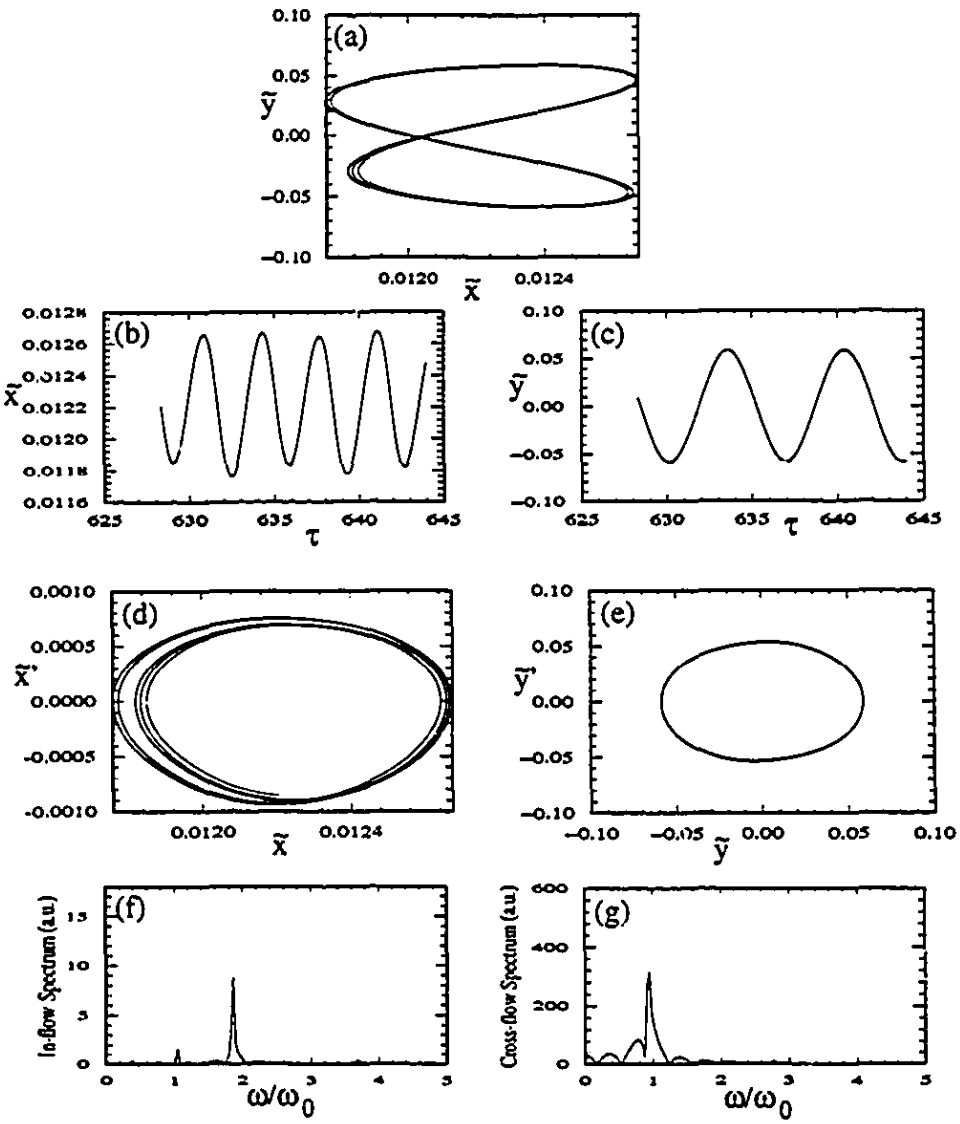

Figure 4.13: Cylinder response at $V = 0.34$: (a) orbital $(\tilde{x}, \tilde{y})$ motion; (b,c) in-flow and cross-flow time traces; (d,e) in-flow and cross-flow phase plane plots; (f,g) corresponding response spectra.

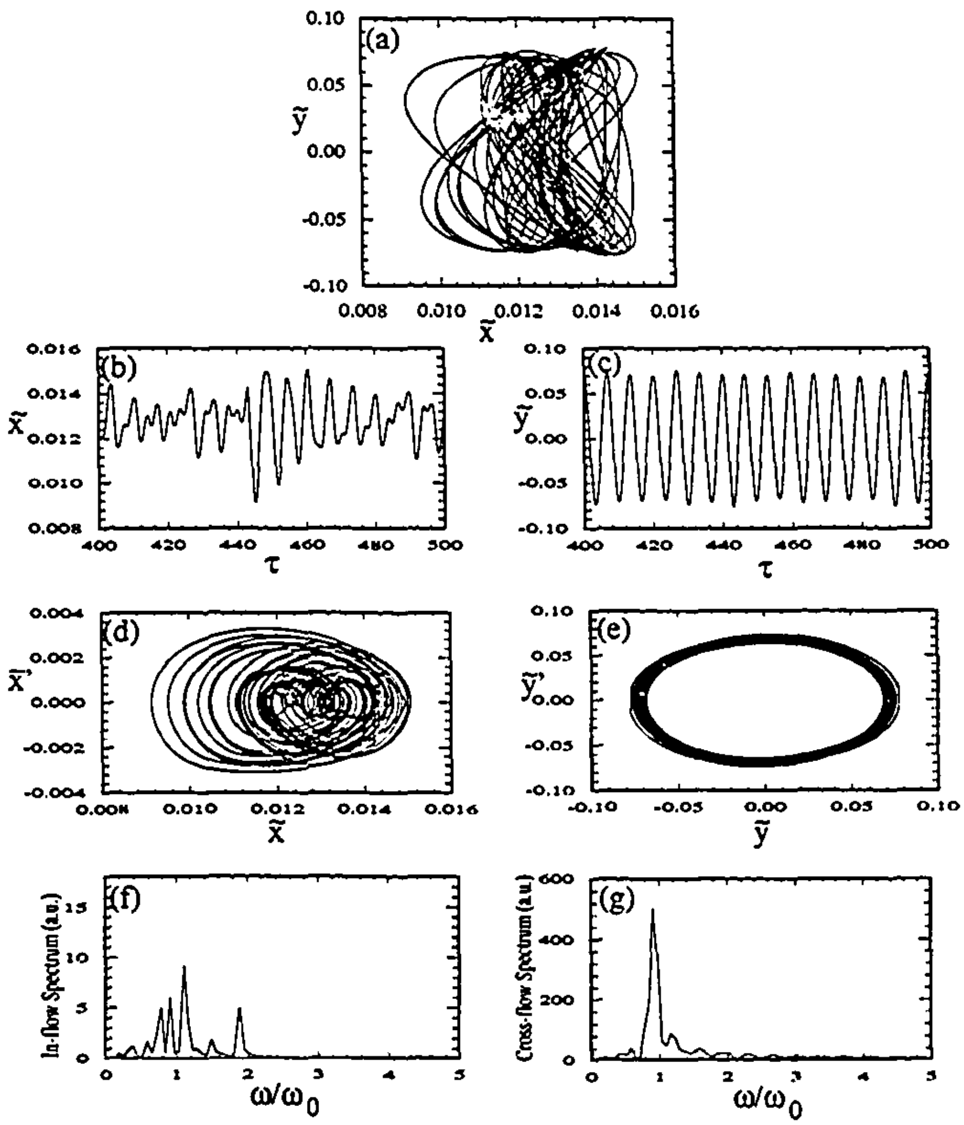

Figure 4.14: Cylinder response at $V = 0.36$: (a) orbital $(\tilde{x}, \tilde{y})$ motion; (b,c) in-flow and cross-flow time traces; (d,e) in-flow and cross-flow phase plane plots; (f,g) corresponding response spectra.

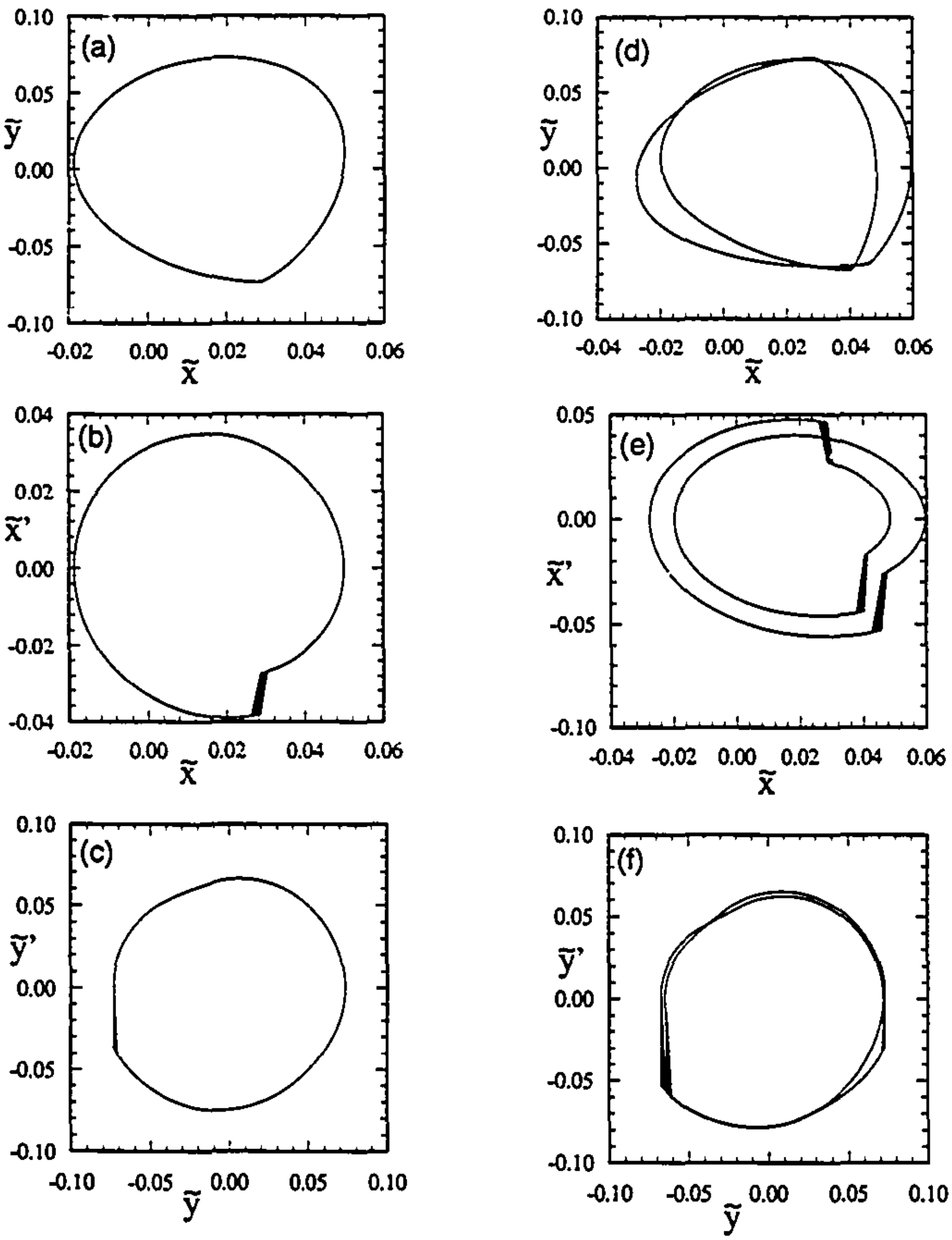

Figure 4.15: Cylinder response for (a-c) $V = 0.40$, (d-f) $V = 0.45$: (a,d) motion in the $(\tilde{x}, \tilde{y})$ plane; (b,e) in-flow phase plots; (c,f) cross-flow phase plots.

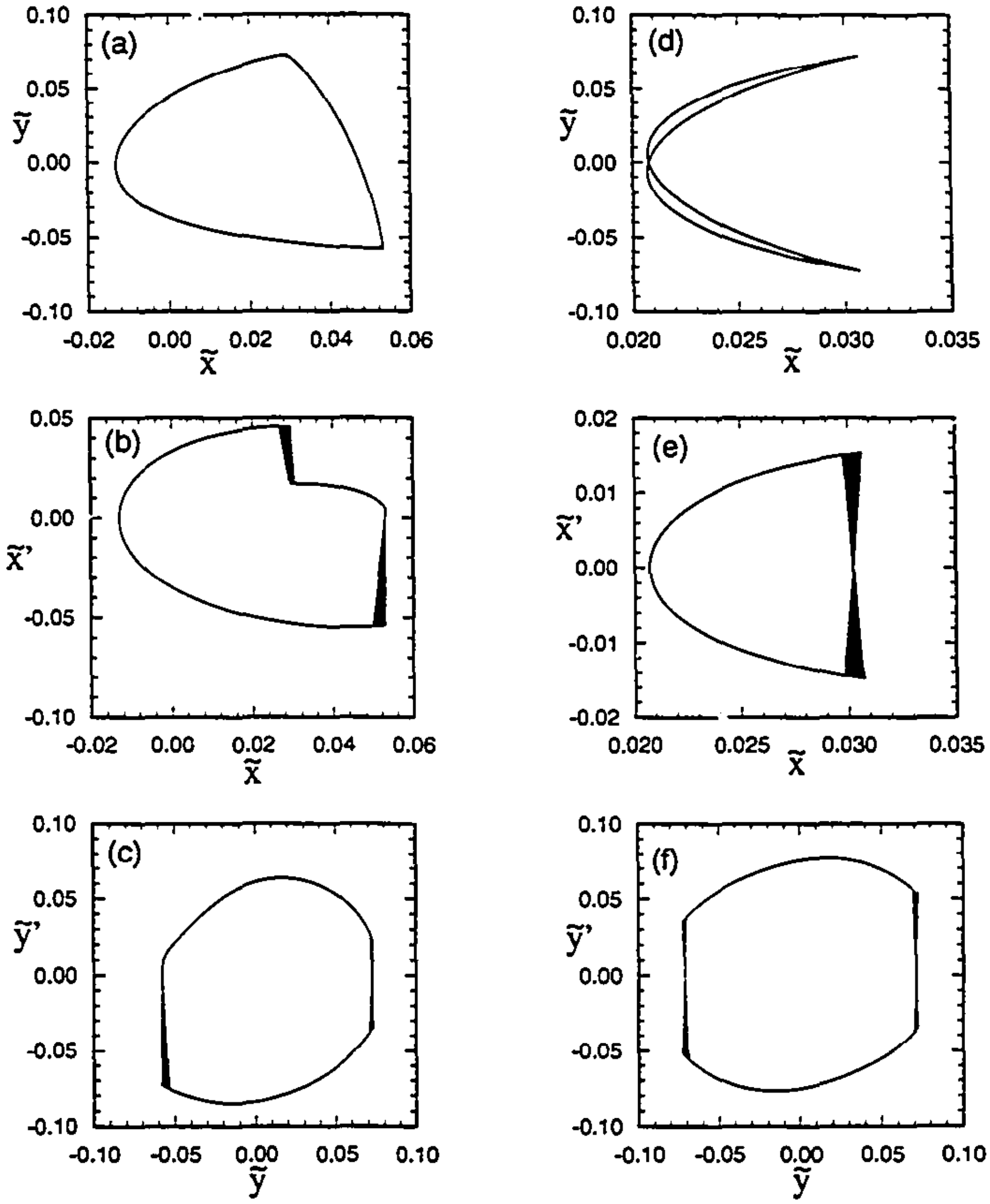

Figure 4.16: The co-existing solutions at $V = 0.57$: (a) and (d) show motion in the $(\tilde{x}, \tilde{y})$ plane; (b) and (e) are in-flow phase plots; (c) and (f) depict cross-flow phase plots.

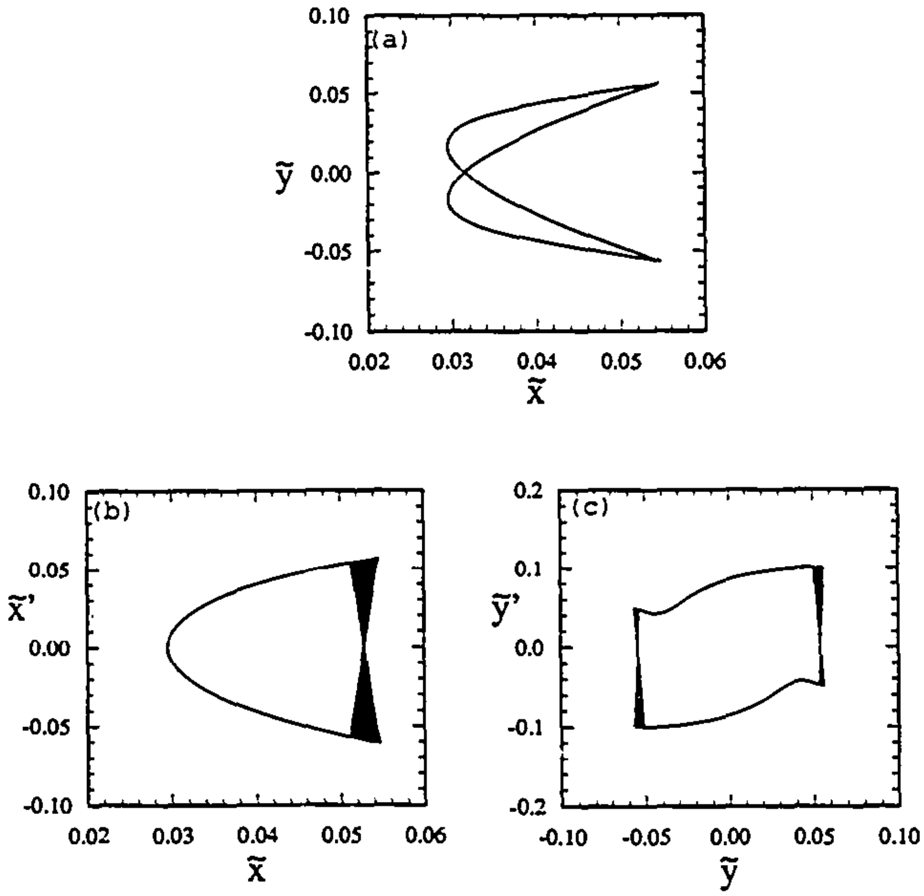

Figure 4.17: The symmetrical solution with a large in-flow component at $V = 1.00$: (a) motion in the $(\tilde{x}, \tilde{y})$ plane; (b) in-flow phase plots; (c) cross-flow phase plots.

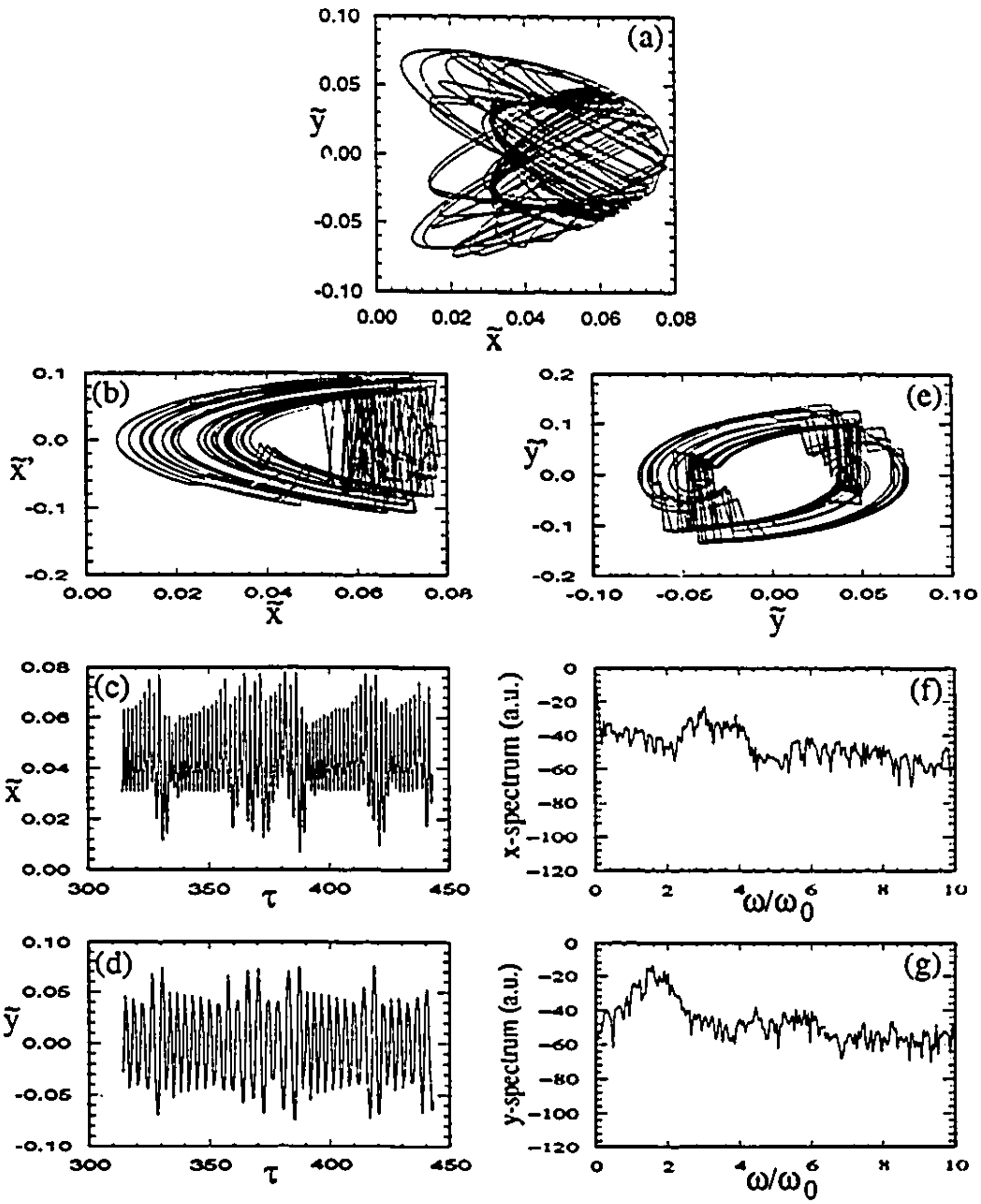

Figure 4.18: Cylinder response at $V = 1.09$: (a) orbital $(\tilde{x}, \tilde{y})$ motion; (b,e) in-flow and cross-flow phase plane plots; (c,d) in-flow and cross-flow time traces; (f,g) corresponding response spectra.

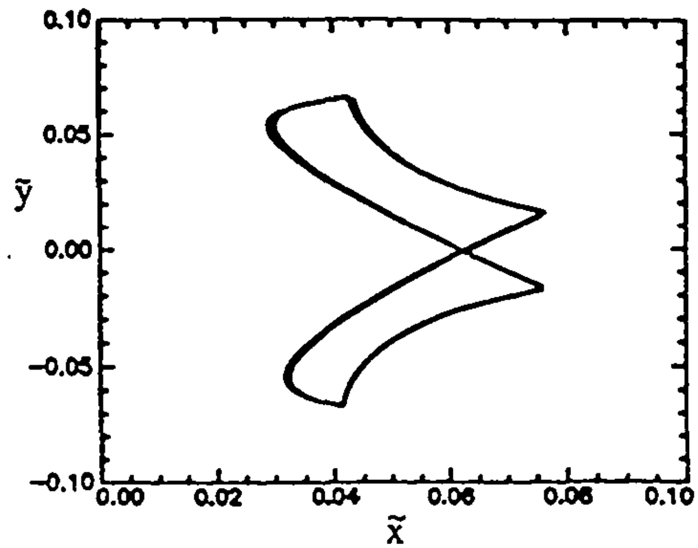

Figure 4.19: Orbital $(\tilde{x}, \tilde{y})$ plot in the periodic window for $V = 1.10$.

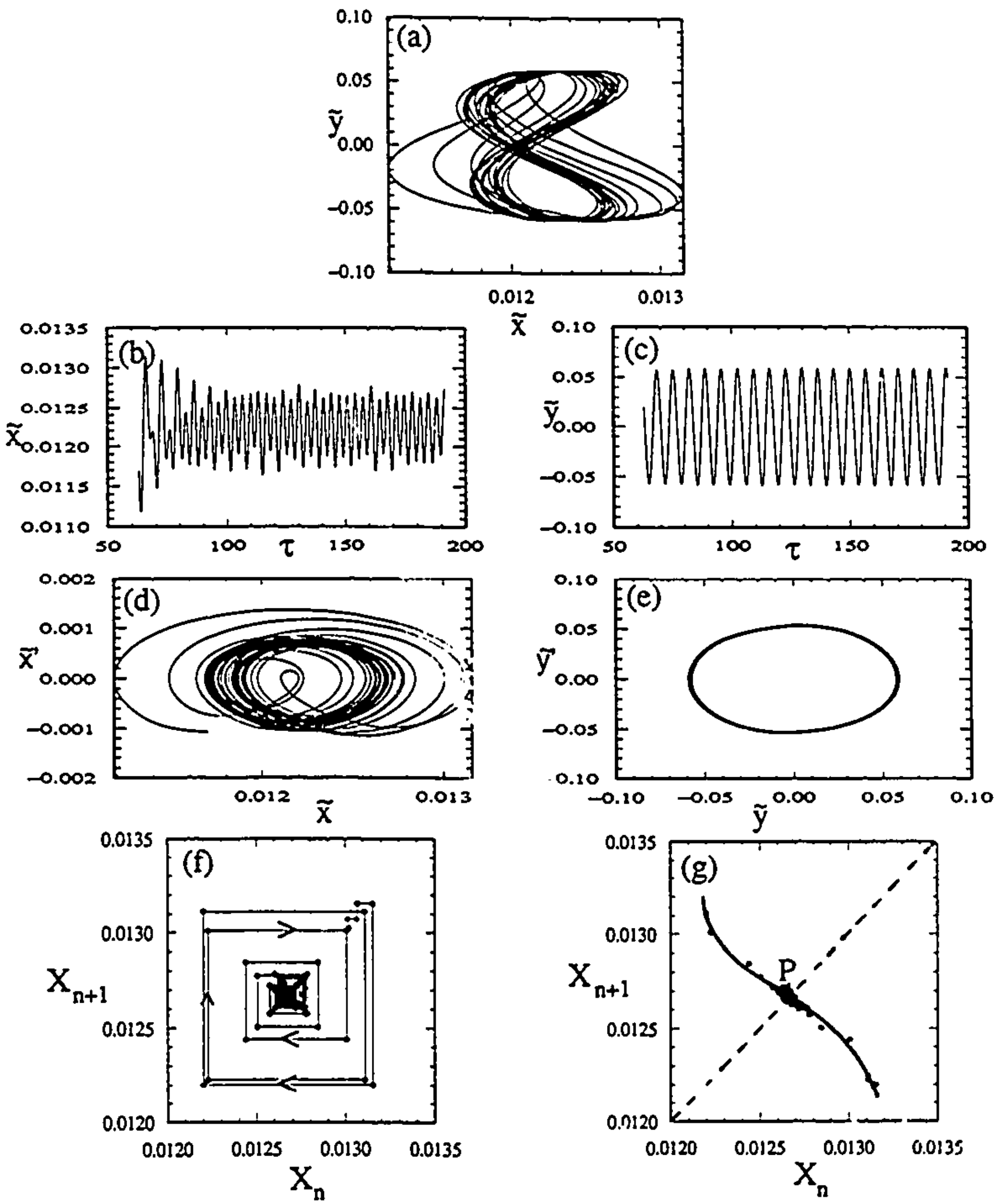

Figure 4.20: Unsteady cylinder response at $V = 0.326$: (a) orbital $(\tilde{x}, \tilde{y})$ motion; (b,c) in-flow and cross-flow time traces; (d,e) in-flow and cross-flow phase plane plots; (f) Poincaré return map showing iteration sequence; (g) same map as in (f) showing only iterates and a curve fitting of the data points.

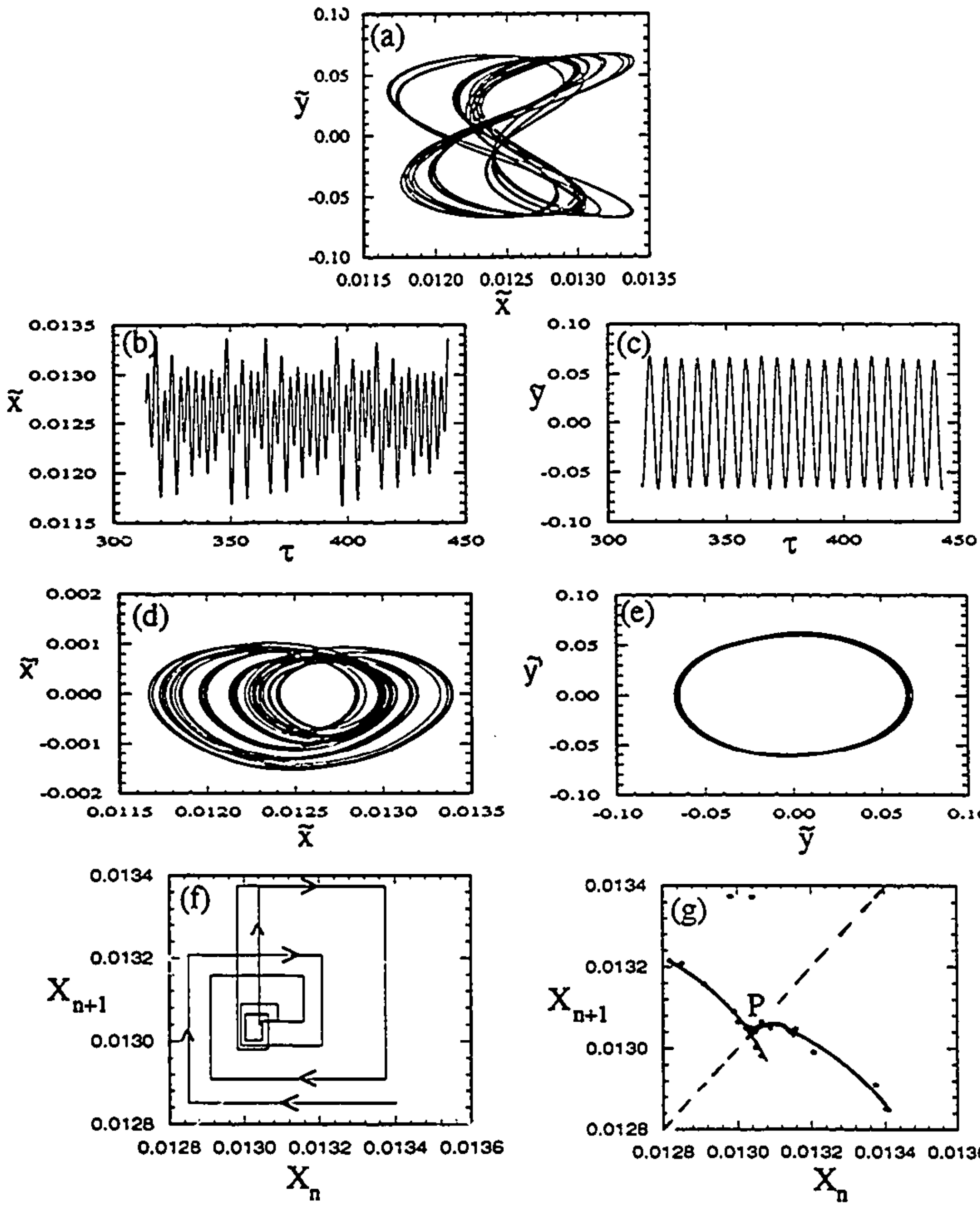

Figure 4.21: Cylinder response at $V = 0.330$: (a) orbital $(\tilde{x}, \tilde{y})$ motion; (b,c) in-flow and cross-flow time traces; (d,e) in-flow and cross-flow phase plane plots; (f) Poincaré return map showing iteration sequence; (g) same map as in (f) showing only iterates and a curve fitting of the data points.

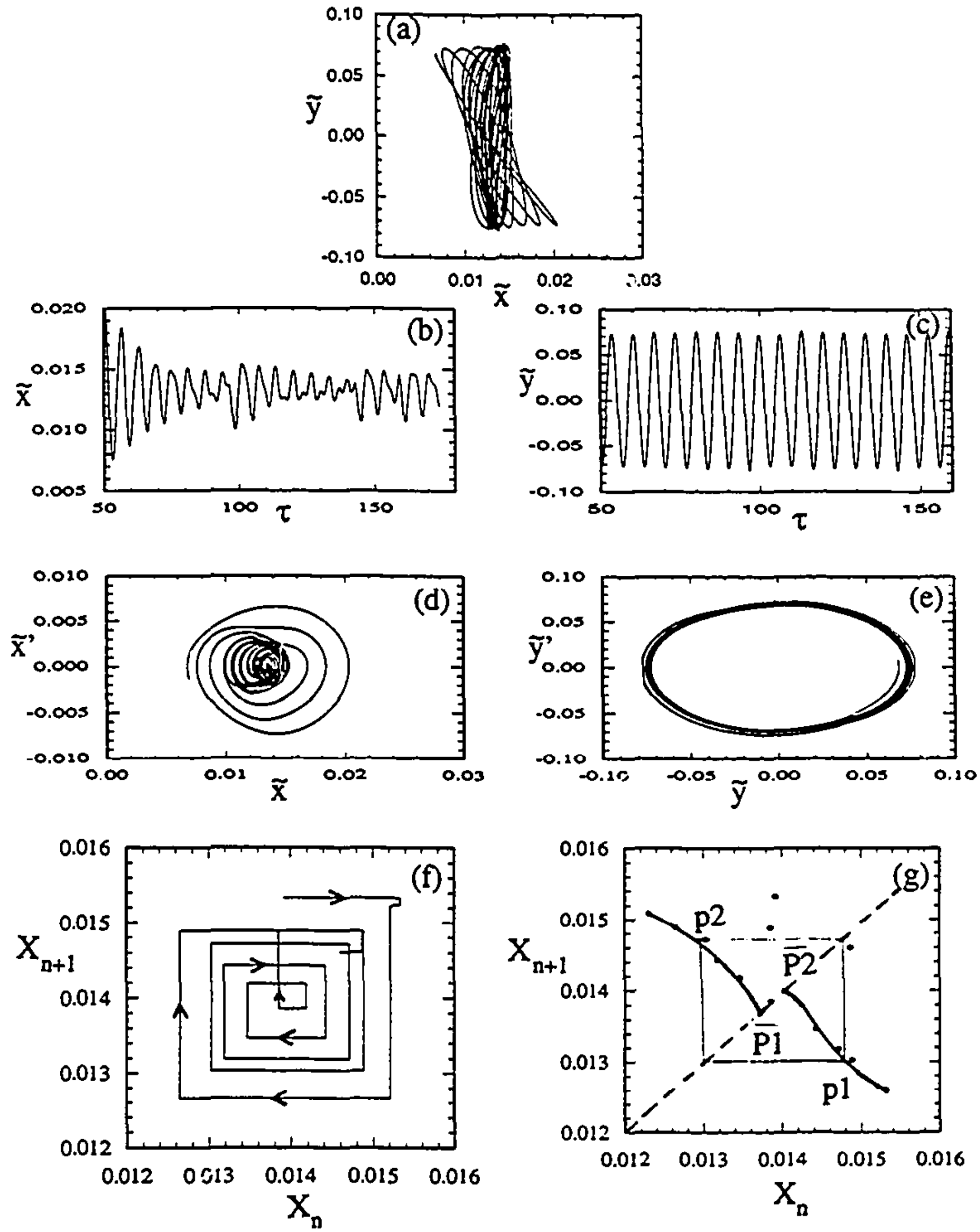

Figure 4.22: Cylinder response at $V = 0.343$: (a) orbital $(\tilde{x}, \tilde{y})$ motion; (b,c) in-flow and cross-flow time traces; (d,e) in-flow and cross-flow phase plane plots; (f) Poincaré return map showing iteration sequence; (g) same map as in (f) showing only iterates and a curve fitting of the data points, including new fixed points, $\overline{P}_1$ and $\overline{P}_2$.

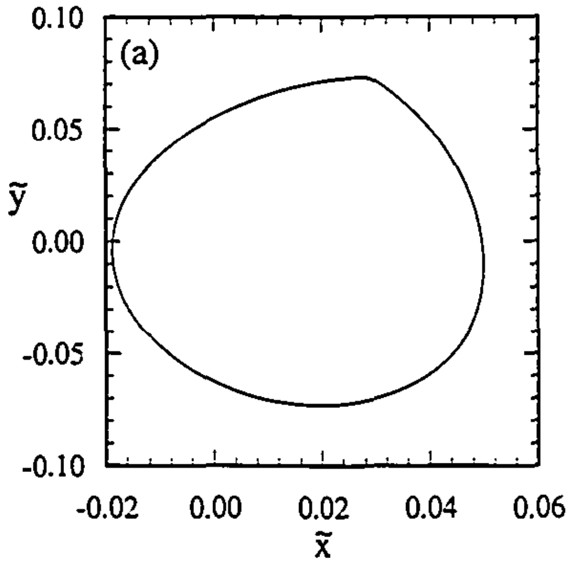

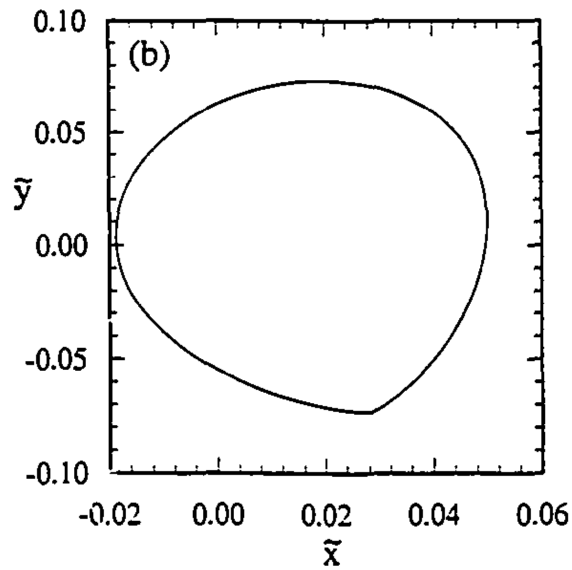

Figure 4.23: Orbital $(\tilde{x}, \tilde{y})$ plots of the asymmetric period-1 motion for $V = 0.40$ and initial cross-flow displacements; (a) $\tilde{y}(0) = 0.04$; (b) $\tilde{y}(0) = -0.04$.

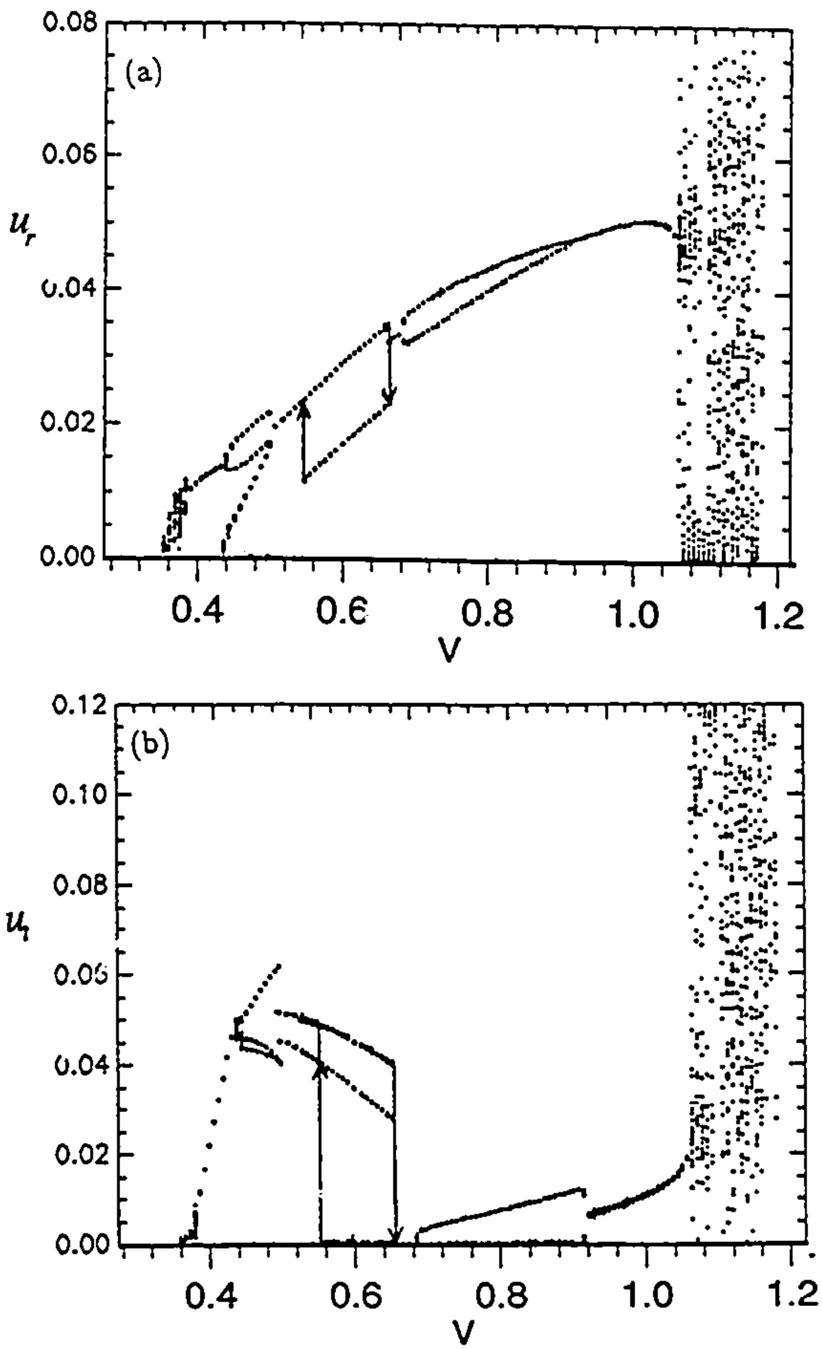

Figure 4.24: Bifurcation diagrams of (a) the radial velocity, u_r, and (b) the tangential velocity, u_t.

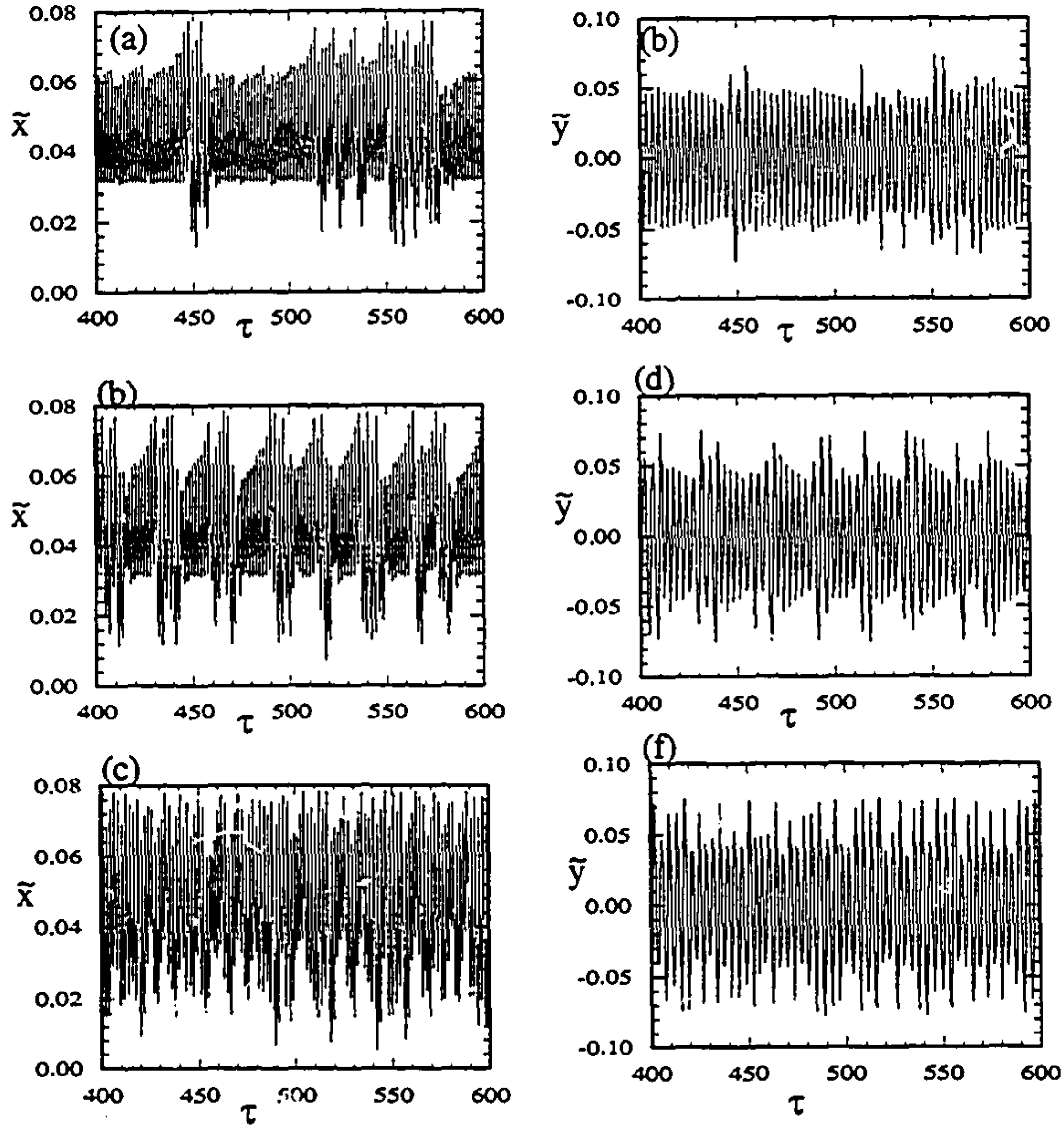

Figure 4.25: Time traces for the flow velocities (a,b)$V = 1.07$, (c,d) $V = 1.09$ and (e,f) $V = 1.15$; (a,c,e) show in-flow motion; (b,d,f) show cross-flow motion.

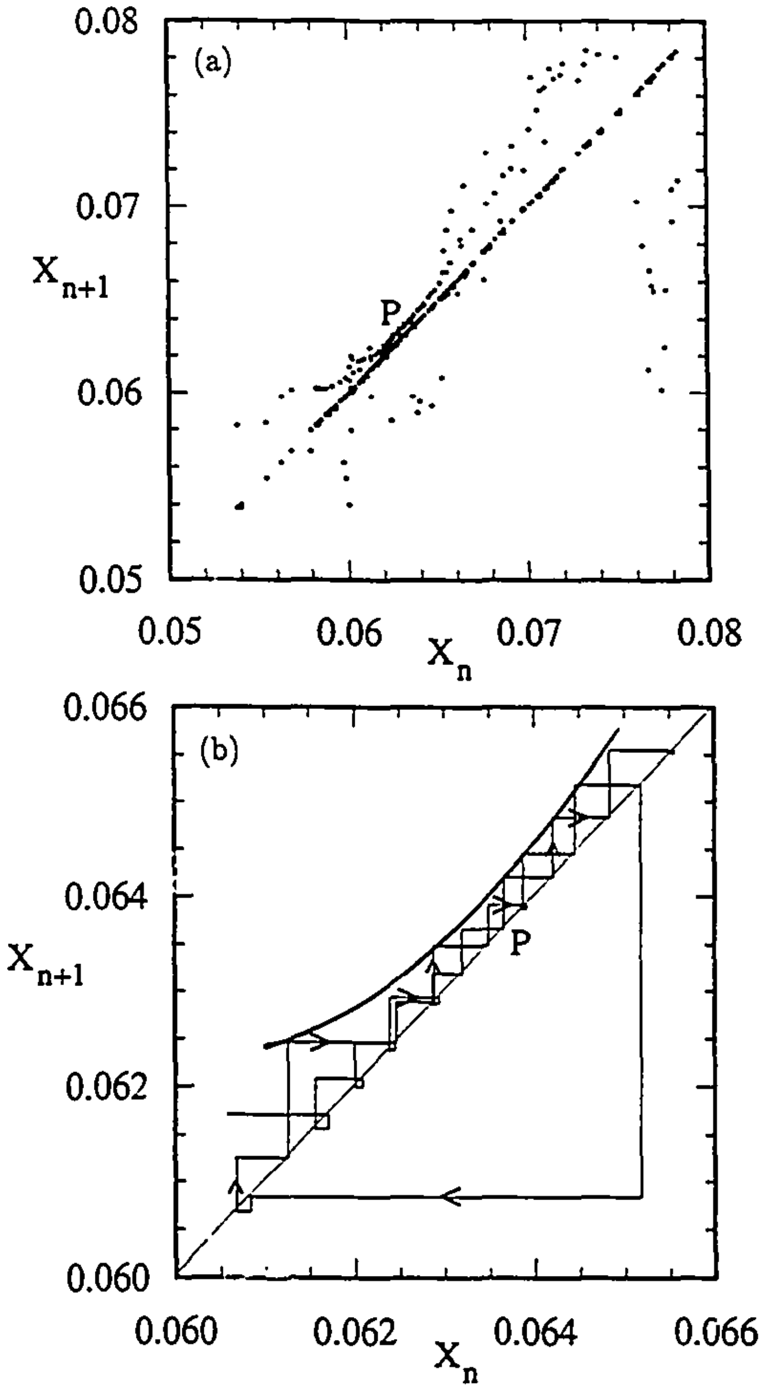

Figure 4.26: Poincaré return map for $V = 1.07$: (a) complete map showing tangency near point P (the laminar region); (b) close up of laminar region showing iteration sequence in the narrow channel.

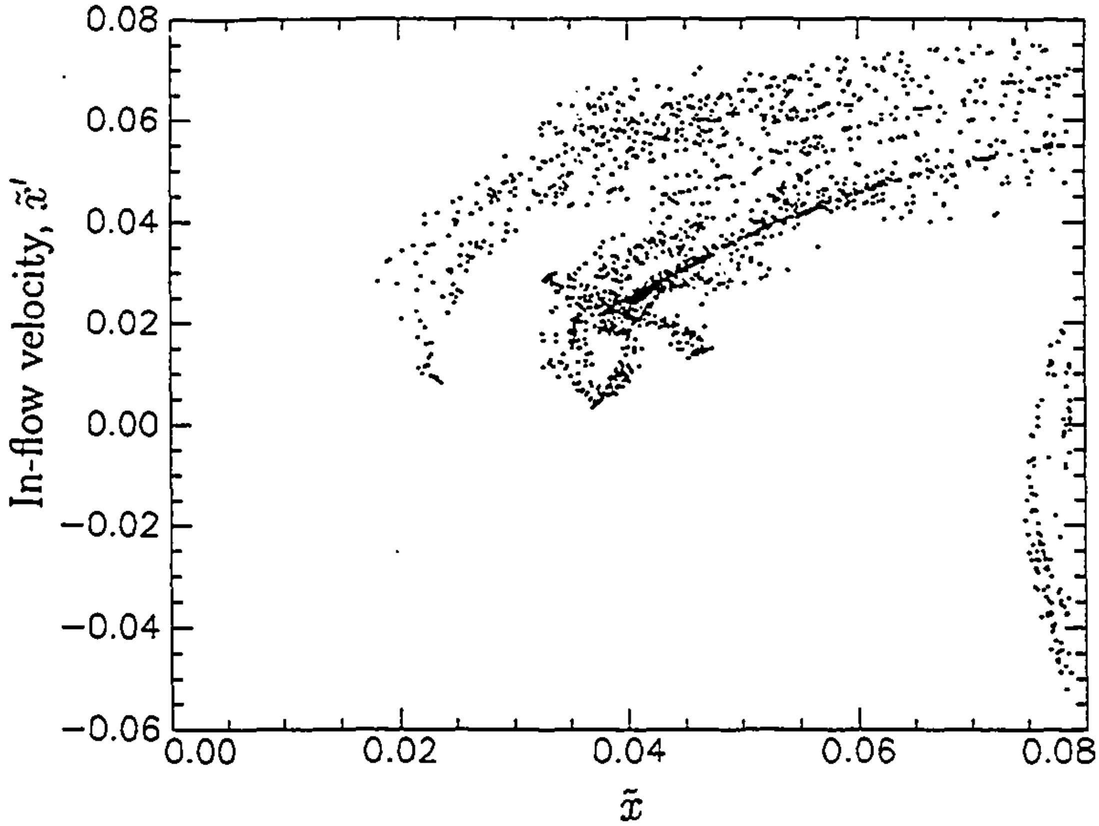

Figure 4.27: Poincaré section at $V = 1.09$; $\tilde{x}$ versus $\tilde{x}'$ when $\tilde{y} = 0$ and $\tilde{y}' > 0$.

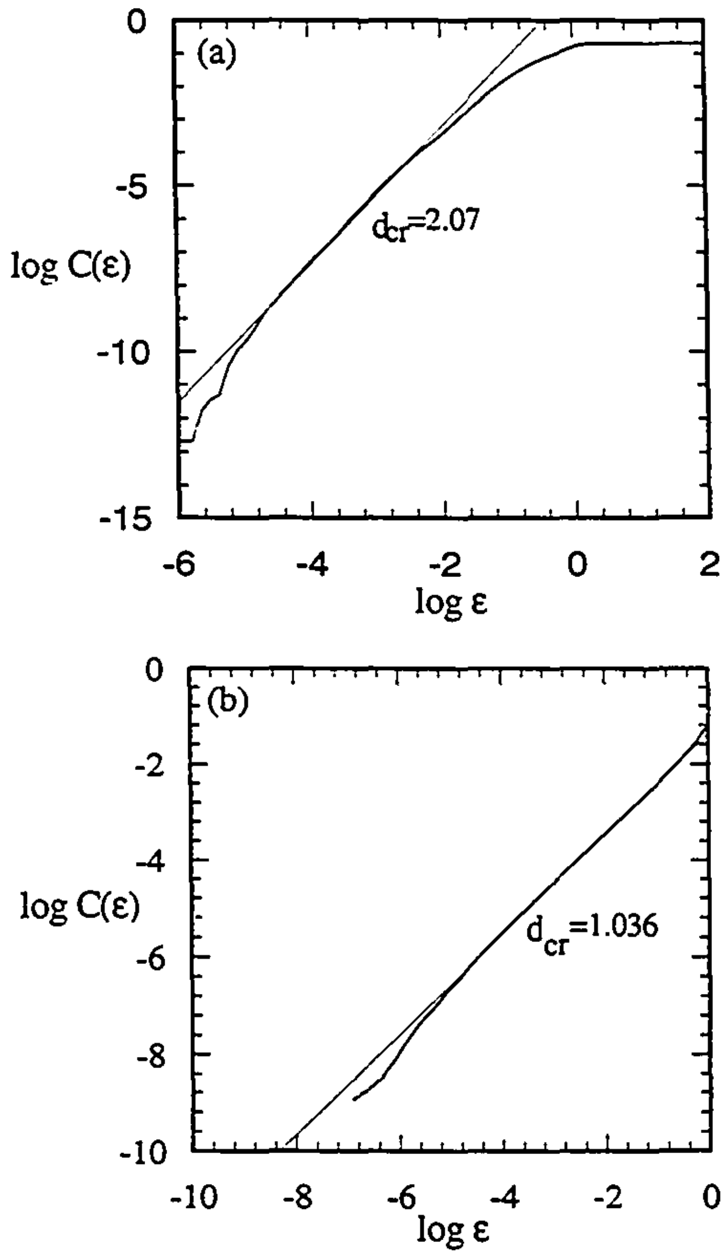

Figure 4.28: Correlation for: (a) chaotic response at $V = 1.09$; (b) period-1 response at $V = 0.40$.

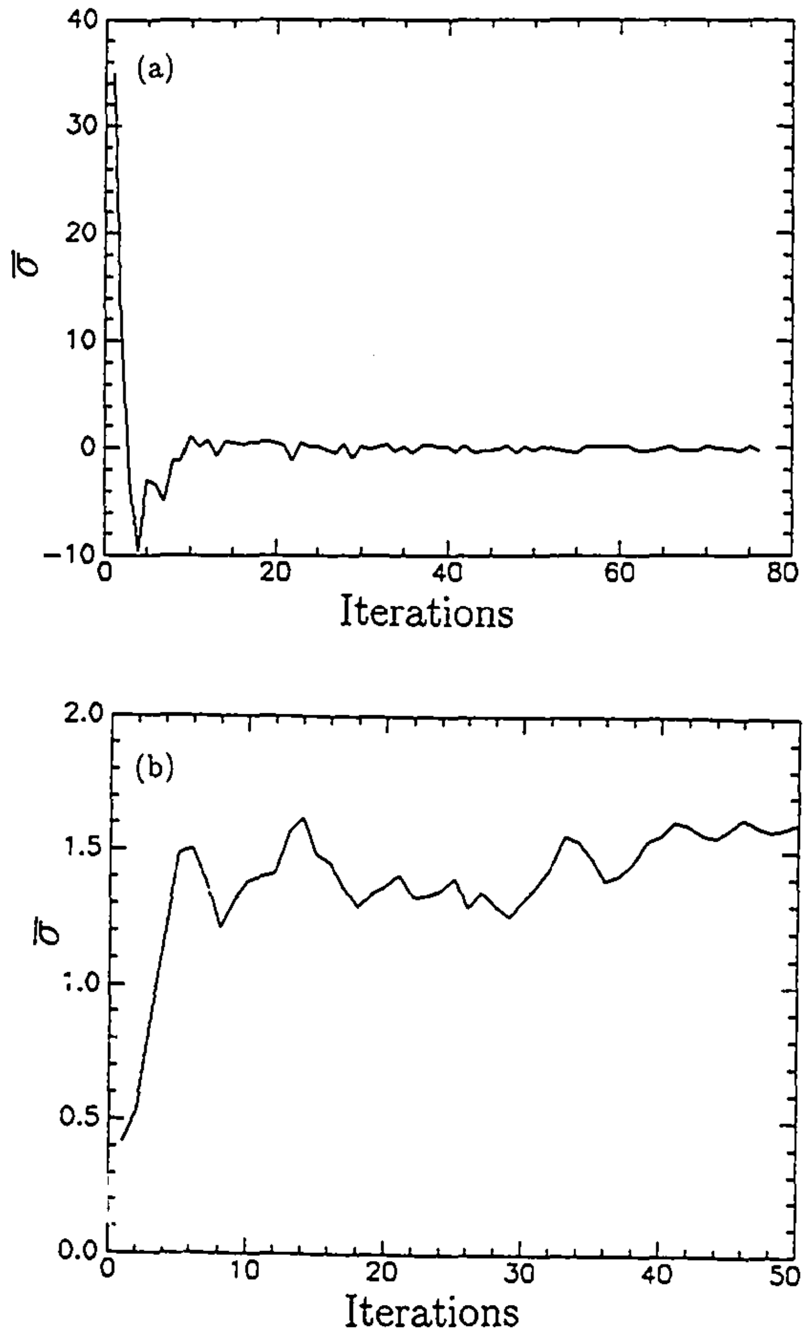

Figure 4.29: Convergence of lyapunov exponent computation for: (a) period-2 motion at $V = 0.45$, giving, $\overline{\sigma} = 0$; (b) chaotic motion at $V = 1.09$, giving, $\overline{\sigma} \simeq 1.4$.

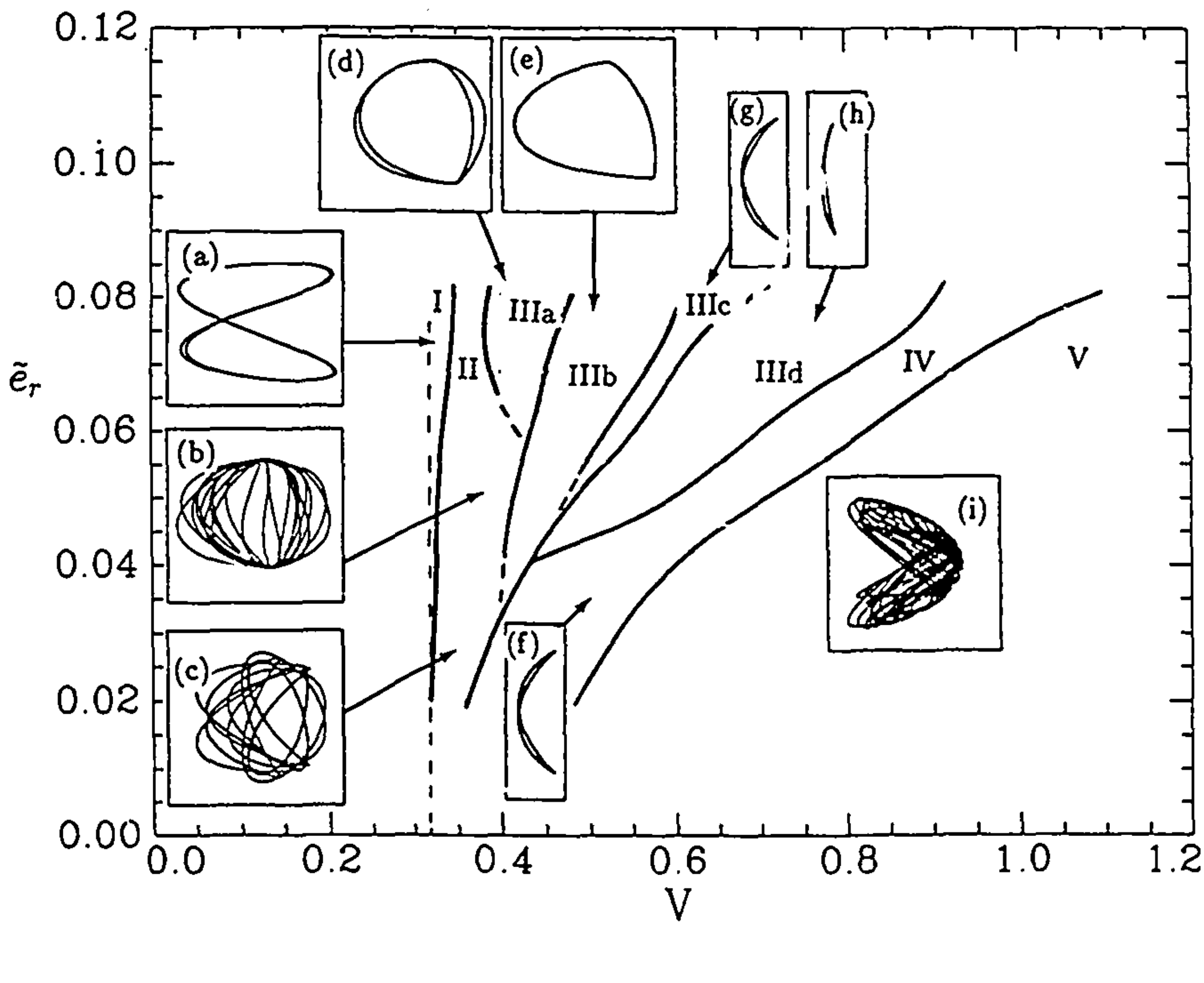

Figure 4.30: Co-dimension 2 qualitative bifurcation diagram in terms dimensionless velocity, V, and gap $\tilde{e}_r$. Inset diagrams show typical motion in the $(\tilde{x}, \tilde{y})$ plane for the $(V, \tilde{e}_r)$ combination indicated.

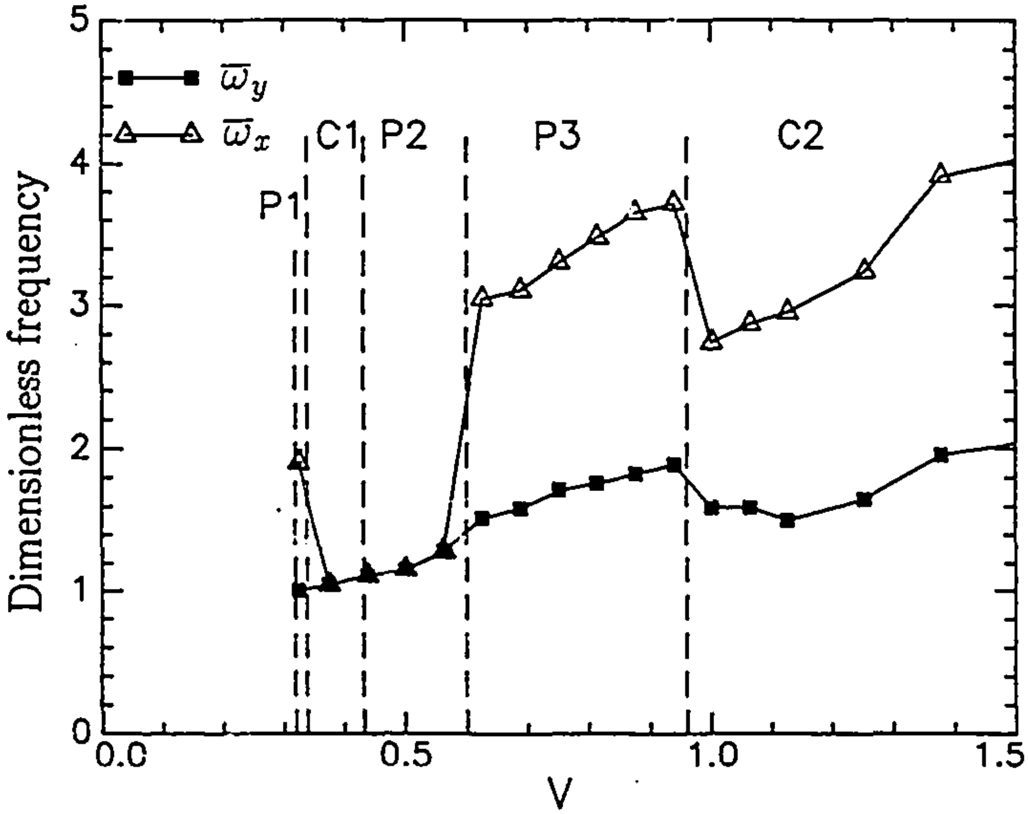

Figure 4.31: The dimensionless frequencies ($\overline{\omega}/\overline{\omega}_0$) versus V: (a) in-flow, $\overline{\omega}_x$; (b) cross-flow, $\overline{\omega}_y$. Regions marked by a P, e.g. P1, indicate that motions are periodic there; C denotes chaotic regions.

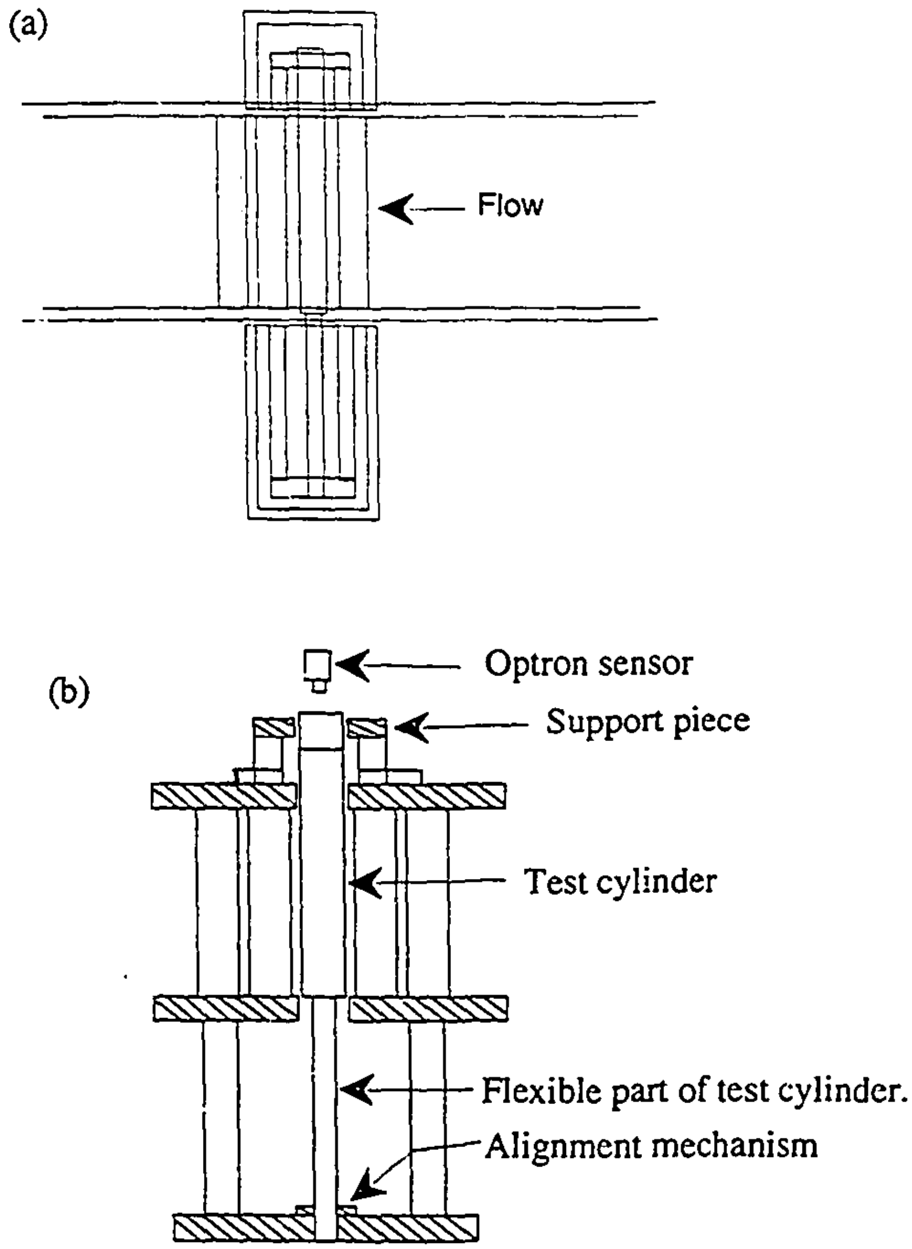

Figure 5.1: (a) View of array within tunnel test-section; (b) array central bundle before insertion into the water tunnel.

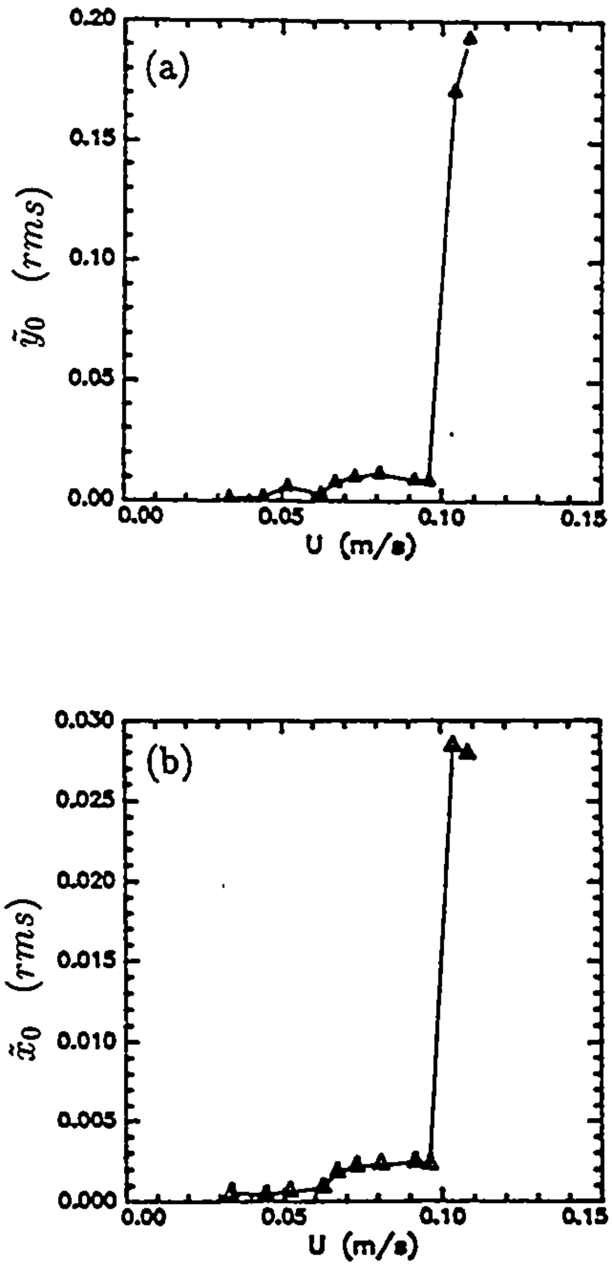

Figure 5.2: Experimental non-dimensional response amplitudes in (a) cross-flow and (b) in-flow directions; $\tilde{m} = 1.87$, $\delta = 0.01$; $Re = 12574\ U\ \ [U(\text{m/s})]$.

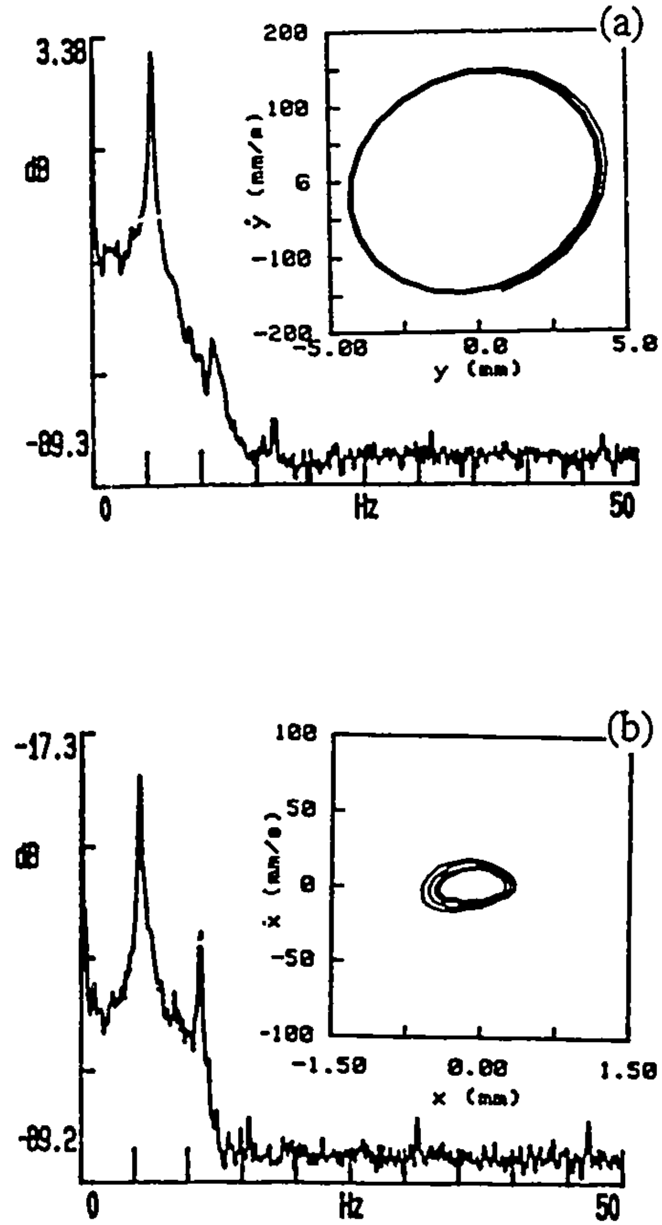

Figure 5.3: Cylinder response at $V = 1.05V_c$. Parts (a) and (b) show the power spectra in cross- and in-flow direction, respectively; the inset diagrams show corresponding phase portraits. For this and all subsequent experimental figures $\tilde{m} = 1.87$, $\delta = 0.01$; $Re = 1320.3\ V/V_c$.

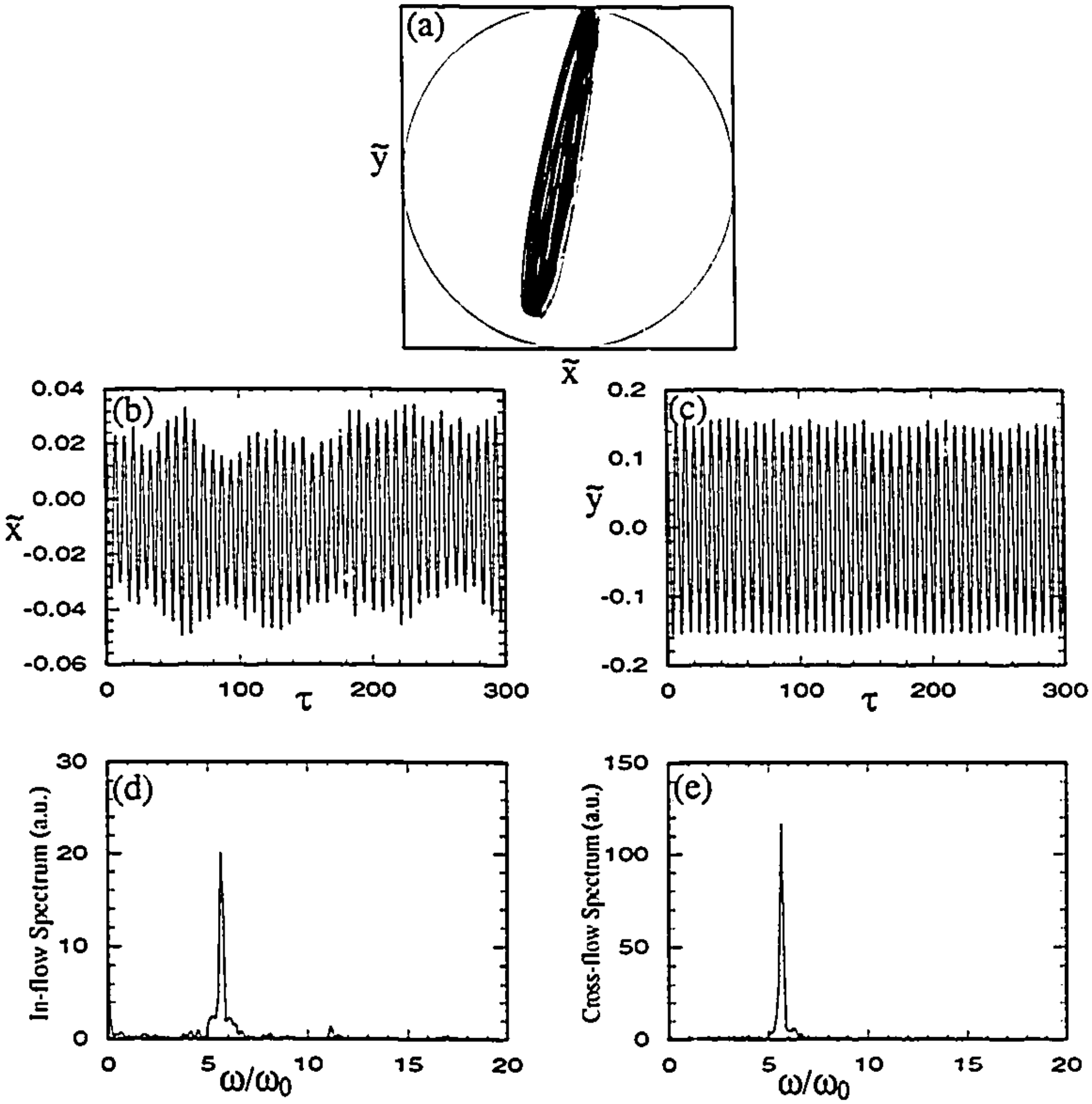

Figure 5.4: The single-sided impacting response for $V = 1.17V_c$: (a) orbital $(\tilde{x}, \tilde{y})$ motion; (b) in-flow and (c) cross-flow time trace, respectively; (d,e) corresponding power spectra. The support gap size $\tilde{e}_r = 0.174$.

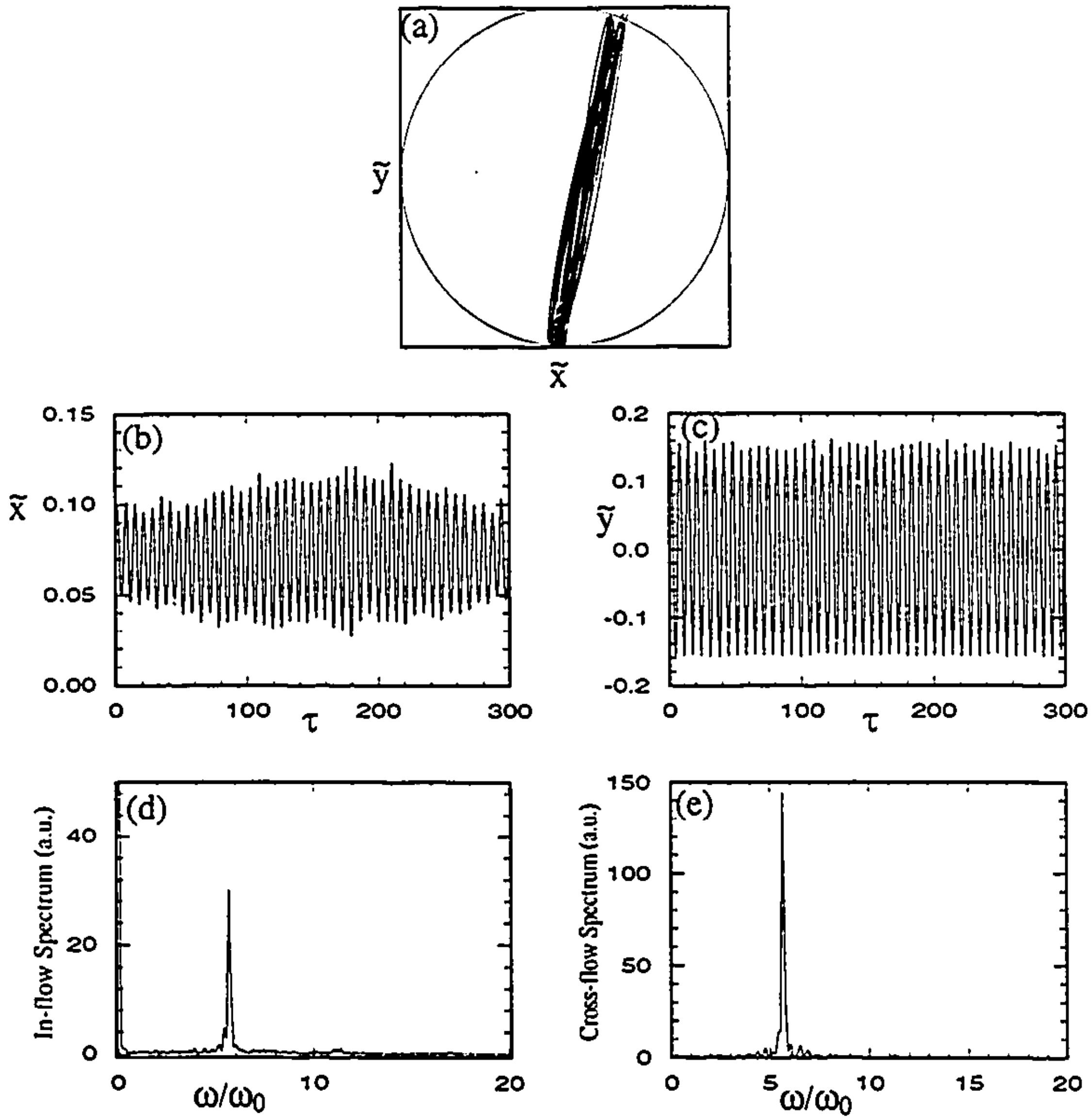

Figure 5.5: Double-sided impacting response at $V = 1.24V_c$: (a) orbital $(\tilde{x}, \tilde{y})$ motion; (b) in-flow and (c) cross-flow time trace, respectively; (d,e) corresponding power spectra; $\tilde{e}_r = 0.174$.

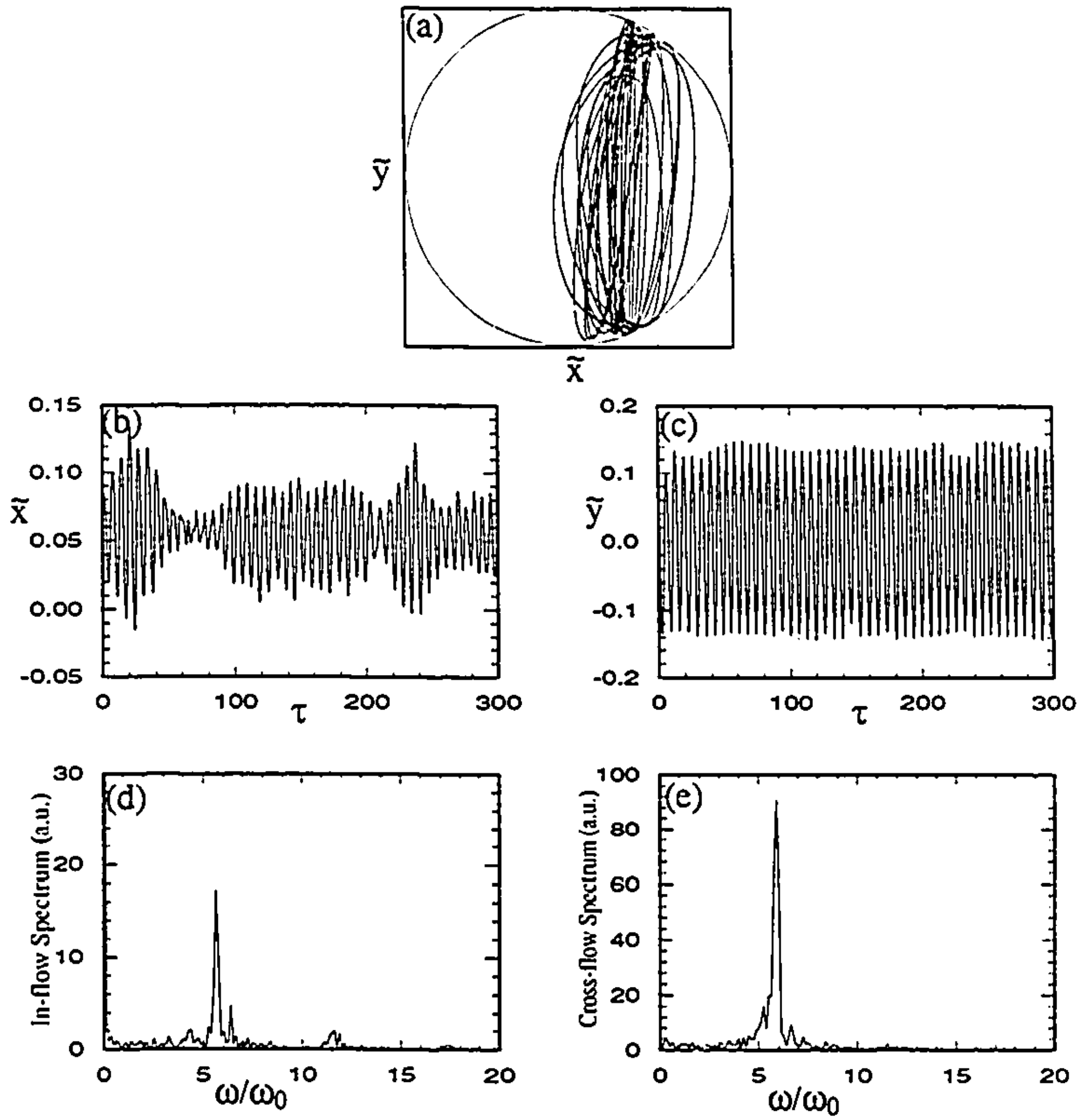

Figure 5.6: Cylinder response exhibiting the intermittent instability of the double-sided impacting motion; $V = 1.47V_c$: (a) orbital $(\tilde{x}, \tilde{y})$ motion; (b) in-flow and (c) cross-flow time trace, respectively; (d,e) corresponding power spectra; $\tilde{e}_r = 0.174$.

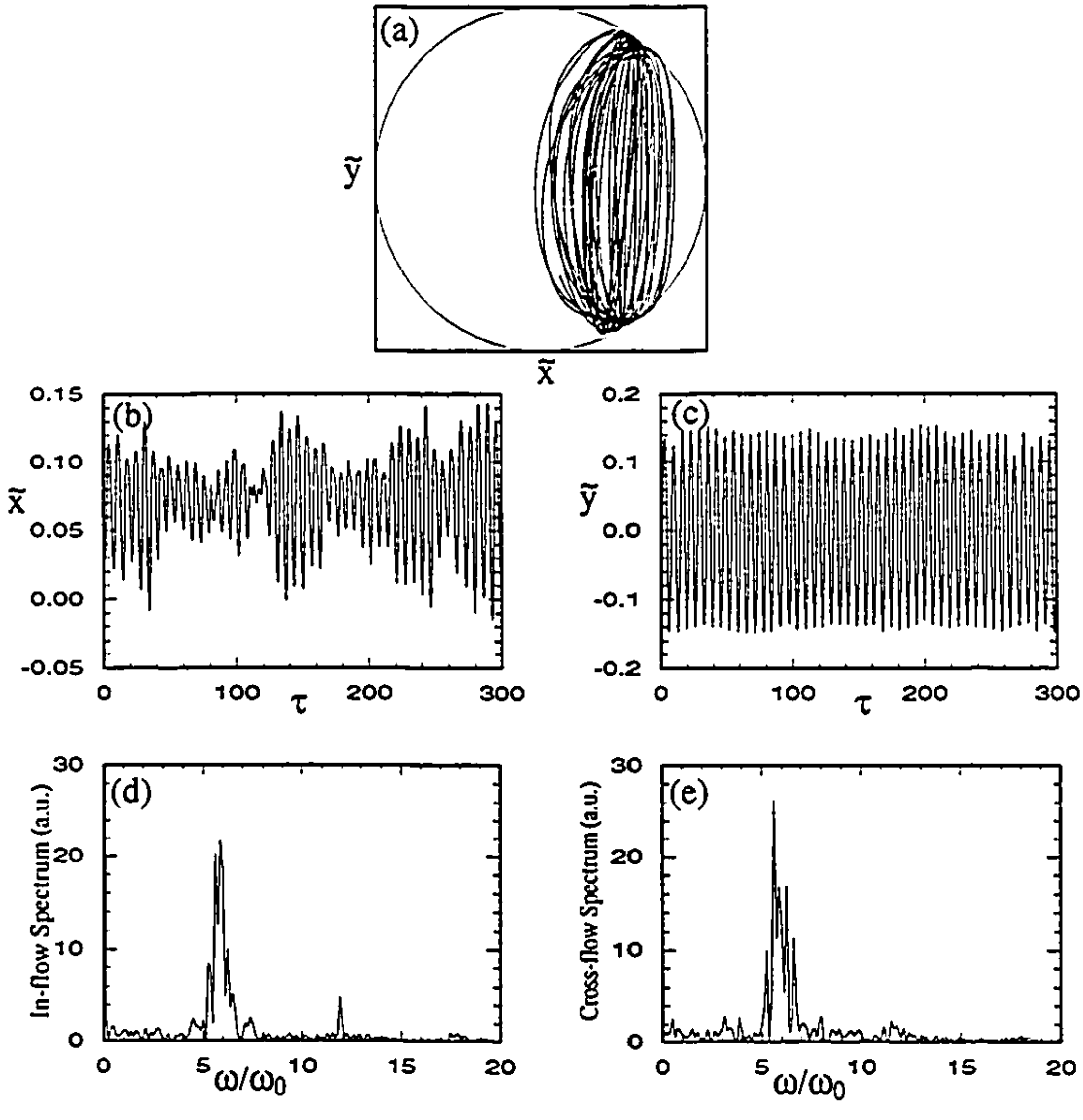

Figure 5.7: Cylinder response showing frequent intermittent amplitude bursts at $V = 1.54V_c$: (a) shows orbital $(\tilde{x}, \tilde{y})$ motion; (b) and (c) are in-flow and cross-flow time trace, respectively; (d,e) are the corresponding power spectra; $\tilde{e}_r = 0.174$.

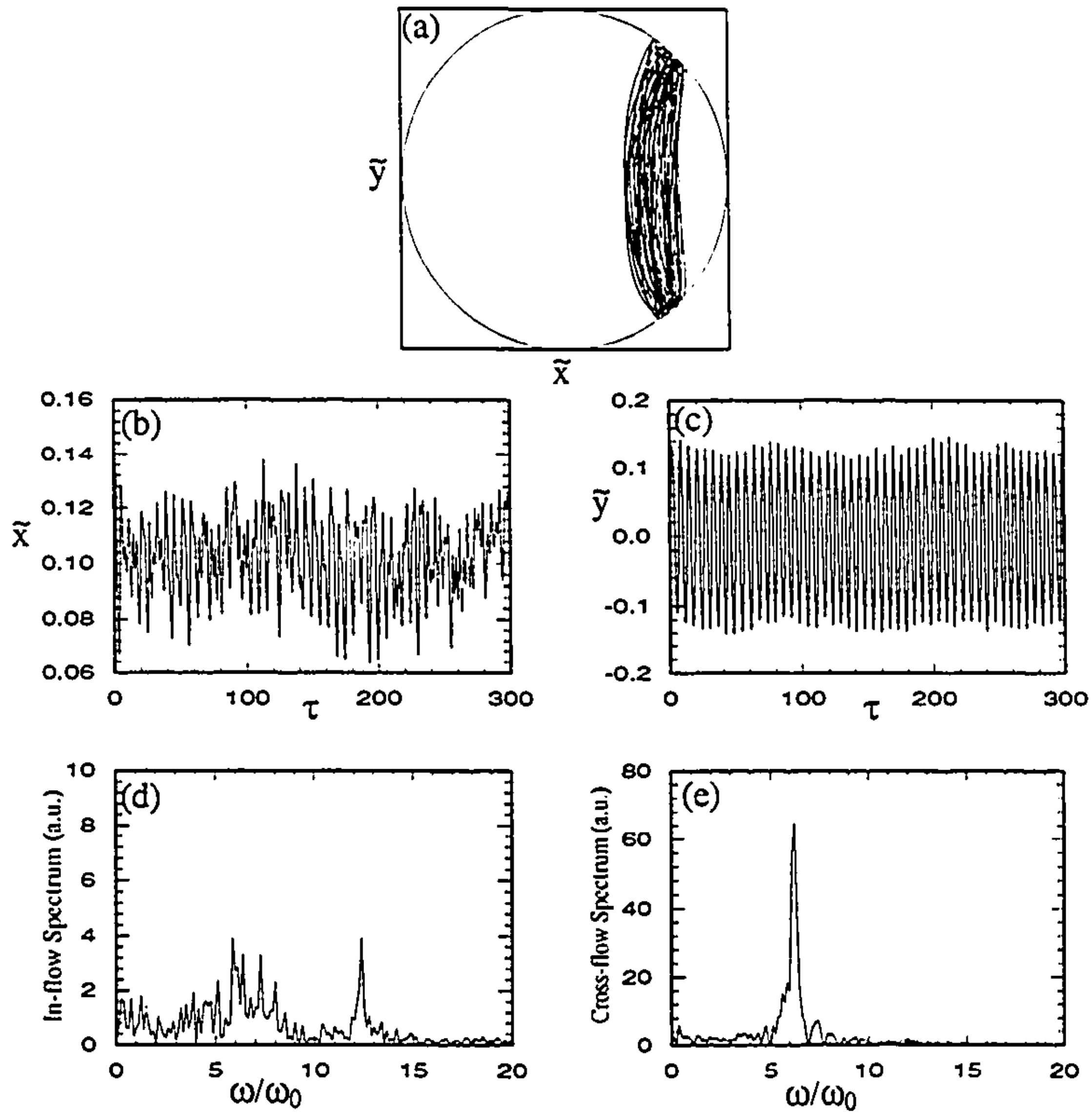

Figure 5.8: The chaotic motion for $V = 1.69V_c$: (a) motion in the $(\tilde{x}, \tilde{y})$ plane; (b) in-flow and (c) cross-flow time trace, respectively; (d,e) corresponding power spectra; $\tilde{e}_r = 0.174$.

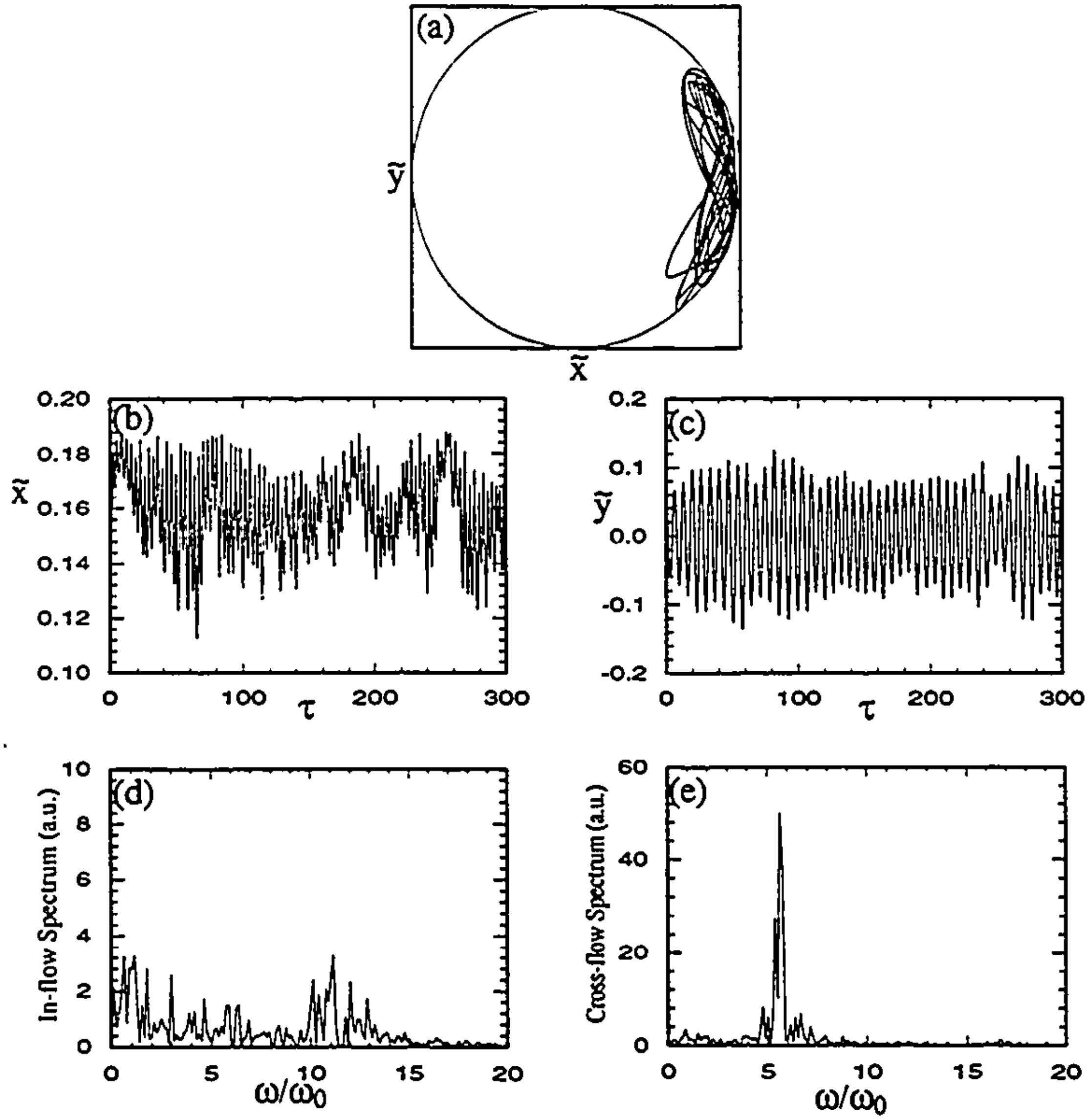

Figure 5.9: The figure-of-eight orbital response following the intermittency regime, here $V = 1.91V_c$: (a) motion in the $(\tilde{x}, \tilde{y})$ plane; (b) in-flow and (c) cross-flow time trace, respectively; (d,e) corresponding power spectra; $\tilde{e}_r = 0.174$.

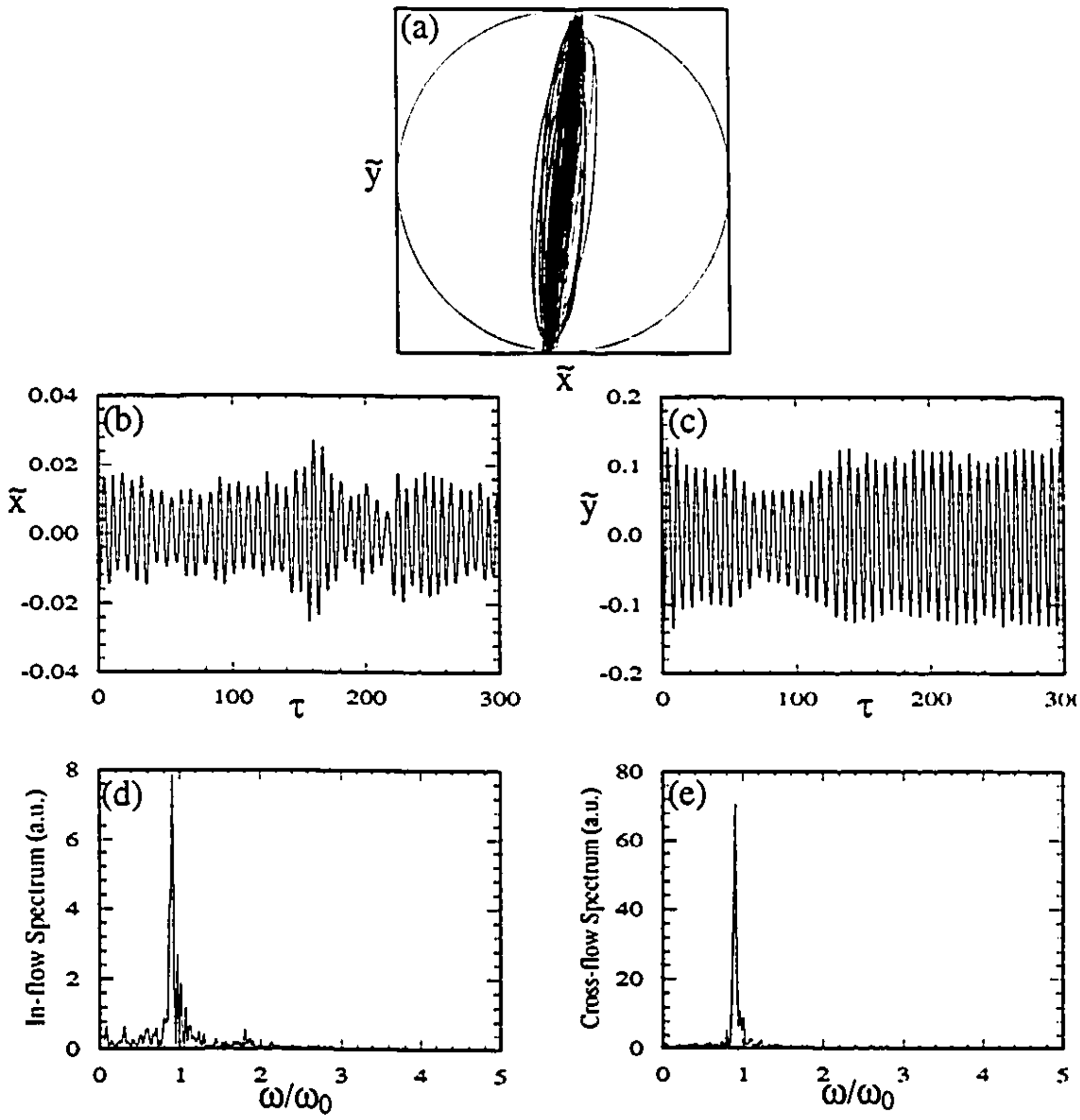

Figure 5.10: Double-sided impacting response for the smaller gap $\tilde{e}_r = 0.132$ at $V = 1.29V_c$: (a) orbital $(\tilde{x}, \tilde{y})$ motion; (b) in-flow and (c) cross-flow time traces respectively; (d,e) corresponding power spectra.

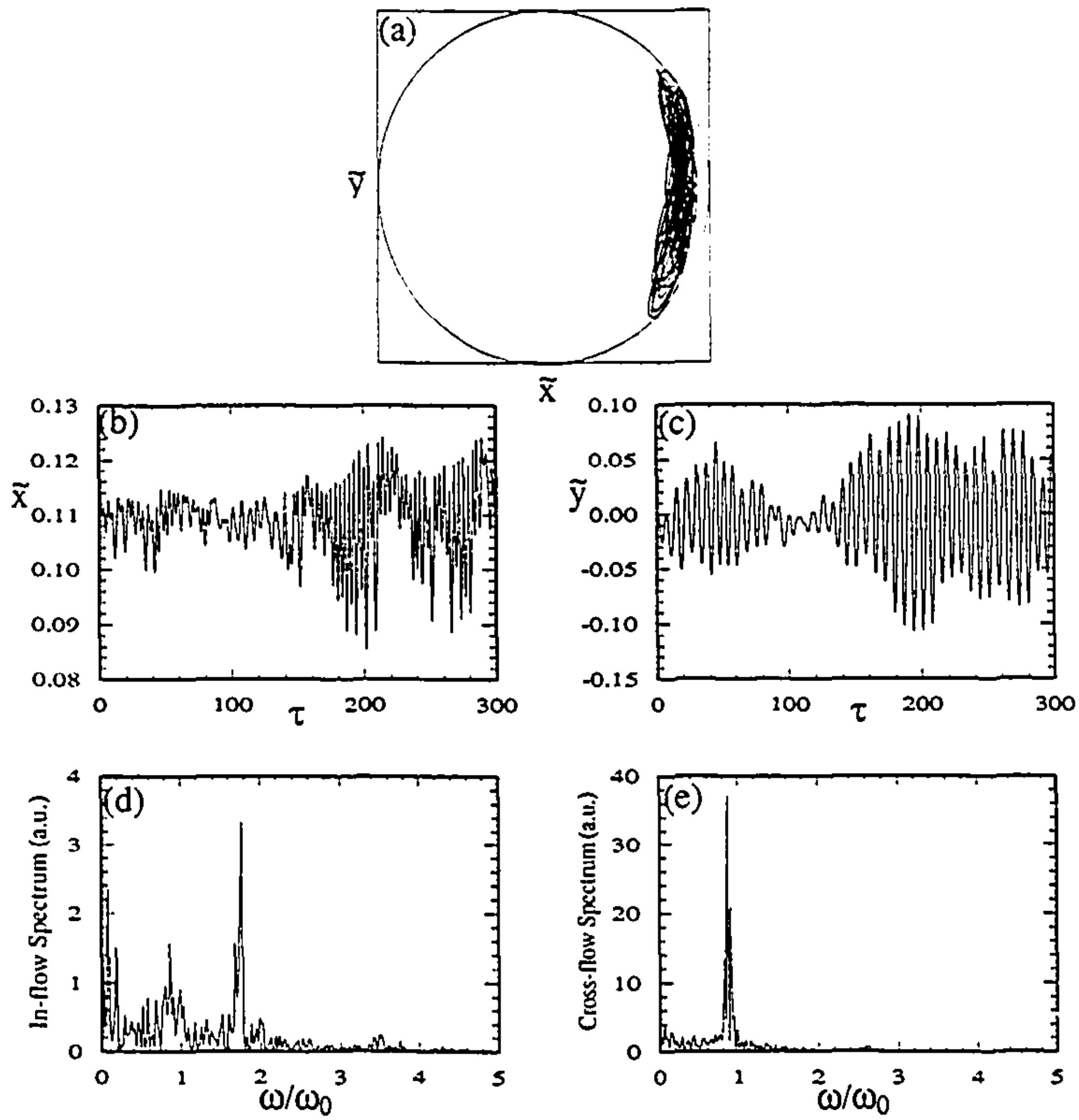

Figure 5.11: The final figure-of eight response for the gap $\tilde{e}_r = 0.132$ at $V = 1.62V_c$: (a) orbital $(\tilde{x}, \tilde{y})$ motion; (b) in-flow and (c) cross-flow time trace, respectively; (d,e) corresponding power spectra.

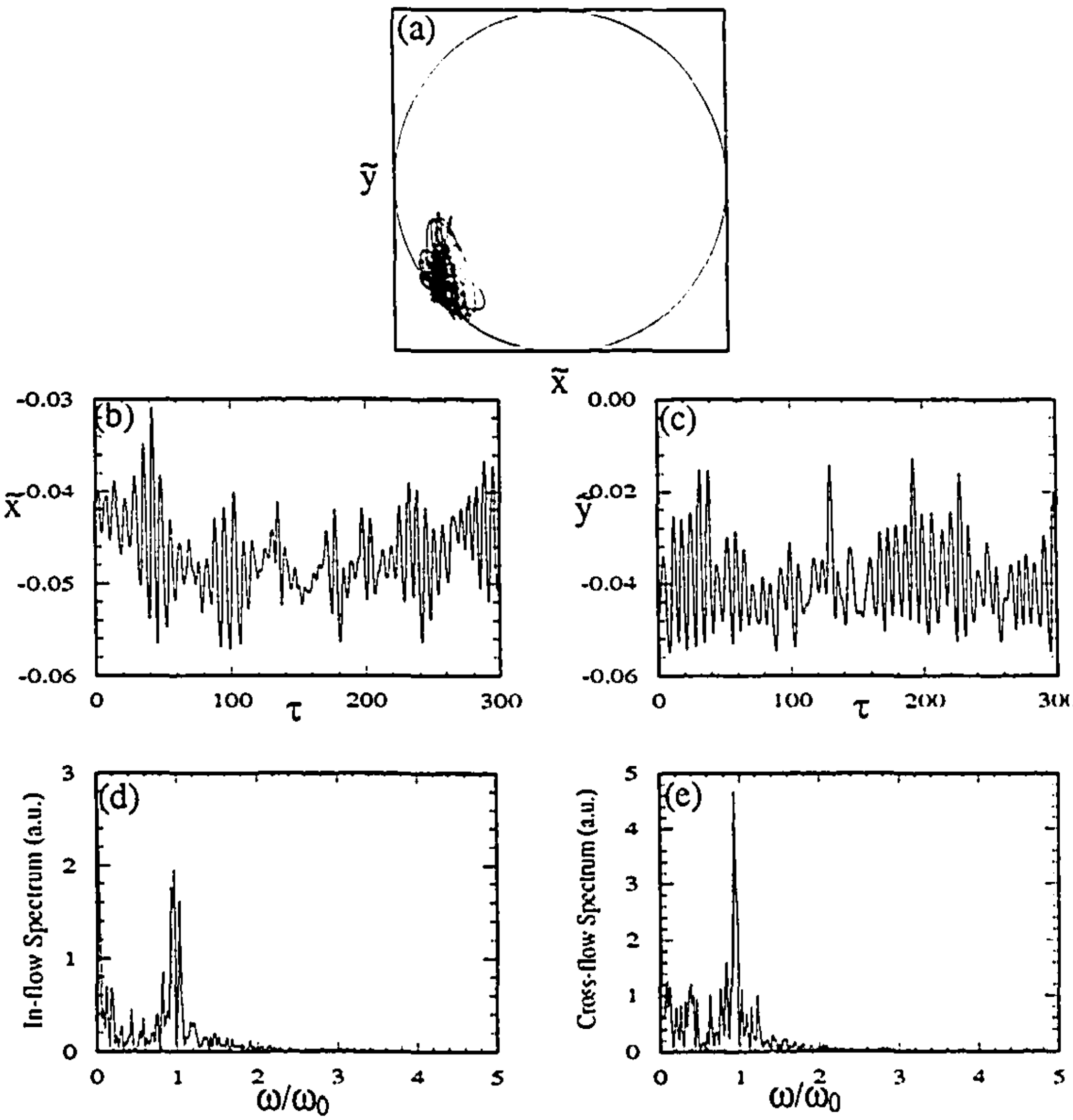

Figure 5.12: Initial post-fluidelastic instability cylinder response, showing effect of preload, for the small gap size $\tilde{e}_r = 0.067$; the flow velocity, $V = 1.10V_c$: (a) shows motion in the $(\tilde{x}, \tilde{y})$ plane; (b,c) show in-flow and cross-flow time traces, respectively; (d,e) are the corresponding power spectra.

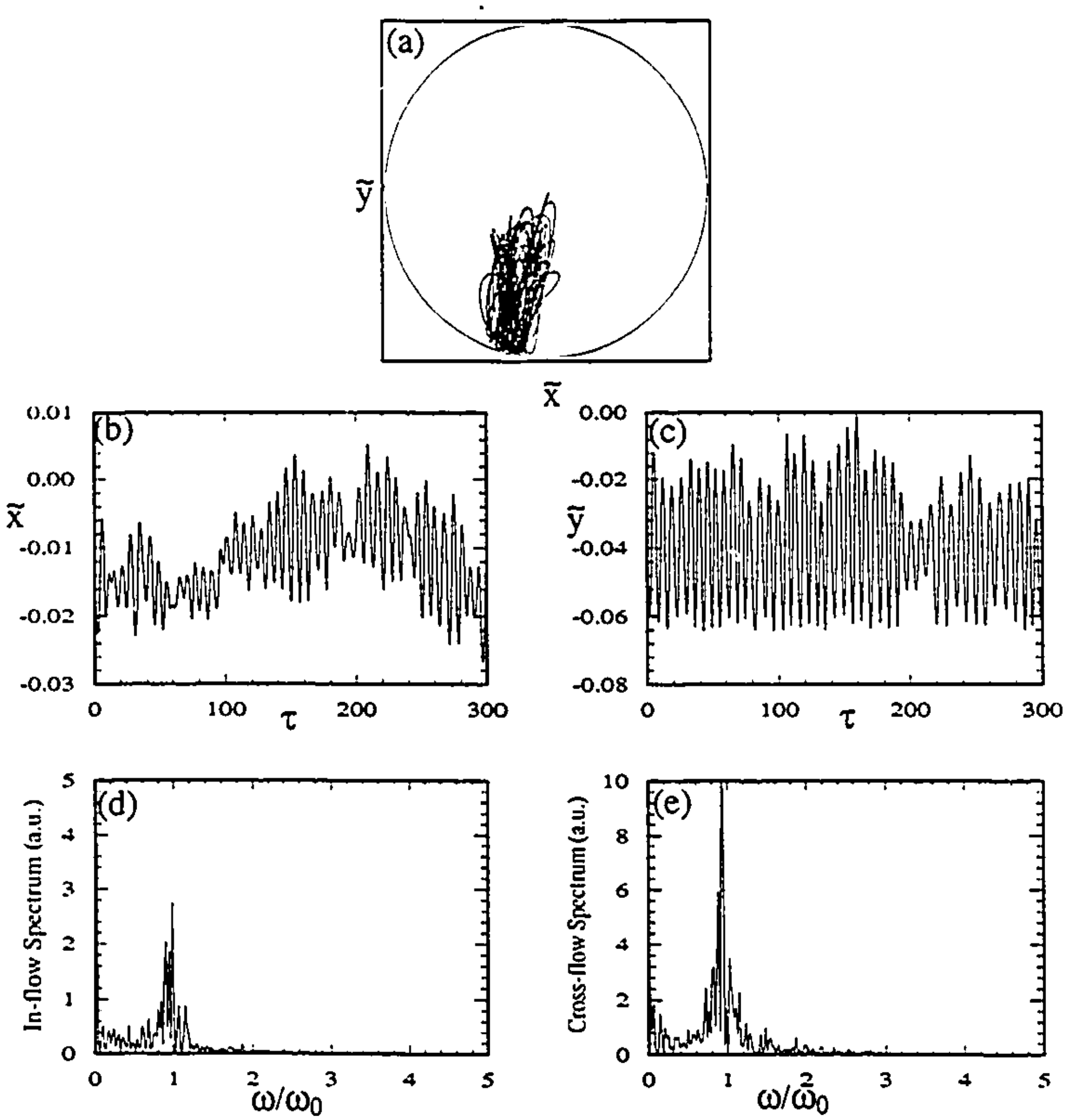

Figure 5.13: Single-sided impacting response at $V = 1.20V_c$ for the small gap size $\tilde{e}_r = 0.067$: (a) motion in the $(\tilde{x}, \tilde{y})$ plane; (b) in-flow and (c) cross-flow time trace, respectively; (d,e) corresponding power spectra.

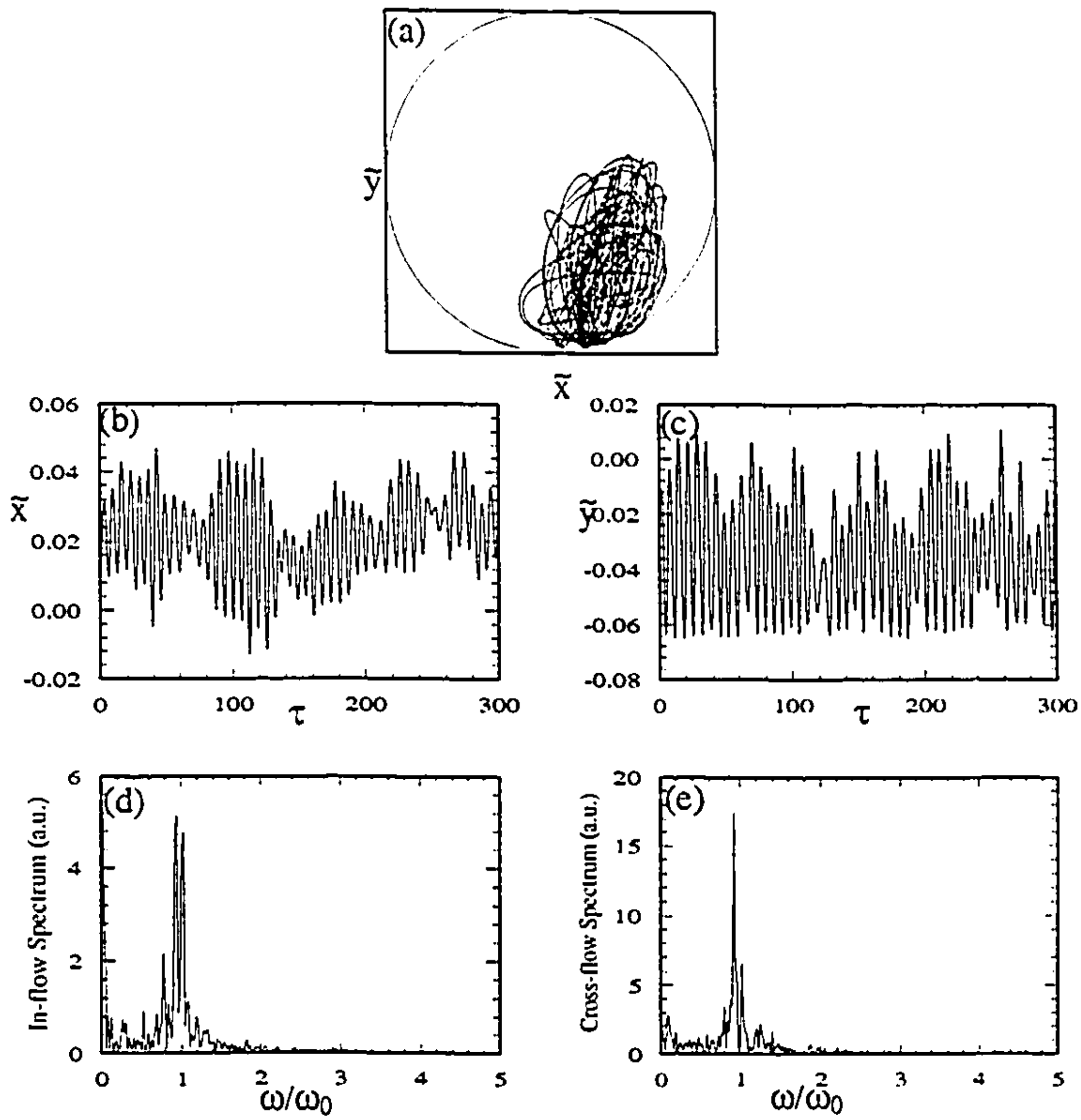

Figure 5.14: Single-sided impacting/orbiting response at $V = 1.43V_c$ for the small gap size $\tilde{e}_r = 0.067$: (a) orbital $(\tilde{x}, \tilde{y})$ motion; (b) in-flow and (c) cross-flow time trace, respectively; (d,e) corresponding power spectra.

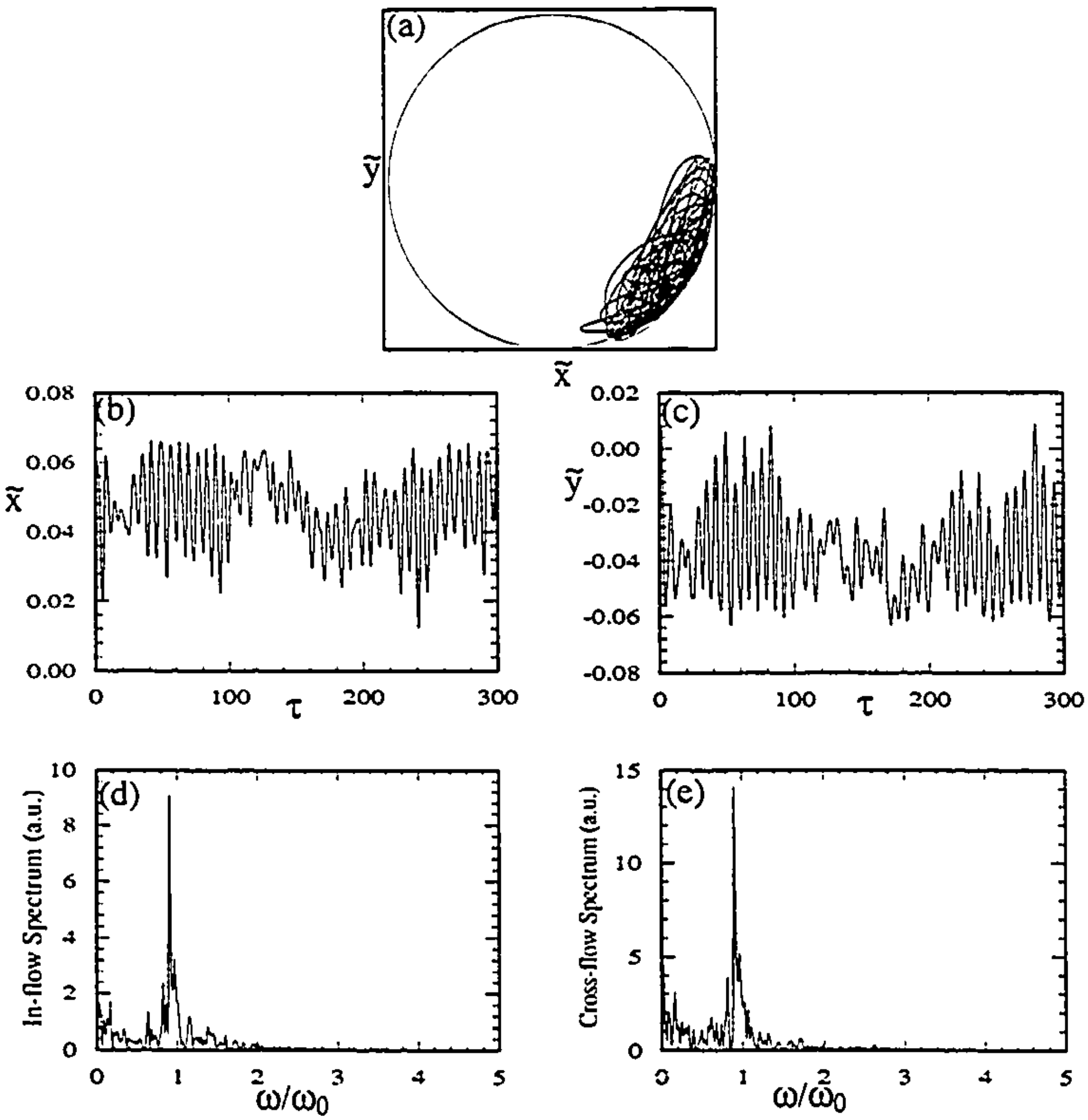

Figure 5.15: The impact/sliding cylinder response at $V = 1.58V_c$ for the small gap size $\tilde{e}_r = 0.067$: (a) motion in the $(\tilde{x}, \tilde{y})$ plane; (b) in-flow and (c) cross-flow time trace, respectively; (d,e) corresponding power spectra.

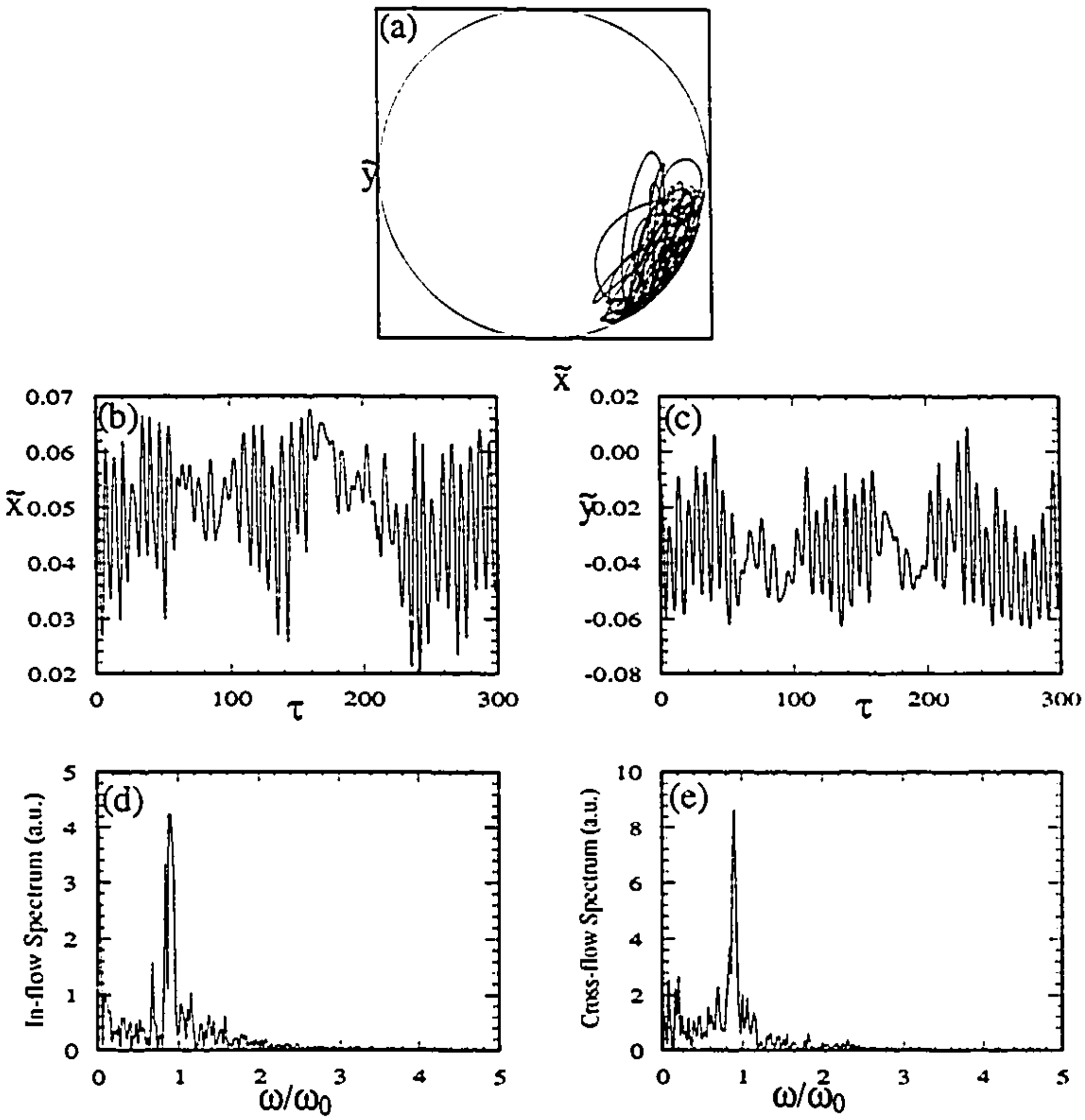

Figure 5.16: The impact/sliding cylinder response exhibiting periods of sticking at $V = 1.71V_c$ for the small gap size $\tilde{e}_r = 0.067$; (a) shows motion in the $(\tilde{x}, \tilde{y})$ plane; (b) and (c) are in-flow and cross-flow time traces, respectively; (d,e) the corresponding power spectra.

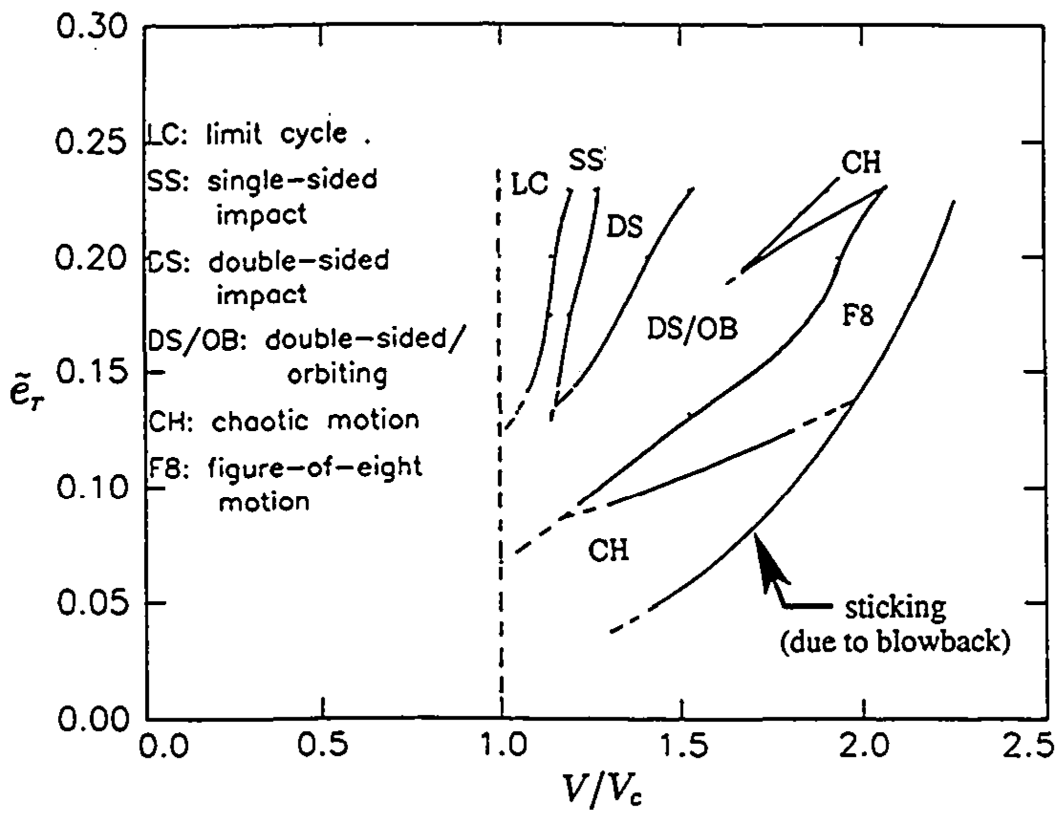

Figure 5.17: Experimental bifurcation diagram as a function of flow velocity, V, and gap size, $\tilde{e}_r$.

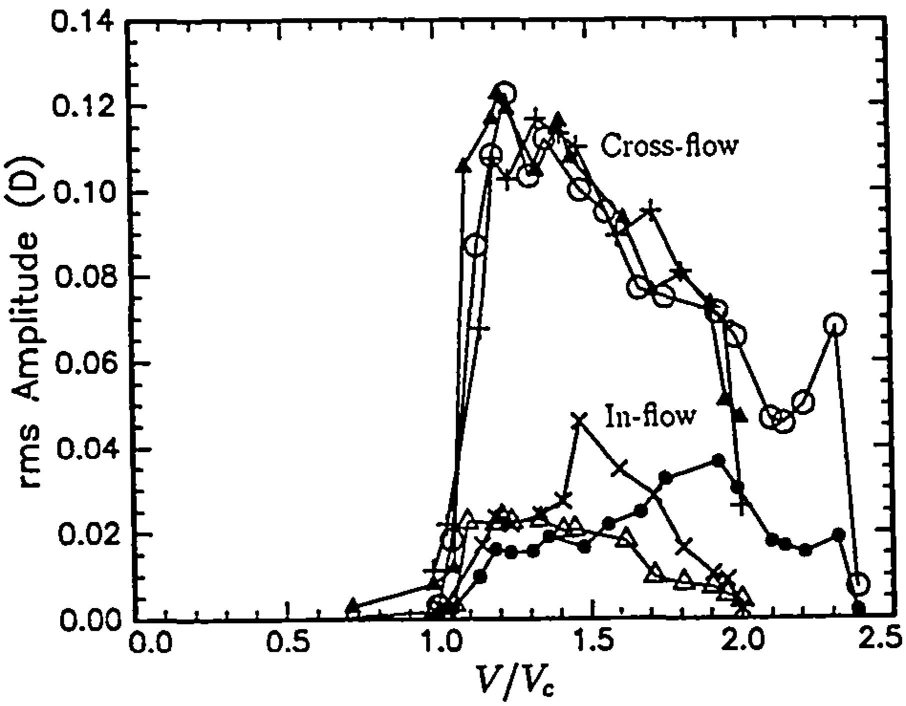

Figure 5.18: Response amplitudes in cross- and in-flow directions for various material combinations: ($\triangle, \blacktriangle$) brass/brass (b/b); ($+, \times$) brass/st. steel (b/s); ($\circ, \bullet$) brass/Delrin (b/d).

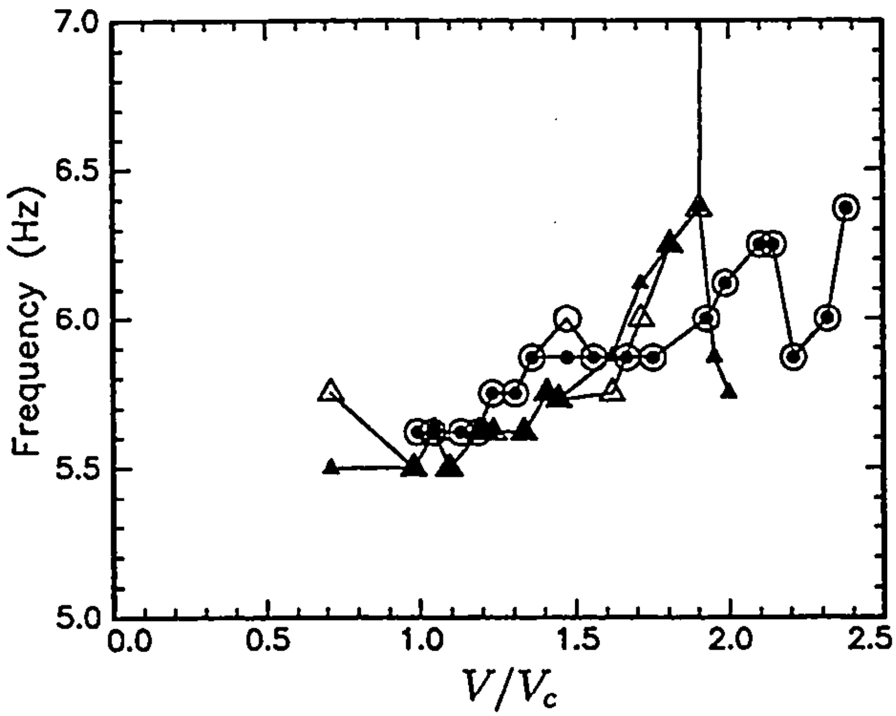

Figure 5.19: Response frequencies for different material combinations: (△, ▲) brass/brass (b/b); (∘, •) brass/Delrin (b/d).

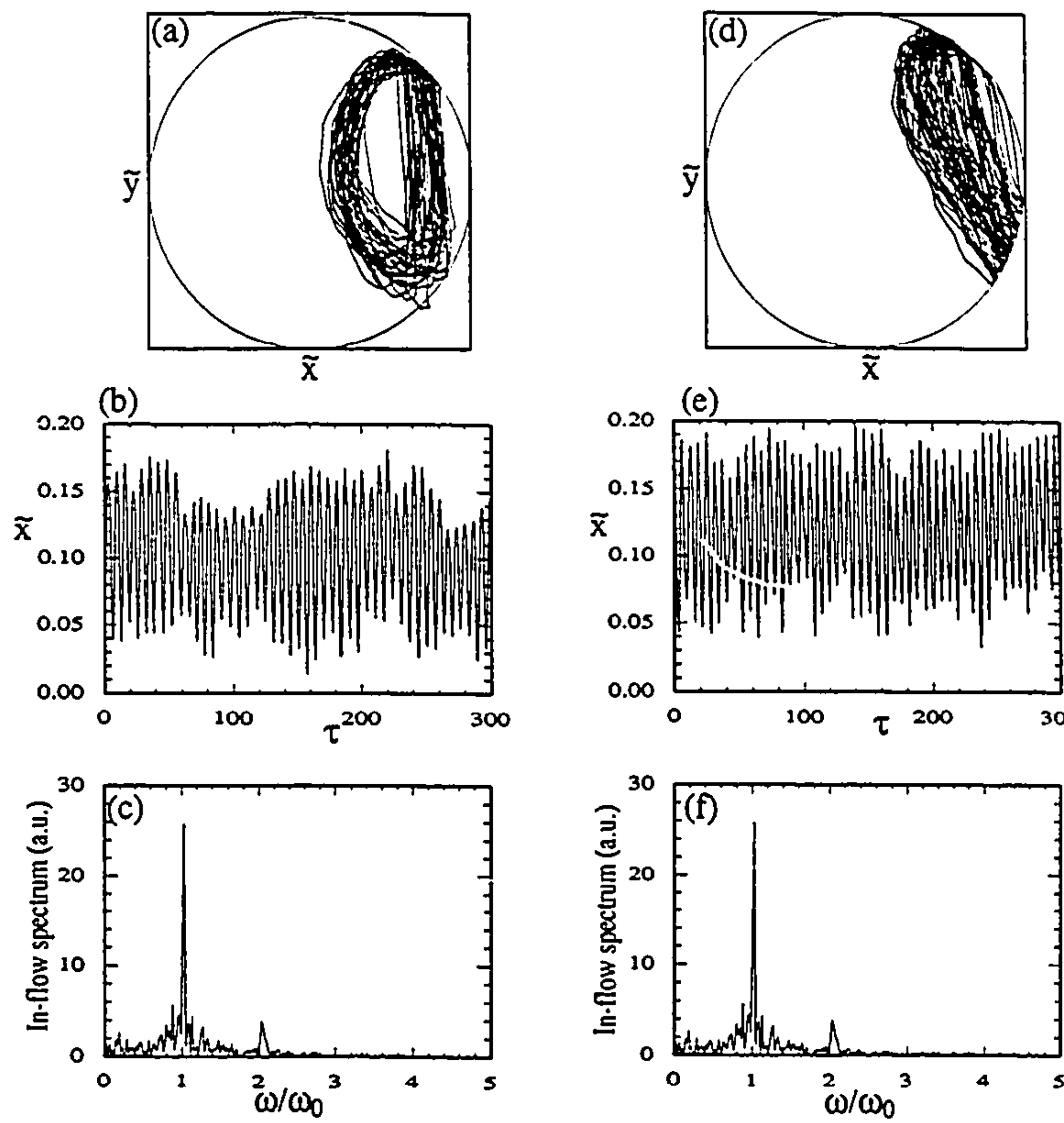

Figure 5.20: Cylinder response for brass/Delrin (b/d) impacting for: (a-c) $V = 1.60V_c$; (d-f) $V = 1.90V_c$; (a,d) show the motion projected in the $(\tilde{x}, \tilde{y})$ plane; (b,c) are in-flow time traces; (d,e) the corresponding power spectra; the gap size, $\tilde{e}_r = 0.200$.

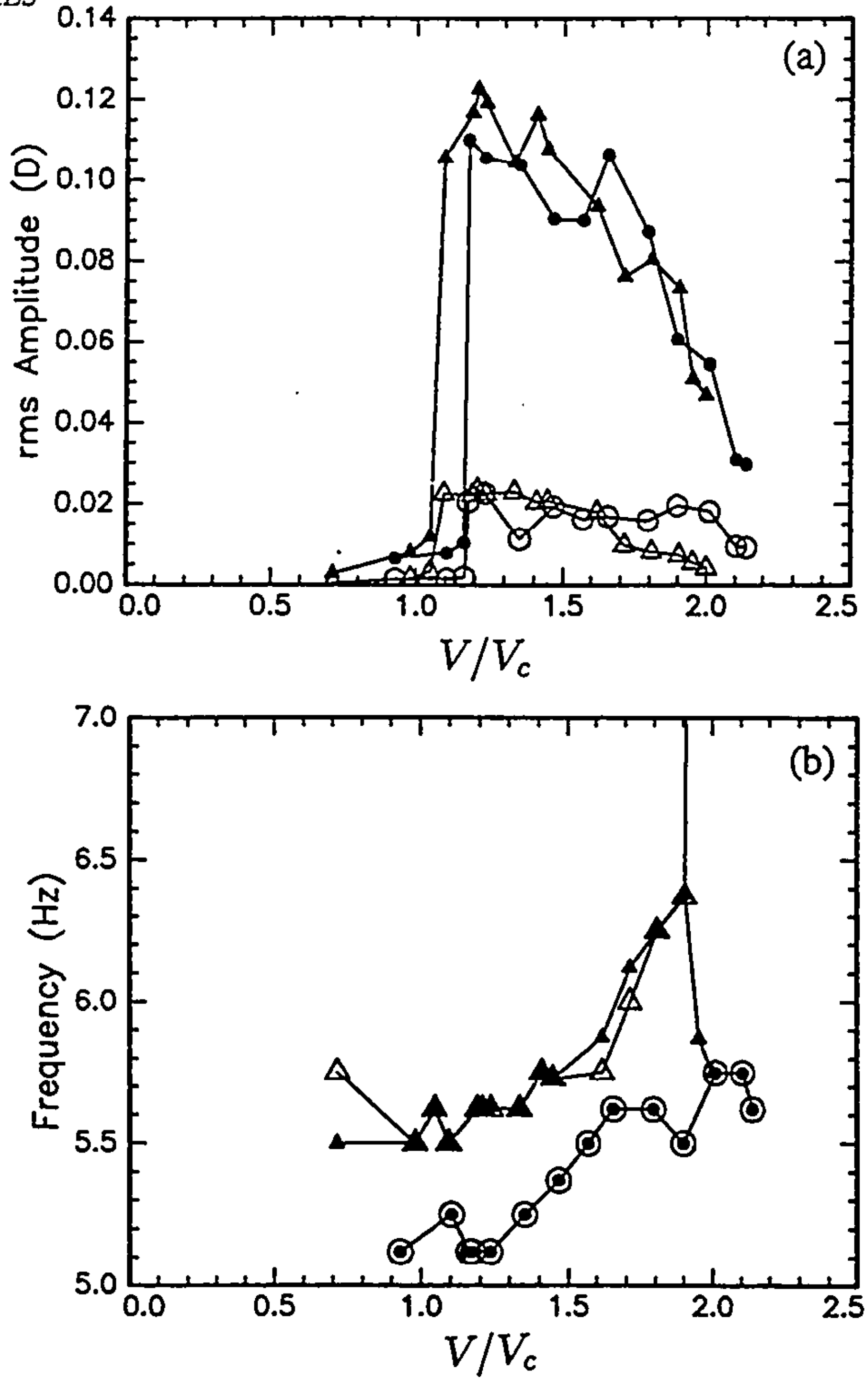

Figure 5.21: Comparison of wet and dry impacting response: (a) rms amplitudes; (b) corresponding frequencies. In both cases: ($\triangle, \blacktriangle$) dry; ($\circ, \bullet$) wet; with open symbols representing in-flow response.

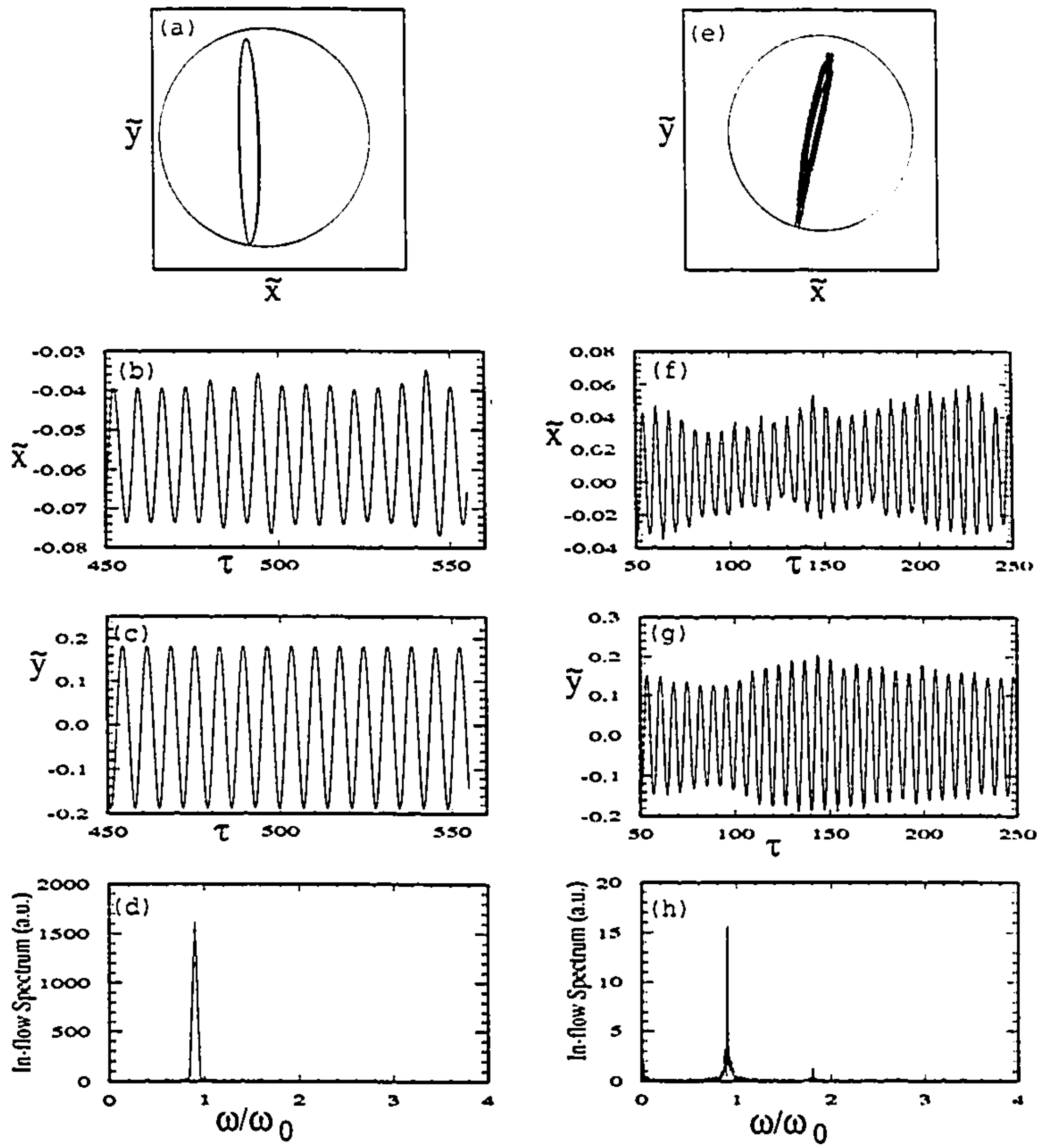

Figure 5.22: Cylinder response at $V = 1.10V_c$: (a-d) theory; (e-h) experiment; (a) and (e) show motion in the $(\tilde{x}, \tilde{y})$ plane; (b) and (f) are in-flow time traces; (c) and (g) are cross-flow time traces; (e) and (h) are power spectra for in-flow motion.

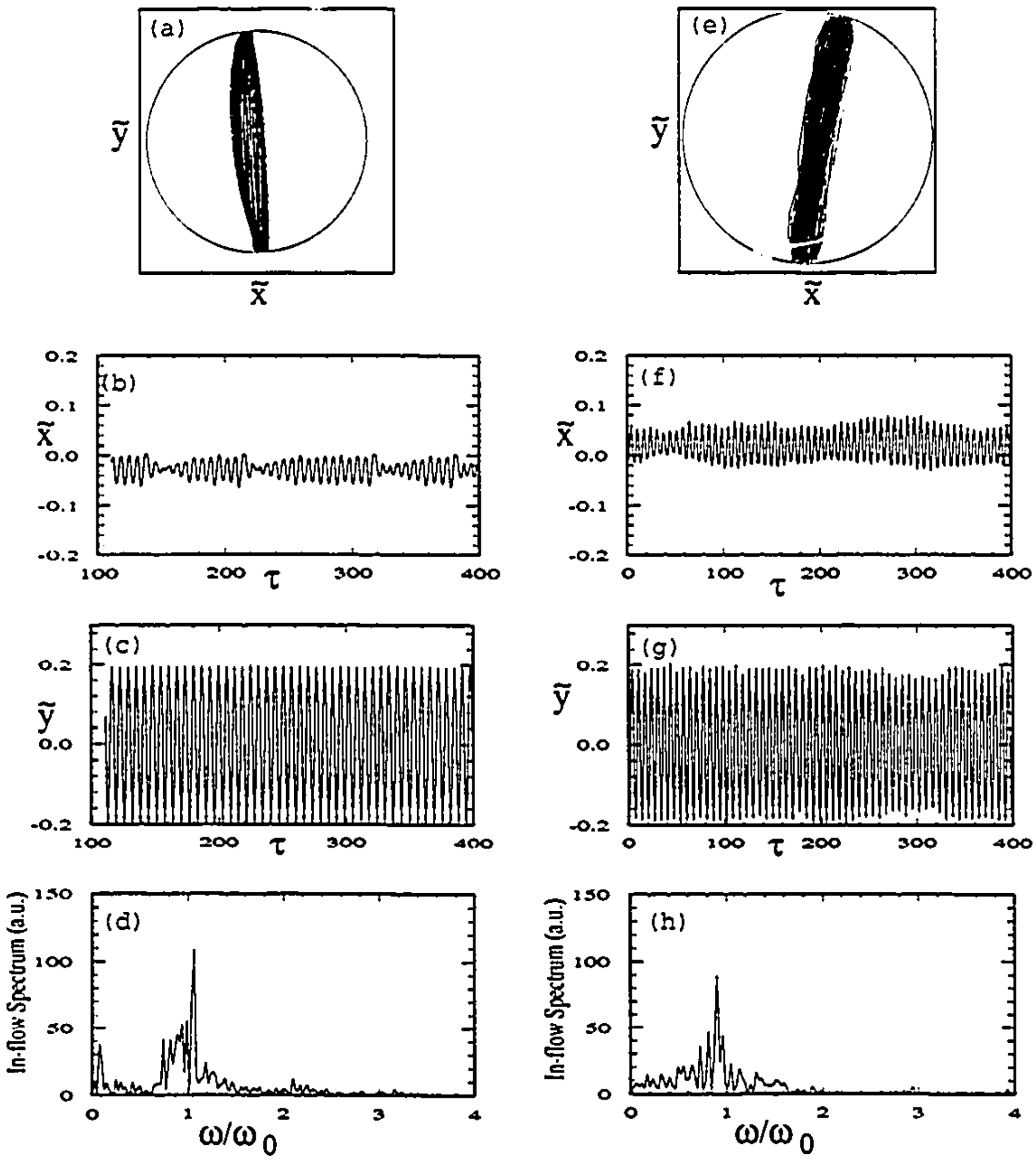

Figure 5.23: The double-sided impacting response: (a-d) theory, $V = 1.29V_c$; (e-h) experiment, $V = 1.21V_c$; (a) and (e) show motion in the $(\tilde{x}, \tilde{y})$ plane; (b) and (f) are in-flow time traces; (c) and (g) are cross-flow time traces; (e) and (h) are power spectra for in-flow motion.

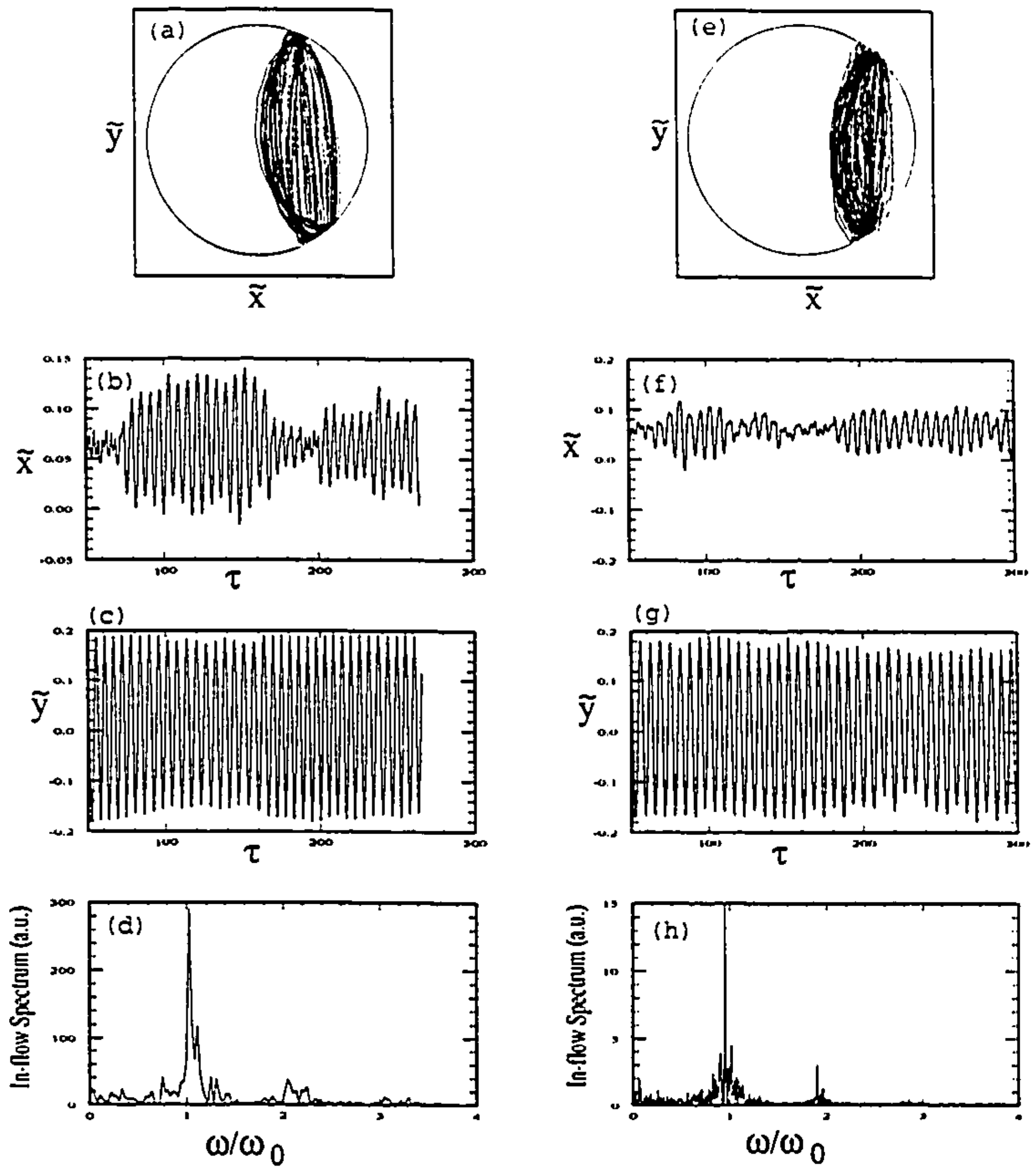

Figure 5.24: Cylinder response in the intermittency regime: (a-d) theory, $V = 1.76V_c$; (e-h) experiment, $V = 1.62V_c$; (a) and (e) show motion in the $(\tilde{x}, \tilde{y})$ plane; (b) and (f) are in-flow time traces; (c) and (g) are cross-flow time traces; (e) and (h) are power spectra for in-flow motion.

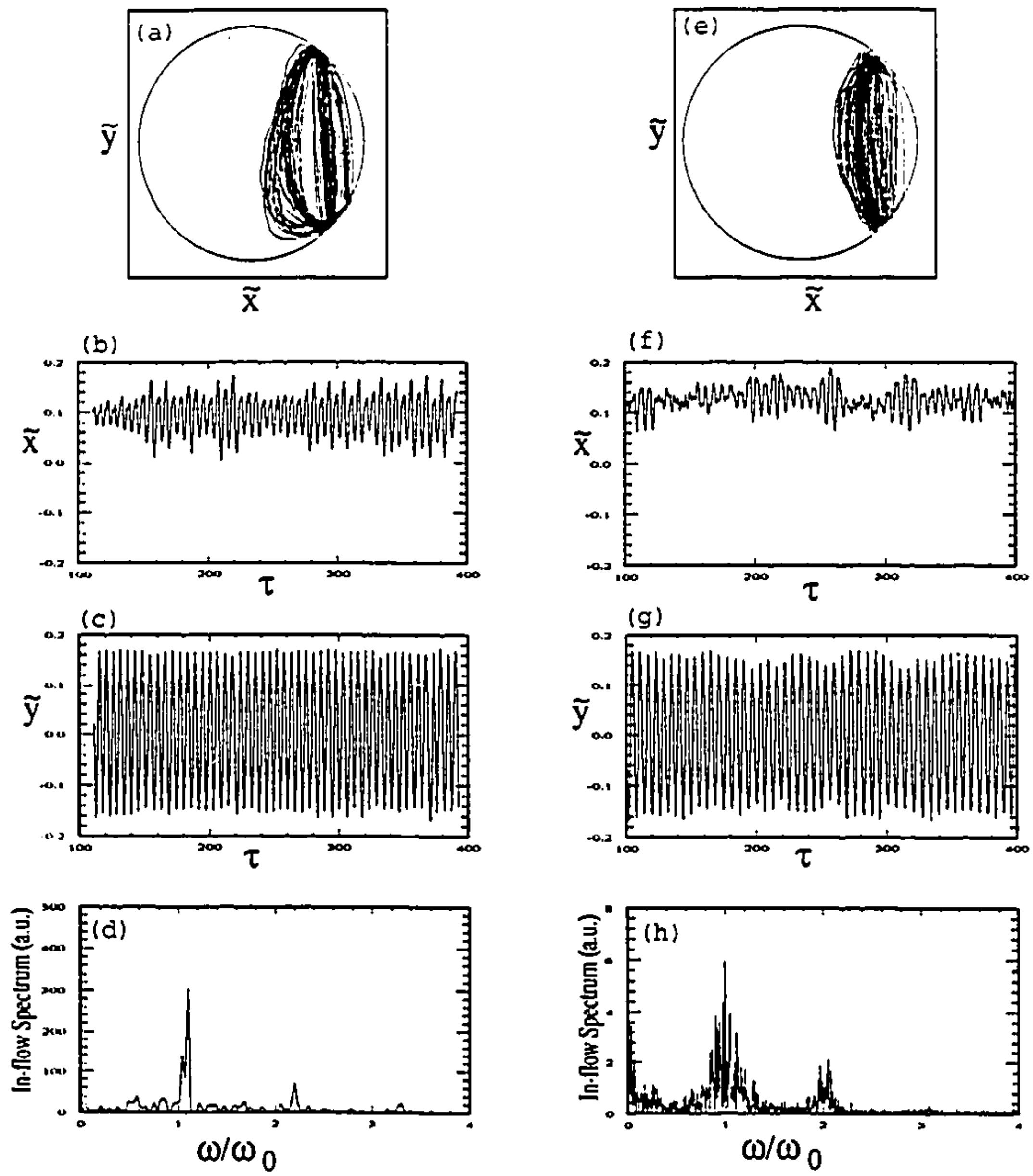

Figure 5.25: Cylinder response in the intermittency regime: (a-d) theory, $V = 1.90V_c$; (e-h) experiment, $V = 1.71V_c$; (a) and (e) show motion in the $(\tilde{x}, \tilde{y})$ plane; (b) and (f) are in-flow time traces; (c) and (g) are cross-flow time traces; (e) and (h) are power spectra for in-flow motion.

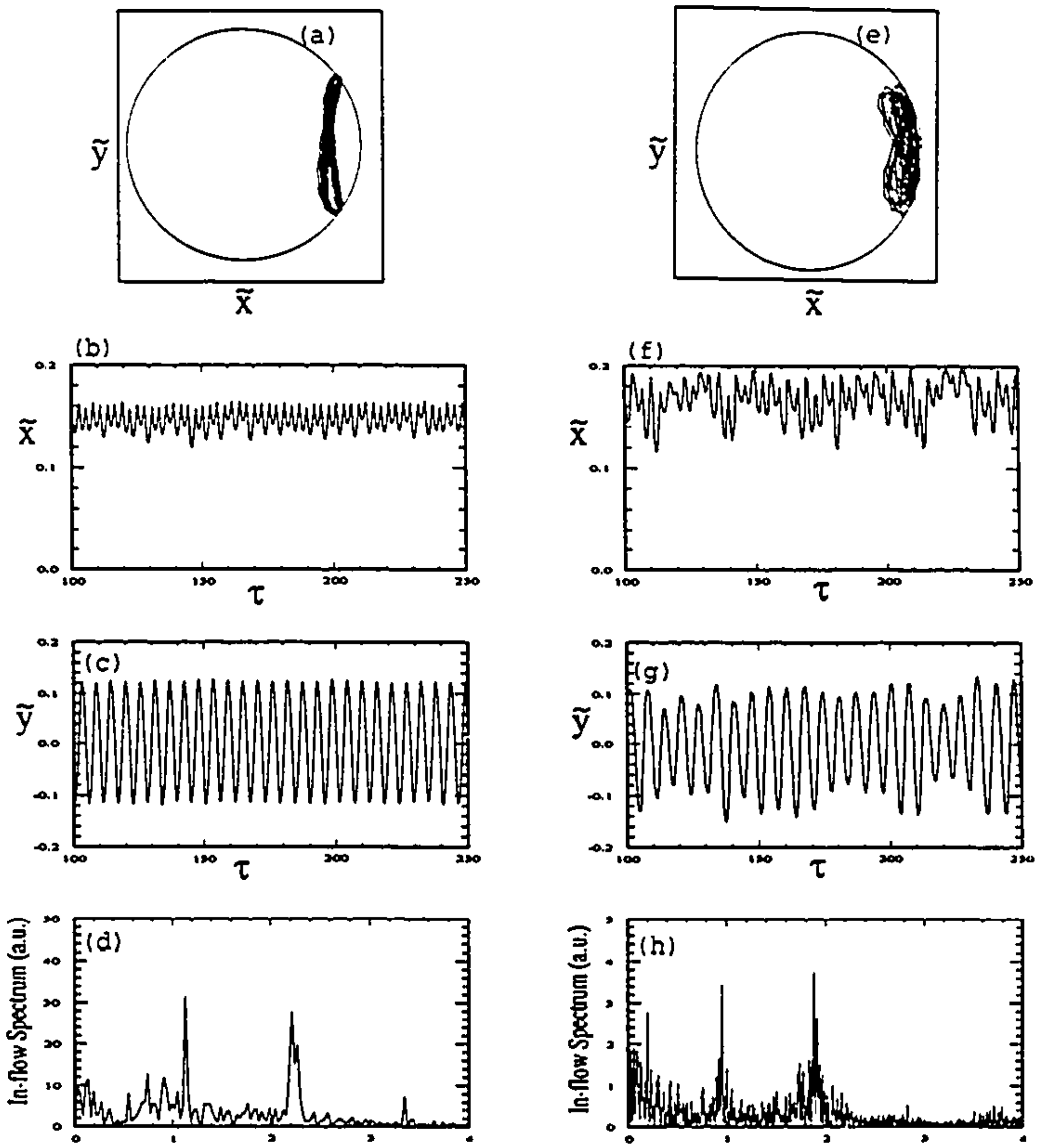

Figure 5.26: Final figure-of-eight orbital motion: (a-d) theory, $V = 2.10V_c$; (e-h) experiment, $V = 1.95V_c$; (a) and (e) show motion in the $(\tilde{x}, \tilde{y})$ plane; (b) and (f) are in-flow time traces; (c) and (g) are cross-flow time traces; (e) and (h) are power spectra for in-flow motion.

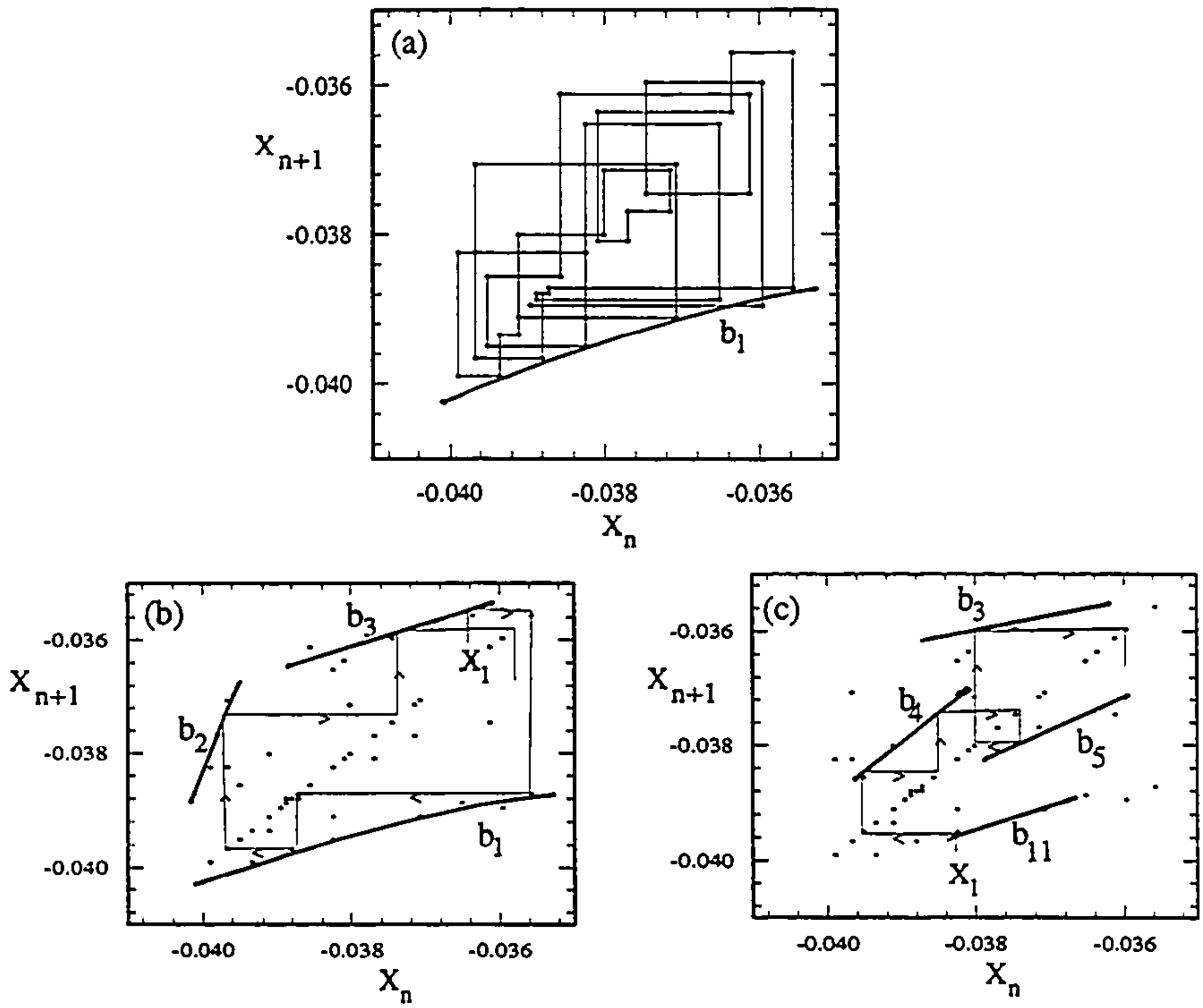

Figure 5.27: (a) Poincaré return map extracted from the theoretical in-flow response at $V = 1.10V_c$: (b) type A trajectory; (c) type B trajectory.

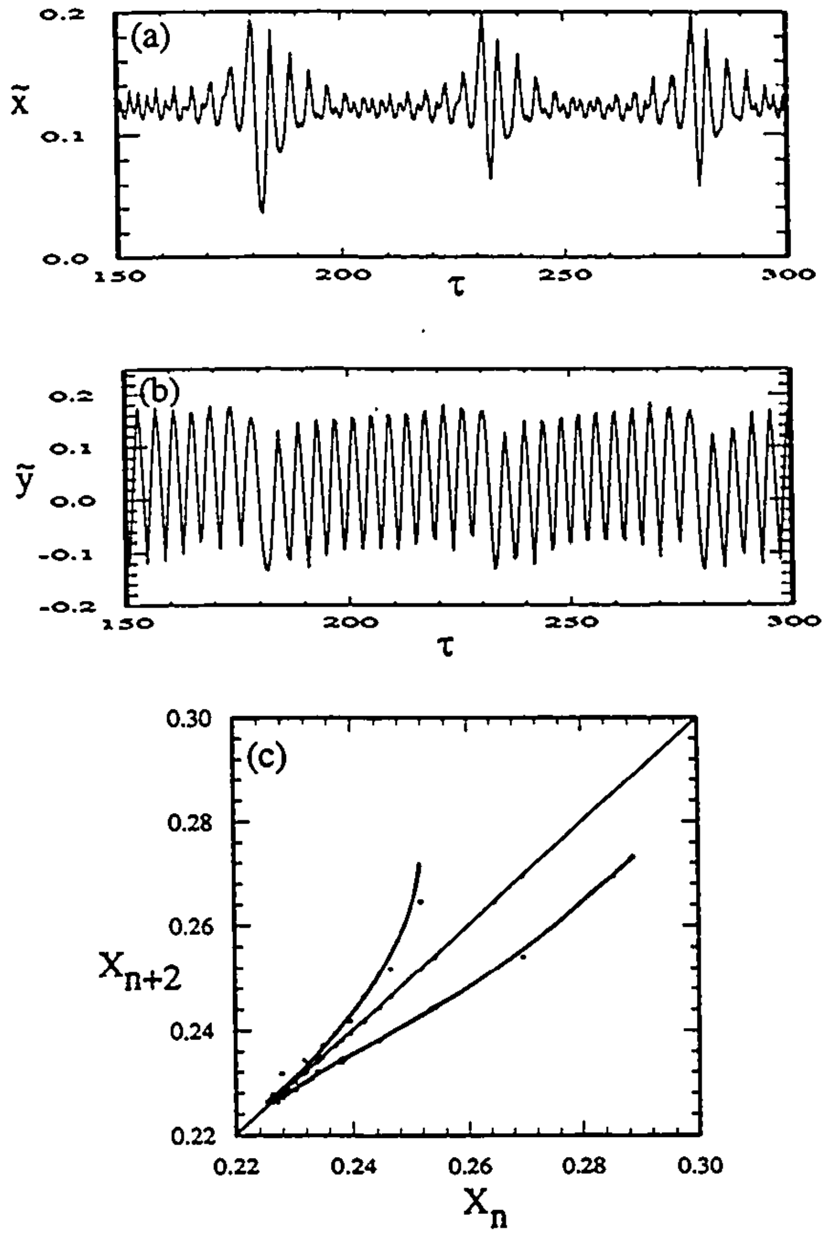

Figure 5.28: Intermittency response from the one-mode model for $V = 2V_c$: (a) in-flow response; (b) cross-flow response; (c) Poincaré second return map from in-flow response.

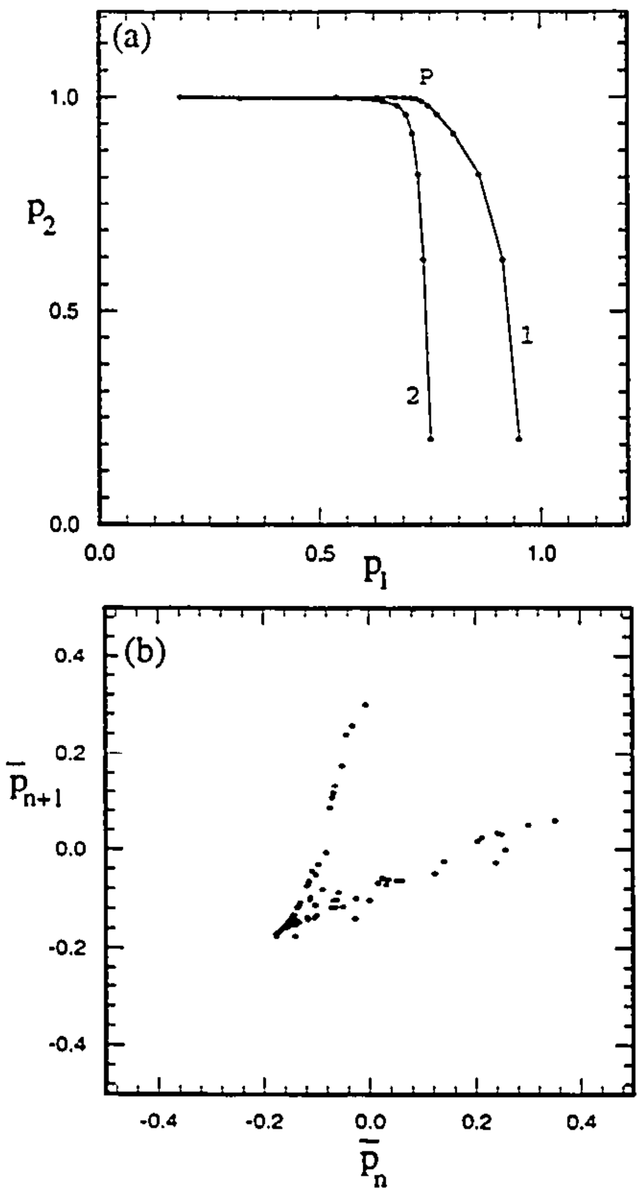

Figure 5.29: Iterations of the modified baker's transformation for two typical trajectories. (b) Return map of a projection onto a direction similar to that of the return map of Fig.5-28(c).

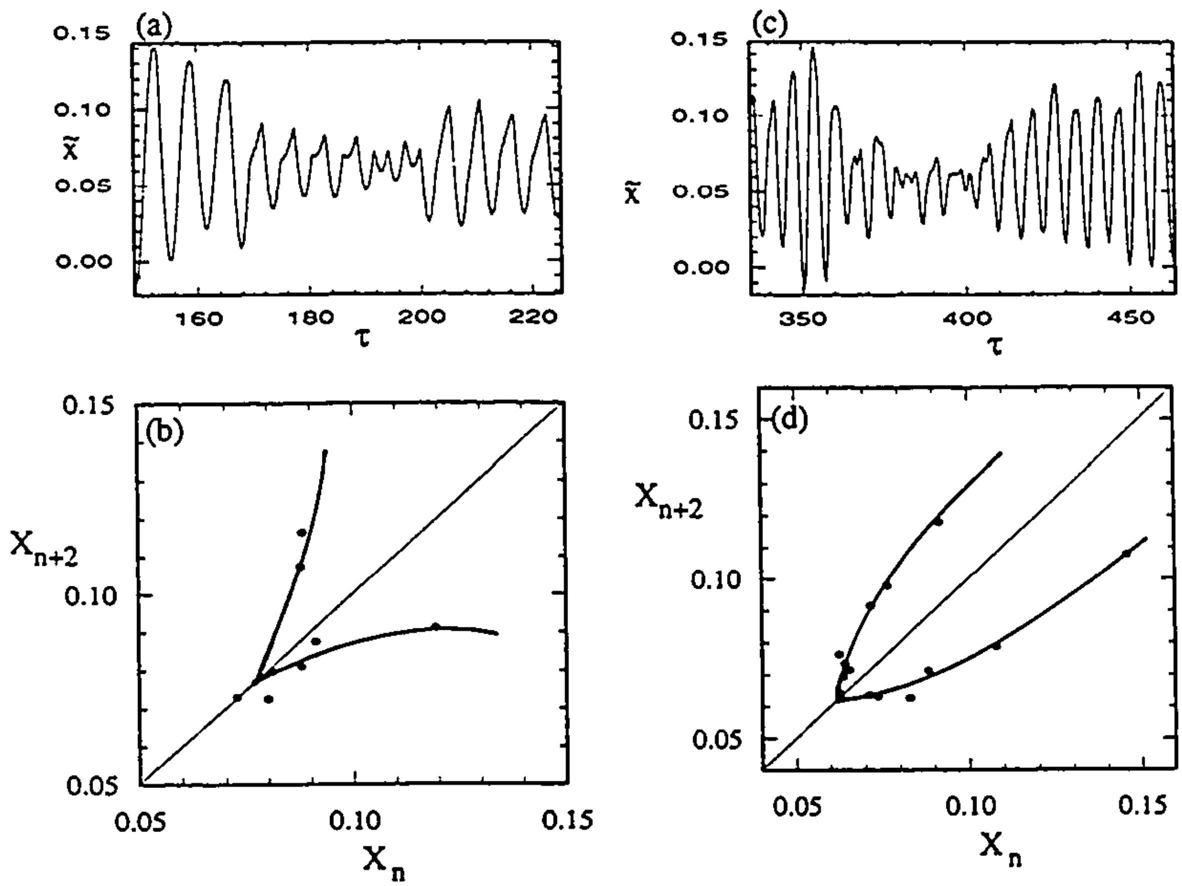

Figure 5.30: (a) Theoretically predicted in-flow laminar phase response at $V = 1.76V_c$; (b) corresponding Poincaré second return map; (c) experimentally measured in-flow laminar phase response at $V = 1.62V_c$; (d) corresponding Poincaré second return map.

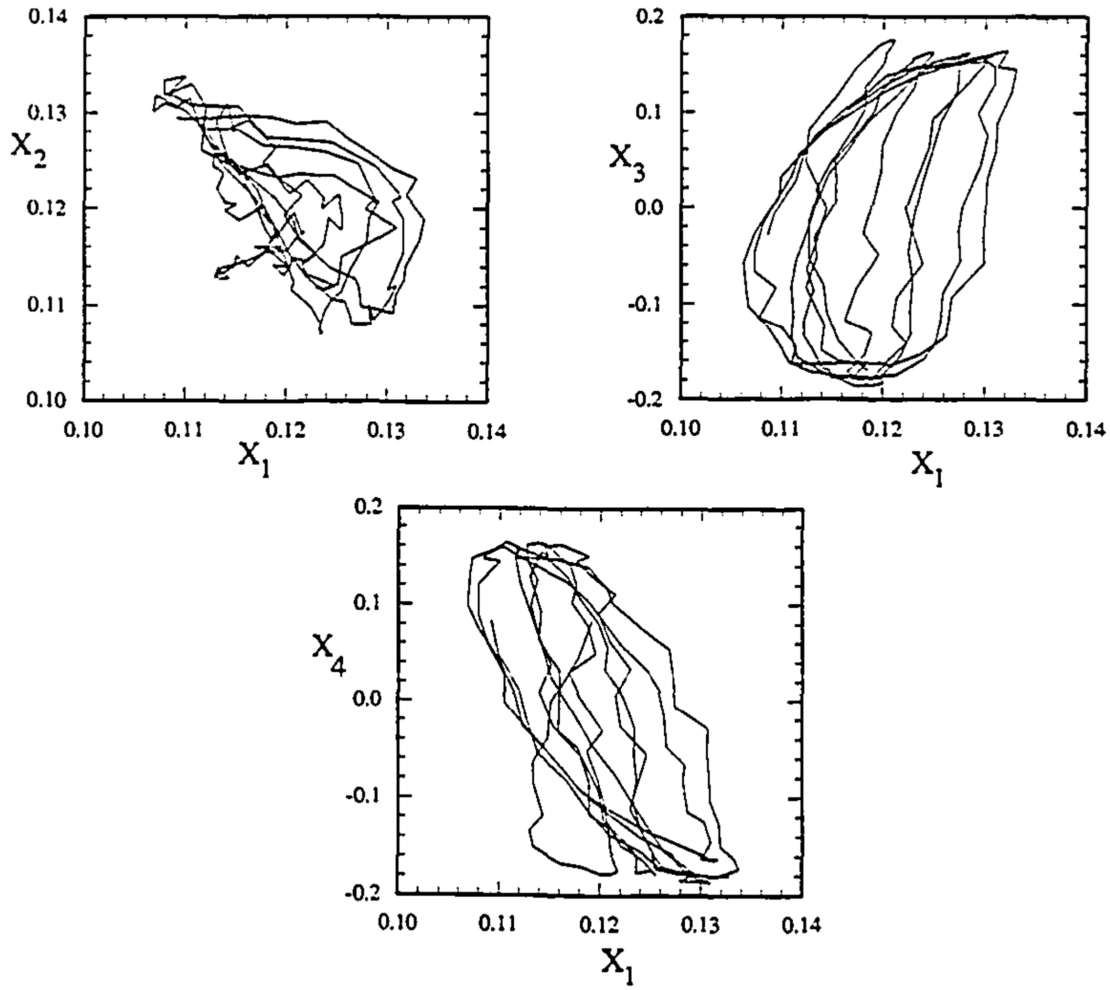

Figure 5.31: 2-D projections of the 4-D reconstructed pseudo-phase space for $V = 1.62V_c$.

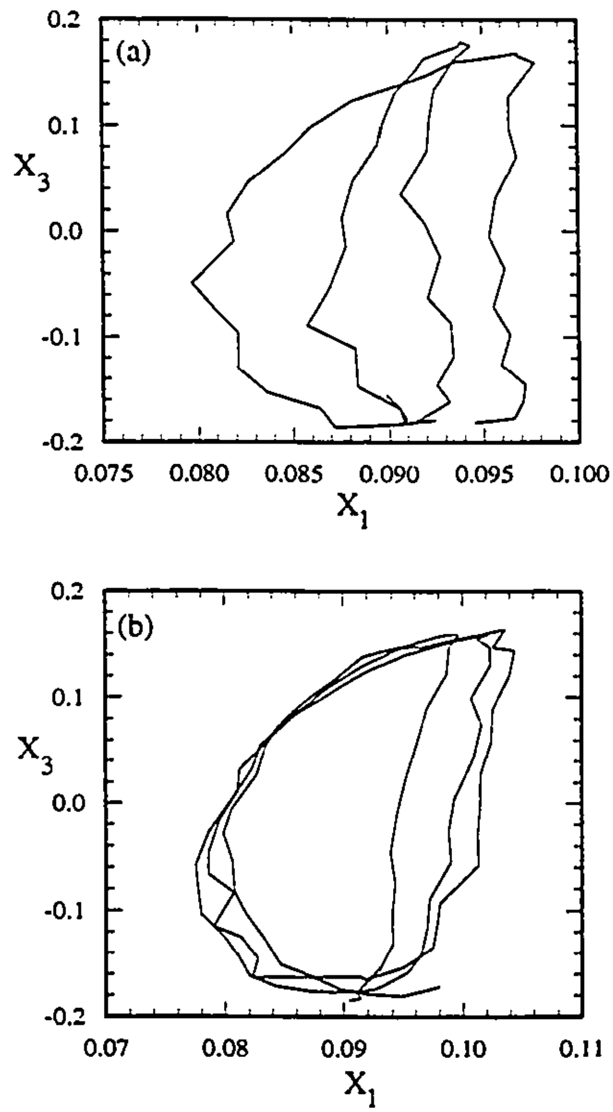

Figure 5.32: Experimental saddle orbits for $V = 1.62V_c$: (a) period-2; (b) period-3.

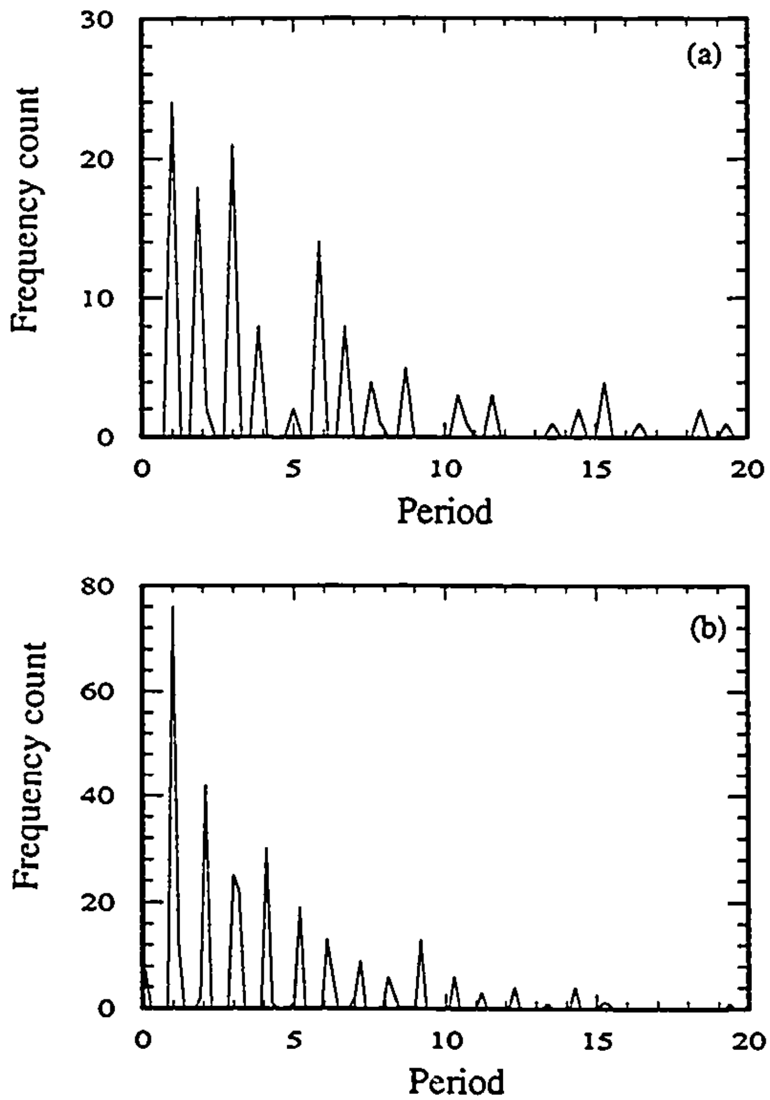

Figure 5.33: Histograms of frequency distribution of saddle orbits for $V = 1.62V_c$: (a) experiment; (b) theory.

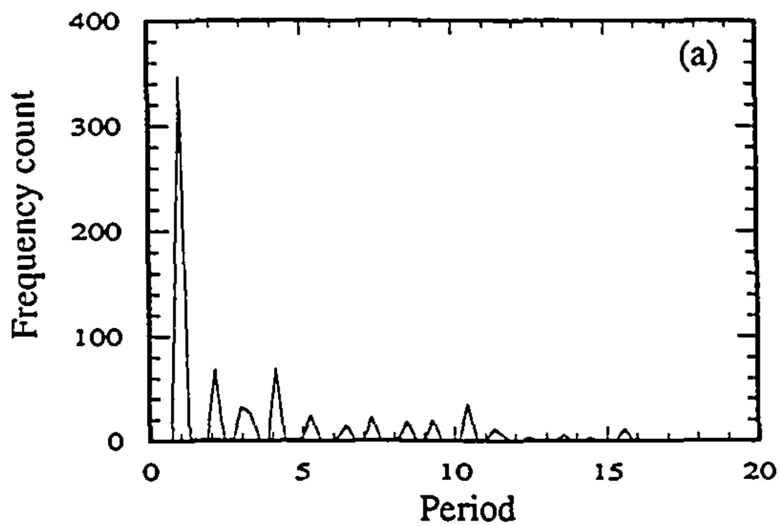

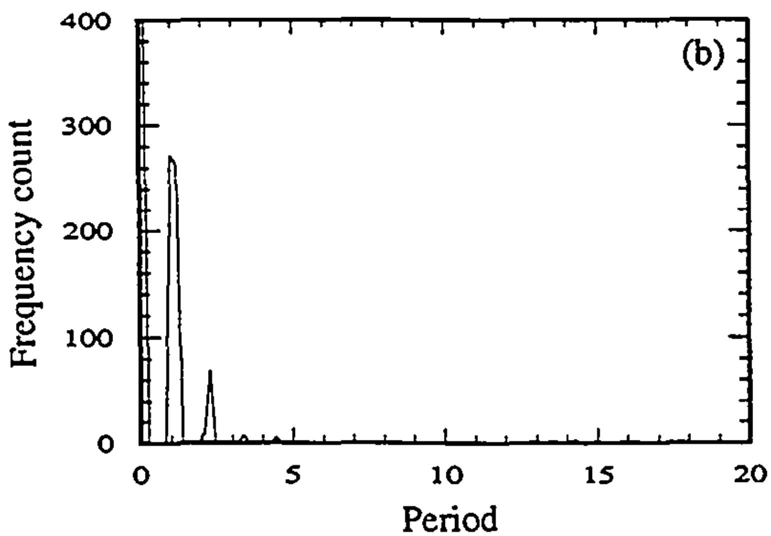

Figure 5.34: Histograms of frequency distribution of saddle orbits for $V = 1.20V_c$: (a) experiment; (b) theory.

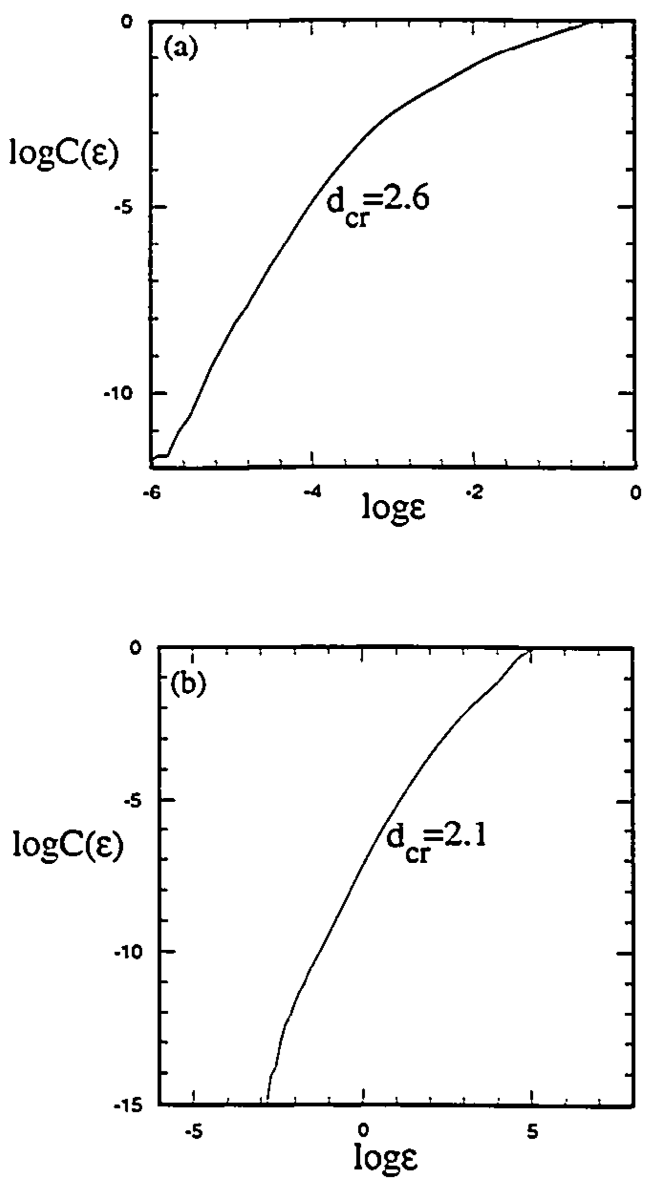

Figure 5.35: Correlation dimension for $V = 1.20V_c$: (a) experiment; (b) theory.

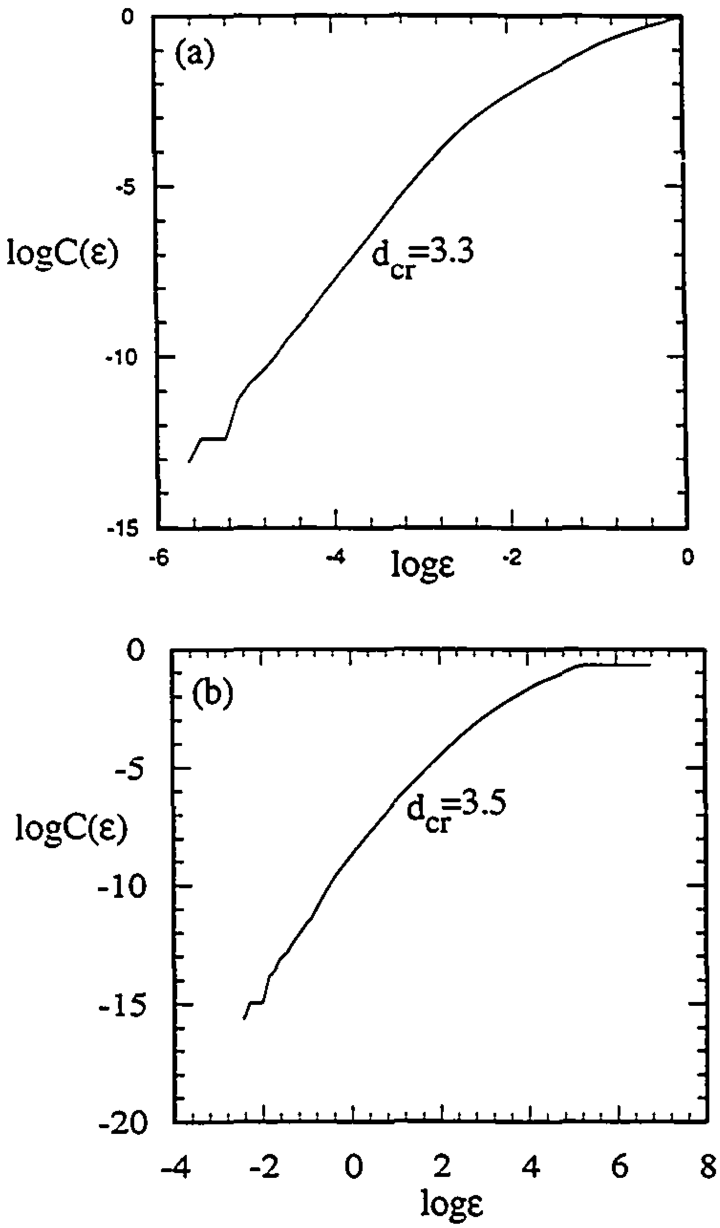

Figure 5.36: Correlation dimension for $V = 1.62V_c$: (a) experiment; (b) theory.

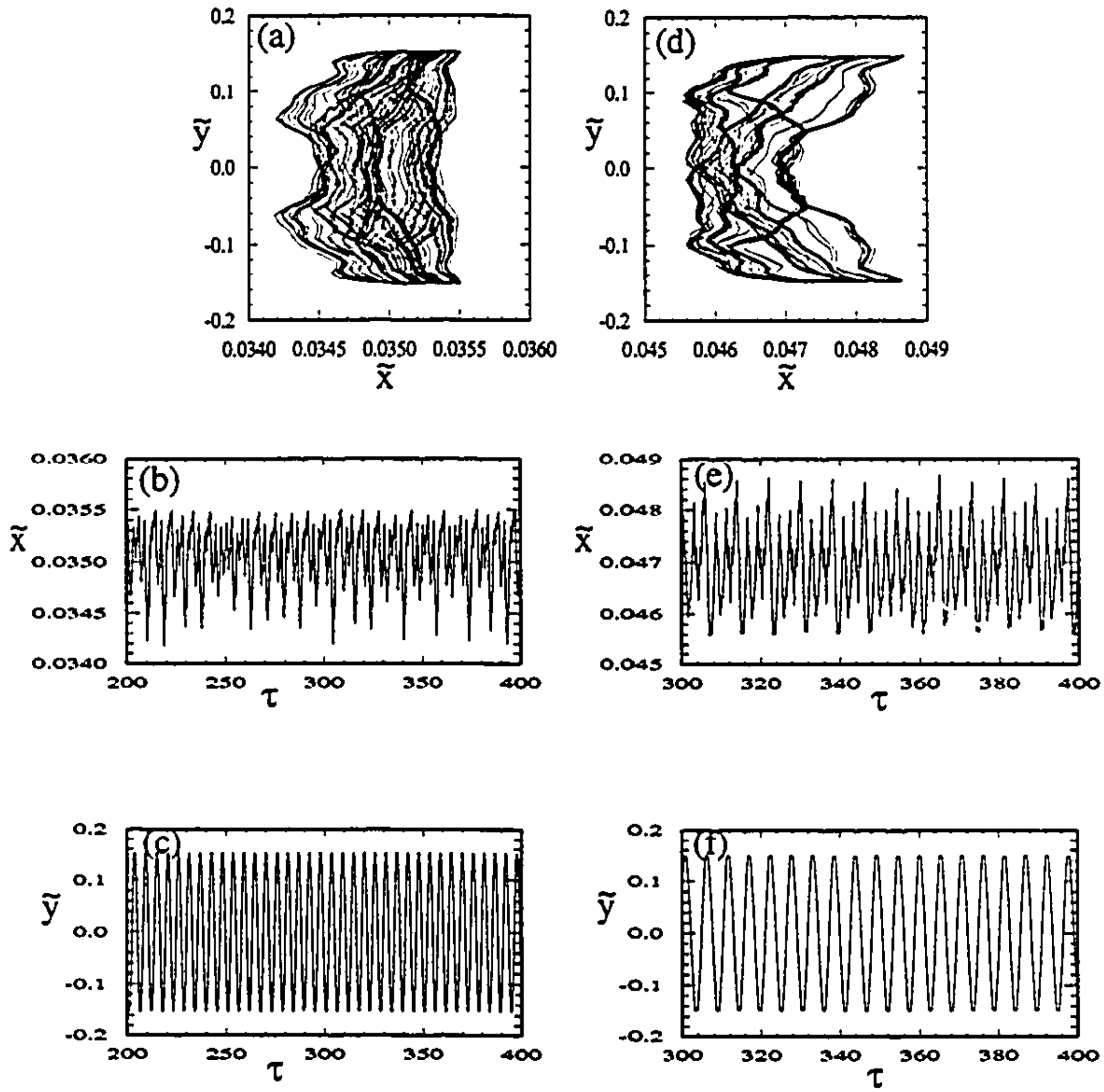

Figure 6.1: (a-c) The complex-periodic response, for $V = 1.25V_c$, occurring at onset of impacting; (d-f) period-6 response at $V = 1.30V_c$; (a) and (d) show motion in the $(\tilde{x}, \tilde{y})$ plane; (b) and (e) depict the in-flow responses for the two flow velocities; (c) and (e) are the corresponding cross-flow responses.

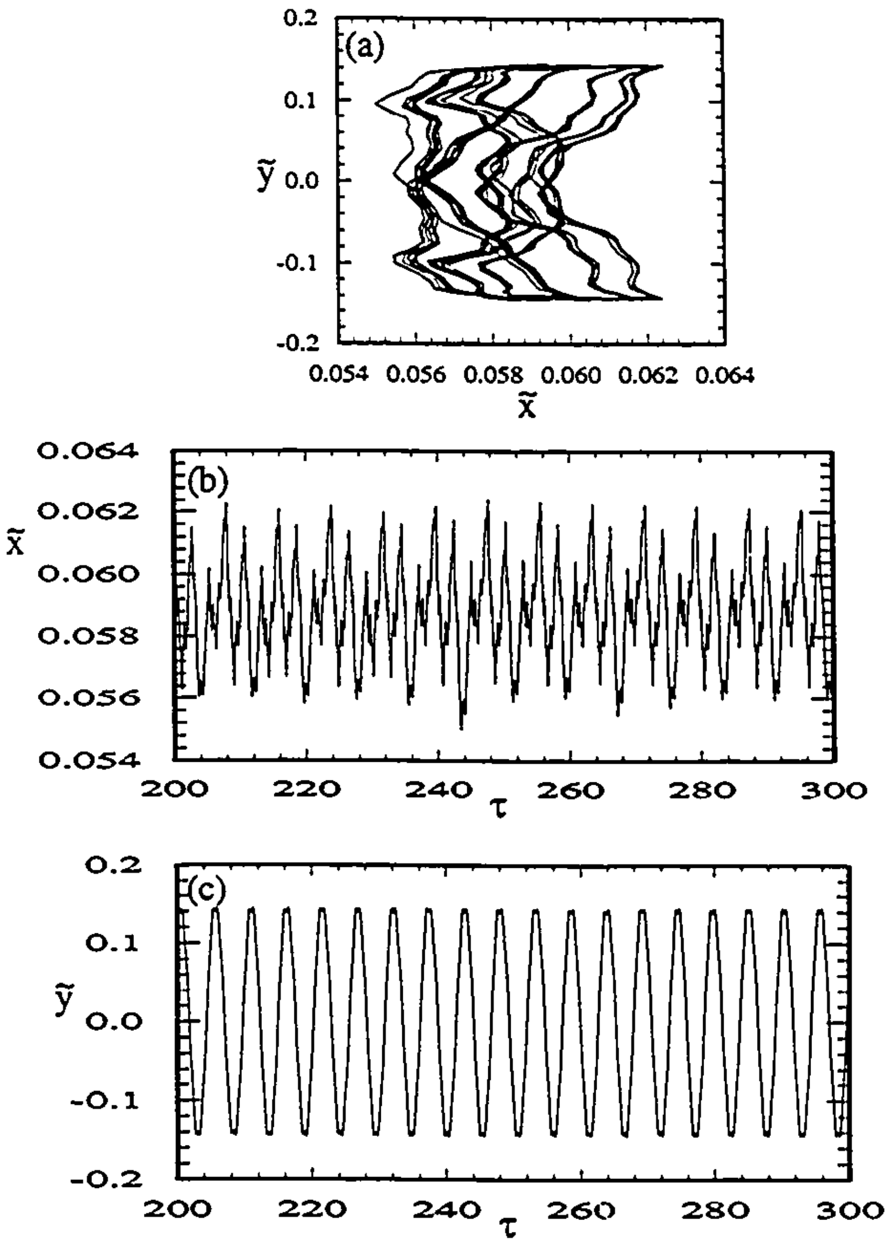

Figure 6.2: Periodic motion exhibited by the uniform cylinder for $V = 1.35V_c$; (a) motion in the $(\tilde{x}, \tilde{y})$ plane; (b) in-flow time trace; (c) cross-flow time trace.

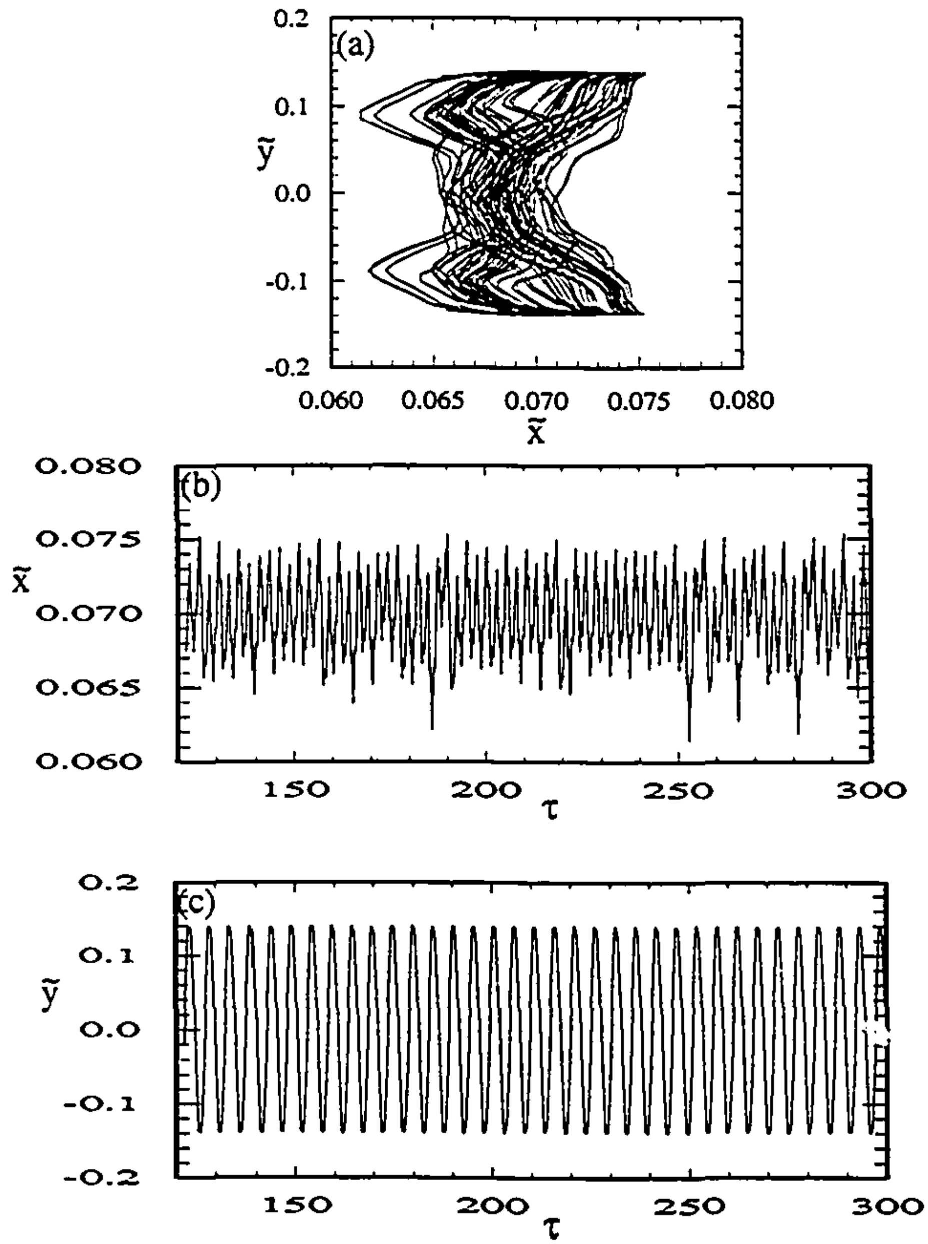

Figure 6.3: Cylinder response in the intermittency velocity range: the flow velocity $V = 1.40V_c$; part (a) shows motion in the $(\tilde{x}, \tilde{y})$ plane; (b) the in-flow time trace; and (c), the cross-flow time response.

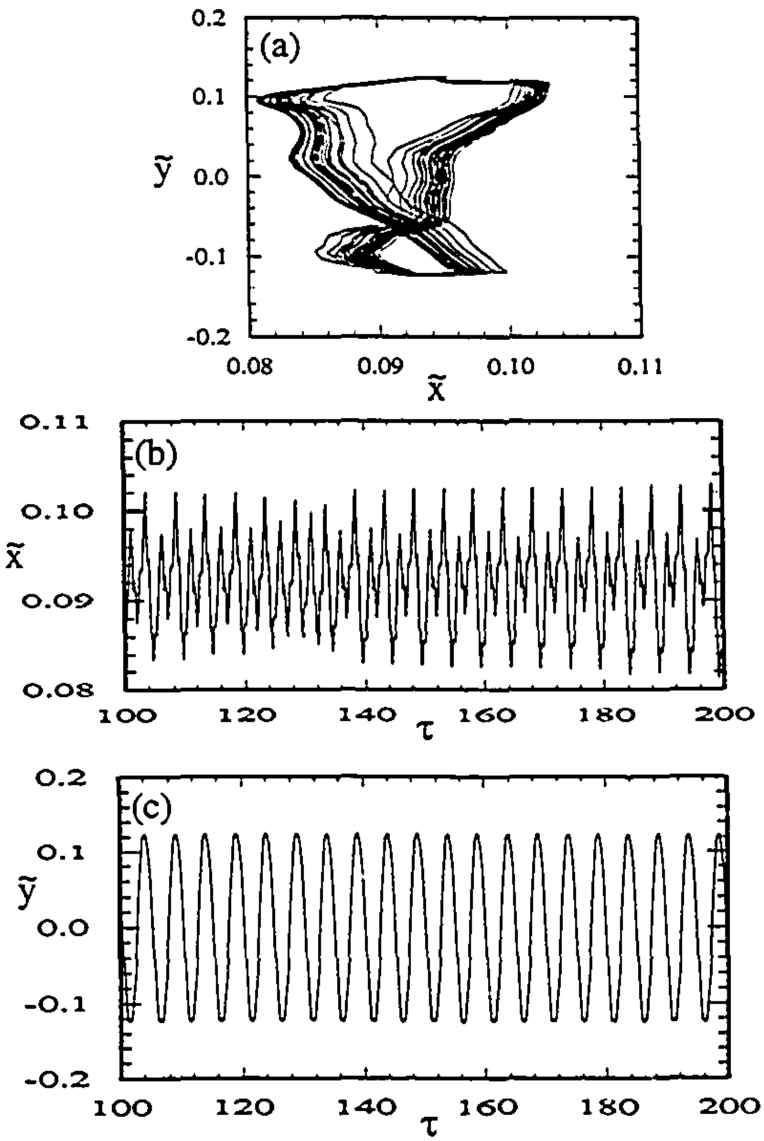

Figure 6.4: Cylinder response for $V = 1.45V_c$ showing reorganization of the response to periodic motion; (a) projection onto the $(\tilde{x}, \tilde{y})$ plane; (b) in-flow and (c) cross-flow time responses.

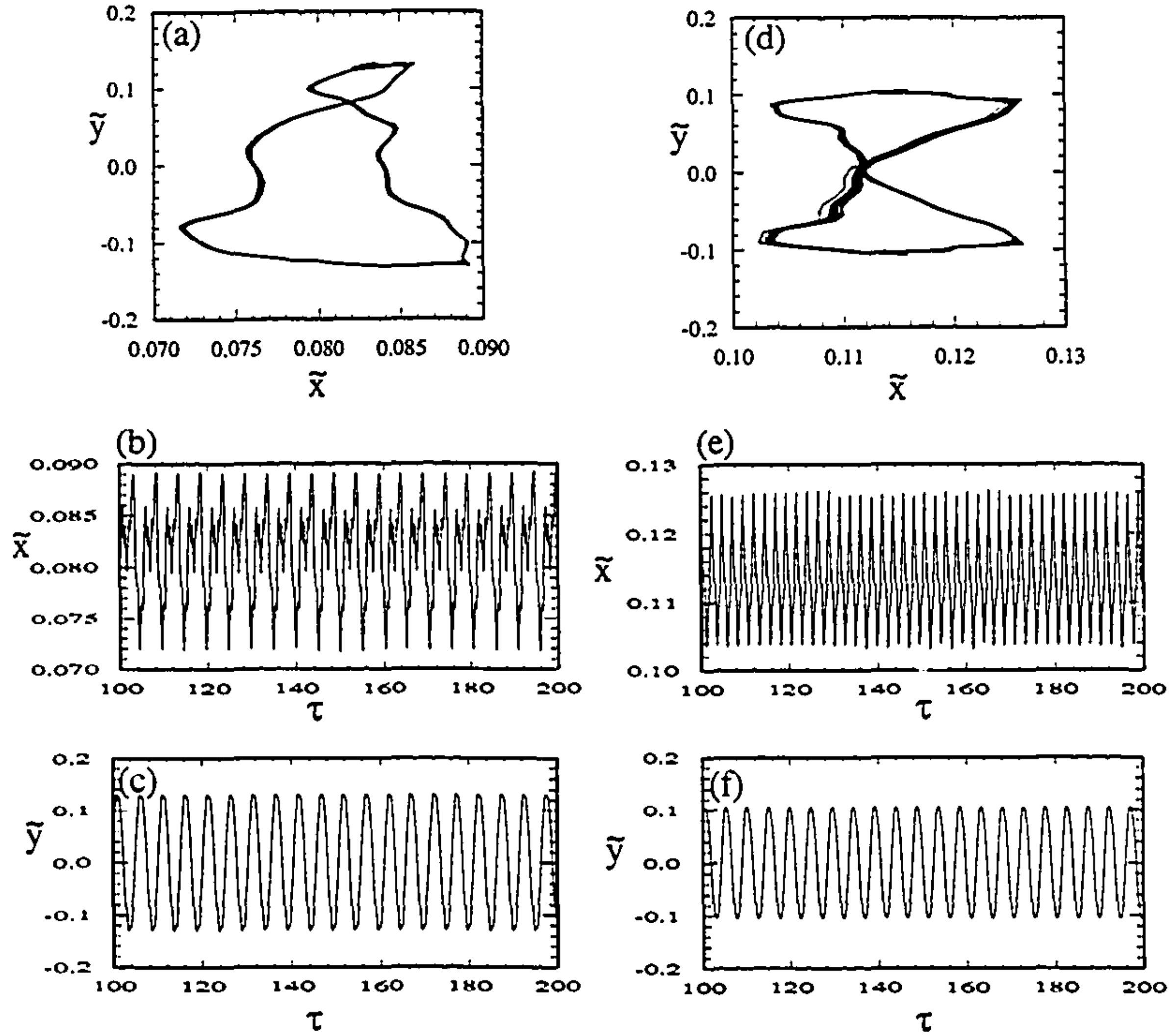

Figure 6.5: The final periodic response for (a-c) $V = 1.50V_c$; (d-f) $V = 1.60V_c$; (a) and (d) show motion in the $(\tilde{x}, \tilde{y})$ plane; (b) and (e) depict the in-flow responses for the two flow velocities; (c) and (e) are the corresponding cross-flow responses.

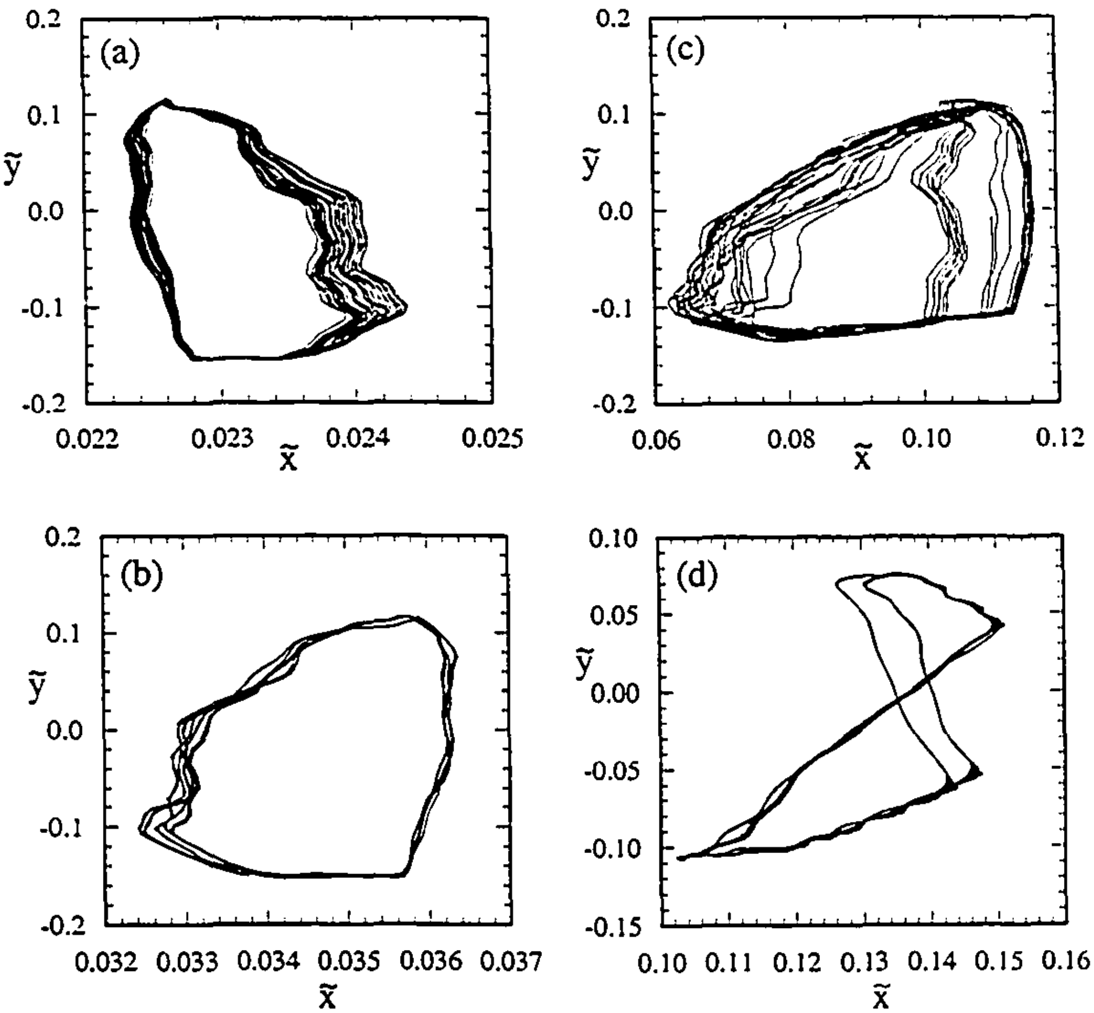

Figure 6.6: Effect of initial cross-flow eccentricity on uniform cylinder response; motion in the $(\tilde{x}, \tilde{y})$ plane is shown for various flow velocities: (a) $V = 1.20V_c$; (b) $V = 1.25V_c$; (c) $V = 1.60V_c$; (d) $V = 1.73V_c$;

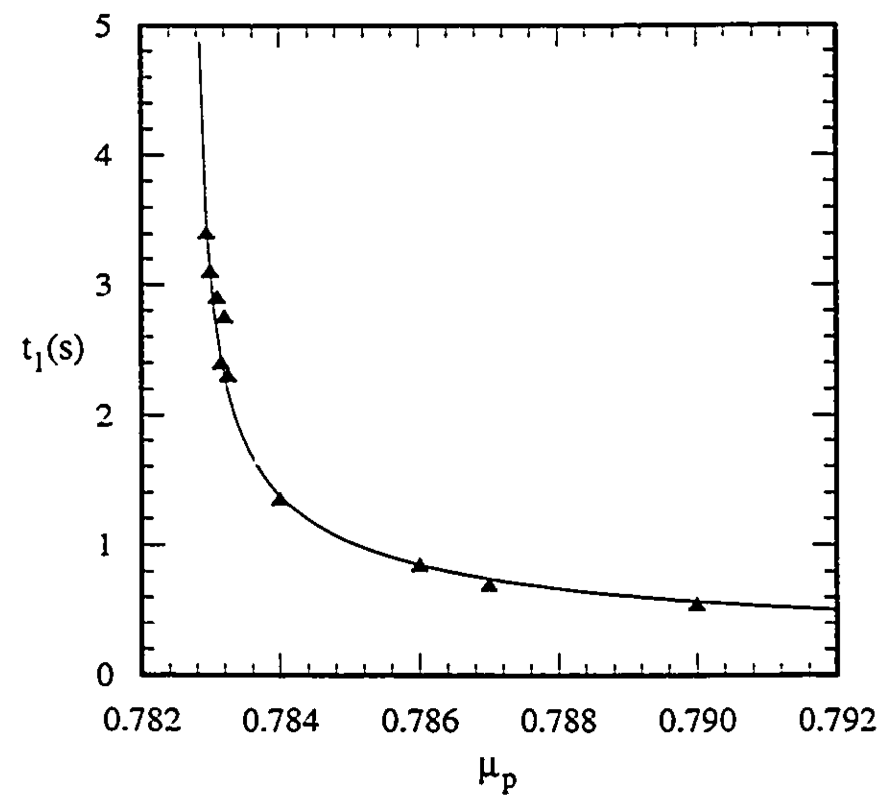

Figure 6.7: Duration of laminar phases as a function of the intermittency parameter μ_p for the 1-d.o.f system studied in Chapter 4. Superimposed on the data is the analytical approximation.

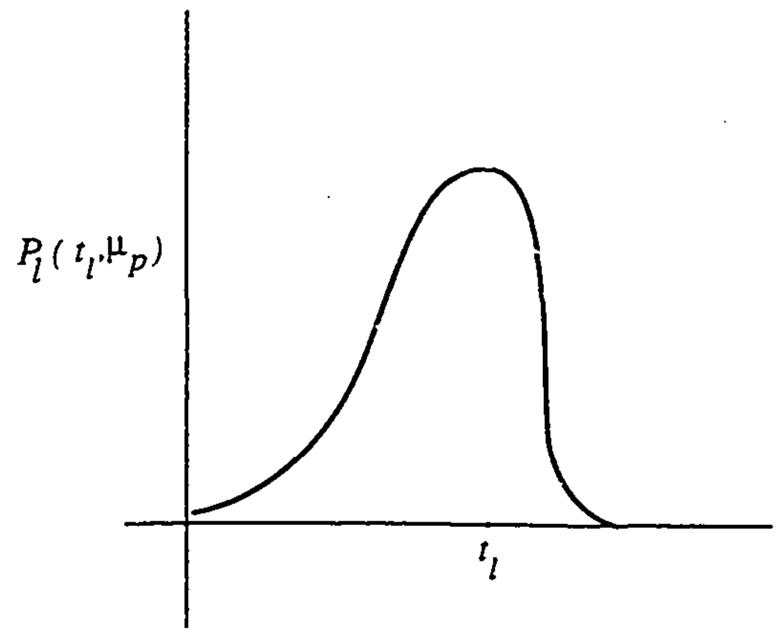

Figure 6.8: Qualitative depiction of expected probability distribution of laminar phases for type I intermittency.

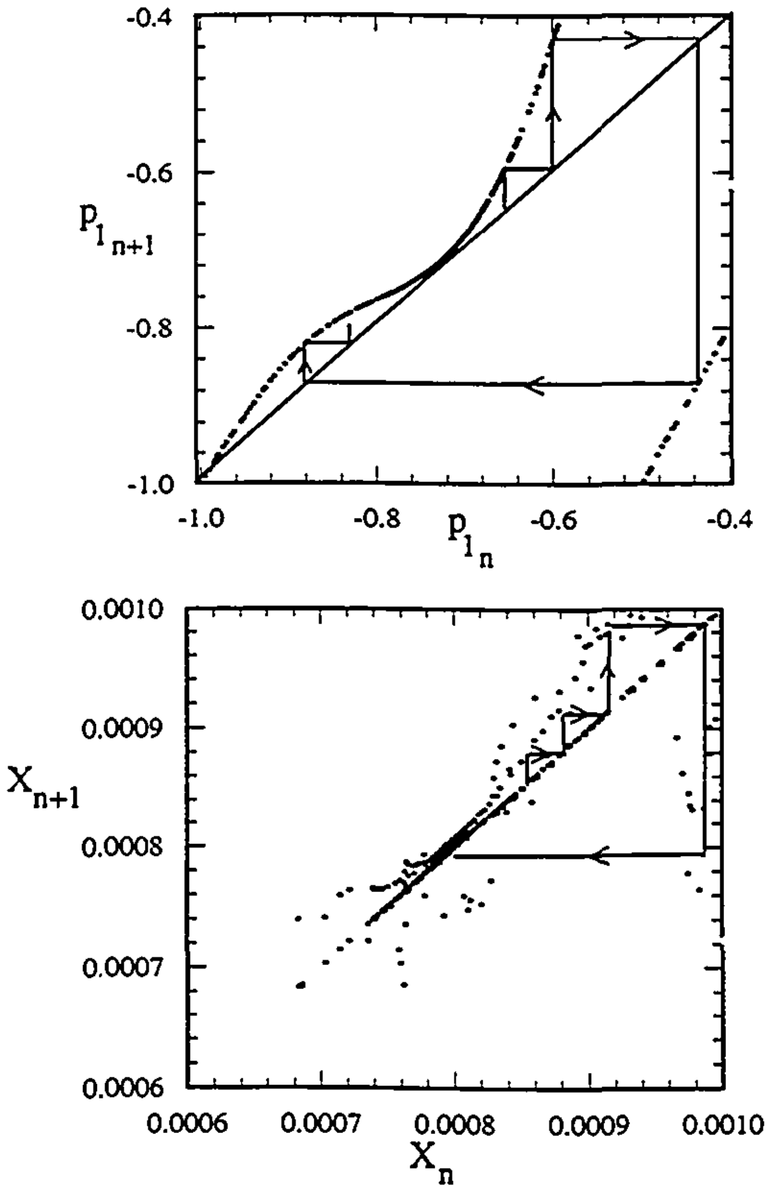

Figure 6.9: Demonstration of the relaminarization process in (a) the baker's transformation, and (b) the 1-d.o.f. system of Chapter 4.

APPENDIX I

DETERMINATION OF SYSTEM MATRICES AND FORCE VECTORS

(Case shown is for two mode expansion)

```
(* INPUT PHYSICAL SYSTEM PARAMETERS *)

l=0.154; lw=.3915; l2=.50841;

n=2;

phi1f=phi1exactf; phi1r=phi1exactr;
phi2f=phi2exactf; phi2r=phi2exactr;

phif[1] = phi1exactf; phif[2] = phi2exactf;
phir[1] = Expand[phi1exactr]; phir[2] = Expand[phi2exactr];

(* final integrals *)

rho=1000;
Df=0.00635;
Dr=0.0127;
Drin=0.01077;
m0=0.05671;      (* mass per unit length, flexible section *)
mr=0.3013;           (* mass per unit length rigid section
Mpiece=0.024;

Cmaf=1.00 ;
Cmar=1.332;              (* added mass coeff in array*)
mabf=rho*Pi*Df^2/4*Cmaf;
mabr=rho*Pi*Dr^2/4*Cmar; (* added mass per unit length,
 wet section*)
Cmab=mabr/m0;
m0b=m0/(a^2*rho*Dr^2);      (* non-D mass                    *)

I0f=3.01846^(-11);
I0r=((Dr/2)^4-(Drin/2)^4)*Pi/4;
```

```
(*  special functions *)

psi1f=1;            (* mass distrbution function              *)
psi1r=mr/m0;

psi3f=mabf/mabr;       (*   0 < x < l1                   *)
psi3r=1.0;          (*  l1 < x < lw               *)
psi3rdry=0.0;          (*  x > lw                    *)

psi4f=1.0;          (* moment of inertia   0 < x < l1      *)
psi4r=I0r/I0f;

psi2flow=1.0;             (* flow vel.  l1 < x < lw      *)
psi2noflo=0.0;

(* THE MASS MATRIX *)


Do[{
   Do[{
      M1[i,j] = NIntegrate[psi1f*phif[i]*phif[j], {x,0,l}],
      M2[i,j] = NIntegrate[psi1r*phir[i]*phir[j], {x,l,l2}],
         M3[i,j] = NIntegrate[psi3f*phif[i]*phif[j], {x,0,l}],
         M4[i,j] = NIntegrate[psi3r*phir[i]*phir[j], {x,l,lw}],
         Mpce[i,j] = Mpiece*phir[i]*phir[j] /. x-> l2,

      M[i,j]=M1[i,j]+M2[i,j]+M3[i,j]+M4[i,j]+Mpce[i,j],
      Print[M[i,j]]

     } ,{j,1,n}],
   } ,{i,1,n}];

Print[MatrixForm[M]];

0.00366
0.00838144
0.00838144
0.127312
MatrixForm[M]
```

```
(* STIFFNESS MATRIX *)

(see output next page )

Do [{
    Do[{
        K[i,j] = NIntegrate[psi4f*D[phif[i],{x,2}]*D[phif[j],{x,2}],
         {x,0,l}],
        Print[K[i,j]],
       } ,{j,1,n}],
   } ,{i,1,n}]
```

```
0.0645449
0.974836
0.974836
1126.75
```

```
(* THE FLUID FORCES *)

yr = 0;
wr = 0;
Do [{
    yr = yr + phir[i]*q[i],
    wr = wr + phir[i]*p[i],
   },{i,1,2}];


CD = 6.5 * 1.5; (* 1.5 is Re factor *)
CL = -31.276*yr + 301.706*yr^3 - 863.689*yr^5;
Print[ Expand[CL]];


(* THE FORCES F1,F1b, D, Db (exluding mechanical damping)*)

Do [{

    F1[i] = V0^2/(2*m0b)*Integrate[Expand[CL*phir[i]], {x,l,lw}],
   F1b[i] = V0^2/(2*m0b)*Integrate[Expand[CD*phir[i]], {x,l,lw}],

    Do[{
        F2[i,j] = -V0/m0b*Integrate[Expand[CL*phir[i]*phir[j]],
         {x,l,lw}],
       F2b[i,j] = -F2[i,j]/2;

       D[i,j] = -V0/(2*m0b)*Integrate[Expand[CD*phir[i]*phir[j]],
       {x,l,lw}],
       Db[i,j] = Cf[i,j]*2;

      } ,{j,1,n}];
   } ,{i,1,n}];



(* FORCE F1 in column Vector FORM *)

F1mat=Table[F1[i],{i,1,n}];MatrixForm[F1mat]
```

$$1.42206\ V0^{2}\ (-0.00935826\ q[1] + 0.000129129\ q[1]^{3} - 5.81371\ 10^{-7}\ q[1]^{5} - 0.0548193\ q[2] +$$
$$0.00172798\ q[1]^{2}\ q[2] - 0.0000101561\ q[1]^{4}\ q[2] + 0.0133463\ q[1]\ q[2]^{2} -$$
$$0.00012609'\ q[1]^{3}\ q[2]^{2} + 0.0470262\ q[2]^{3} - 0.0011421\ q[1]^{2}\ q[2]^{3} -$$
$$0.0064777\ q[1]\ q[2]^{4} - 0.0168388\ q[2]^{5})$$

$$1.42206\ V0^{2}\ (-0.0548193\ q[1] + 0.000575992\ q[1]^{3} - 0.00000203122\ q[1]^{5} - 0.517645\ q[2] +$$
$$0.0133463\ q[1]^{2}\ q[2] - 0.0000630469\ q[1]^{4}\ q[2] + 0.141079\ q[1]\ q[2]^{2} -$$
$$0.0011421\ q[1]^{3}\ q[2]^{2} + 0.591295\ q[2]^{3} - 0.0129554\ q[1]^{2}\ q[2]^{3} - 0.084194\ q[1]\ q[2]^{4} -$$
$$0.238572\ q[2]^{5})$$

```
(* FORCE F1b in Column Vector Form*)
F1bmat=Table[F1b[i],{i,1,n}];MatrixForm[F1bmat]
```

$$0.114829\ V0^{2}$$

$$0.772585\ V0^{2}$$

```
(* FORCE F2 in Matrix Form  *)
(* see output next page *)
F2mat=Table[F2[i,j],{i,1,n},{j,1,n}];MatrixForm[F2mat]
```

$$-2.84412\ V0\ (-0.000349053\ q[1] + 0.00000507047\ q[1]^3 - 2.36724\ 10^{-8}\ q[1]^5 - 0.00178047\ q[2] + 0.0000597729\ q[1]^2\ q[2] - 3.71432\ 10^{-7}\ q[1]^4\ q[2] + 0.000414251\ q[1]\ q[2]^2 - 0.00000413423\ q[1]^3\ q[2]^2 + 0.00135531\ q[2]^3 - 0.000034386\ q[1]^2\ q[2]^3 - 0.000183681\ q[1]\ q[2]^4 - 0.000458191\ q[2]^5)$$

$$-2.84412\ V0\ (-0.00178047\ q[1] + 0.0000199243\ q[1]^3 - 7.42864\ 10^{-8}\ q[1]^5 - 0.0152578\ q[2] + 0.000414251\ q[1]^2\ q[2] - 0.00000206711\ q[1]^4\ q[2] + 0.00406593\ q[1]\ q[2]^2 - 0.000034386\ q[1]^3\ q[2]^2 + 0.0162326\ q[2]^3 - 0.000367361\ q[1]^2\ q[2]^3 - 0.00229096\ q[1]\ q[2]^4 - 0.00630779\ q[2]^5)$$

$$-2.84412\ V0\ (-0.00178047\ q[1] + 0.0000199243\ q[1]^3 - 7.42864\ 10^{-8}\ q[1]^5 - 0.0152578\ q[2] + 0.000414251\ q[1]^2\ q[2] - 0.00000206711\ q[1]^4\ q[2] + 0.00406593\ q[1]\ q[2]^2 - 0.000034386\ q[1]^3\ q[2]^2 + 0.0162326\ q[2]^3 - 0.000367361\ q[1]^2\ q[2]^3 - 0.00229096\ q[1]\ q[2]^4 - 0.00630779\ q[2]^5)$$

$$-2.84412\ V0\ (-0.0152578\ q[1] + 0.000138084\ q[1]^3 - 4.13423\ 10^{-7}\ q[1]^5 - 0.172485\ q[2] + 0.00406593\ q[1]^2\ q[2] - 0.000017193\ q[1]^4\ q[2] + 0.0486978\ q[1]\ q[2]^2 - 0.000367361\ q[1]^3\ q[2]^2 + 0.218881\ q[2]^3 - 0.00458191\ q[1]^2\ q[2]^3 - 0.0315389\ q[1]\ q[2]^4 - 0.0927262\ q[2]^5)$$

(* FORCE F2b in Matrix Form *)

(F2b=F2/2)

(* FORCE D in Matrix Form (no mechanical damping)*)

```
Cfmat=Table[Cf[i,j],{i,1,n},{j,1,n}];MatrixForm[Cfmat]
-0.00414865 V0  -0.0243022 V0

-0.0243022 V0   -0.229479 V0
```

(* FORCE Db in Matrix Form *)

```
Cfbmat=Table[Cfb[i,j],{i,1,n},{j,1,n}];MatrixForm[Cfbmat]
-0.00829729 V0  -0.0486043 V0

-0.0486043 V0   -0.458958 V0
```